universität wien

DISSERTATION / DOCTORAL THESIS

Titel der Dissertation /Title of the Doctoral Thesis

Novel Quantum Optical Experiments featuring Quantum Coherence and Quantum Communication

verfasst von / submitted by

Johannes Pseiner

angestrebter akademischer Grad / in partial fulfillment of the requirements for the degree of

Doktor der Naturwissenschaften (Dr. rer. nat)

Wien, 2022 / Vienna 2022

Studienkennzahl lt. Studienblatt / degree programme code as it appears on the student record sheet:	UA 796 605 411
Studienrichtung lt. Studienblatt / degree programme as it appears on the student record sheet:	Physik
Betreut von / Supervisor:	Priv. Doz. Ass. Prof. Mag. Dr. Marcus Huber

Abstract

The investigation and demonstration of novel and counter-intuitive phenomena, conducted in two quantum optical experiments featuring quantum coherence and quantum communication, shall be the main objectives of this thesis. Furthermore, the consequences in terms of developing quantum technology are investigated. In that sense, the manipulation of individual photonic quantum systems, which exploit the counter intuitive properties of photons, represent a plethora of possibilities to search for consequences on quantum mechanic's foundations and applicable fields in quantum information.

The first experiment demonstrates the properties of quantum coherence and indistinguishability of the photon, which can be seen as both the cornerstone of quantum theory and a prerequisite for the superior measurement accuracy of some quantum technologies compared to their classical counterparts. In detail, a first- and second-order interference effect of down-converted photon pairs created by a parametric process in two nonlinear crystals being far apart from each other (several 10^1 m) are investigated.

Subsequently, another quantum optical experiment in the field of quantum communication is conducted. As multi-pair emissions with increasing pump power in the Spontaneous Parametric Down-Conversion (SPDC) process limit the secure key rate generation of a given photon-based QKD system, an additional degree of freedom in entangled photons, namely their wavelength, is exploited. The introduced approach is based on a method commonly known in optical communication as "wavelength division multiplexing" (WDM) and is expected to play a major role in future implementations of quantum communication.

The overall aim of this dissertation is to fundamentally understand the quantum nature of SPDC photons and their coherence properties with novel experimental setups, but also to use the unique features of entanglement combined with the photon's intrinsic property of their wavelength for future applications.

Vorwort

Die Untersuchung und Demonstration neuartiger und kontraintuitiver Phänomene in zwei quantenoptischen Experimenten mit dem Fokus auf Quantenkohärenz und Quantenkommunikation soll das Hauptziel dieser Arbeit sein. Darüber hinaus werden die Konsequenzen im Hinblick auf die Entwicklung von Quantentechnologien untersucht. In diesem Sinne stellt die Manipulation individueller photonischer Quantensysteme, worin die counter intuitiven Eigenschaften von Photonen ausgenutzt werden, eine Fülle von Möglichkeiten dar, um nach Konsequenzen für die Grundlagen der Quantenmechanik und die Anwendungsgebiete der Quanteninformation zu suchen.

Das erste Experiment demonstriert die Eigenschaften der Quantenkohärenz und Ununterscheidbarkeit des Photons, die sowohl als Grundpfeiler der Quantentheorie als auch als Voraussetzung für die überlegene Messgenauigkeit von einigen Quantentechnologien, verglichen zu ihren klassischen Pendants, angesehen werden können. Im Detail wird ein Interferenzeffekt erster und zweiter Ordnung von Photonenpaaren, die durch einen parametrischen Prozess in zwei weit voneinander entfernten nichtlinearen Kristallen (einige 10^1 m) erzeugt werden, untersucht.

Zum anderen wird ein weiteres quantenoptisches Experiment aus dem Bereich der Quantenkommunikation durchgeführt. Da Emissionen höherer Ordnung mit zunehmender Pumpleistung im SPDC-Prozess die Erzeugung eines sicheren Quantenschlüssels begrenzen, soll ein zusätzlicher Freiheitsgrad der verschränkten Photonen, nämlich ihre Wellenlänge, ausgenutzt werden. Die verwendete Vorgehensweise ist angelehnt an eine Methode, die in der optischen Kommunikation allgemein als "wavelength division multiplexing" (WDM) bekannt ist und eine tragende Rolle in zukünftigen Implementierungen der Quantenkommunikation spielen soll.

Das übergeordnete Ziel dieser Dissertation ist es, die Natur der SPDC-Photonen und ihre Kohärenzeigenschaften mit neuartigen Versuchsaufbauten fundamental zu verstehen, aber auch die einzigartigen Eigenschaften der Verschränkung in Kombination mit der dem Photon intrinsischen Eigenschaft der Wellenlänge für zukünftige Anwendungen zu nutzen.

Contents

List of Abbrevations

AoA Angle-of-arrival

APD Avalanche photodiode

BS Beam splitter

BPF Bandpass filter

cps Counts per second

CW Continuous wave

CWL Central wavelength

DM Dichroic mirror

dHWP Dual-wavelength half-wave plate

dPBS Dual-wavelength polarizing beam splitter

EPR Einstein-Podolsky-Rosen

FC Fiber coupler

FPC Fiber polarization controller

FoV Field of view

FPGA Field programmable gate array

FWHM Full width at half maximum

HWP Half-wave plate

i Idler photon

MMF Multi mode fiber

p Pump photon

PBS Polarizing beam splitter

PPKTP Periodically poled KTiOPO4

QKD Quantum key distribution

QPM Quasi-phase matching

QWP Quarter-wave plate

s Signal photon

SHG Second-harmonic generation

SMF Single-mode fiber

SNR Signal-to-noise ratio

SPDC Spontaneous parametric down-conversion

TTL Transistor-transistor logic

TTM Time-tagging module

TTU Time-tag unit

VHG Volume Holographic Grating

WM Wavelength multiplexing

Chapter 1

Introduction

1.1 Motivation

Photons are the perfect candidate to perform experiments in order to investigate foundational quantum mechanics due to their lack of charge and their ability to remain coherent, meaning to keep their quantum properties while being exposed to perturbating environment. Furthermore, the spatial guidance of coherent light sources, such as lasers, in the form of e.g. dielectric mirrors and lenses can be performed not only at room temperature but also in an ordinary air-conditioned room at atmospheric pressure. The field of quantum optics possesses advantages such as low-noise quantum systems with high-fidelity control and suitability for long-distance transmission in either waveguides or free space.

The advancement of the field of quantum technology has been partly driven by applicable considerations, but mainly from appreciation of foundational quantum physics. Therefore, this thesis shall form a bridge linking the foundation of quantum mechanics to quantum technology.

1.2 Thesis overview

This dissertation inhabits the following structure: An introductory overview of the relevant concepts of quantum information is given in chapter 2. Here, the emphasis lies on measuring qubits, where information is encoded in the polarization degree of freedom of photons. Apart from that, the generation of photon pairs via SPDC in nonlinear crystals and their fundamental properties in terms of their spatial and spectral behavior are treated.

In chapter 3, a detailed study and step-by-step instruction of an experimental implementation of the two-photon nonlinear interference in free space of SPDC photon pairs in a ppKTP crystal is covered. First, the underlying formalism of nonlinear interference between two nonlinear sources of photon pairs is treated, followed by the design and technical implementation of the sending and receiving stations. Thus the measurement results are shown, which are subsequently discussed and summarized at the end of this chapter.

Closing with chapter 4, a novel approach to increase the secure key rate of a QKD system by exploiting the spectral degree of freedom of entangled photon pairs is introduced. Starting by introducing the polarization-entangled photon source, this chapter then discusses a theoretical

error model for secure key rate estimation. Later in that chapter it is shown, in what way the finite timing resolution of single-photon detectors can be circumvented to effectively increase the secure key rate of certain QKD systems. The measurement results are presented and scalability arguments are discussed. Closing, the findings are summarized and a brief outlook on future applications is given.

Chapter 2

Background

A thorough understanding of the physical phenomenology of the experiments presented in this thesis as well as an interpretation of the experimental results require a profound examination of the underlying theoretical formalism and shall be dealt with as follows.

The primary focus of attention will be the manipulation and measurement of information encoded in photonic systems, which requires a quantum mechanical formalism of describing single-photon states. Furthermore, as the theoretical description of the creation of two-photon states in non-linear crystals and their propagation behavior in free space forms a foundation of many new applications in the field of quantum information, a brief overview shall be given. For reasons of clarity and comprehensibility, in-depth mathematical treatment of the formalisms was avoided. For that, the reader shall be referred to introductory quantum mechanics and quantum optics literature [1–4].

2.1 Encoding information in photons

Intrinsic properties of excitations of the electromagnetic field, photons [5], bear tremendous potential regarding encoding information, due to their non-local behavior such as superposition and entanglement. Properties of composite quantum systems such as entangled photons can be exploited for unconditional secure exchange of information and also build the foundation for fundamental experiments through their non-local nature.

2.1.1 Basic concepts of quantum information

Qubit

In classical information theory, the basic unit of information is 1 *bit*, which is a portmanteau word from "binary digit". It represents a logical state and can be assigned either one of two values: "0" or "1". As the classical bits can be freely copied, shared, measured, and deleted, the breakthrough of the classical transistor computing systems was inevitable, also because of their scalable behavior ("Moore's Law" [6]).

In quantum information theory, where information processing is performed by using quantum systems, the corresponding basic information unit is the quantum bit or *qubit*. Quantum states

of quantum systems such as the *qubit* are represented as vectors in a complex vector space, the *Hilbert* space $\mathcal{H}$, which is a complete inner product space. If the elements of an orthonormal basis are defined in this space $|0\rangle$ and $|1\rangle$, then a normalized two-dimensional vector can take the form

$$|\psi\rangle = \mathcal{A}|0\rangle + \mathcal{B}|1\rangle, \qquad |\mathcal{A}|^2 + |\mathcal{B}|^2 = 1, \tag{2.1}$$

where $\mathcal{A}, \mathcal{B} \in \mathbb{C}$. In mathematical nomenclature, 'bra' ($|\cdot\rangle$) and 'ket' ($\langle\cdot|$) refer to the first and second argument of the inner product $\langle\cdot|\cdot\rangle$, respectively. In the notation used above, 'ket' refers to a vector $|\Psi\rangle$ in the *Hilbert* space, and 'bra' refers to a (co-) vector in the *dual Hilbert* space $\mathcal{H}^*$, which is isometrically isomorphic to $\mathcal{H}$. The complex amplitudes provide more freedom in terms of possible measurement outcomes compared to classical bits, as long as the normalization (see Eq. 2.1) holds. However, there exist restrictions on how quantum information can be copied, shared [7], measured, and deleted [8]. In fact, the *no-cloning theorem* [9] refers to the fact that quantum information cannot be copied with perfect fidelity and nullifies the possibility of faster-than-light communication.

Superposition and projection measurement

Superposing two or a series of states forming a final quantum state is a fundamental principle in quantum mechanics, as there exists no classical analogy to quantum superposition. An arbitrary superposed state takes the form

$$|\psi\rangle = \sum_j C_j \, |\phi_j\rangle \,, \tag{2.2}$$

where $C_j \in \mathbf{C}$ and $|\phi_j\rangle$ forms an orthonormal set of basis vectors.

Mathematically spoken, the state in Eq. 2.2, as well as a *qubit*, forms a linear combination of two or more vectors in the complex Hilbert space. The coefficients in these states are complex probability amplitudes that play a major role in projective measurements of a quantum state. A measurement operation of observables on a quantum state can be described by hermitian operators $\hat{\mathcal{O}}$, which yield, in terms of the orthogonal projection operator $\hat{\mathcal{P}}_i$, the following form:

$$\hat{\mathcal{P}}_i = |m_i\rangle\langle m_i| \,, \qquad \hat{\mathcal{O}} = \sum_i m_i \hat{\mathcal{P}}_i, \tag{2.3}$$

with the eigenvalues m_i of $\hat{\mathcal{O}}$ as possible measurement outcomes. The probability of a quantum state $|\Psi\rangle$ residing in the state $|m_i\rangle$ is equal to

$$P\left(m_i\right) = \left\langle \psi \middle| \hat{\mathcal{P}}_i \middle| \psi \right\rangle = |\langle\psi|m_i\rangle|^2 \,. \tag{2.4}$$

After the projection operation, the system is described by the eigenvector $|m_i\rangle$. In other words, performing a projection measurement leads to the collapse of the former quantum state into one of the mutually exclusive measurement outcomes [10]. Any additional projection $\left(\hat{\mathcal{P}}^2 = \hat{\mathcal{P}}^n = \hat{\mathcal{P}}\right)$ of the state results in $|m_i\rangle$ with a probability equal to unity. In fact, the more information about the state is revealed by the measurement outcome, the larger the disturbance on the system [11]. The correlation of information and disturbance in quantum measurements can be understood as the

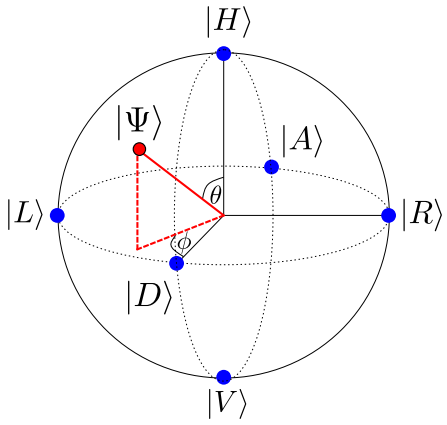

Figure 2.1: A visual representation of a two-level quantum state $|\psi\rangle$ with the polarization degree of freedom on the *Poincaré*-sphere is given. Here, the linear polarization states lie on a circle along the north pole (indicated by the horizontal polarization state $|H\rangle$) and south pole (indicated by the vertical polarization state $|V\rangle$). Furthermore, the diagonal ($|D\rangle$) and anti-diagonal ($|A\rangle$) polarization states are also included in the linear polarization states. The left and right circular polarization states are on the left-hand ($|L\rangle$) and right-hand ($|R\rangle$) side of the sphere's equator, respectively.

following trade-off: increased obtained information is accompanied by an increase of disturbance. Born's rule [12] postulates that the probability of a measurement outcome is given by the square of the modulus of state's complex amplitudes, given that the measured observable corresponds to a self-adjoint operator $\hat{\mathcal{O}}$ with discrete spectrum (see Eq. 2.3) and the measurement is performed on a system described by a normalized wave function. In the case of a pure state such as given in Eq. 2.1, the probabilities are equal to $|\mathcal{A}|^2$ and $|\mathcal{B}|^2$, corresponding to the states $|0\rangle$ and $|1\rangle$, respectively. The Born Rule can be understood as the fundamental bridge between experimental measurement and theoretical prediction [13].

Polarization

An intrinsic property of a single photon, namely the polarization, can be exploited to encode information by assigning

$$|0\rangle \equiv |H\rangle, \quad |1\rangle \equiv |V\rangle, \tag{2.5}$$

where H and V correspond to the horizontal and vertical polarization, respectively. An intuitive approach for visualizing single-photon states of polarization is the representation on the *Poincaré* sphere as depicted in Fig. 2.1. The polarization state of a single photon, where the polarization describes the transverse oscillation of a wave such as electromagnetic waves, can be expressed in terms of a coherent superposition of $|H\rangle$ and $|V\rangle$, with the pure quantum state now taking the form:

$$|\psi\rangle = \cos(\theta)|H\rangle + e^{i\phi}\sin(\theta)|V\rangle, \tag{2.6}$$

with $0 \leqslant \theta \leqslant \pi$ being the polar angle and $0 \leqslant \phi \leqslant 2\pi$ the azimuthal angle of the Poincaré sphere.

Within the representation of the Poincaré sphere, the coordinate axes are the eigenvectors of the 2×2 hermitian Pauli operators:

$$\hat{\sigma}_1 = \begin{pmatrix} 0 & 1 \\ 1 & 0 \end{pmatrix}, \hat{\sigma}_2 = \begin{pmatrix} 0 & -i \\ i & 0 \end{pmatrix}, \hat{\sigma}_3 = \begin{pmatrix} 1 & 0 \\ 0 & -1 \end{pmatrix}, \tag{2.7}$$

which, together with the identity operator $\hat{\sigma}_0 = \mathbb{1}$, form a complete basis for 2×2 Hermitian operators.

Followed by this, every single-qubit polarization density operator can be written as

$$\hat{\rho}(a) = \frac{1}{2}(\mathbb{1} + \mathbf{a} \cdot \boldsymbol{\sigma}), \tag{2.8}$$

where $\mathbf{a} \in \mathbb{R}^3$ is a three-dimensional vector in the Poincaré sphere and $\boldsymbol{\sigma} = (\sigma_1, \sigma_2, \sigma_3)$. Pure states described by $|\mathbf{a}| = 1$ reside on the surface of the Poincaré sphere, while mixed states are located inside ($\mathbf{a} < 1$).

With respect to the basis formed by $|H\rangle$ and $|V\rangle$, other polarization states can be expressed as a superposition of the two states:

$$\begin{aligned} |H\rangle &= \begin{pmatrix} 1 \\ 0 \end{pmatrix} \quad , |V\rangle = \begin{pmatrix} 0 \\ 1 \end{pmatrix}, \\ |D\rangle &= \frac{1}{\sqrt{2}} \begin{pmatrix} 1 \\ 1 \end{pmatrix}, |A\rangle = \frac{1}{\sqrt{2}} \begin{pmatrix} 1 \\ -1 \end{pmatrix}, \\ |R\rangle &= \frac{1}{\sqrt{2}} \begin{pmatrix} 1 \\ i \end{pmatrix}, |L\rangle = \frac{1}{\sqrt{2}} \begin{pmatrix} 1 \\ -i \end{pmatrix}, \end{aligned} \tag{2.9}$$

corresponding to horizontal (H) and vertical (V), diagonal (D) and antidiagonal (A) as well as right-handed circular (R) and left-handed circular (L) polarization.

2.1.2 Entanglement

Standing in the center of interest in countless both physical and philosophical questions for decades, the concept of *quantum entanglement* never ceases to amaze us. The exploitation of the entanglement phenomenon paves the way for novel technologies such as quantum key distribution, quantum computing, and quantum metrology. Erwin Schrödinger defined in his intriguing paper from 1935 an *entangled* quantum state as two or more systems which cannot be described by a product of the states, hence they cannot be assigned individually to a state of their own [14]. Hence, even with large distances between them, quantum systems show correlations that cannot be explained within the framework of classical mechanics. It can be shown that these correlations are so strong that no physical theory according to an intuitive definition of locality can describe this phenomenon.

A short overview and insight about this topic shall be given in the following section, as well as the connection to presented results in this thesis.

On the EPR paradox

Einstein, Podolsky, and Rosen raised the question of the completeness of quantum mechanics and claimed to have found a contradiction within quantum theory [15]. Their argument was

based on their interpretation of reality, that "*a sufficient condition for the reality of a physical quantity is the possibility of predicting it with certainty, without disturbing the system*", as well as of completeness, as "*every element of the physical reality must have a counterpart in the physical theory*". Measuring one of two non-commuting physical quantities implies, that the other quantity is maximally unknown, which leads to their conclusion that either quantum theory is not complete or non-commuting quantities do not have simultaneous reality.

However, measurements on a composite quantum system including two particles being e.g. in a pure polarization state, where the Pauli operator commutation relations $[\hat{\sigma}_i \hat{\sigma}_j] = 2i\epsilon_{ijk}\hat{\sigma}_k$ hold, imply that two non-commuting quantities indeed can have reality at the same time, "*since at the time of measurement the two systems no longer interact, no real change can take place in the second system in consequence of anything that may be done to the first system*". The latter statement combined with the previous argument of the non-existence of two quantities having simultaneous reality leads to a contradiction and caused EPR to believe that quantum mechanics was not complete.

Bell's inequality

Almost 30 years later, an experimentally testable prediction discovered by John Bell [16] tackled EPR's premises of locality and realism on the quality of correlations between outcomes of distant measurements on a pair of quantum systems. Locality implies that the outcome is independent of the remote measurement. The so-called *Bell* inequalities can be violated by quantum mechanics. The inequality describes correlations of measurement outcomes of a scheme including two receivers, Alice and Bob, randomly switching between two measurement settings, a_1 or a_2 and b_1 or b_2, with only two possible outcomes, e.g. +1 and -1, respectively. These correlations satisfy certain inequalities, assuming local realism. In fact, if the results of the Bell test obey the inequality, the system evolves such that past information was passed on within postulated hidden variables. Hence, physical systems violating the inequality rely on the assumption of statistical independence of the measurement settings with respect to probable past events that might have influenced them [17]. Dropping the assumption of statistical independence in the physical world goes hand in hand with the recently attention-gaining theory of superdeterminism [18].

A rather realistic experimental approach to formulate this inequality is represented by the Clauser-Horne-Shimony-Holt (CHSH) [19] inequality, which says that according to a local hidden variable theory, the correlations are limited by

$$S = |\mathcal{E}(a_1 b_1) + \mathcal{E}(a_1 b_2)| + |\mathcal{E}(a_2 b_1) - \mathcal{E}(a_2 b_2)| \leqslant 2, \tag{2.10}$$

where $\mathcal{E}(a_i\ b_j)$ is the expectation value of the product of the outcomes of the experiment, hence for Alice measuring at setting a_i and Bob at setting b_j, respectively.

Experimental tests of local realism were performed numerous times, especially with photons [20–25]. For a polarization-entangled quantum state such as the one shown in the following subsection, the measurement settings become measurements along certain directions, while the maximum S-value breaking the Bell inequality are along the measurement directions $a_1, a_2, b_1, b_2 = 0^\circ, 45^\circ, 22.5^\circ, 67.5^\circ$, leading to an S-value of $2\sqrt{2}$, thus violating Eq. 2.10.

Bell states

Previously, individual systems (e.g., *qubits*) described by state vectors $|\psi\rangle$ or density matrices ρ defined in a certain *Hilbert* space were considered. However, one can encode more than one *qubit* of quantum information into a respective quantum system, when joint quantum systems

are considered. Two particles A and B, while each is described by the Hilbert spaces $\mathcal{H}_A$ and $\mathcal{H}_B$, can be characterized in a combined Hilbert space $\mathcal{H}$ by the tensor product and is given by

$$\mathcal{H} = \mathcal{H}_A \otimes \mathcal{H}_B, \tag{2.11}$$

while the tensor product of Hilbert spaces is again a Hilbert space with dimension $\dim(\mathcal{H}_A \otimes \mathcal{H}_B) = \dim(\mathcal{H}_A) \cdot \dim(\mathcal{H}_B)$.

The composite *separable* two-qubit quantum state of two particles can be written as

$$|\Psi\rangle = |\psi\rangle_A \otimes |\psi\rangle_B, \tag{2.12}$$

while the tensor product is omitted when the context does not require it: $|\psi\rangle_A \otimes |\psi\rangle_B = |\psi\rangle_A|\psi\rangle_B = |\psi_A, \psi_B\rangle$.

As mentioned above, when subsystems as elements of a composite quantum system cannot be described independently from each other ($|\Psi\rangle \neq \bigotimes_j |\psi_j\rangle$), they are called *entangled*. The crucial property of entangled systems is that their quantum mechanical states cannot be factorized into fractions corresponding to the respective subsystems. An important class of entangled states, namely the four orthogonal maximally entangled two-qubit states, are the *Bell* states, here presented in the polarization degree of freedom:

$$\begin{aligned} \left|\psi^{\pm}\right\rangle &= \frac{1}{\sqrt{2}}(|HV\rangle \pm |VH\rangle) \\ \left|\phi^{\pm}\right\rangle &= \frac{1}{\sqrt{2}}(|HH\rangle \pm |VV\rangle), \end{aligned} \tag{2.13}$$

including 3 symmetric quantum states $|\psi^+\rangle$, $|\phi^+\rangle$, $|\phi^-\rangle$ and the antisymmetric singlet state $|\psi^-\rangle$. Bipartite entangled quantum states such as those shown in Eq. 2.13 bear correlations of counter intuitive nature as described above: Measurements performed on one of the particles lead to a collapse of the wavefunction, hence instantaneously assigning the measurement outcomes on both sides.

Separability criterion and fidelity

The detection of photon states is of great importance to an experimenter and therefore requires an extensive discussion. Due to the imperfection of measurement devices and inevitable noise, this task can be an experimental challenge. Numerous theoretical criteria exist in order to identify an entangled state and for a more intensive treatment, the reader is referred to [26]. A short overview of the possible approaches regarding separability criteria for identifying entanglement of quantum systems shall be given as follows.

A sufficient entanglement criterion in terms of directly measurable observables shall be used. A useful operator not only for identifying bipartite but also multi-particle entangled states is the *entanglement witness* W, which is defined as

$$\begin{aligned} Tr\,(W\varrho_s) &\geqslant 0, \\ Tr\,(W\varrho_e) &< 0, \end{aligned} \tag{2.14}$$

for all separable ϱ_s and for at least one entangled ϱ_e. Conveniently, a useful construction of W considers the experimental imperfectness of an entangled state, which describes the "closeness" to a maximally entangled state $|\psi\rangle$:

$$\mathrm{W} = \gamma\mathbb{1} - |\psi\rangle\langle\psi|. \tag{2.15}$$

The quantity

$$F_\psi(\hat{\rho}) = \mathrm{Tr}\left(\hat{\rho}\,|\psi\rangle\langle\psi|\right) \tag{2.16}$$

describes the overlap fidelity of the quantum state $\hat{\rho}$ with the entangled pure state $|\psi\rangle$. In the case that the fidelity F exceeds a critical value γ, the witness's expectation value becomes negative, followed by the fact that the state $\hat{\rho}$ is entangled. For a perfect overlap with the ideal Bell state, the fidelity of a generated state has the value 1, while e.g. for a maximally mixed state with dim = 4, the fidelity is 0.25. For two-qubit states, entanglement is verified when the threshold fidelity is exceeded, namely $F > 0.5$. For the theoretically derived proof, the reader is referred to Ref. [27]. The value γ can be determined regarding a sufficient separability criterion by $\gamma = \max_{\hat{\rho}\to sep.} |\langle\psi|\phi\rangle|^2$ [26].

Common experimental methods of verifying whether a bipartite mixed state is entangled require the detection of both photons, involving coincidence measurements. A direct measurable method can be used [28] by considering a two-qubit density matrix

$$\hat{\rho} = \frac{1}{4}\sum X_{ij}\hat{\sigma}_i \otimes \hat{\sigma}_j \tag{2.17}$$

where X_{ij} are the expectation values $Tr\left(\hat{\rho}\left(\hat{\sigma}_i \otimes \hat{\sigma}_j\right)\right)$ for a certain polarization measurement ($\hat{\sigma_0}$ is the unity operator and $\hat{\sigma}_i$ for $i = 1, 2, 3$ are the Pauli-operators).

Hence, the fidelities regarding the ideal *Bell* states can be expressed as

$$\begin{aligned} F_{\Phi\pm}(\hat{\rho}) &= \frac{1}{4}(1 + \langle\Psi|\sigma_1 \otimes \sigma_1|\Psi\rangle \pm \langle\Psi|\sigma_2 \otimes \sigma_2|\Psi\rangle \mp \langle\Psi|\sigma_3 \otimes \sigma_3|\Psi\rangle) \\ F_{\Psi\pm}(\hat{\rho}) &= \frac{1}{4}(1 - \langle\Psi|\sigma_1 \otimes \sigma_1|\Psi\rangle \pm \langle\Psi|\sigma_2 \otimes \sigma_2|\Psi\rangle \pm \langle\Psi|\sigma_3 \otimes \sigma_3|\Psi\rangle), \end{aligned} \tag{2.18}$$

where the expectation values of the joint polarization measurements of a typical photonic polarization analysis scheme in the respective Pauli basis are called *visibilities* of the measured quantum state $|\Psi\rangle$, being $\mathcal{V}_{HV} = \langle\Psi|\sigma_3\otimes\sigma_3|\Psi\rangle$, $\mathcal{V}_{DA} = \langle\Psi|\sigma_1\otimes\sigma_1|\Psi\rangle$ and $\mathcal{V}_{RL} = \langle\Psi|\sigma_2\otimes\sigma_2|\Psi\rangle$ [26]. Therefore, standard ways of proving entanglement in a bipartite quantum state require coincidence measurements, thus the detection of both particles simultaneously.

Experimental circumstances with respect to limitations of space and availability of experimental elements sometimes prevent the possibility of detecting correlations in three mutually unbiased bases. Measurements in these bases are maximally unbiased, enabling the proof of true randomness or security with respect to the results [29]. A derivation of an entanglement criterion for measuring in two complementary bases has been performed [30]. A compact form of the criterion for a lower bound for the fidelity can be estimated based on the average of the visibility measurements in two mutually unbiased bases, e.g. the HV and DA basis [31]:

$$\frac{\mathcal{V}_{HV} + \mathcal{V}_{DA}}{2} \leqslant F\left(\rho, |\Psi_{\text{Bell}}\rangle\right) = \text{Tr}\left(\rho\, |\Psi_{\text{Bell}}\rangle\langle\Psi_{\text{Bell}}|\right). \tag{2.19}$$

2.2 Spontaneous parametric down-conversion (SPDC)

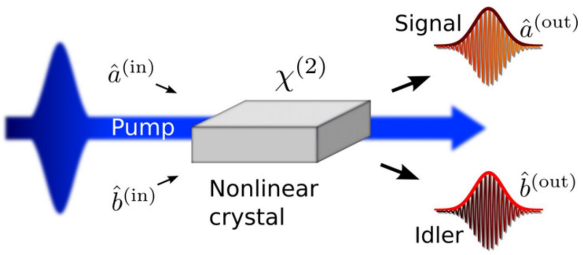

Figure 2.2: A schematic depiction of the Spontaneous Parametric Down-Conversion (SPDC) process is shown. A coherent pump fields illuminates a nonlinear crystal with the optical nonlinearity $\chi(2)$, where it interacts with two vacuum modes $\hat{a}^{(in)}$ and $\hat{b}^{(in)}$, finally emerging as signal ($\hat{a}^{(out)}$) and idler ($\hat{b}^{(out)}$) photons, whose frequencies sum up to the frequency of the pump photon. Adapted from [32].

Numerous to-date experimental implementations involving photonic quantum information processing rely on the process of spontaneous parametric down-conversion (SPDC) [5, 33, 34]. The comprehensive understanding of the spontaneous conversion of one photon into two photons in a nonlinear medium and their properties proves to be crucial for the experiments treated in this thesis. With a small probability ($\sim 10^{-7}$ [35]), a so-called pump photon splits into two photons, both having lower energy, which are historically called "signal" and "idler" (see Fig. 2.2). Within the parametric creation of these strongly correlated photon pairs, whose correlations were first observed by Burnham and Weinberg [33], no energy transfer between photons and the medium with a certain second-order optical nonlinearity [$\chi(2)$] occurs [36]. These correlations arise due to energy and momentum conservation within the process, enabling the generation of entangled photons. These prove useful in foundational physical concepts in loophole-free tests of Bell's inequality or to test optical quantum information theory.

The non-local nature of light has been demonstrated historically by violating Bell's inequality with the two-photon decay of free atoms [37], but unlike in this scenario, the propagation directions of the SPDC photon pairs are strongly correlated. The confined directions of the propagation of the photons lead to the fact that by measuring one photon, the direction of the partner can be predicted. SPDC is a quantum-mechanical phenomenon, as it is not possible to simply rely on classical field theory. Due to the assumed high intensity, the pump field is described by classical means, with the signal and idler fields however have to be quantized. For a more in-depth theoretical description, the reader is referred to literature devoted to SPDC formalism and derivations [38–41].

2.2.1 SPDC two-photon state

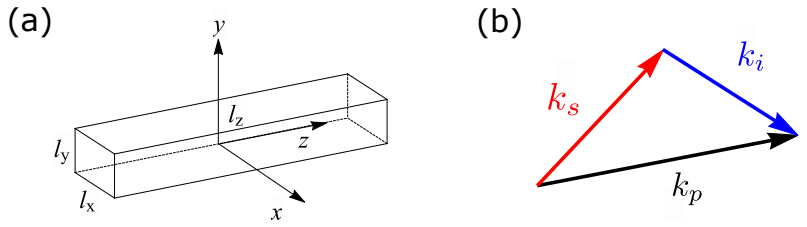

Figure 2.3: (a) The geometry of the nonlinear medium and its spatial dimensions, while the propagation direction of the incoming field is along the z-direction, is shown. The xy-plane corresponds to the transverse plane. (b) The wave vectors of the partaking electromagnetic fields are depicted, showing that momentum conservation holds.

The fundamental understanding of the strong spatial and spectral correlations between the photon pairs created in SPDC as well as their propagation behavior aid in the investigation of quantum theory's foundations and its interpretation. Hence, it will prove to be indispensable for the profound understanding of the measurement results, to theoretically treat the parametric interaction of a quantum field in a nonlinear crystal with an incoming electromagnetic field, which will lead to the final down-converted two-photon state.

With a perturbative treatment the interaction Hamiltonian $\hat{H}_I$ of an electromagnetic field interacting with a quantum field within a nonlinear crystal with volume $V = l_x \times l_y \times l_z$ (see Fig. 2.3) and the nonlinear response function in the form of a second-order susceptibility $\chi^{(2)}_{ijk}$ is given by

$$\hat{H}_I = \frac{1}{2}\int_V d\mathbf{r}\chi^{(2)}_{ijk}\hat{E}^{(+)}_i(\mathbf{r},t)\hat{E}^{(-)}_j(\mathbf{r},t)\hat{E}^{(-)}_k(\mathbf{r},t) + \text{H.C.} \tag{2.20}$$

where $\hat{E}^{(+)}(\mathbf{r},t)$ are quantum fields, which can be written as

$$\hat{E}^{(+)}(\mathbf{r},t) = \frac{1}{\sqrt{\upsilon}}\sum_{\mathbf{k},\zeta}\mathbf{e}_{\mathbf{k},\zeta}\epsilon_{\mathbf{k},\zeta}\hat{a}_{\mathbf{k},\zeta}e^{i(\mathbf{kr}-\omega t)} = \left[\hat{E}^{(-)}(\mathbf{r},t)\right]^{\dagger} \tag{2.21}$$

with υ being the quantization volume of the quantum field and

$$\epsilon_{\mathbf{k},\zeta} = \sqrt{\frac{\hbar\omega(\mathbf{k},\zeta)}{2\epsilon_0 n^2(\mathbf{k},\zeta)}} \tag{2.22}$$

with $\hat{a}_{\mathbf{k},\zeta}$ being the photon annihilation operator, $\mathbf{k}$ the wave vector, $\mathbf{r}$ an arbitrary space vector, $\mathbf{e}_{\mathbf{k},\zeta}$ is the polarization vector in two dimensions, ϵ_0 the free-space permittivity, $n(\mathbf{k},\zeta)$ the linear refractive index of the crystal, ω the frequency, $\hbar$ reduced Planck constant, and $H.C.$ stands for Hermitian Conjugate. The sum over the orthogonal components of the polarization vector labeled by the index ζ and all possible wave vectors $\mathbf{k}$ consider an expansion of the field modes. By inserting Eq. 2.21 into Eq. 2.20, the quantum Hamiltonian in terms of the three partaking fields (signal, idler and pump, indicated by the indices s, i and p, respectively) is obtained:

$$\begin{aligned}\hat{H}_I =& \frac{1}{2\hbar v^{3/2}} \sum_{\mathbf{k}_s,\zeta_s} \sum_{\mathbf{k}_i,\zeta_i} \sum_{\mathbf{k_p},\zeta_p} \mathcal{G}^*_{\mathbf{k}_s,\zeta_s} \mathcal{G}^*_{\mathbf{k}_i,\zeta_i} \mathcal{G}_{\mathbf{k}_p,\zeta_p} \hat{a}^\dagger_{\mathbf{k},\zeta} \hat{a}^\dagger_{\mathbf{k},\zeta} \hat{a}_{\mathbf{k},\zeta} \\ & \times \chi^{(2)}_{ijk} \left(\mathbf{e}_{\mathbf{k}_s,\zeta_s}\right)^*_i \left(\mathbf{e}_{\mathbf{k}_i,\zeta_i}\right)^*_j \left(\mathbf{e}_{\mathbf{k}_p,\zeta_p}\right)_k e^{i(\omega_s+\omega_i-\omega_p)t} \\ & \times \int_V e^{-i(\mathbf{k}_s+\mathbf{k}_i-\mathbf{k}_p)\mathbf{r}} d\mathbf{r} + H.C.\end{aligned} \tag{2.23}$$

with

$$\mathcal{G}_{\mathbf{k}_j,\zeta_j} = i\sqrt{\frac{\hbar\omega\left(\mathbf{k}_j,\zeta_j\right)}{2\epsilon_0 n^2\left(\mathbf{k}_j,\zeta_j\right)}}. \tag{2.24}$$

All terms which do not conserve energy were eliminated and moreover the following was defined

$$\chi^{(2)}_{ijk} \equiv \chi^{(2)}_{ijk}\left(\omega_p = \omega_s + \omega_i\right) + \chi^{(2)}_{ijk}\left(\omega_i = \omega_s + \omega_p\right) + \chi^{(2)}_{ijk}\left(\omega_s = \omega_i + \omega_p\right) \tag{2.25}$$

with

$$\chi^{(2)}_{ijk}\left(\omega = \omega' + \omega''\right) = \int_0^\infty dt' \int_0^\infty dt'' \chi^{(2)}_{ijk}\left(t', t''\right) e^{-i\left(\omega' t' + \omega'' t''\right)}. \tag{2.26}$$

Assuming the χ_{ijk} being spatially constant in the crystal, the spatial integration over the crystal volume V leads to

$$\begin{aligned}\int_V e^{-i(\mathbf{k}_s+\mathbf{k}_i-\mathbf{k}_p)\mathbf{r}} d\mathbf{r} &= \prod_{m=0}^{3} \int_0^{l_m} e^{-i\left(\mathrm{k}_s^m + \mathrm{k}_i^m - \mathrm{k}_p^m\right)\mathrm{r}^m} d\mathrm{r}^m \\ &= V \prod_{m=0}^{3} e^{-\frac{1}{2}i\left(\mathrm{k}_s^m + \mathrm{k}_i^m - \mathrm{k}_p^m\right) l_m} 2\,\mathrm{sinc}\left[-\frac{1}{2}\left(\mathrm{k}_s^m + \mathrm{k}_i^m - \mathrm{k}_p^m\right) l_m\right],\end{aligned} \tag{2.27}$$

where the index m indicates the three spatial dimension of the crystal of lengths l_x, l_y and l_z as described in Fig. 2.3. The sinc-function in the last line is mainly responsible for the efficient interaction, the so-called phase-matching condition, which shall be of interest later on.

The quantum state at time t can then be obtained by applying the time evolution operator $\hat{\mathcal{U}}(t)$ on the initial quantum state $|\Psi(0)\rangle$ as follows, where the expansion of the exponential function is allowed if the weak-gain regime is assumed[1]:

$$\begin{aligned}|\Psi(t)\rangle = \hat{\mathcal{U}}(t)|\Psi(0)\rangle &= e^{1/i\hbar \int_0^t \hat{H}\left(t'\right)dt'} |\Psi(0)\rangle \\ &= |\Psi(0)\rangle + \frac{1}{i\hbar}\int_0^t H\left(t'\right) dt' |\Psi(0)\rangle + ...\end{aligned} \tag{2.28}$$

Under the assumption that at $t = 0$ the state is in the vacuum state[2] $|\Psi(0)\rangle = |vac\rangle|vac\rangle$, inserting Eq. 2.23 into Eq. 2.28 and performing the integration over time t leads to the time dependent SPDC photon state including higher orders:

[1] In other words, it is assumed that the pump field amplitude is sufficiently small, resulting in the fact that the interaction time is small compared to the average time between down-conversion processes [38].

[2] A vacuum state describes a field mode occupying the lowest energy state [42].

$$
\begin{aligned}
|\Psi(t)\rangle = |vac\rangle|vac\rangle + \frac{V}{2i\hbar V^{3/2}} \sum_{\mathbf{k}_s,\zeta_s} \sum_{\mathbf{k}_i,\zeta_i} \sum_{\mathbf{k_p},\zeta_p} & \mathcal{G}^*_{\mathbf{k}_s,\zeta_s} \mathcal{G}_{\mathbf{k}_i,\zeta_i} \mathrm{v}_p\left(\mathbf{k}_p,\zeta_p\right) \\
& \times \chi^{(2)}_{ijk}\left(\mathbf{e}_{\mathbf{k}_s,\zeta_s}\right)^* \left(\mathbf{e}_{\mathbf{k}_i,\zeta_i}\right)^* \left(\mathbf{e}_{\mathbf{k}_p,\zeta_p}\right) \\
& \times \int dt' e^{i(\omega_s+\omega_i-\omega_p)t'} \\
& \times \prod_{m=1}^{3} e^{-i\left(\mathrm{k}_s^m+\mathrm{k}_i^m-\mathrm{k}_p^m\right)l_m/2} \operatorname{sinc}\left[-\left(\mathrm{k}_s^m+\mathrm{k}_i^m-\mathrm{k}_p^m\right)l_m/2\right] \\
& \times |\mathbf{k}_s,\zeta_s\rangle\,|\mathbf{k}_i,\zeta_i\rangle \\
& + \mathcal{O}^2
\end{aligned}
\tag{2.29}
$$

where the quantum pump field was replaced by a classical electromagnetic field with the classical amplitude $\mathrm{v}_p\left(\mathbf{k}_p,\zeta_p\right)$ and the photon annihilation operator $\hat{a}(\mathbf{k},\zeta)$, which is justified as coherent states are eigenstates of the annihilation and creation operators [43]. Furthermore, $|\mathbf{k}_s,\zeta_s\rangle, |\mathbf{k}_i,\zeta_i\rangle$ correspond to the single-photon Fock states in the respective modes.

Eq. 2.29 represents the general form of the SPDC photon state including higher-order terms. In experiments, due to the stochastic nature of SPDC pair sources, these multi-pair emissions play a crucial role in terms of single-photon detection techniques. In the following, the vacuum state can be neglected, as the state of interest is the two-photon SPDC quantum state. With increasing pump power, however, these higher-order emissions can lead to *saturation in time* of the photon detectors, depending on the timing resolution of the detection system. In other words, the temporal overlap of the photon pair's coherence times t_{coh} within a finite measurement timing window increases the probability of falsely identifying uncorrelated photon pairs. Uncorrelated photon pairs contribute to a noise floor, which effectively decreases the degree of entanglement. The influence of the higher-order emissions of SPDC will be treated in more detail in section 2.2.4.

With the following assumptions, the final two-photon contribution in Eq. 2.29 can be simplified. Since the state of equilibrium is of interest, the boundaries of the integration time can be extended to infinity ($t_1 \to -\infty$ and $t_2 \to \infty$), which leads to a term which ensures energy conservation within the process:

$$
\int dt' e^{-i(\omega_p-\omega_s-\omega_i)t'} \to \delta\left(\omega_p-\omega_s-\omega_i\right). \tag{2.30}
$$

By furthermore assuming that, first, the wave-vector distribution of the pump, signal, and idler fields is preferably situated along the propagation direction (z-axis), and second, that l_x and l_y can be extended to infinity as the crystal is large enough in the direction of the x and y axis to contain the whole pump beam transverse profile, the following transformation is valid:

$$
\begin{aligned}
&\prod_{m=1}^{3} e^{-i\left(\mathrm{k}_s^m+\mathrm{k}_i^m-\mathrm{k}_p^m\right)l_m/2} \operatorname{sinc}\left[-\left(\mathrm{k}_s^m+\mathrm{k}_i^m-\mathrm{k}_p^m\right)l_m/2\right] \to \\
&\delta\left(\mathbf{q}_s+\mathbf{q}_i-\mathbf{q}_p\right) \operatorname{sinc}\left[\left(\mathrm{k}_s^z+\mathrm{k}_i^z-\mathrm{k}_p^z\right)L/2\right],
\end{aligned}
\tag{2.31}
$$

where $\mathbf{q}_j = \left(\mathrm{k}_j^x, \mathrm{k}_j^y\right)$ is the transverse (xy) component of $\mathbf{k}_j$ and $L = l_z$ is the crystal length.

This leads to a simplified expression of the final two-photon state:

$$|\Psi\rangle_{SPDC} = \sum_{\zeta_s\zeta_i} \int d\omega_s \int d\omega_i \int d\mathbf{q}_s \int d\mathbf{q}_i \times \phi_{\zeta_s\zeta_i}(\mathbf{q}_s, \mathbf{q}_i, \omega_s, \omega_i) |\mathbf{q}_s, \omega_s, \zeta_s\rangle |\mathbf{q}_i, \omega_i, \zeta_i\rangle, \tag{2.32}$$

whereby the quantization volume can be considered to be large enough to allow the summations over k to be replaced by integrals. The terms $\mathcal{G}_{\mathbf{k}j\zeta_j}$ as well as $\chi^{(2)}_{ijk}$ are slowly-varying functions of $\mathbf{q}_j$; so taking them out of the interval considered for $\mathbf{q}_j$ is justified. The two-photon mode function $\phi_{\zeta_s\zeta_i}$ can be written down as

$$\phi_{\zeta_s\zeta_i} \approx C_{\zeta_s\zeta_i} L \mathrm{v}_p(\mathbf{q}_s + \mathbf{q}_i, \omega_s + \omega_i) \operatorname{sinc}[\Delta \mathrm{k}^z L/2], \tag{2.33}$$

where $C_{\zeta_s\zeta_i}$ represents the effective nonlinear coupling constant, comprising the nonlinear susceptibility $\chi^{(2)}$ as well as $\mathcal{G}$, and k^z is wave-vector mismatch (see definition below). Within the classical amplitude of the pump field $\mathrm{v}_p(\mathbf{q}_s + \mathbf{q}_i, \omega_s + \omega_i)$ the two-photon mode function contains information of the spectral distribution of the pump. Note that the pump beam only includes the so-called extraordinary polarization, which refers to the extraordinary (e) axis of uniaxial nonlinear crystals, while the respective orthogonal axis is called ordinary (o) [34]. The two-photon mode function $\phi_{\zeta_s\zeta_i}$ can be associated with the two-dimensional probability distribution of the signal and idler emission frequencies [44]. A major contribution to the conversion efficiency is given by the z-component of the wave-vector mismatch for a periodically poled nonlinear crystal with the poling period Λ. That is, the period of the electrode pattern on the crystal surface, which defines for which wavelengths the phase-matching condition is fulfilled [45]:

$$\Delta \mathrm{k}^z = \mathrm{k}^z_p(\boldsymbol{q}_s + \boldsymbol{q}_i, \omega_s + \omega_i) - \mathrm{k}^z_s(\boldsymbol{q}_s, \omega_s) - \mathrm{k}^z_i(\boldsymbol{q}_i, \omega_i) - \frac{2\pi}{\Lambda}, \tag{2.34}$$

which dictates the distribution of energy and momentum between the signal and idler fields. Deeper insight and consequences of the spectral distribution, which shall be crucial in the experiments presented in this thesis, is given in the following sections.

2.2.2 Quasi-phase-matching

As discussed above, the phase-matching condition (see Eq. 2.27 and Eq. 2.34) is an intrinsic consequence of the SPDC intensity derivation. Generally, the phase-matching condition defines the direction of propagation of the SPDC fields and therefore the degree of (non-)degeneracy within the wavelength distributions.

For an efficient interaction, the phase velocities of the pump, signal, and idler photons have to be adjusted accordingly to compensate for the frequency-dependent dispersion of the nonlinear medium. Phenomenologically, the different phase velocities of the partaking fields in the crystal, given the lack of fulfilling the phase-matching condition, lead to a phase mismatch, where after the distance d destructive interference occurs. Hence, momentum conservation is not fulfilled throughout the nonlinear medium, but it can be regained by tailoring the refractive index and the angles of propagation [46].

This can be tackled by the repeated inversion of the relative phase between waves after $n \times d/2$ with n being an integer, ensuring a respective growth of the amplitudes of the signal and idler

waves. That requires a harmonic modulation of the crystal's nonlinearity with a period $\Lambda = 2\pi\Delta\mathrm{k}$ [47].

One way to invert the phase is to change the sign of the nonlinear coefficient within the entire nonlinear crystal, which is called quasi-phase-matching. This is achieved by periodical inversion of the material's nonlinear coefficient, which leads to a reduction of the effective nonlinearity by a factor of $2/(\pi m)$, where m is an odd integer that denotes the phase-matching order [41]. In quasi-phase-matched crystals, the signal and idler waves travel collinearly, considering the Taylor expansion of the three longitudinal wave vectors (see [48] for more details) and are limited to a narrow range where the zero-order contribution of the phase-mismatch (Eq. 2.34) vanishes:

$$\Delta\mathrm{k}^{z(0)} = \mathrm{k}_p^z - \mathrm{k}_s^z - \mathrm{k}_i^z - \frac{2\pi}{\Lambda} = 0. \tag{2.35}$$

In the nonlinear crystals used in the experiments of this thesis, periodical poling has been implemented, which can be tuned by different temperatures. Changing the temperature within the crystal leads to different magnitudes in wave vectors, which furthermore alters the wavelengths of the fields. This correlates the spatial modes of signal and idler photons in the way that if one photon is measured at a known angle with respect to the crystal axis, the adjoint photon is determined too.

It is important to realize that the choice of phase-matching configuration also influences the effective strength of the nonlinearity because it determines the directions of the electric fields involved with respect to the crystal axes. Hence the polarization plays an essential role regarding the types of SPDC processes that can be phase-matched. In a type-I phase-matched configuration, signal and idler are parallel polarized but orthogonal to the pump photons. This is commonly described as an '$e-oo$' or an '$o-ee$' type scheme, where both outputs have the same polarization, whereas the input wave has perpendicular polarization. In the ordinary polarization the electric field vector is perpendicular to the plane formed by the optic axis and the propagation direction, while for the extraordinary polarization electric field vector is parallel to the plane formed by the optic axis and the propagation direction [49]. In a type-II phase-matching configuration, the signal and idler fields are orthogonally polarized ('$e-oe$' or '$o-eo$'). Finally, in the type-0 configuration, all partaking fields share the same polarization ('$e-ee$' or '$o-oo$').

The nonlinear coefficient (see Eq. 2.33) in periodically poled KTP crystals, which were used for SPDC photon-pair production in this work, dictates the efficiency of the SPDC process. In fact, the collinear type-0 phase-matched configuration, where all the optical frequencies have the same polarization, allows for large nonlinear coefficients in the nonlinear material [50]. Comparing the two phase-matching configurations within nonlinear crystals presented in this work, the nonlinear coefficient of the type-II phase-matching has been measured to be $d_{yyz} = 3.64\,\mathrm{pm/V}$, while the one for the type-0 has the value $d_{zzz} = 16.9\,\mathrm{pm/V}$ [51]. This leads to the fact, that the brightness B, hence the number of photon pairs per time increment, produced in type-0 media can be larger than the ones of type-II [41].

2.2.3 Spectral properties of SPDC two-photon states

The two-photon mode function $\phi_{\zeta_s\zeta_i}$ (see Eq. 2.33), as part of the two-photon quantum state governs the spectral and temporal distribution of the photon pairs created in the SPDC process. From the two-photon mode function, information about the quantum correlations between the SPDC photon pairs can be distilled. In form of the pump field amplitude v_p, the shape and

profile of the pump beam influences the tempo-spectral distribution of the photon pairs as well as the phase-matching amplitude $\mathrm{sinc}(\Delta \mathrm{k}_z L/2)$.

The spectral output field distribution can be approximated by a Gaussian distribution [52], and a simulation of the two-photon intensity, commonly known as the joint spectral intensity (JSI), can be performed. Fig. 2.4 shows the two major contributions to the JSI (see Fig. 2.5), the pump envelope intensity and the phase-matching intensity as a function of the signal and idler frequencies.

The JSI contains interesting information about the structure and the joint spectrum properties of the SPDC photon pairs. Depending on the material and optical properties of the nonlinear medium and assuming a Gaussian-shaped pump field amplitude [52], the joint spectral amplitude (JSA) takes the form of a (tilted) two-dimensional Gaussian distribution (see Fig. 2.5). It clearly shows an anti-correlation in the signal and idler frequencies: $\omega_s = \omega_p - \omega_i$. These joint intrinsic wavelength correlations of the photon pairs will be of utter importance in the wavelength multiplexing experiment in section 4.

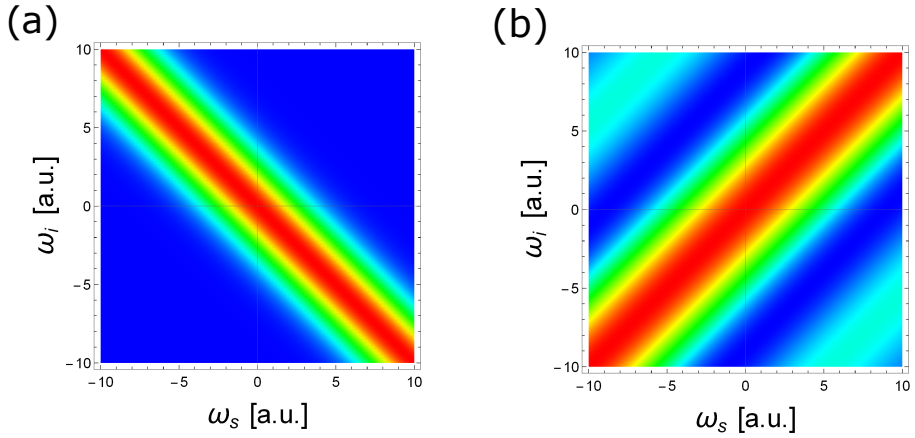

Figure 2.4: (a) The simulation of the pump envelope intensity as a function of the signal (ω_s) and idler (ω_i) frequencies is depicted. For the pump amplitude, a Gaussian distribution of the pump field was assumed. The width of the pump envelope intensity equals the bandwidth of the pump field distribution. (b) The phase-matching intensity follows the sinc-function, where the width corresponds to the reciprocal length of the crystal, $1/L$. The tilting angle of the phase-matching intensity is determined by the group velocities of the three fields in the SPDC process [48]. Finally, the slope of the phase-matching intensity is set by the gradient of Δk [53]

The spectral distribution of the photon pairs created in the SPDC process is of utmost importance as it governs their spectral correlation purity. Hence, a profound characterization of the photon's spectrum dictates the success of any measurement based on, e.g., interference or entanglement, as conducted in the experiments presented in this thesis.

Assuming a fixed spectral distribution of the pump field v_p, which is a valid assumption due to the stable operation of state-of-the-art pump lasers, the phase-matching intensity bears further potential for experimental manipulation. The nonlinear media used in this thesis relied on collinear quasi-phase-matching configurations, and hence shall be in the center of interest for the following considerations. Setting the quasi-phase-matching condition of the SPDC process accordingly (see Eq. 2.35) ensures momentum conservation throughout the medium. This includes

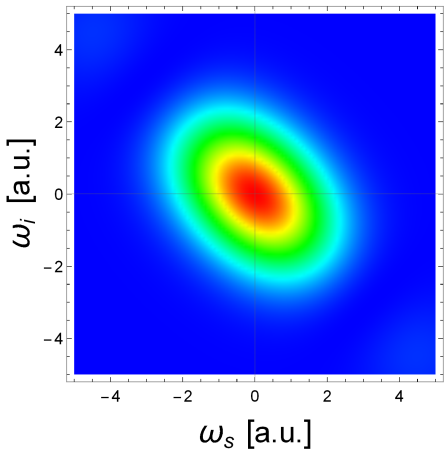

Figure 2.5: The formation of the joint spectral intensity for signal (ω_s) and idler (ω_i) as a product of the pump envelope intensity and phase-matching intensity depicted in Fig. 2.4 is shown.

choosing the poling period Λ and the optical properties of the nonlinear material. Knowledge of the refractive indices n_j helps to characterize the photon's spectra, with the j labeling the signal, idler, and pump photons. The phase-matching condition in terms of the refractive indices n_j can be estimated via

$$\begin{aligned} \Delta\mathrm{k}(\omega_p, \omega_s, \omega_i) &= \mathrm{k}_p(\omega_p) - \mathrm{k}_s(\omega_s) - \mathrm{k}_i(\omega_i) - \frac{2\pi}{\Lambda} = 0 \\ \Delta\mathrm{k}(\omega_p, \omega_s, \omega_i, T) &= \frac{2\pi n_\mathrm{p}\left(\lambda_p, T\right)}{\lambda_p} - \frac{2\pi n_\mathrm{s}\left(\lambda_s, T\right)}{\lambda_s} - \frac{2\pi n_\mathrm{i}\left(\lambda_i, T\right)}{\lambda_i} - \frac{2\pi}{\Lambda(T)} = 0 \\ 0 &= \frac{n_\mathrm{p}\left(\lambda_p, T\right)}{\lambda_p} - \frac{n_\mathrm{s}\left(\lambda_s, T\right)}{\lambda_s} - \frac{n_\mathrm{i}\left(\lambda_i, T\right)}{\lambda_i} - \frac{1}{\Lambda(T)}, \end{aligned} \tag{2.36}$$

with λ_s, λ_i and λ_p being the wavelength of the signal, idler, and the pump photons, respectively. As shown, the refractive indices n_j as well as the poling period Λ are temperature dependent, meaning that scanning the temperature alters the spectral properties of the photons pairs. The variations of the refractive indices of $n_i = n_i(\lambda, T)$ by wavelength (usually referred to as Sellmeier equations) and the thermal expansion coefficients are empirically obtained from individual experimental measurements [54]. The general form of the JSI and its temperature dependence can be comprehended and theoretically engineered by measuring it with a high-resolution spectrometer and altering the nonlinear medium's phase-matching temperature. Fig. 2.6 shows a measured spectrum of SPDC photon pairs while scanning the temperature of the nonlinear crystal. Clearly, it shows the altering spectral characteristics with changing thermal conditions, as the central wavelengths (CWL), as well as the bandwidths of the photon pairs, change their value, respectively, always according to the frequency conservation. The photon's spectra and the CWLs were recorded with a near-IR single photon spectrometer (Ocean Optics QE65000), with a spectral resolution of approximately 0.19 nm according to the datasheet provided by the manufacturer [55]. The Sellmeier equations and the thermal expansion coefficients help to predict the spectral behavior of the photon pairs, which will be utilized in this thesis in the respective sections treating the technical implementation of the experiments.

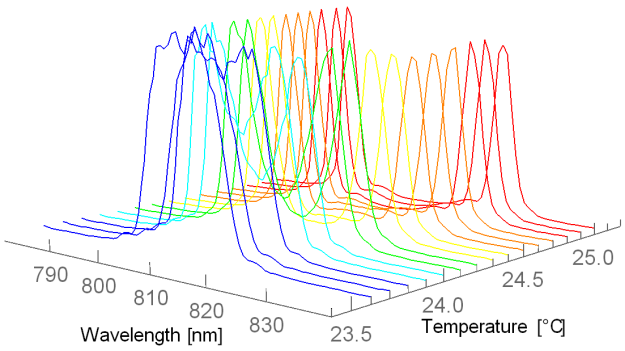

Figure 2.6: The measured cross-section intensities of the photon pair's spectra created in a type-0 ppKTP 3cm-long crystal for various quasi-phase-matching temperature settings (23.6°C- 25°C). With increasing temperature of the crystal, the non-degeneracy with respect to the CWLs of signal and idler, increases, too.

For practical reasons, the bandwidths of the photons spectra can be easily calculated by assuming a delta function around the pump frequency for the pump envelope intensity $\mathrm{v}_p(\omega) \approx \delta(\omega - \omega_p)$ in the two-photon mode function, which results in the spectrum being dictated by the phase-matching intensity.

Hence, the spectral bandwidth's full width at half maximum $\Delta\omega$ can be calculated by solving

$$\mathrm{sinc}^2[\frac{L}{2}\Delta\mathrm{k}(\Delta\omega)] = \mathrm{sinc}^2(1.39) = 1/2. \tag{2.37}$$

Followed by straightforward calculations involving the Taylor expansion of Δk [41], for the non-degenerate frequency case ($\omega_s \neq \omega_i$) this leads to

$$\Delta\omega_{non-deg} \sim \frac{4 \times 1.39}{L|D|}, \Delta\lambda_{non-deg} \sim \frac{8 \times 1.39}{\omega_0^2}\frac{\pi c}{L|D|} \tag{2.38}$$

with

$$D = \frac{1}{v_\mathrm{s}} - \frac{1}{v_\mathrm{i}} \tag{2.39}$$

describing the difference between the inverse group velocities of the signal v_s and idler v_i photons, which are defined as $v_g^j = \frac{c}{n_j - \lambda_0 \frac{\partial n_j(\lambda_0)}{\partial \lambda_0}}$, with λ_0 being the wavelength in vacuum and c the speed of light and ω_0 being the center frequency of the SPDC photon pairs. For the degenerate frequency case ($\omega_s = \omega_i$) however, D vanishes, so the Taylor expansion of Δk up to the second order has to be performed leading to the following bandwidth:

$$\Delta\omega_{deg} \sim \sqrt{\frac{4 \times 1.39}{LG}}, \Delta\lambda_{deg} \sim \sqrt{\frac{8 \times 1.39}{\omega_0^2}\frac{\pi c}{LG}}, \tag{2.40}$$

with

$$G(\omega_0) \equiv \frac{\partial}{\partial\omega}\left(\frac{1}{v_g(\omega)}\right)_{\omega=\omega_0} \tag{2.41}$$

being the group velocity dispersion.

2.2.4 Higher-order emission in SPDC

The SPDC process forms a non-deterministic single-photon source, due to the fact that the conversion of a pump photon into two photons occurs spontaneously. Hence, the timing resolution of the detection system to verify the emission of a specific photon-number state plays an essential role. For a pulsed photon source, the photon pairs within a pulse are indistinguishable from each other in the temporal regime, as the multi-pairs within their respective temporal modes are within a single pulse.

In the case of continuous-wave (cw) sources, given that the coherence time t_{coh}^{DC} of the SPDC photons and the timing resolution of the detection system are small compared to the coincident timing window t_c, the higher-order contributions, can be distinguished from each other. Commonly used single-photon avalanche photodiodes (APD) however, are not number-resolving. Via post-selection and recording a great number of distinguishable single-photon events, however, the quantum state can be determined, while taking into consideration that the number distribution of an inherent probabilistic n photon-pair source takes the following form [56]:

$$P(n) \simeq e^{-\mu}\frac{\mu^n}{n!}, \tag{2.42}$$

where μ is the mean photon pair number per time unit, where the latter usually equals the coincident timing window t_c.

In order to investigate the impact of multi-pairs on a polarization analysis measurement on polarization-entangled photons, the following situation is assumed: An entangled photon-pair source emits a $|\Psi^-\rangle$ state with mean photon pair number μ_{source} to Alice and Bob, where the photons experience a link loss of η_A and η_B. At the receiver ends, the polarization of the photons is measured by propagating through a half-wave plate for basis choice and then split by polarization with the help of a polarizing beam splitter (PBS), which transmits only photons in p- (parallel) polarization and reflects only in s- (German: "senkrecht") polarization. Hence, the photons undergo local projective measurements on both detection modules, analyzed by their polarization degree of freedom. Maximal photon pair counts for a $|\Psi^-\rangle$-state are expected in the (pairwise) orthogonal polarization outputs of two polarizing beam splitters in both HV and the mutually unbiased DA basis, due to its invariance under basis transformations. Therefore, minimum counts will occur at the equal polarization output ports of the PBS. This setup is finally followed by single-photon detectors, hence the receiver modules act as polarization resolving stages. Note that the link loss includes, among others, transmission loss and detection efficiencies. The quantity describing the degree of agreement of the detected number state with the desired state is the fidelity $F(\hat{\rho})$ (see Eq. 2.18) which can be estimated by the *visibility*, which was introduced in section 2.1.2:

$$\mathcal{V} = \frac{\text{maximum counts - erroneous counts}}{\text{total counts}}. \tag{2.43}$$

Furthermore, it is assumed that the source emits an ideal state, where also the transmission channel or optical elements lack influence on the polarization correlations. Hence, the erroneous counts arise only from the accidental coincident counts, to which any by the detectors registered uncorrelated photon pairs are assigned. Following the probability $P(n > 2)$ that more than 2 photon pairs are emitted within a certain timing window, e.g., the coincident timing window t_c, Eq. 2.42 can be expanded in its Taylor series [57] while assuming a symmetric scenario, namely that the count rates $\mathcal{C}_A = \mu/t_c$ of the two detectors (A, B) are equal:

$$P(n > 2) = 1 - P(0) - P(1) \approx \mu^2 = \mathcal{C}_A^2 t_c^2, \tag{2.44}$$

under the approximation, that the threshold detectors were far from saturated ($\mathcal{C}_A t_c \ll 1$). Equally, this result is applicable to the accidentally registered coincident counts in the asymmetric case on both receivers, namely $\mathcal{C}_{acc} = \mathcal{C}_A \mathcal{C}_B t_c$ [58]. Note that in the asymmetric case, a maximally random distribution with respect to the detecting events is assumed. However, the source ideally emits strongly correlated, in fact, entangled photon pairs. In other words, Eq. 2.44 acts as an upper bound of the accidental coincident counts, as correlated counts contribute positively to the visibility.

With this, as derived in Appendix A1 (Eq. A10), the visibility considering accidental coincident counts takes the following form:

$$\mathcal{V}_{acc} = \frac{\mu_{source}\eta_A\eta_B}{\mu_{source}\eta_A\eta_B + 2(\mu_{source}\eta_A + D_A)(\mu_{source}\eta_B + D_B)}, \tag{2.45}$$

with D_i with $i = A, B$ being the dark count detection probabilities. If the ideal case is assumed that the dark count detection probability is significantly lower than the source photon detection probability, Eq. 2.45 simplifies to

$$\mathcal{V}_{acc} = \frac{1}{1 + 2\mu_{source}}. \tag{2.46}$$

Assuming cw-sources, in the temporal regime, the emission characteristics of SPDC photons hold a finite probability of emitting two or more photon pairs within a given timing window, [59]. These multi-pairs are uncorrelated to each other and contribute to 'false' or accident coincidences $\mathcal{C}_{acc}$ in the detectors, which create a noise background in the signal [60]. This affects the visibility once the source pair rate B becomes large compared to the timing window t_c, which becomes apparent with the following relation: $\mu_{source} = B \cdot t_c$. Increasing the source pair rate gives rise to a higher probability of detecting uncorrelated higher-order emission per coincident timing window t_c, which in turn leads to a significant decrease in entanglement visibility and therefore the fidelity of the output to a photon state. On the other hand, a small t_c could interfere with the timing resolution of the detection system, so an optimal value of μ_{source} for an experimental setup is crucial. This limit can solely be attributed to the emitted photon pairs, almost irrespective of the link loss. An effective approach to decrease the influence of higher-order emissions is by multiplexing in a photon's degree of freedom such as spatial correlations [38,61,62], temporal correlations [63] or exploiting wavelength correlations by wavelength multiplexing [64], as performed in an experiment presented in this thesis (see section 4). In theory, the brightness B of the SPDC source can be arbitrarily increased, depending on the detecting infrastructure (filtering, timing resolution of the detectors) and the respective properties of the single photons (e.g. bandwidth of the spectrum). Technically, the damage threshold of the nonlinear medium withstanding the pump intensity poses an upper bound of the brightness.

Chapter 3

Nonlinear photon interference effect in free space

The phenomenon of interference of quantum particles forms a crucial pillar for the understanding of quantum mechanics. The scientific community stood in awe as the interpretation of Young's double-slit experiment performed with quantum particles set up the foundation for the interpretation of quantum theory, as devised within the Copenhagen interpretation. The classical understanding of this experiment is that either the model of particles holds, where the particles follow a path through one of the two slits, respectively, or the behavior can be explained within a wave-like description. An intrinsic characteristics of a plane wave is the possibility to superpose amplitudes, leading in the case of a double-slit arrangement to interference. Both models can be assigned to quantum particles, hence this predicament unfolds within the "*inherent inadequacy of the language of classical physics in the quantum domain*" [40]: Quantum properties are measured with a classical apparatus; hence, assigning a certain property to a quantum particle, such as momentum and position or particle and wave, is only adequate with respect to the experimental arrangement, which examines the respective property. Quantum mechanics offers a catalog of outcomes for a certain experimental setup, hence solely stating probability statements [14]. Any attempt to determine any information about the coherent superposition, in which the quantum particle resides, leads to decoherence and therefore no quantum interference occurs[1]. In other words, even if this information is accessible in principle, the collapse of the wave function, which describes the system, will prevent the interference from taking place. Hence, decoherence can be described as the tendency of quantum systems to lose their quantum character.

But the following question arises now: What is it that interferes with each other? An adequate answer can solely be given with respect to an experimental arrangement. Within the double-slit experiment, the quantum particle resides in a coherent superposition in propagating through one or the other slit. Measuring in which path the interfering particle propagates introduces a momentum transfer from the respective detector onto the particle, which in turn leads to decoherence of the quantum system and the interference pattern vanishes [40]. What can be deduced from this is that the term *distinguishability* plays a major role in consideration. In that context, quantum interference occurs, whenever it is impossible to distinguish through which one

[1]Naturally, in that case the measurement has to be performed in the quantum state's defined computational basis. In that sense, no decoherence occurs when measuring in the superposition basis.

of the two spatially separated domains the particle propagates [65].

The quantum properties such as interference and coherence of quantum particles can be exploited leading e.g. to enhancement in the resolution of imaging [66] as well as spectroscopy [67] when compared to classical arrangements. In this thesis, a nonlinear interference effect of nonclassical SPDC photon pairs will be presented, with potential impact in the fields of quantum sensing [68] and quantum metrology [69]. Photons show outstanding behavior appealing to the demand of scalability in the form of maintaining their quantum properties over long distances in free space [70–73]. In the following section, nonlinear interference of photon pairs is studied and the technical implementation is shown, which spans to the best of our knowledge the longest distance ever achieved. The findings of the scaling behavior of nonclassical correlations in terms of propagation distance are believed to become vital for both foundational questions and possible applications.

3.1 Nonlinear interference

Nonlinear interferometers comprise a class of interferometers involving interference of quantum particles from two or more spatially separated nonlinear processes. Given that the two (or more) possibilities to create quantum particles via nonlinear effects cannot be distinguished from each other, interference fringes are observed. The first to observe this kind of nonlinear interference was Bloembergen in second-harmonic generation (SHG)[2] [74]. The interference effects occur due to the fact that the phases of the pump and the nonlinear signal are in a non-random relationship during propagation.

The phase sensitivity of optical measurements $\Delta\phi$ performed with classical linear interferometers is limited by the shot-noise limit (or the standard quantum limit, SQL), defined by $\Delta\phi \geqslant \bar{n}^{-1/2}$, with $\bar{n}$ being the (average) number of photons used in the process of measurement. More precise measurements surpass this limit by exploiting quantum effects, e.g., measurements involving entangling gates, reaching the so-called Heisenberg-limit ($\Delta\phi \geqslant \bar{n}^{-1}$) [75] and an even lower bound called quantum Cramèr-Rao bound [76]. Gravitational-wave detectors such as LIGO harness these precise quantum measurement techniques using quantum resources [77]. High phase sensitivity of measurements in nonlinear interferometers is given by the fact that the phase of the interference fringes depends on the phase delay between the phase of the pump and the nonlinear signals. As a consequence, given a vacuum or phase squeezed state as an input state, the noise can be effectively set to the level of the input, hence offering a possibility of lowering the SQL [78–81]. Hence, these setups can be of use for precise measurement techniques such as quantum metrology and quantum sensing as nonlinear interferometers enable to reach the Heisenberg limit [82–85]. These nonlinear scheme's simplicity of implementation and the possibility of acquiring information about dispersion properties of frequencies, where direct detection is effortful, provides an advantage in spectroscopy as well. In that regard, highly precise measurements of e.g. the infrared (IR) dispersion of optical properties such as refractive index or absorption coefficient of a gas can be performed [86]. The spatial resolution of two objects[3] set by the Rayleigh limit [87,88] can be overcome by quantum imaging, a technique exploiting quantum correlations and interference of nonlinear signals [66]. Quantum imaging also offers the astounding technique of obtaining an image of an object by detecting photons that never interacted with the object [89], which also features quantum correlations and coherence.

[2] In SHG, two photons are converted within a nonlinear process into one photon with twice the energy of each of the photons, hence being the opposite process of SPDC.

[3] In other words, the ability to identify the spatial distance between two objects as distinct points.

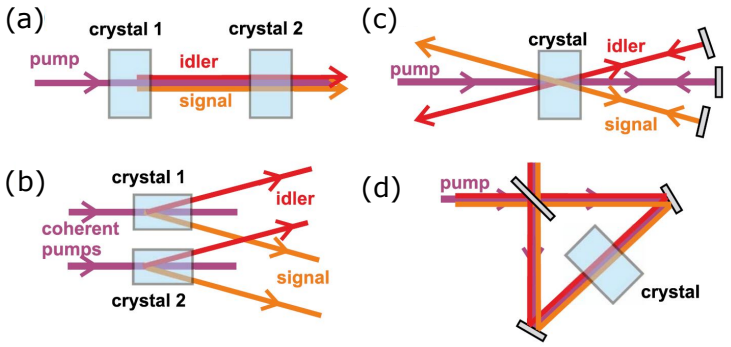

Figure 3.1: Several types of nonlinear interferometers are presented; adapted from [82]. (a) In the "Mach-Zehnder" setup the nonlinear signal and the pump propagate collinearly within the same mode in between the two sources and overlap with the nonlinear signal created in the second source. (b) This setup shows resemblance to the double-slit experiment (hence "Young"-setup), where the signal and idler fields of the respective sources are overlapped and become indistinguishable in the far-field regime. (c) The "Michelson" arrangement allows for independently manipulating the phases of the fields by external mirrors. (d) The nonlinear medium is pumped bidirectionally and the nonlinear signal overlaps on a beam splitter. This arrangement is in fact a "Sagnac" interferometer.

Implementations involving nonlinear interference such as the ones depicted in Fig. 3.1 (a-d) form a group of so-called "SU(1,1) interferometers", as theoretically introduced by Yurke [83]. As in contrast to e.g. linear Mach-Zehnder interferometers, the beam splitters are not described by the SU(2) group [90], but by Bogolyubov transformations, which are related to the SU(1,1) group.

3.2 SPDC bi-photon interference

The sources of single photons for (multi-) photon interference range from second-harmonic generation [74] to spontaneous emission of an atom placed in the vicinity of a dielectric mirror [91]. In the latter case, the spontaneous emission rate is modified depending on the position of the mirror. One of the interpretations is that the photon can reach the detector either directly or via the mirror, leading to interference effects due to indistinguishability of the two cases [40].

The effect of spontaneous parametric down-conversion was after its first observation by Burnham and Weinberg [33]. Since then, it is at the center of interest for numerous scientific groups, especially in the field of photonic quantum information processing. Section 2.2 covers a theoretical insight of the formalisms of both the creation and properties of SPDC photons. This parametric effect comes into play also as the nonlinear effect of choice for nonlinear interferometers, including the implemented experiment of this thesis. In the following, a few experimental implementations showing interference of SPDC photon pairs and their observations are discussed, which shall pave the way for consistent treatment and understanding of this thesis' proposed and realized experiment.

In 1987, Chung Ki Hong, Zhe Yu Ou, and Leonard Mandel observed two-photon interference on a single beam splitter, provided that the photons entering both input sides of the beam splitter were indistinguishable in both space and time, hence within their coherence time [92]. Here, second-order interference effects occur, which were demonstrated by the coincident count rate between detectors placed in both output ports of the beam splitter. Second-order interference effects

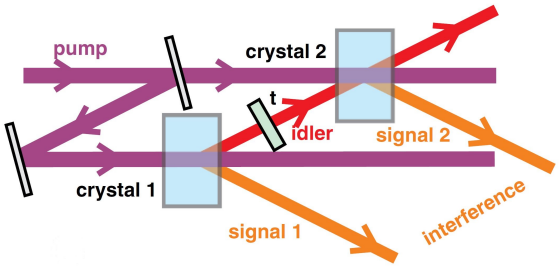

Figure 3.2: The experimental setup of induced coherence as performed firstly by Mandel et al. [94] is depicted. Interference effects of down-converted signal photons, namely *signal 1* and *signal 2* originating from two different nonlinear media (*crystal 1* and *crystal 2*) while removing the which-crystal information from their partner photons, namely the idler photons, were observed. This was done by aligning the idler paths such that no information about where the idler photons were created is present. Introducing a transmission filter with transmittivity t leads to a decrease in visibility of the interference fringes. Adapted from [82].

can be observed when interference of intensities occurs, which especially becomes relevant in coincident photon counting experiments. The lack of second-order interference was ruled out since the signal and idler photon have no definite phase, thus being mutually incoherent [92].

Ou, Wang, and Mandel proposed an additional experimental setup in order to observe the rate of coincident detection from overlapping down-converted photons arising from two nonlinear media while emphasizing that the vacuum field plays a major role in the interference [93]. Finally, Mandel et al. successfully performed the experiment that shows the sinusoidal behavior of the count rate of SPDC signal photons when no information is present of the origin of their partner photons, namely the idler beams, while scanning the phase difference between the two signal photons [94] (see Fig. 3.2). This remarkable effect was observed by aligning the idler photon paths for the two nonlinear crystals such that they were indistinguishable from each other. Overlapping the idler modes arising from two sources respectively leads to induction of coherence. It follows, that the first-order interference effect vanishes when the first idler photon is blocked, hence the term "induced coherence" [95]. Note that first-order interference effects are described by the interference of electric fields, rather than intensities. Apparently, this occurs due to the fact that the signal and idler produced in an SPDC process are defined in a product state and hence the phases are in turn defined as a sum [96] (see section 3.2.1).

As mentioned above, this technique can be used for an imaging method where the photons illuminating an object are not detected [89]. The idea of superposing the idler beam paths in such a way that the *which-crystal* information is removed leads to a striking method of introducing entanglement in multipartite and high-dimensional quantum systems [97].

In 1994, a first and second-order interference experiment was performed by Herzog et al. [98] [see Fig. 3.1 (c) and Fig. 3.3]. Here, the dependency of the count rate of overlapping down-converted photons originating from one and the same nonlinear crystal on the phase difference between the pump and the down-conversion beams, respectively, was investigated. A topologically similar experiment was performed by Wu in 1985, where the phase dependence of noncollinear SHG sources was observed [99]. In the first step, a down-converted photon pair is created by an SPDC process and is then emitted in certain spatial modes s_1 and i_1 [see Fig. 3.3 (a)], while in the second and third step the pump beam, as well as the respective forward signal and idler photons,

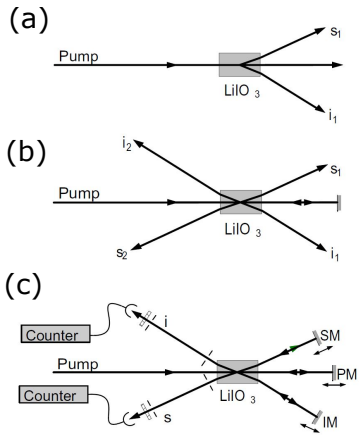

Figure 3.3: The main idea of the "frustrated down-conversion" interference experiment performed by Herzog et. al [98] is outlined. Adapted from [40]. (a) A pump beam creates a photon pair via spontaneous parametric down-conversion in a nonlinear crystal - signal photon s_1 and idler photon i_1. (b) A mirror (PM) returned the pump beam via back-reflection to the crystal to produce an additional photon pair s_2 and i_2. (c) The photon pairs created in scenarios (a) and (b) are spatially overlapped by placing not only PM but also additional mirrors SM and IM and were measured with the detectors placed on the left-hand side of the setup. This leads to interference effects observed in sinusoidal behavior in signal and idler count rates while moving the mirrors.

are allowed to propagate back to the crystal via mirrors [see Fig. 3.3 (b-c)]. The latter leads to an additional possibility to create down-converted photon pairs in the modes s_2 and i_2, where the photons are detected by detectors located on the side of the pump laser source.

If the mirrors are placed such that the signal and idler beams created after the first passage overlap spatially and temporally with the ones created in the second passage, interference effects occur while moving the mirrors. Here, a definite phase relation of the down-conversion photon phases with the pump phase only exists for the whole product state. Depending on the phase delay of the partaking fields, either enhancement or total suppression (hence the term "frustrated down-conversion") of spontaneous emission of the photon pairs can be achieved. Hence, in relation to the Mandel experiment, a sinusoidal behavior in the single count rate of a detector measuring the idler photons can be observed while moving the mirror that returns the signal photons to the crystal.

Here, we investigate a first and second-order interference effect of down-converted photon pairs created in two nonlinear crystals within a parametric process which are far apart from each other [4] and its implementation. The pump photons and the SPDC photon pairs created in a nonlinear medium travel collinearly to an additional SPDC source where the possibility of creating another down-converted beam leads to interference effects, hence suppression and enhancement of spontaneous emission of SPDC photon pairs occur. The SPDC emission takes place in well-defined spatial and temporal modes governed by the phase-matching conditions. In other words, the SPDC wave packets created in the first crystal can be annihilated by sending them through a second crystal while collinearly propagating within the same mode of the pump photons. This nonclassical effect can solely be explained by quantum mechanics (see discussion in section 3.4.5

[4] Past experiments involving nonlinear interference (including, but not limited to, the experiments presented in [66, 78, 79, 82–85, 89, 93, 95, 98]) did not exceed distances of several meters.

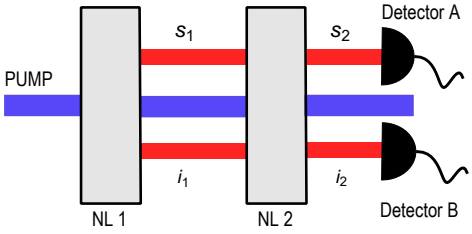

Figure 3.4: A schematic picture of the simplified experimental arrangement is depicted. A continuous-wave pump laser was used to create a down-converted photon pair in a nonlinear crystal in the modes s_1 and i_1. Within the same modes the pump beam propagated collinearly to the second crystal so an additional possibility for creating photon pairs indicated by s_2 and i_2 arises. Aligning both signal and idler beams such that the which-crystal information is removed, interference fringes can be observed while scanning the phase difference between the pump and down-conversion beams. These effects shall be observed with increased spatial separation of the crystals.

and Refs. [96, 100]). Interestingly, frustrated SPDC is an effect intrinsically lacking the possibility to encode and distribute information. It is an interference effect, which bases not on the destruction of information but fundamentally on the non-creation of information. In this experiment, the scalable behavior in terms of how different processes of single-photon creation can be spatially separated without losing their non-classical properties can be examined. Quantum superpositions depend sensitively on the coherence of the photons, which can be shown by constructive or destructive interference.

In that sense, the results of this experiment get to the bottom regarding the fundamental limits of quantum physics. Scalable behavior of quantum physics is the aim of numerous experiments such as the double-slit behavior of molecule masses [101], superposition of masses [102], the highest number of orbital angular momentum entanglement of photons [103], entanglement over long distances in free space [104] and highest number of information encoded in a photon pair [105].

Therefore, the results of this experiment shall aid the expansion of our knowledge for the scope of application of quantum physics, as quantum theory predicts a vast area of validity. As long as no empirical tests are performed, these areas of validity are solely hypothetical. Hence, the expertise gained from experiments involving the superposition of photons (such as long-distance coherent photon pair creation) can also lead to highly sensitive measurement techniques over large distances. An intriguing example has been given above, where spectroscopy of linear materials such as gases can be conducted [86], which could be applicable in e.g. the field of metrology. There exists a high demand in research about the limit of individual quanta preserving their quantum-mechanical properties, e.g. their coherence [106]. Finally, these findings can pave the way for understanding multiphoton interferences with the goal to certify the nonclassicality of quantum states for potential future applications and how they can manifest themselves in large networks [107].

3.2.1 Count rate of interfering two-photon down-conversion

In resemblance to the experiment performed by Herzog [98] and Mandel [94] as well as in the field of nonlinear interferometers [66,78,79,82–85,89,93,95], a setup is reported showing first and second-order quantum interference of two spatially separated SPDC sources, where the distance between the sources shall exceed distances of the ones conducted in similar past experiments, which were in the order of several meters. This leads to increasing effects on the decoherence of the two-photon state, which shall be examined and quantified.

Therefore, a theoretical overview of the first- and second-order interference, which manifests itself within the coincident and single count rates, shall be given. For reasons of clarity and comprehensibility, the phenomenological formalism of interfering two SPDC beams shall be done in the first quantization, while for the more extensive treatment the second quantization method shall be used and will be outlined in the following section. Note that the following calculations are mainly based on the work of other authors and the reader shall be referred to the respective literature [39, 40, 82, 93, 98].

General quantum mechanical description of the two-photon interference

A photon pair created via SPDC in a nonlinear crystal (as derived in section 2.2) by a pump field with amplitude A can be described in the first quantization by the following simplified state:

$$|\Psi\rangle = |vac\rangle|vac\rangle + A|1\rangle_{s_1}|1\rangle_{i_1} + \dots, \tag{3.1}$$

which consists of a tensor product of two Hilbert spaces for the two photon modes s_1 and i_1. Note that higher-order emission processes in the order of $O\left(|A|^2\right)$ are neglected in the following, as the amplitude A is supposed to be small due to the low gain regime. The pump beam is supposed to be in a coherent state and its amplitude remains roughly the same after the process as $|A|^2 \ll 1$.

An experimental setup as shown in Fig. 3.4 shall be considered now, where a coherent pump beam creates a photon pair in the bi-photon state in a nonlinear crystal via SPDC with amplitude A as described in Eq. 3.1. They collinearly propagate to a second nonlinear crystal, resulting in the two-photon state of the down-converted photon pairs, given in the form

$$|\psi\rangle = Ae^{i(\phi_s+\phi_i)}|1\rangle_{s_1}|1\rangle_{i_1} + Be^{i\phi_p}|1\rangle_{s_2}|1\rangle_{i_2}, \tag{3.2}$$

where here only the modes in s_2 and i_2 from the second crystal are considered and ϕ_p is the phase translated by the pump photons to the photon pairs created in the second crystal compared to the first photon pair, and ϕ_s, ϕ_i are the phases of the signal and idler photons accumulated during the propagation between the two nonlinear crystals. Also, the amplitude of the photon pairs created in the second crystal is assumed to be B, as also here the low-gain regime of the pump intensity prevents a contribution of higher-order emissions, compared to the two-photon contribution. When indistinguishability between the two-photon pairs is obtained, meaning that the which-crystal information is removed, one can set

$$|1\rangle_{s_1} = |1\rangle_{s_2} \longrightarrow |1\rangle_s \tag{3.3}$$

and

$$|1\rangle_{i_1} = |1\rangle_{i_2} \longrightarrow |1\rangle_i \tag{3.4}$$

so the state in Eq. 3.2 can be rewritten as

$$|\psi\rangle = A(e^{i(\phi_s+\phi_i)} + e^{i\phi_p})|1\rangle_s|1\rangle_i, \tag{3.5}$$

where the amplitudes were supposed to have the same magnitude now, so $|A| = |B|$. This can be experimentally realized quite easily, as will be explained in detail later. Note that the state in Eq. 3.5 does not describe a four-photon but a two-photon state, as the amplitude of the SPDC process A was assumed to be small and higher-order processes occur with negligible probability. Two-photon interference effects can yield quantum entanglement [108], and the state in Eq. 3.5 can be considered possessing a signature of nonlocality due to the fact that it depends on the sum of the two phases ϕ_s and ϕ_s (minus the pump phase) [40].

Count rates of the two-photon interference

The count rate calculation requires a more detailed treatment. The following formalism follows the explication of Glauber in regard to standard photodetection theory [40, 109]. Superposing the idler and the signal fields, the intensity at the two detectors can be estimated by the following function

$$\mathcal{C}_{s/i} = \int_{-\frac{\mathcal{T}}{2}}^{\frac{\mathcal{T}}{2}} C_{s/i}^{(1)}(t)dt \tag{3.6}$$

with

$$C_{s/i}^{(1)}(t) = \left\langle \psi \left| E_{s/i}^{(-)}(t) E_{s/i}^{(+)}(t) \right| \psi \right\rangle, \tag{3.7}$$

where $C_{s/i}^{(1)}$ describes the first-order correlation function for signal (s) and idler (i) fields, respectively, $\mathcal{T}$ is the measurement time and the electric field operators are defined as introduced in section 2.2 (see Eq. 2.21).

For a more complete description of the two-photon emission the finite frequency bandwidth has to be taken into account. Apart from that, the pump and the down-converted fields have to be represented by plane waves. Note that for a more complete description the second quantization formalism is required. In the following, perfect phase-matching in the SPDC two-mode state (Eq. 2.32) is assumed, which enables the substitution of the sinc-functions by δ-functions. With the above assumption, Eq. 3.5 can be rewritten as:

$$\begin{aligned} |\psi\rangle = |vac\rangle|vac\rangle + A \int d\omega_p \mathrm{v}_p(\omega_p) \int d\omega_i \int d\omega_s \delta(\omega_p - \omega_i - \omega_s) \\ \times \left[e^{i(\omega_s\tau_s + \omega_i\tau_i)} G_1^s(\omega_s) G_1^i(\omega_i) + e^{i\omega_p\tau_p} G_2^s(\omega_s) G_2^i(\omega_i) \right] |\omega_s\rangle_s |\omega_i\rangle_i , \end{aligned} \tag{3.8}$$

where the probability amplitudes A for the creation of the two-photon pairs in the modes $|\omega_s\rangle_{s_1}|\omega_i\rangle_{i_1}$ and $|\omega_s\rangle_{s_2}|\omega_i\rangle_{i_2}$ are equal, τ_p is the time the pump photons propagate between the two sources and v_p is the classical amplitude as introduced in section 2.2.1. The two-mode function $\phi_{\zeta_s\zeta_i}$ can be simplified in terms of G_j^s, G_j^i with $j = 1, 2$, which represents the wavelength

distribution of the signal and idler fields defined by interference filters. Provided that the two-photon pair creation is indistinguishable (see Eqs. 3.3, 3.4), inserting Eq. 3.8 into Eq. 3.6 leads after straightforward calculations (see [39, 40, 93]) to the single count rate for signal and idler respectively:

$$\mathcal{C}_{s/i} = 2|A|^2 \mathcal{I}_p \bar{f}_{s/i}[1 + \mathrm{V}_p \mathrm{V}_{s/i} \cos(\omega_s \tau_s + \omega_i \tau_i - \omega_p \tau_p)], \tag{3.9}$$

with

$$\begin{aligned} \bar{f}_{s/i} &= \int d\omega f_{s/i}^2(\omega) \\ \mathrm{V}_p &= \frac{1}{\mathcal{I}_p} \int d\omega_p \mathrm{v}_p(\omega_p)^2 e^{i\omega_p(\tau_{av} - \tau_p)} \\ \mathrm{V}_{s/i} &= \frac{1}{\bar{f}_{s/i}} \int d\omega f_{s/i}^2(\omega) e^{i\omega(\tau_s - \tau_i)}, \end{aligned} \tag{3.10}$$

where $\mathcal{I}_p$ is the pump intensity, τ_s and τ_i denote the propagation time of the signal and idler photons between the sources and $\tau_{av} \equiv \frac{\tau_s + \tau_i}{2}$. Here, f_s and f_i are functions that describe effects due to filtering. In our case, the fixed directions of the fields propagating to the detectors as well as fields with frequency distributions defined by the interference filters are assumed. Note that the assumption was made that the pump bandwidth is much smaller than the bandwidth of the down-converted light. Eq. 3.9 shows the interfering behavior of down-converted photons created in two sources. The argument within the cosine-function states the relationship between the pump phase and the down-conversion photon's phase. Interference fringes can be observed by scanning the phases with respect to each other. Moreover, the interference pattern depends on the sum $\phi_s + \phi_i$ of the signal- and idler-phase, as shown in Eq. 3.9. Hence, changing the phase of the signal photons leads to an observable intensity oscillation in the idler count rates.

The magnitude of interference is governed by the visibility, which depends on the functions V_p and $\mathrm{V}_{s/i}$. For simplicity, it is assumed that the pump, signal, and idler fields inhabit a Gaussian-shaped spectrum with coherence lengths l_{coh}^p and l_{coh}^{DC}, respectively[5]. From the form of both V_p and $\mathrm{V}_{s/i}$ together, it can be deduced, that at the point of the spatial overlap in the second source (where the interference takes place), the down-converted beams from the first source have to propagate within the coherence length of the pump beam l_{coh}^p (see Fig. 3.5). In other words, the pump's coherence length l_{coh}^p does not have to exceed the distance between *both* crystals, but has to be greater than the path length *difference* of the down-converted and the pump beams. This fact can be interpreted insofar that the information, in which of the crystals the down-conversion occurs, has to be erased. Set the case, that the wave packets of both down-converted and pump photons propagate within the same mode right after the first crystal. When, on their way to the second crystal, the wave packets diverge outside of the pump's coherence length l_{coh}^p, which-crystal information regarding the birth of the down-converted photon pairs can be deduced. This results in a lower visibility, but can be recovered by adjusting the path lengths of the photons, accordingly. Importantly, not the absolute distances but the *relative* path lengths are relevant. The Eqs. 3.9 and 3.10 allow the absolute distances to be arbitrarily long. However, the spatial mode's behavior of both down-converted and pump photons during propagation between the crystals are of great importance for interference to occur.

[5]Here, degenerate type-II phase-matching is assumed, hence the coherence lengths of the signal and idler fields are equal.

The coincident count rates can be calculated by

$$\mathcal{C}_{\mathcal{C}} = \int_{-\frac{\mathcal{T}}{2}}^{\frac{\mathcal{T}}{2}} dt_s \int_{t_s-\frac{\Delta\mathcal{T}}{2}}^{t_s+\frac{\Delta\mathcal{T}}{2}} dt_i C^{(2)}\left(t_s, t_i; t_i, t_s\right), \tag{3.11}$$

where second-order signal-idler correlation function $C^{(2)}$ can be expressed with the electric field operators

$$C^{(2)}\left(t_s, t_i; t_i, t_s\right) = \left\langle \psi \left| E_s^{(-)}\left(t_s\right) E_i^{(-)}\left(t_i\right) E_i^{(+)}\left(t_i\right) E_s^{(+)}\left(t_s\right) \right| \psi \right\rangle. \tag{3.12}$$

This function gives the probability of detecting signal and idler photon at times t_s and t_i, respectively, within the coincident timing time window $\Delta\mathcal{T}$. Inserting now Eq. 3.8 into Eq. 3.11 and using the same assumptions as for the single count rates, this leads after straightforward calculations to

$$\mathcal{C}_c = 2|A|^2 \mathcal{I}_p \bar{f}_s \bar{f}_i [1 + \mathrm{V}_p \mathrm{V}_c \cos\left(\omega_s \tau_s + \omega_i \tau_i - \omega_p \tau_p\right)], \tag{3.13}$$

with

$$\mathrm{V}_c = \frac{1}{\bar{f}_s \bar{f}_i} \int d\omega f_s^2(\omega) f_i^2(\omega) e^{i\omega(\tau_s - \tau_i)}. \tag{3.14}$$

The form of Eq. 3.13 is nearly identical with the single count rate Eq. 3.9, except that the function $\mathrm{V_c}$ depends on the product of the filter functions in both the signal and idler arm.

For our purposes, a slight reformulation of Eq. 3.13 and Eq. 3.9 shall be helpful for the interpretation of the measurement results. For the introduction of useful parameters, a situation as depicted in Fig. 3.5 shall be considered [110]. Two independent SPDC sources are shown, where each of the pump and signal photons travel along propagation paths l_{jm}, respectively, where the index j denotes the pump and the down-conversion fields p, s and i and m the two different possibilities of creating a photon pair, a and b. The resemblance to the experiment shown in this thesis (see Fig. 3.4) can be seen by overlapping the paths with indices by a and b such that the sources are in line. Finally, the detectors $\mathrm{D_A}$ and $\mathrm{D_B}$ record the overlap of both SPDC signals[6], where the single count rates with the newly introduced parameters now take the following form [110]:

$$\mathcal{C}_{s/i} = |A|^2 \mathcal{I}_p \bar{f}_{s/i} [1 + \mathrm{V}_p \mathrm{V}_{s/i} \cos\left(\mathrm{k}_p \Delta\mathcal{L} + \mathrm{k}_{avg} \Delta\mathcal{L}' + \Delta\Phi\right)] \tag{3.15}$$

with

$$\begin{aligned} \Delta\mathcal{L} &\equiv l_a - l_b = \left(\frac{l_{sa} + l_{ia}}{2} + l_{pa}\right) - \left(\frac{l_{sb} + l_{ib}}{2} + l_{pb}\right), \\ \Delta\mathcal{L}' &\equiv l'_a - l'_b = \left(l_{sa} - l_{ia}\right) - \left(l_{sb} - l_{ib}\right). \end{aligned} \tag{3.16}$$

[6] In Fig. 3.5, the spatial overlap can be done via a beam splitter.

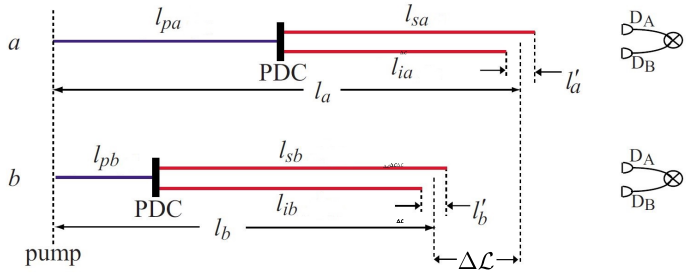

Figure 3.5: An illustration of the propagation paths of down-conversion photon pairs and pump photons in two sources in a typical two-photon interference experiment is shown. The signal and idler photon paths are indicated by l_{sa} (l_{sb}) and l_{ia} (l_{ib}) produced by pump photon with path length l_{pa} (l_{pb}), where $a(b)$ indicates the paths for the first (second) nonlinear source, here labelled by PDC. The total path lengths of the down-conversion photons combined with the ones of the pump photons are indicated by l_a and l_b, where the biphoton path length difference $\Delta\mathcal{L}$ is defined as $\Delta\mathcal{L} = l_a - l_b$. Another important parameter is the biphoton path-asymmetry-length difference $\Delta\mathcal{L}' = l'_a - l'_b$, where l'_a and l'_b are the path-asymmetry lengths for the path a and b. Adapted from [110].

Here, $\Delta\mathcal{L}$ denotes the biphoton path length difference between down-conversion and pump photons (see Fig. 3.5), k_p is the wave vector in vacuum of the pump photon and $\mathrm{k}_{avg} \equiv \frac{\mathrm{k}_s - \mathrm{k}_i}{2}$ is the mean vacuum wave vector magnitude of the signal and idler photons. The phase difference arising from the biphoton path-asymmetry length difference is denoted by $\Delta\mathcal{L}'$, and $\Delta\Phi$ denotes the phase difference between the fields that in contrast to the dynamical phase is acquired due to reflections and geometric phase [110,111]. Note that $\Delta\Phi$ did not arise from the reformulation of Eq. 3.9 but was added to consider the above-mentioned phases.

As not only the down-converted beam has a coherence length l^{dc}_{coh}, but also the pump beam and the down-converted beam are coherent to each other, the two ways of creating photon pairs lead to an interference effect, which makes itself noticeable with oscillation fringes within the count rates, while scanning $\Delta\mathcal{L}$ between the pump and the down-conversion beam before they reach the second source.

Interference effects occur as long as the following relations hold:

$$\begin{aligned} \Delta\mathcal{L}' &< l^{\mathrm{DC}}_{\mathrm{coh}}, \\ \Delta\mathcal{L} &< l^{p}_{\mathrm{coh}}, \end{aligned} \tag{3.17}$$

where $l^{\mathrm{p}}_{\mathrm{coh}}$ is the coherence length of the pump photons, which are in line with the statements regarding the visibilities $\mathrm{V}_{s/i}$, V_c and V_p with the definitions shown in Eq. 3.10 and Eq. 3.14. In this case, the requirement of the coherence length of the SPDC photons $l^{\mathrm{DC}}_{\mathrm{coh}}$ being much smaller than $\Delta\mathcal{L}$ is ensured automatically, as the idler and signal beams of the two different crystals are within the same mode and hence not manipulated independently (see Fig. 3.4). Hence, under the assumption of the degeneracy of the signal and idler frequencies (hence $\mathrm{k}_{avg} = 0$) the coincident count rates with the newly introduced quantities take the following form:

$$\mathcal{C}_c = |A|^2 \mathcal{I}_p \bar{f}_s \bar{f}_i [1 + \mathrm{V}_p \mathrm{V}_c \cos(\mathrm{k}_p \Delta\mathcal{L} + \Delta\Phi)]. \tag{3.18}$$

The biphoton path length difference between down-conversion and pump photons $\Delta\mathcal{L}$ can be changed in the presented experimental arrangement (see Fig. 3.4) by splitting the down-conversion fields from the pump field in between the two SPDC sources. Then, the path lengths can be changed with an interferometer, where the photons are combined again before propagating through the second source. The non-dynamical phase difference $\Delta\Phi$ includes wavefront distortions acquired through free-space propagation and considers the fact that the group velocities of the pump and the SPDC photons are not equal, leading to walk-off effects, caused by the difference in velocities and directions of energy and phase propagation [36].

3.3 Technical realization

The desirable goal at this point of the experiment was the design and implementation of an experimental arrangement enabling two-photon pair interference with the possibility to increase the distance between the two photon-pair sources. Due to the collinear propagation of both the pump and the SPDC photons the sending/receiving optical elements (additional to the optical elements in between them) required operative readiness for the respective wavelengths. Another crucial part was the introduction of a phase difference between the pump and the SPDC photons, which should–in cooperation with the detection system–exhibit and quantify the interference effects. A schematic diagram of the experimental setup is displayed in Fig. 3.6 comprising, in general, the sending station and the receiving station, including a nonlinear photon-pair source on each side. In the following, the most crucial technical elements and their function shall be shown, while furthermore an alignment process for eventually achieving the defined goal is presented.

3.3.1 Photon-pair source

Pump laser source

The photon pairs were created via the SPDC interaction within a nonlinear medium, which was pumped by a coherent laser source. The pump light source was a single-mode continuous-wave (cw) laser beam produced in a compact laser diode module manufactured by Ondax with a central wavelength (CWL) of around 405.5 nm. The pump's spectral distribution had a full-width at half-maximum (FWHM) bandwidth of $\Delta\nu = 160\,\text{MHz}$ according to the manufacturer [112], resulting in a coherence time of $t^p_{coh} = 2\,\text{ns}$ and a coherence length of $l^p_{coh} = 596\,\text{mm}$.

The maximum power of the pump beam at the location of the first nonlinear medium was measured with a powermeter (PM100A Thorlabs) and yielded $15.40\,\text{mW}\pm0.05\,\text{mW}$, resulting to an intensity of $7740.88\,\text{W/cm}^2\pm25.13\ \text{W/cm}^2$ at the focal point. The above laser intensity and the choice of the properties of the nonlinear crystal (see below) led to a brightness of $B = 4.8\times10^5 s^{-1}$, which indicates the photon pairs created at the source per second[7]. The laser module was operated at maximum output power, ensuring a strong SPDC signal, but keeping in mind that the impact of higher emission SPDC photons on the visibility is detrimental (see discussion in section 2.2.4). The pump beam, which is assumed to have a Gaussian beam intensity profile[8], passed a quarter-wave (QWP) and a half-wave plate (HWP) in order to increase the conversion efficiency of the down-conversion beam, as only the projection of linearly polarized

[7] The brightness B was estimated with the single count rates $\mathcal{C}_{A,B}$ and coincident count rate $\mathcal{C}_c$ via $B = \frac{\mathcal{C}_A\cdot\mathcal{C}_B}{\mathcal{C}_c}$, where preliminary background induced counts Δ and accidental coincident counts $\mathcal{C}_{acc}$ are ignored (using Eqs. A1 and A4). Note that these assumptions require measuring the brightness with low ambient light and sufficiently low pump power.

[8] A Gaussian beam profile was ensured by coupling the laser beam into a single-mode fiber (Thorlabs S405HP).

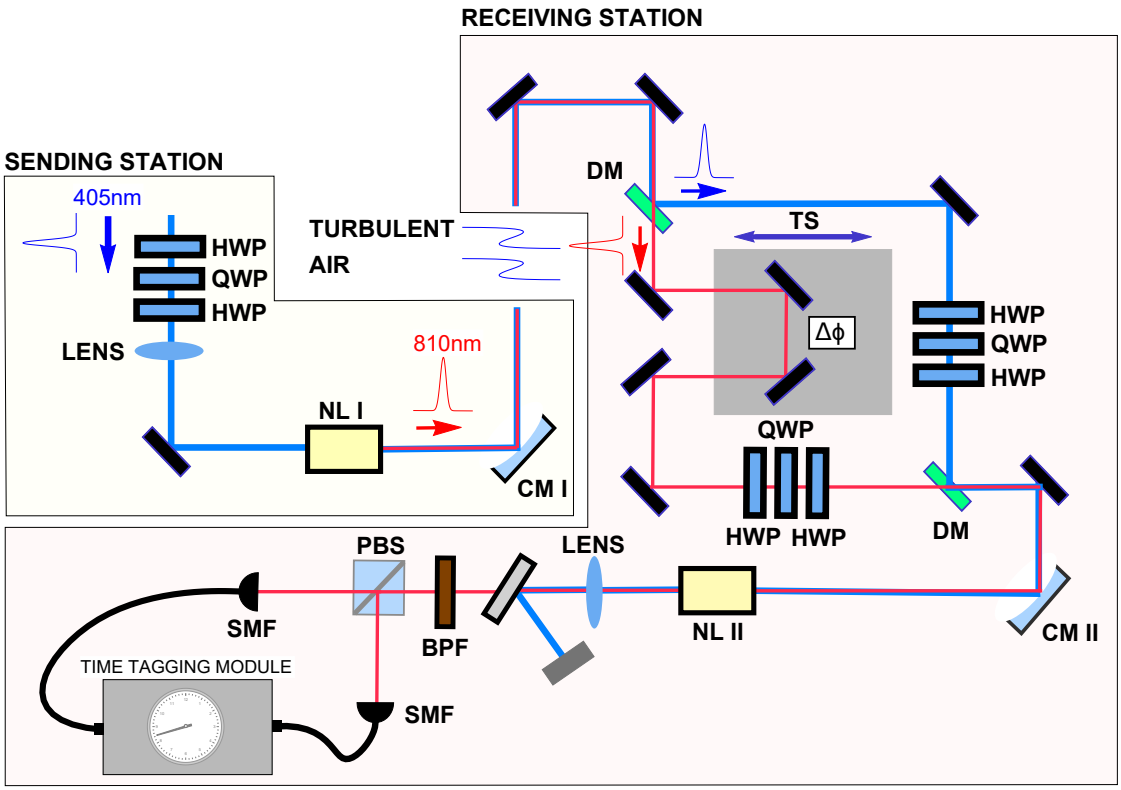

Figure 3.6: A schematic picture of the experimental setup, which contains the coherent pumping of two nonlinear crystals (NL I at the sending station and NL II at the receiving station) with pump and down-converted beams propagating collinearly, is shown. The phase difference $\Delta\phi$ was introduced via a trombone system (TS) within a Mach-Zehnder interferometer after splitting up the pump and the down-converted beam and combining them again with a dichroic mirror (DM). To avoid chromatic aberration of the lenses between pump and SPDC photons, two concave mirrors (CM I and II) for both sending and receiving the signals were used. To filter out the undesired pump signal as well as to narrow down the wavelength distribution, bandpass filters (BPF) were implemented in the detection system. The recorded detection events were labeled with a timestamp provided by a time tagging module. Simultaneous clicks within a coincident timing window t_c, which was chosen to be 1.5 ns, were identified as coincidences.

light contributes to the conversion efficiency. In the presented case, maximum efficiency was achieved for vertically polarized light (s-polarized). Rotating the polarization away from 90° (V- or s-polarization) of the pump beam leads to a decrease of the down-conversion signal until it vanishes at 0° (H- or p-polarization) and due to dark count rates solely the background signal will remain.

Focus parameters

Quantitatively derived calculations for optimizing the focus parameters have been studied for degenerate type-II SPDC with spectral filtering [41, 113]. In terms of the heralding efficiency, defined as $h_{s/i} = \mathcal{C}_c/\mathcal{C}^{i/s}_{sing}$ [59,114], with $\mathcal{C}_j$ being count rates for coincident (c) and singles ($sing$), respectively, and the brightness B, a trade-off is fundamentally present, preventing a maximal brightness and a maximal heralding efficiency with one and the same focus parameters in a given system. The cause of the trade-off can be outlined starting with the definition of the heralding efficiency $h_{s/i}$, which can be described as the probability that one photon triggers via its detection the partner photon in the conjugate spatial mode [41]. A loosely focused pump beam produces SPDC photon pairs with little angular deviation, due to momentum conservation, which results in the emission of the photon pairs symmetrically with respect to the optical axis of the beam. Hence, the probability of collecting photon pairs increases, as both photons propagate most likely in the same spatial mode, given, that the detection mode equals an area close to the optical axis of the pump beam. On the other hand, tight focusing conditions in the nonlinear crystal force more pump photons to travel in the same spatial mode, namely in the center of the pump beam. However, due to the wide beam spread of the SPDC photons, the probability for both being collected in the same mode (given a fixed collection mode close to the optical axis of the pump photons) decreases.

The focusing condition is commonly expressed in terms of the focal parameter $\xi = \frac{L}{\mathrm{k}\omega^2}$, which indicates for values with $\xi << 1$ corresponding to weak focusing, and hence high heralding efficiency h, and $\xi >> 1$ for strong focusing, which results in a higher brightness B. Although a high number of photons was desired in the presented experiment, the focus parameter had to be chosen according to the available optical elements and with having an eye on the propagation behavior in free space. Most importantly, the available concave mirror with given focal length f and the finite aperture areas of the optical elements between the sending and receiving site, demanded lose focusing condition. In other words, with the fixed focal length of the sending concave mirror, the beam waist of the pump beam in the first nonlinear crystal dictates the collimated beam radius. However, strongly focusing would result in a bigger collimated beam radius, leading to substantial geometrical loss with respect to the finite aperture areas of the optical elements following the sending module. According to the results in Refs. [41, 113], the chosen focal parameter for the pump beam of $\xi_p = 0.056$ in a type-II SPDC scenario indicates a weakly focused beam and therefore high heralding efficiency. Initial tests at an early stage of the setup, where local measurements on the crystal were performed, yielded a symmetric heralding efficiency of $h \sim 27\%$ (with detector efficiencies $\sim 40-55\%$), hence agreeing with the above-made statements.

Under the assumption of a Gaussian beam (and hence the paraxial approximation [52]) with beam waist ω_0 propagating through a focusing lens with focal length f, the beam radius ω exiting the lens can be calculated via the equation

$$\omega = \frac{\lambda f}{\pi \omega_0}. \tag{3.19}$$

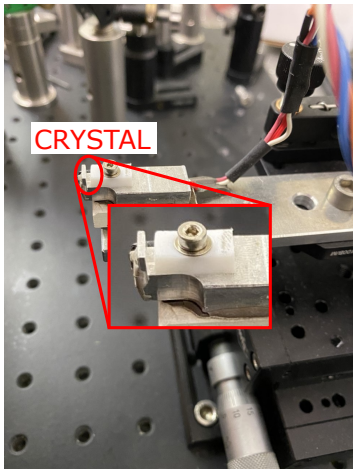

Figure 3.7: A photograph of the KTiOPO4 nonlinear bulk crystal (red circle) within a custom-made temperature-controlled oven with the possibility for translation in the x, y, and z directions via a combination of crossed-roller aluminum linear stages (Newport M-426) and 90° angle brackets (Newport M-460P-90BK) is depicted.

The outcoupling stage of the pump beam comprised of a five-axis single-mode fiber aligner (Newport 9131-M) and a plan achromat objective (Olympus RMS40X), which leads with its optical parameters to a collimated beam radius of 1.55 mm. Subsequently, the beam was focused into the nonlinear medium with a UV-coated $f = 300\,\text{mm}$ lens, with f being the focal length. The focusing condition resulted in a beam waist of $\omega^p_{focus} = 25\,\mu\text{m}$, in agreement to the focal parameter of $\xi_p = 0.056$, with the crystal length $L = 1\,\text{mm}$. Hence, the Rayleigh length ($z_R = \frac{2\pi\lambda}{\omega}$), which determines the length across which the beam can be regarded as a plane wave, was approximately 4.85 mm. Therefore, the assumption that the pump beam was a plane wave throughout the 1 mm-long medium, was valid. To avoid chromatic aberration[9] between SPDC ($\lambda_{s/i} = 810\,\text{nm}$) and pump ($\lambda_p = 405\,\text{nm}$) photons, two dielectric concave mirrors (Thorlabs CM750-500) with a diameter of 75 mm (one each on the sending and receiving site) were implemented.

Regarding the propagation in free space, a focal length of $f_{CM} = 500\,\text{mm}$ ensured a Rayleigh length of 51.6 m for the pump beam, which suffices in terms of the divergence angle with respect to the aperture diameter of the optical elements ($1'' = 25.4\,\text{mm}$) used in the setup. A more detailed discussion of the beam parameters with respect to free-space propagation follows in section 3.3.2.

Nonlinear crystals

For the creation of down-converted photon pairs two identical $1{\times}2{\times}1\,\text{mm}^3$ ($x \times y \times z$) periodically poled KTiOPO4 nonlinear bulk crystals manufactured by Raicol with poling period $\Lambda = 10.5$ μm were used (see Fig. 3.7). The crystals were both embedded in a fixation located on an aluminum block. A PT100 platinum resistor measured the temperature which was controlled with a Peltier module, located under the fixation. To maintain a stable temperature within the range of 0.1° C, a temperature controller (Thorlabs TC200) providing electronic feedback was implemented. As discussed in section 2.2.1, the highly scattering nature of the SPDC process leads to the fact that the output is governed by the phase-matching conditions [115].

[9] Chromatic aberration describes shift of a lense's focal length depending on the impinging beam's wavelength.

Index	A	B	C	D
n_x	2.1146	0.89188	0.20861	0.01320
n_y	2.1518	0.87862	0.21801	0.01327
n_z	2.3136	1.00012	0.23831	0.01679

Table 3.1: The Sellmeier equation coefficients for KTP [116, 117] for estimation of the refractive index of the nonlinear medium are depicted.

Furthermore, each crystal was cut for the type-II phase-matching, meaning that the signal and idler beams have perpendicular polarization to each other ('$e-oe$'- or '$o-eo$'- polarization, see section 2.2.2). This cut provided SPDC-generated photon pairs in the visible optical range, hence the crystal is highly transparent for the optical frequencies used for these purposes. The photons were collected in a collinear geometry, where the spatial modes were defined by two single-mode fibers (SMF) at the detection system on the receiving site. The phase-matching among three optical waves determines the direction of light propagation. In the collinear case, the quasi-phase-matching condition is reduced from the vector form to the zero-order contribution of the phase-mismatch (see Eq. 2.35). The visibility depended highly on the indistinguishability of the SPDC photons within the crystal (signal and idler, respectively) as well as the indistinguishability between the two nonlinear sources. Hence, the degenerate case ($\lambda_s = \lambda_i = \frac{\lambda_p}{2}$) was desired for our purposes.

For purposes of comprehension, the experimentally measured spectral distribution of signal and idler, which is represented by the two-photon mode function $\phi_{\zeta_s\zeta_i}$ (see section 2.2.3), can be compared with the theoretical prediction based on the Sellmeier equations (describing the refractive indices n of the electromagnetic fields in nonlinear media) as well as the poling period Λ and the crystal length L. Vanherzeele and Bierlein [116, 117] studied the nonlinear optical properties of KTP and derived from empirically obtained data the refractive indices in x, y and z directions:

$$n_i(\lambda)^2 = A_i + B_i/\left[1 - (C_i/\lambda)^2\right] - D_i\lambda^2, \tag{3.20}$$

where the index i represents the spatial directions x, y and z, while the coefficients A, B, C and D are depicted in Table 3.1. A solution can be distilled for the degenerate case by solving the equation $\Delta k(n(\lambda), \Lambda) = 0$ (see Eq. 2.36), which presumes perfect phase-matching. However, a change in temperature, which has been studied for KTP by Wiechmann [118], allows for a higher degree of manipulation for the experimenter in terms of achieving degeneracy of the spectral distributions of the two SPDC sources. The deviations in temperature of the refractive indices follow the following formulas:

$$\begin{aligned}
\partial n_x/\partial T &= \left(1.427\lambda^{-3} - 4.735\lambda^{-2}\right. \\
&\quad \left.+8.711\lambda^{-1} + 0.952\right)\left(10^{-6}/^{\circ}\mathrm{C}\right) \\
\partial n_y/\partial T &= \left(4.269\lambda^{-3} - 14.761\lambda^{-2}\right. \\
&\quad \left.+21.232\lambda^{-1} - 2.113\right)\left(10^{-6}/^{\circ}\mathrm{C}\right) \\
\partial n_z/\partial T &= \left(12.415\lambda^{-3} - 44.414\lambda^{-2}\right. \\
&\quad \left.+59.129\lambda^{-1} - 12.101\right)\left(10^{-6}/^{\circ}\mathrm{C}\right),
\end{aligned} \tag{3.21}$$

where T describes the temperature of the crystal in °C. Note that the input dimension of the

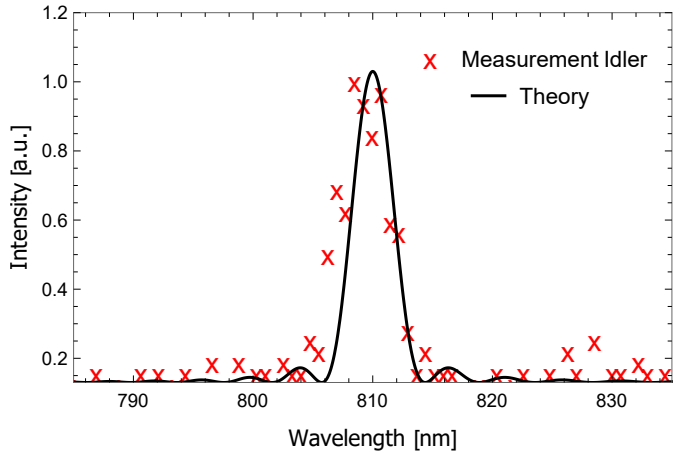

Figure 3.8: A comparison of measured data of the SPDC idler's wavelength distribution (red crosses) with the theoretical model (black solid line) is depicted. The crystal was set to a temperature of 166.10° C, read off from the temperature controller. The signal's spectrum shows equal distribution due to the degenerate phase-matching condition.

wavelength for both Eqs. 3.20 and 3.21 is in μm. Given the poling period of $\Lambda = 10.5$ μm and the length in the direction of propagation of the pump beam $L = 1\,\text{mm}$ of the nonlinear crystal (as provided by the manufacturer), solving $\Delta k(\Lambda) = 0$ (see Eq. 2.36) leads to a temperature of degeneracy of 155.22° C. However, the measurements with the spectrometer showed that degeneracy was achieved at a temperature of 166.10° C. Solving the phase-mismatch equation for the experimentally found temperature leads to an effective poling period $\Lambda^{eff} = 10.533\,\mu$m. This discrepancy can be explained by the fact that the crystal dimensions, especially the poling period Λ, are subjected to manufacturing tolerances. Moreover, a small deviation of the pump beam's angle of incidence with respect to the crystal surface results in an effective change of the phase-matching condition [119]. The impact of the thermal expansion of the nonlinear crystal in x-direction [120], which is accompanied by an altering $\Lambda^{eff'}$ on the spectral distribution, is negligible [119].

Fig. 3.8 shows the theoretical prediction derived above in comparison to the measured spectrum of one partner of the photon pairs. This was done by coupling the SPDC signal into an SMF, which was connected to a single-photon spectrometer. Note that the background counts of the measured signal on the left and right side of the peak lead to a difference in amplitudes in the theoretical and experimental case, which was not accounted for here, as the intensities were normalized to each other.

KTiOPO4 is an optically non-isotropic transparent and biaxial medium, where the principle crystal axes are accompanied by different polarization-dependent refractive indices (see Sellmeier equation Eq. 3.20). In a type-II cut KTiOPO4 crystal, where the photon pairs created the SPDC process created are perpendicularly polarized (H- and V-polarization), the fact mentioned in the last sentence leads to a difference in their group velocities and hence a time delay after propagation through the birefringent media. Different arrival times of the photon pair partners could lead to a certain degree of distinguishability, hence lowering the interferometric visibility $\mathcal{V}$ observed in the count rates, which also depends on the coherence time of the SPDC photons t_{coh}^{DC} (see Eq. 3.15 and Eq. 3.18). However, Eq. 3.15 and Eq. 3.18 predict a high degree of visibility $\mathcal{V}$, if the biphoton path-asymmetry-length difference $\Delta\mathcal{L}'$ (see Fig. 3.5) is much smaller

than the coherence length l_{coh}^{DC}. These quantities are associated with the difference in time delays of the photon pairs created in the first nonlinear crystal $\Delta\tau_1^{DC}$ with respect to the time delay introduced in the SPDC photon pairs created in the additional crystal $\Delta\tau_2^{DC}$. The above statement regarding the coherence length and path differences is equivalent to the following: the difference in time delays higher than the coherence time of the SPDC photon pairs leads to decreasing visibility, which can be formulated in the following inequality as a requirement for high visibility:

$$|\Delta\tau_1^{DC} - \Delta\tau_2^{DC}| \ll t_{coh}^{DC}. \tag{3.22}$$

The maximal time delay τ_{delay} introduced within a nonlinear crystal can be computed with considering the group velocities associated with the respective refractive indices and the length L:

$$\tau_{delay} = LD, \tag{3.23}$$

with D being the difference between the inverse group velocities $1/v_g^j$ for the signal and idler beams (see Eq. 2.39).

Inserting the Sellmeier equations from Eq. 3.20 and Eq. 3.21 into Eq. 2.39 and then into Eq. 3.23 with the crystal length of $L = 1\,\text{mm}$ leads to an introduced maximal time delay of $\tau_{delay} = 309\,\text{fs}$. The coherence time of the SPDC photons t_{coh}^{DC} depends on the interference filters implemented in the setup. The resulting bandwidth in the experimental arrangement was around 3 nm, which yielded a coherence time of $t_{coh}^{DC} = 232\,\text{fs}$ and a coherence length of $l_{coh}^{DC} = c\,t_{coh}^{DC} = 69.7\ \mu\text{m}$. A difference in time delays of the SPDC photon pairs from the two nonlinear sources $|\Delta\tau_1^{DC} - \Delta\tau_2^{DC}|$ equal to the coherence time would lead to an undesired decrease in visibility to 50%.

Fig. 3.9 shows the influence of the birefringence and the accompanying difference in group velocities on the time delay between the perpendicularly polarized SPDC photons pairs after propagating through the two nonlinear media. Assuming that the polarizations remain equal between the two crystals, the lack of geometric rotation of the identical crystals (hence equal birefringent conditions) with respect to the z direction would lead to a mean time delay[10] of $\Delta\tau_1^{DC} = -\frac{3}{2}\Delta\tau$ [see Fig. 3.9 (a)]. Rotating the crystals with respect to to each other by $\theta_2 = 90^\circ$ compensates the maximal time delay introduced by the first crystal [$\Delta\tau_1^{DC} = -\Delta\tau$, see Fig. 3.9 (b) (ii)], but yields an absolute time delay for the photon pairs created at the end of the crystal, without prior time delay [see Fig. 3.9 (b) (i)]. Subsequently, the mean time delay of the photon pairs at this point is $\Delta\tau_1^{DC} = \frac{\Delta\tau}{2}$. The photon pairs created in the second nonlinear crystal experience without any further compensation element for both $\theta_2 = 0^\circ$ and $\theta_2 = 90^\circ$ (with $\theta_1 = 0^\circ$) a maximal absolute possible time delay of $\Delta\tau$, would result in a mean time delay of $\Delta\tau_1^{DC} = \frac{\Delta\tau}{2}$. However, only the setting $\theta_2 = 90^\circ$ introduces a mean time delay of $+\frac{\Delta\tau}{2}$ [see Fig. 3.9 (c)], which leads to the fact that the left-hand side of Eq. 3.22 vanishes, ensuring high visibility of the system. Hence, the second crystal acts as a compensating medium, while an additional approach, naturally, would be rotating the polarization of both the SPDC and the pump beam with respect to the identical nonlinear crystals, accordingly, resulting in the same outcome.

[10] Maximal indistinguishability is ensured with a perfect temporal overlap of the SPDC photon pair's wave packets, when the mean time delay was compensated [121].

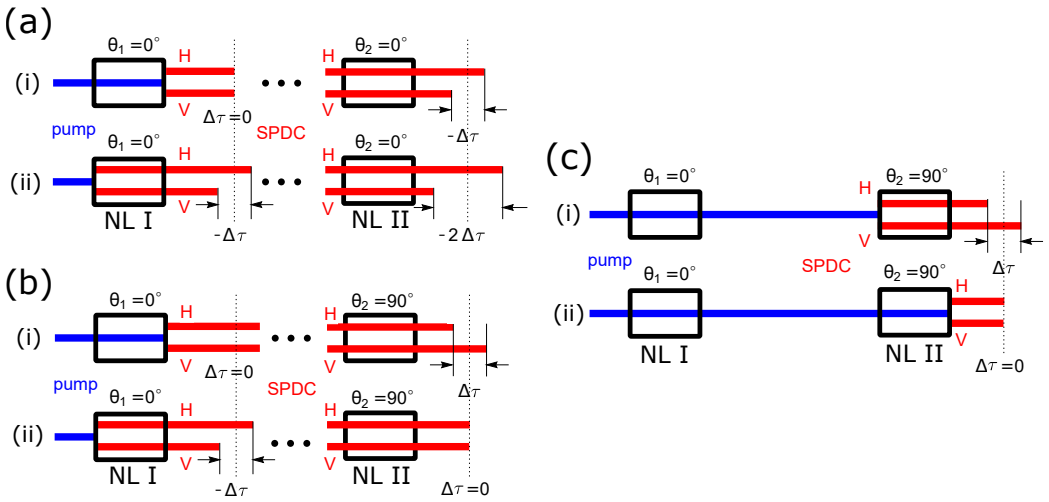

Figure 3.9: A graphical scheme of the compensation of the intrinsic temporal shift introduced by birefringence within the identical nonlinear crystals, leading to different group velocities for H- and V-polarized photon pair partners is shown. (a) The lack of spatial rotation along the direction of the crystalline axis (z-direction) of the identical nonlinear crystals to each other ($\theta_1 = 0°, \theta_2 = 0°$) leads to the possible time delays between H- and V-polarized photon pair partners created in the first crystal (NL I) of $-\Delta\tau$ (i) and $-2\Delta\tau$ (ii), corresponding to a total mean time delay of $\Delta\tau_1^{DC} = -\frac{3}{2}\Delta\tau$, after the propagation through the second nonlinear crystal (NL II). (b) Rotating the nonlinear crystals by 90° along the z-direction with respect to each other ($\theta_1 = 0°, \theta_2 = 90°$) leads to a possible time delay of $\Delta\tau$ (i) and the total compensation of the time delay (ii), corresponding to a total mean time delay of $\Delta\tau_1^{DC} = \frac{\Delta\tau}{2}$. (c) Without introducing any polarization compensation on the photon pairs created in the second nonlinear crystal, the mean time delay is $\Delta\tau_2^{DC} = \frac{\Delta\tau}{2}$ [a maximum time delay of $\Delta\tau$ (i) and no time delay (ii)], which is equal to the case in (b). In that case, no further compensation (in the form of a compensation medium) has to be implemented.

3.3.2 Free-space propagation in the lab

The proposed experiment's most important feature was the potential to increase the distance between the SPDC sources, which was essentially limited technically by the choice of beam parameters and therefore of the optical elements implemented in the setup (and their availability). Due to the difference in wavelengths of the SPDC beam ($\lambda_{s,i} = 810\,\text{nm}$) and the collinearly propagating pump beam ($\lambda_p = 405\,\text{nm}$), the respective interaction with the optical elements as well as the propagation behavior had to be taken into consideration in terms of the technical implementation.

As introduced in section 3.3.1, to avoid chromatic aberration between SPDC and

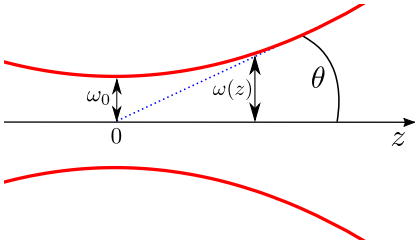

Figure 3.10: The propagation behavior of a Gaussian beam's beam radius $\omega(z)$ is depicted (red). At the origin, the (minimum) beam waist is indicated with ω_0. In the far-field regime, the beam divergence is described by the angle θ.

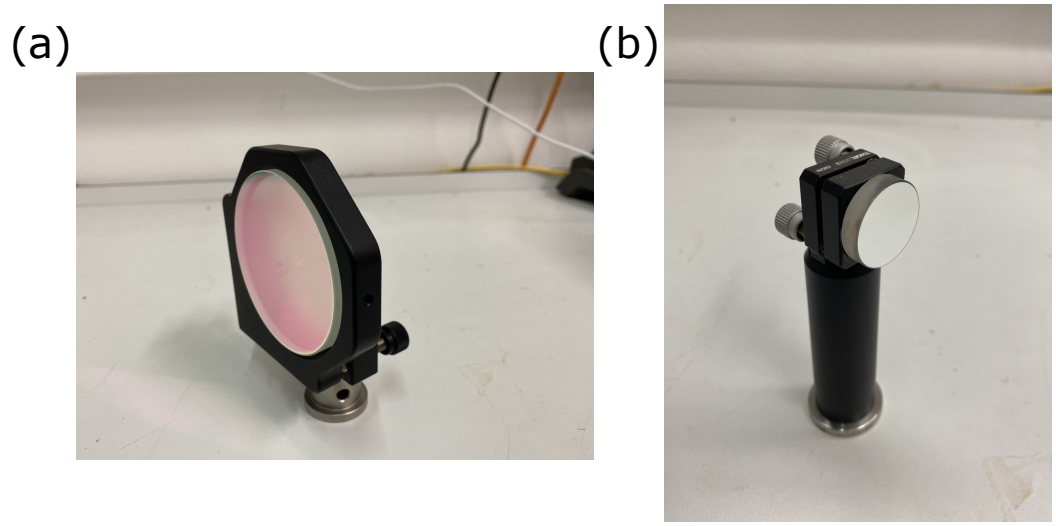

Figure 3.11: (a) The implemented dielectric-coated concave mirror (Thorlabs CM750-500) with a diameter of 75 mm, which prevents chromatic aberration of the collinear propagating pump (405 nm) and SPDC (810 nm) beams, is depicted. (b) Depiction of the implemented 25.4 mm ultra-broadband mirror (Semrock MM2-311S-25.4) on the respective compact kinematic mirror mount (Thorlabs KMS), which offers a mean reflectivity of 99% for a wide range of optical wavelengths (350 – 1100 nm).

pump photons, two dielectric-coated concave mirrors with 75 mm (Thorlabs CM750-500) diameter were implemented as sending and receiving optical elements. The curved shape of a concave mirror prevented the beams with different wavelengths from focusing into different spots, as would be the case with BK7 lenses, where the wavelength-dependent refractive index leads to differing refraction angles (see Fig. 3.12). Hence, the usage of dielectric-coated concave mirrors [see 3.11 (a)] ensured the collinear propagation as well as spatial and temporal distinguishability throughout the setup for both pump and SPDC beam. Note that BK7 bi-convex lenses were used within the setup but were solely acting on either the pump or the SPDC beam.

A laser beam can be described as a Gaussian-beam wave within the paraxial approximation [52]. The pump field used in this experiment to create SPDC photons was initially filtered with respect to its spatial distribution by an SMF, ensuring an approximately Gaussian propagation behavior through the entire experimental setup. Hence, in vacuum, a beam traveling along the z direction can be described as a Gaussian-beam wave, with the beam radius $\omega(z)$ behaving as

$$\omega(z) = \omega_0 \sqrt{1 + \frac{z^2}{z_R^2}}, \tag{3.24}$$

with $\omega(0) = \omega_0$ being the beam waist at position $z = 0$ and z_R being the Rayleigh length (see Fig. 3.10). From Eq. 3.24 can be deduced, that the beam radius varies along the propagation direction, which can be assigned to the phenomenon of diffraction. Apart from that, in the far-field regime, the beam divergence follows the relation $\theta = \frac{\lambda}{\pi\omega_0}$ and hence, the beam experiences stronger divergence for smaller waists and longer wavelengths.

The focal lengths of the two concave mirrors were chosen to be $f_{CM} = 500$ mm throughout all propagation distances. This ensured, with the pump waist at the position of the first nonlinear

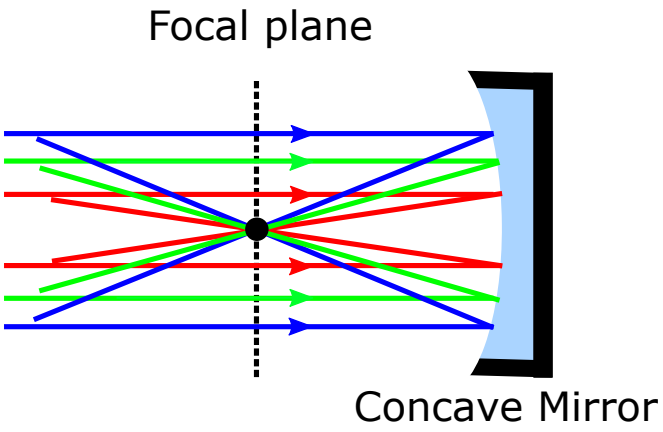

Figure 3.12: The functionality of a concavely shaped mirror is shown. Due to the curved formation of the dielectric surface, the light, independent of its wavelength, is reflected at different angles at different positions on the mirror onto the same point in the focal plane. This is due to the fact that the normal to the mirror surface is different for each position.

crystal being $\omega_p = 25\,\mu$m and a resulting collimated beam radius of $\omega_p^{coll} = 2.58\,$mm, a Rayleigh length of 51.6 m for the pump beam. Close-to-optimal coupling efficiency for a given pump beam waist ω_p was found experimentally for the following relationship between the pump and SPDC focal parameters: $\xi_{s/i} \approx \sqrt{2.84\xi_p}$ [113]. Hence, the theoretical SPDC beam waist with $\xi_{s/i} = 0.40$ was $\omega_{s/i} = 13.6\,\mu$m, leading to a collimated beam radius of $\omega_{s/i}^{coll} = 9.48\,$mm, resulting in a Rayleigh length of 348.6 m. In theory, after 70 m the beam radii reach $\omega_p^{coll70} = 4.35\,$mm and $\omega_{s/i}^{coll70} = 9.67\,$mm, respectively. Hence, over a maximum distance of 70 m, the diffraction limit for the Gaussian-shaped beams does not exceed the diameter of 25.4 mm, the maximum aperture diameter of the optical elements used in the setup. In reality, the beam divergence exceeds the diffraction limit, which, in combination with misalignment and the used alignment technique for greater distances, could lead to loss of the signal, which will be discussed below.

This maximum propagation distance of 70 m was chosen in consideration of the finite length of the optical table and the finite number of ultra-broadband coated BK7 mirrors [Semrock MM2-311S-25.4, see Fig. 3.11 (b)] which were used to let the beams propagate from the sender to receiver (see the arrangement in Fig. 3.13). Multiple 25.4 mm ultra-broadband mirrors were placed at both ends of the optical table in the lab to let the beams travel from the sending station to the receiving station, while the mirrors were arranged in such a way, that the beam was reflected from one end to the other multiple times. In fact, for the maximum propagation distance (70 m), the mirrors were implemented such that double reflections per mirror were possible. The alignment procedure for double reflection to increase the propagation distance is depicted in Fig. 3.14 (a-d). To exploit the whole area of the mirror, double reflections per mirror, which are located in two rows on either end of the optical table, were implemented. Furthermore, narrow mirror mounts with two adjustment knobs for rotation and hence precise alignment were used [see Fig. 3.11 (b)].

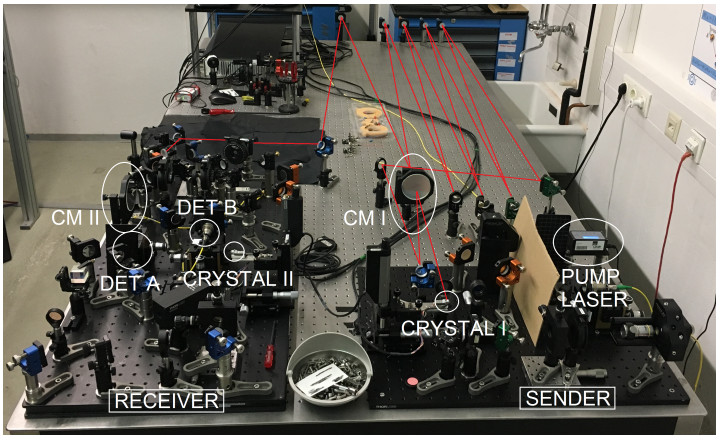

Figure 3.13: A photograph of the experimental setup and the mirror arrangement for increasing propagation distance is depicted. The laser module (PUMP LASER) provided a coherent pump beam to produce SPDC photon pairs in the nonlinear medium (CRYSTAL I) at the sending station (SENDER). A concave mirror (CM I) collimates both pump and SPDC photons. The red lines indicate the propagation path of the SPDC and pump photons from the sending station to the receiving station (RECEIVER), collected by the second concave mirror (CM II). The SPDC photon pairs created in CRYSTAL I are overlapped with the SPDC photon pairs produced in the second nonlinear medium (CRYSTAL II), produced by the collinearly propagating pump photons. Finally, the SPDC photon pairs are distributed to the detection system (comprising DET A and DET B). Note that in this specific experimental arrangement (20 m) each mirror reflects the beams just once, in contrast to the case of maximum propagation distance of 70 m (see text).

Firstly, three mirrors are arranged as depicted in Fig. 3.14 (a), where the incoming beam is reflected from mirror M1 to M2 and back again. One can convince oneself of the position of the beam by using a photosensitive detection card for the alignment or pump laser's respective wavelength. The mirror M3 is placed as close to the beam propagation path as possible facing the mirror M2, without blocking the beam. The closer the mirror M3 to M1, the easier the alignment process becomes, also owing to the fact that the beam hits the mirrors M2 and M3 on the lower end of the mirrors (see Fig. 3.14). In the next step, the angles θ_2 and θ_3, by which the mirrors M2 and M3 are rotated in an axis perpendicular to the plane of the optical table, respectively, are introduced such that the beam propagates from M3 back to the source [see Fig. 3.14 (b)]. The non-zero beam radius requires careful alignment to prevent spatial cut-off by not accurately hitting the mirror area, which ultimately would lead to signal loss. Afterwards, M3 is rotated such that the beam propagating to M2 is reflected back into the direction of M2 but closely next to the mirror [see Fig. 3.14 (c)]. The choice of the beam diameter with respect to the mirror aperture and the angles of the beam reflections dictates the geometrical loss introduced by hitting the mirror area not accurately. Finally, by placing an additional mirror M4 (M5) closely behind M2 (M3) and only changing the rotation angle of one mirror pair (here: M4 and M5), a stacked arrangement of mirrors can be implemented to increase the propagation distance even further [see Fig. 3.14 (d)]. Note that in order to reach any desired propagation distance, the Rayleigh length z_R and hence the beam parameters with respect to the mirror areas have to be altered respectively.

The geometrical loss on the mirror apertures as well as reflectivity probability of the respective wavelength of the dielectric coated mirror dominates the signal loss during propagation through

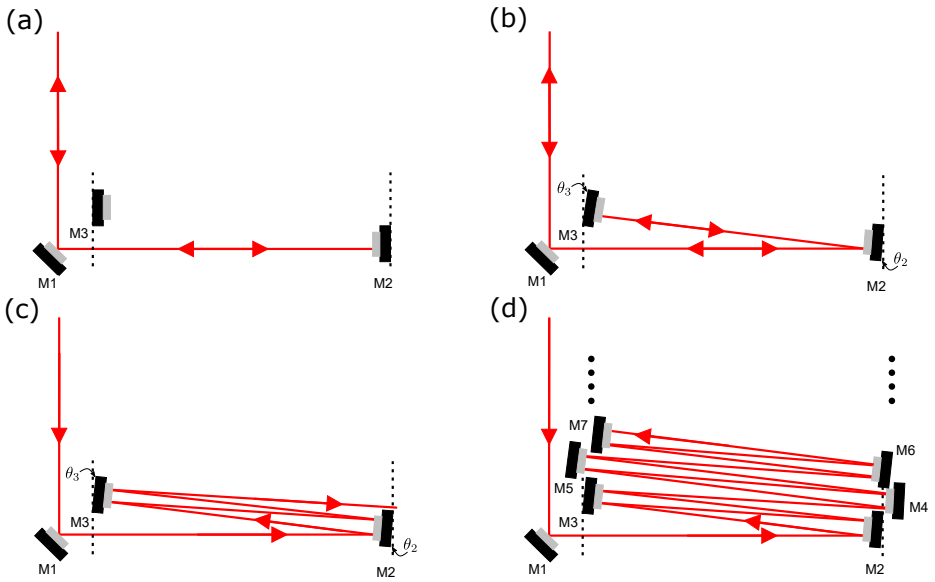

Figure 3.14: An alignment procedure of the mirror double reflection arrangement to increase the propagation distance of the collinearly propagating pump and SPDC photons is given.

the above-introduced mirror arrangement as well as other optical elements implemented in the setup. Assuming a mean reflectivity of 99% of in total 30 optical elements throughout the setup and a reflection probability of $\sim$ 80% of CM II[11], this leads to a total loss of 2.28 dB for the pump beam. By measuring the pump power ($\lambda_p = 405\,\text{nm}$) with a powermeter at the locations of the first and second nonlinear crystal, a loss of 2.84 dB was measured, which can be explained by misalignment and geometrical loss. A substantially higher loss for the same propagation distance has been observed for laser light with a central wavelength of $\lambda_{laser} = \lambda_{s/i} = 810\,\text{nm}$, namely 14.27 dB[12], although the coatings of the concave mirrors were fitting the IR range better ($>$ 99.8% reflectivity for 810 nm). The loss of the IR laser compared to the UV pump beam can be explained by the difference in the beam divergence angle θ, which leads to a higher geometrical loss. The difference in loss will translate to the photon count rates, especially when comparing the SPDC photon pairs created in the two nonlinear crystals. However, a sufficiently high pump power, the specific design of the nonlinear crystal (e.g., effective nonlinear coefficient d_{eff} and crystal length L), as well as the choice of the focal parameter ξ can influence the number of photon pairs for the collection of sufficient statistics in order to show the interference effect.

The wavelength-dependent refractive index of the atmosphere leads to a temporal shift Δt between photons with different wavelengths. Eq. 3.15 and Eq. 3.18 predict a decrease in interferometric visibility, when the photons of the collinearly propagating pump and SPDC photons are not within the respective temporal mode or exceeding the coherence time of the cw-pump laser

[11]The E03-coated dielectric concave mirror located at the sending station (CM I) is designed for wavelengths in the IR-range. However, for *s*-polarized beams in the UV range specifically, the probability for reflection is reasonable ($\sim$ 80%).

[12]The loss was validated with coincident measurements via $\eta_\text{A} = \frac{\mathcal{C}_c}{\mathcal{C}_B} = -16.29\,\text{dB}$ and $\eta_\text{B} = \frac{\mathcal{C}_c}{\mathcal{C}_A} = -15.77\,\text{dB}$ (using Eqs. A1 and A4), where the dark counts $\Delta_{A,B}$ were measured in a separate measurement and under the assumption of low accidental coincident counts $\mathcal{C}_{acc}$. The latter can be fairly assumed at this pump power regime, due to the low signal-to-noise ratio (see discussion in section 2.2.4).

$t^p_{coh} = 2\,\text{ns}$. The temporal shift Δt of two beams with different wavelengths introduced by group velocity dispersion over propagation distance l in atmosphere can be calculated by $\Delta t = \frac{l}{c}\Delta n$, with c being the speed of light and Δn the difference in the wave length dependent refractive index in air, $\Delta n = n(\lambda_{pump}) - n(\lambda_{s/i})$. For the maximum propagation distance of $l = 70\,\text{m}$ and $\Delta n = 236.3 \times 10^{-7}$ [122], this leads to $\Delta t = 5.51\,\text{ps}$, which is negligible compared to the coherence time t^p_{coh} of 2 ns.

Phase difference introduction

The count rates for detecting overlapping SPDC photon pairs created in two nonlinear sources predict a harmonic oscillation by changing the phase between pump and SPDC photons (see Eq. 3.15 and Eq. 3.18). To change the path length difference $\Delta\mathcal{L}$ between them, a Mach-Zehnder interferometer with the possibility to change the path length in one arm has been implemented (see Fig. 3.6). After propagating through the mirror system designed with different propagation distances (2, 20 and 70 m), the down-conversion beam was split from the pump beam with the help of a dichroic mirror (Semrock DM FF705, with a cut-on edge wavelength of 705 nm). The implemented dichroic mirrors are dielectric mirrors that exhibit differing transmission and reflection intensities depending on the incoming light's wavelengths. Hence, depending on the cut-on edge wavelength, the dichroic mirror is transparent for a wavelength regime, where probable reflections from the mirror's rear side need to be taken into account. This can be tackled by an anti-reflection (AR) coating located on the backside, which reduces the undesired reflection effect. The pump beam was reflected entering the upper arm of the interferometer and the down-conversion beam enters the lower arm via transmission through the DM, while finally overlapping the beams again with the help of a second DM. Now it was possible to manipulate the two beams independently from each other, for example, introducing a phase difference or performing unitary transformations such as changing their polarization by wave plates.

The introduction of a path length difference was done with the help of a trombone system (TS), which contains 4 mirrors in total implemented on a motorized linear translation stage (Newport Model 436) including a crossed-roller bearing for a motorized actuator (Newport Model LTA-HS 50 mm travel range) and a remotely controlled single-axis DC motor motion controller (Newport SMC100CC). Via a computer program, the stepper motor can be continuously moved with a minimum incremental motion distance of 100 nm resulting in velocities of $v_m = 100\,\text{nm/s}$ and higher.

While moving the trombone system, $\Delta\mathcal{L}$ changes, and therefore the phase difference between pump and down-conversion photons to each other are scanned. So, by moving the trombone system while measuring down-conversion photons created in crystal I and crystal II simultaneously, periodic oscillations are expected with an oscillation period equal to half the wavelength of the pump photons λ_p, when the count rate is displayed over the distance moved by the trombone system. This can be easily understood due to the fact that the photons reflected by the TS mirrors have to propagate twice (back and forth) the trombone system's driving distance in one direction.

The sampling rate $\tau_s = 1/t_{int}$ of the detection system, where t_{int} is the integration time, and the motor velocity v_m of the trombone system play a major role in the signal processing, especially with respect to the oscillation frequency and stability of the output signal. Oscillations of the measured count rates originating from other sources arise due to, e.g., the unstable temperature of the crystals and the laser, as well as beam wandering and angle-of-arrival (AoA) fluctuations after propagating through turbulent air. Crucially, in signal processing, the sampled signal has to be reconstructed with a sufficient degree of accuracy, with the important parameters being

the signal's expected oscillation period and the sampling detection rate τ_s. The choice of the absolute values are limited within technical restrictions[13], while this the product of the sampling rate and the motor velocity $\tau_s v_m$ is limited within theory. With the wavelength of the pump λ_p and hence the expected oscillation period of the count rate, namely being $v_m/(\lambda_p/2)$, one can estimate a lower limit for the sampling rate $\tau_s > v_m/\lambda_p$ via the Nyquist–Shannon sampling theorem [123].

In order to rule out effects other than interference causing oscillation fringes in the count rate, the following approach can be conducted. In section 3.4.4 a method will be discussed in detail that identifies the frequency of the oscillations within a signal and compares it with the expected oscillation period with help of the sampling rate $\tau_s = 1/t_{int}$ and the motor velocity v_m. It also involves a Fourier analysis which decomposes a signal into harmonic functions with certain frequencies ν, as the Fourier space shows contributions of frequencies within the signal, equipped with characteristic positions. Proving that the expected frequency equals the one obtained with the Fourier analysis while ensuring to rule out the causes described above, leads to the fact that no explanation but interference can be given.

Note that the measurements can be done, generally spoken, by moving the TS by a small amount to change the phase difference $\mathrm{k}_p \Delta\mathcal{L}$ and measure single-photon count rates while the trombone system stands still. However, this requires the phase difference to remain constant[14], which is not the case. This could be tackled technically by a locking system within the interferometer with closed-loop control of a reference mirror [124]. By choosing the respective measurement integration time of the detection system (see discussion below), motor velocities in the order of 100 nm/s are sufficient to observe interference fringes in the count rate of the down-conversion photons.

At the exit of the interferometer, the pump photons and the SPDC photons are overlapped again on the second dichroic mirror, where afterwards the beams are focused into the second crystal by the concave mirror CM II. Here, the pump photons have a finite probability to create SPDC photon pairs once more. At this point of the setup, due to the collinear propagation of the pump and SPDC photons, the overlap of photons created in two nonlinear sources takes place, resulting in interference effects.

3.3.3 Detection system

After the pump and the SPDC photons were focused into the second nonlinear crystal on the receiving site, both beams were separated from each other, as solely the SPDC photons were of interest. This was done with optical filtering elements as introduced below. Also, a BK7 lens with $f = 200\,\mathrm{mm}$ was implemented for the SPDC photons to enter the detection system with a collimated propagation mode.

Bandpass filters and PBS

Before entering the core of the detection system consisting of two single-mode fibers (Thorlabs 780HP) connected with single-photon avalanche photodiodes (APD), one had to make sure to block the pump beam and let down-conversion photons transmit only, which was done by a dichroic mirror (Semrock DM FF705, the cut-on wavelength of 705 nm) followed by additional

[13] The absolute values can solely be chosen in restriction to technical limitations, e.g. the discrete velocity and the technical performance of the stepper motor as well as the discrete integration time and the timing resolution of the detection system. Moreover, the detected photon number limits the sampling rate τ_s, too.

[14] Due to the fact that SPDC photon number distribution obey Poissonian statistics, the intensity measurements inhabit non-vanishing fluctuations and have to be taken into account in the signal processing (see section 3.4).

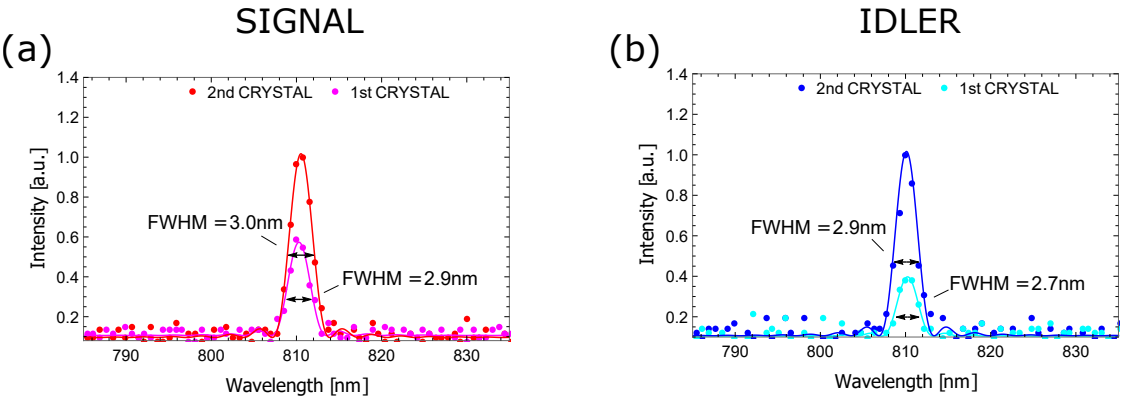

Figure 3.15: The measured wavelength distributions of the photon pairs created in two nonlinear crystals are depicted. The spectrum of the signal and idler photons from the nonlinear crystal located at the sending station (1st crystal) and the receiving station (2nd crystal) are depicted. The dots indicate the data points, and the straight lines are fitting curves to the sinc-function, consistent with the theoretical prediction introduced in section 2.2.3. (a) Through filtering with bandpass filters with FWHM=3 nm, the signal photons have roughly the same bandwidth. Setting the temperature of the identical crystals at 166.10° C, the degeneracy of the CWL of the photon pairs for both crystals can be obtained. (b) The idler photon's CWL is not only equal to the signal photon's within one single crystal, but also with respect to the idler photons created in the two identical crystals, ensuring spectral indistinguishability within the observed interference effect. Note that due to loss obtained during propagation, the intensity of the SPDC photons arising from the first and second nonlinear crystal can be matched experimentally via filters or by changing the SPDC conversion efficiency via rotating the pump photon's polarization.

bandpass filters. The latter were also used to narrow the frequency bandwidth of the down-conversion beam, acting as interference filters. This technique is often used in quantum optical interference experiments, as narrowing frequency bandwidths of interfering laser beams lead to an increase in indistinguishability, as less information about the respective beams is present in the temporal regime. The SPDC photons were filtered by 3 nm FWHM interference filters ensured by the respective bandpass filter implemented in the setup (see Fig. 3.15). High interferometric visibility can be obtained by overlapping the central wavelengths of the signal and idler, respectively. Hence, precise tuning of the phase-matching temperature of the identical nonlinear crystals is mandatory to match the central wavelengths of the photons pairs.

Due to the type-II SPDC process, the orthogonal polarization of the photons was exploited to spatially separate them from each other by a polarizing beam splitter (Newport 10FC16PB.5). Succeeding the bandpass filters, which acted on both signal and idler photons, the collinearly traveling photon pairs were separated into two spatial modes by a polarizing beam splitter (PBS). Finally, these modes were coupled into the detectors via SMF.

Single-photon avalanche photodiode and coincidence logic

The core of the detection system comprises a polarizing beam splitter, followed by two mirrors for each of two propagation paths for signal and idler. The mirrors allow to guide the light with the help of an objective (Newport 5726-B-H 10× magnification plan achromat objective with $f_{10\times} = 15.3\,\text{mm}$) focusing into a single-mode fiber (SMF). The latter acts as a spatial filter, as solely the TEM_{00} mode enters the SMF, hence ensuring spatial indistinguishability of the incoming photons.

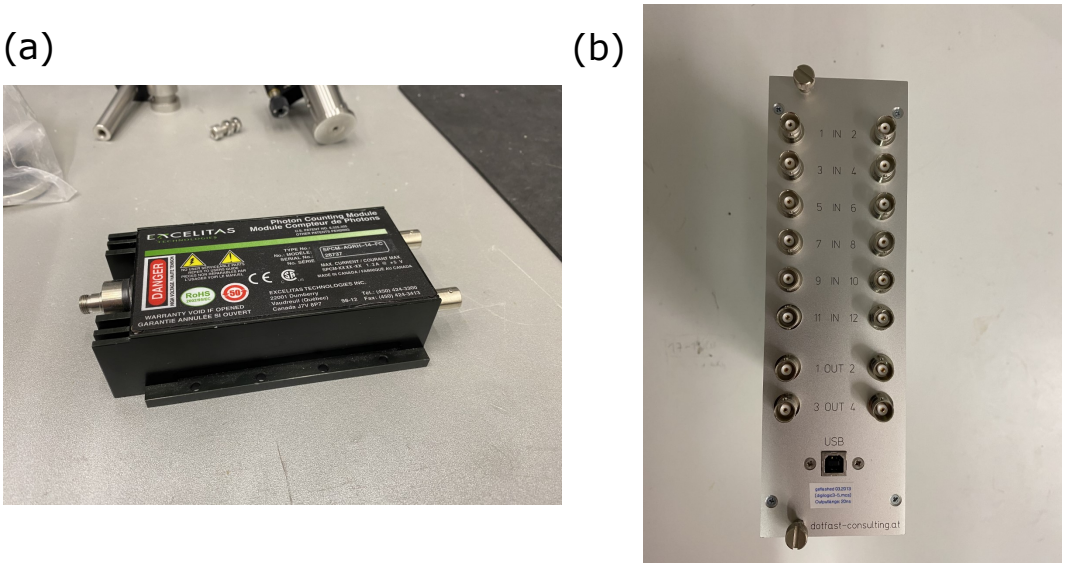

Figure 3.16: The photographs of the main elements of the detection system are depicted. (a) The single-photon counting module was manufactured by Excelitas Technologies equipped with a single-photon avalanche photodiode for detecting single photons over the wavelength range of $400 - 1060\,\mathrm{nm}$ (SPCM-AQRH). (b) The custom-made coincidence logic comprised 12 input channels, which were fed by the detectors' TTL-signals, from which the data, logically sorted, was routed to a time-tag unit (TTU) via the 4 output channels.

Each of the two fibers was connected to single-photon avalanche photodiodes (APD) [Excelitas Technologies SPCM-AQRH, see Fig. 3.16 (a)] operated in Geiger-mode, where a transistor-transistor logic (TTL) pulse was triggered with the logic levels "0" and "1" corresponding to 0 V and 2.2 V, respectively. The generated pulses within the signal and idler modes were compared with the help of a custom-made coincidence logic with a coincident timing window of approximately $t_c = 1.5\,\mathrm{ns}$ [see Fig. 3.16 (b)] via Bayonet Neill-Concelman (BNC) connector cables. The logic consisted of 12 input channels, 4 output channels and was based on a field-programmable gate array (FPGA) [see Fig. 3.16 (b)]. By additionally choosing the respective delay time induced by the path length difference of the path to the two detectors, one can count coincidences, that identify simultaneously incoming photon pairs. This was done remotely via a USB link, where the observed photon count rates were transferred to a PC. A self-programmed *LabVIEW* program was used as an interface to monitor the count rates and setting parameters such as integration measurement time and time delay between signal and idler. Within the detection system, the difference in path lengths from PBS to the detector input was considered by defining a constant time delay of 1.56 ns within the measurement.

With m photons impinging threshold detectors, the photons can trigger the inner process of the device, where the response probability of getting a click per time unit can be modeled using [125]

$$P_m = 1 - (1 - p_{\mathrm{dc}})\,(1 - \eta_T \eta_{\mathrm{det}})^m\,, \tag{3.25}$$

where p_{dc} equals the dark count probability per time unit, η_{det} is the single-photon detector efficiency, and η_T is the link transmission efficiency including, e.g., absorption and scattering

effects experienced by the photons. The quantum efficiency of the detectors for the expected wavelength around 810 nm is indicated with $\eta \sim 40 - 55\%$, while the timing resolution is 350 ps. Where the quantum efficiency aids the estimation of the total loss in the setup, the timing resolution of the detectors dictates the minimal time frame, in which two simultaneous events from two detectors can be resolved, hence it defines a minimal coincident timing window t_c.

3.3.4 Influence of turbulences in air

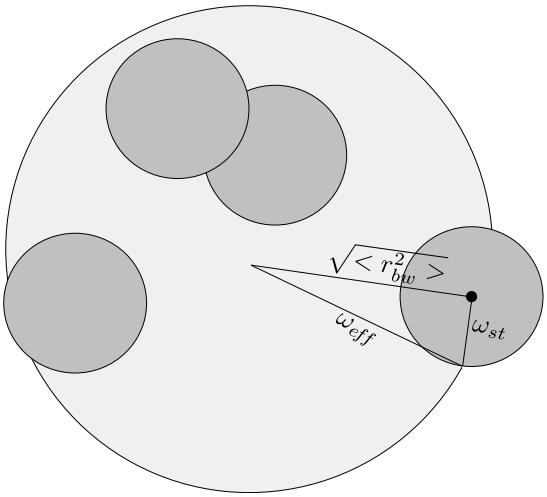

Figure 3.17: The influence of turbulent eddies in the air on the beam's propagation behavior is shown. Spatial beam wandering around the center of the time-averaged intensity is indicated by $\langle r_{bw}^2 \rangle^{\frac{1}{2}}$ and short term beam spreading by ω_{st}. Both quantities sum up to the effective beam radius ω_{eff}. Figure modified from Ref. [126].

All evaluations and considerations regarding the propagation of the photons made above omitted the turbulences in the air and their influence on the propagation behavior. As introduced in section 3.3.2, the SPDC and pump beam traveling in vacuum along the z direction can be described within the paraxial approximation as a Gaussian-beam wave, with the beam radius $\omega(z)$ behaving as shown in Eq. 3.24.

Turbulent eddies within the atmosphere cause temporal and spatial shiftings of the refractive index n, causing temporal intensity fluctuations and phase fluctuations of the electromagnetic field [127]. Moreover, the turbulences in the air lead to beam wandering, which causes spatial fluctuations with respect to the center of intensity, and beam spreading, which exceeds the effect from the beam's intrinsic Gaussian diffraction and can be summarized in the effective beam radius ω_{eff} [126, 128]:

$$\left\langle \omega_{eff}^2 \right\rangle = \left\langle \omega_{st}^2 \right\rangle + \left\langle r_{bw}^2 \right\rangle, \tag{3.26}$$

where $\left\langle r_{bw}^2 \right\rangle^{\frac{1}{2}}$ describes the radius of the beam which wanders in the plane perpendicular to the propagation direction and ω_{st} is the short-term radius caused by the beam spreading effect (see Fig. 3.17). The sum of those two quantities, the effective long-term beam radius, can be obtained by imaging the beam with an exposure time longer than the short-term beam wandering jumps

caused by the turbulences; usually within the time scales of 1 kHz. Within this time window, the beam "jitters" around the center of the beam, which can translate into the detection system in the form of intensity fluctuations. The magnitude of these beam wanderings, $\left\langle r_{bw}^2 \right\rangle^{\frac{1}{2}}$, can be written as [129]:

$$\left\langle r_{bw}^2 \right\rangle^{\frac{1}{2}} = \sqrt{2.87 \cdot C_n^2 \cdot L^3 \cdot \omega_0^{-\frac{1}{3}}}, \tag{3.27}$$

with C_n^2 being the refractive index structure parameter that characterizes the turbulence by giving a measure of the fluctuations of the refractive index n, and L being the propagation distance.

Chromatic effects in beam wandering solely due to the difference in wavelengths of the collinearly propagating photons have been studied in the UV to IR range, where the authors concluded that these effects are non-vanishing [130], but negligible for our purposes[15] [131]. This fact paves the way for adaptive optics systems [132], which rely on different wavelengths experiencing the same turbulence characteristics. However, the beam waists of the SPDC and pump beams are not equal (see section 3.3.2), hence differing fluctuation behavior can be expected. In fact, Eq. 3.27 predicts a greater radius of beam wandering with respect to the centroid of the beam for smaller beam waists.

Moreover, the (short-term) beam spreading effect scales as:

$$\omega_{\mathrm{st}} \propto \frac{\lambda L}{\pi \omega_0}. \tag{3.28}$$

Here, the ratio of wavelength to beam waist, λ/ω_0, as well as the propagation distance L dictate the short-term beam radius introduced by turbulences.

These fluctuations will translate to the detection system in the form of intensity oscillations and depending on their magnitude, this leads to an effective decrease in coupling efficiency into the single-mode fiber, which finally results in a decrease in visibility, which will be shown later on. Both the effects of beam wandering (Eq. 3.27) and the short-term beam spreading (Eq. 3.28) on the intensity oscillations depend on the receiving aperture and preceding optical lenses of the detection system. While, naturally, an increased beam wandering $\left\langle r_{bw}^2 \right\rangle^{\frac{1}{2}}$ leads to an increase in intensity oscillations, an increase in beam spreading ω_{st} decreases them.

Fig. 3.18 shows the intensity fluctuations for SPDC photons propagating through the experimental arrangement with a distance of 70 m between the nonlinear crystals. The difference in beam waists at the location of crystal I of the pump and SPDC photons (estimated via $\xi_{s/i} \approx \sqrt{2.84\xi_p}$ [113]) translates into a difference in the collimated beam radii $\omega_{s/i}^{coll}/\omega_p^{coll} = 9.48/2.58$. Accompanied by the beam spreading dependency of the wavelength-to-beam-waist-ratio ($\lambda_{s/i}/\omega_{s/i} < \lambda_p/\omega_p$), the pump beam experiences stronger fluctuations, which translates into detected intensity fluctuations of the SPDC photons in crystal II. The effect of more intense fluctuations at shorter wavelengths compared to longer wavelengths in the above-mentioned context is well-known and has been observed [130]. For longer distances ($> 10^3$ m free-space link) and stronger expected turbulences, fluctuations induced by small eddies within the atmosphere lead to observations of blurred beam images exhibiting a pronounced speckle pattern [133], that

[15] The latter statement holds true for photonic beams with different wavelengths but equal beam parameters (see also Ref. [131]).

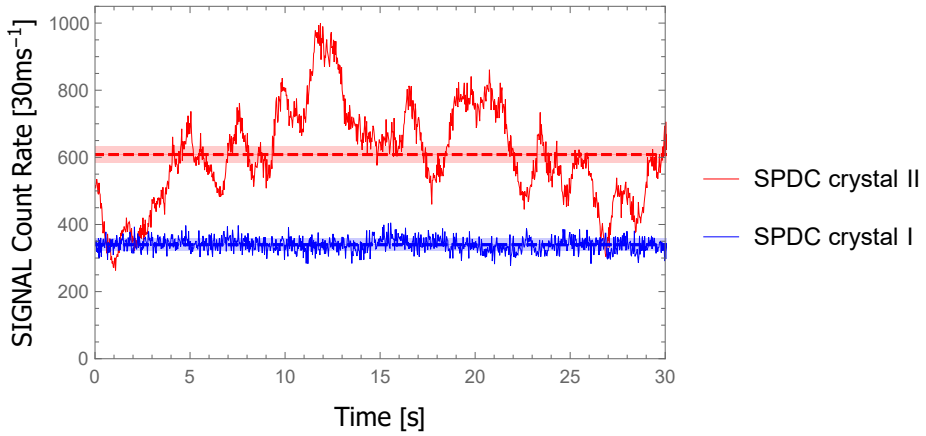

Figure 3.18: The fluctuations in single count rates of the different SPDC sources due to influences of turbulent air, showing the impact of a pointing error on fading at different wavelengths are depicted. The photons propagated through the experimental setup as depicted in Fig. 3.6 over 70 m between the nonlinear crystals. The intensity oscillations of SPDC photons created in crystal I after propagating for 70 m (blue) are shown. The dashed blue line indicates the mean value of the photon number $\bar{n}$ and the light blue area is equal to $\sqrt{\bar{n}}$, the standard deviation assuming Poissonian distribution. A clear increase in intensity fluctuations of the photons created in crystal II (red) compared to crystal I can be observed. Here, the pump photons propagated through turbulent air and experienced turbulences in higher magnitude due to the different beam waist and smaller beam spreading. Hence, the fluctuations shown in red can not be explained by Poissonian fluctuations alone.

can be described as self-interfering effects of the photons. Note, that the difference in average number of photons $\bar{n}$ of SPDC photons created in crystal II compared to crystal I is due to the differing transmission losses of pump and IR photons over the free-space propagation path (see section 3.3.2).

Experimentally, the mismatch in experienced scintillations for the different wavelengths over a turbulent link can be tackled by choosing the beam parameters of the pump beam on the sending site considering a trade-off between higher intensity fluctuations but a lower loss of the SPDC signal. On the one hand, one could change the beam parameters such that the intensity fluctuations of the pump beam is lowered at the cost of a higher loss of the SPDC photons due to beam spreading. The higher loss in SPDC signal can be tackled by choosing the respective aperture sizes of the optical elements on the receiving site (in addition, as in the presented case, during the propagation between the two sites). On the other hand, the mismatch in beam radii can be changed within one arm of an implemented interferometer on the sending site, also in a Mach-Zehnder configuration, with a respective magnification (two-lens) system.

A commonly used quantity to describe atmospheric links can be given through field of view (FoV), which gives a measure of the angle for which a detector is sensitive to an incoming signal. The detection system's FoV can be calculated with the help of the mode field area (MFA) of the SMFs and the focal length of the focusing lens $f_{10\times}$. The MFA is a measure of the light's beam width traveling through a SMF. More specifically, it is the diameter at which the optical power is reduced to $1/e^2$ with respect to its maximum level. In order to maximize the coupling efficiency due to AoA fluctuations caused by the wavefront distortions the beam experiences while propagating through turbulent air [134], the field of view of the detectors has

to be greater than the AoA fluctuations of the incoming beam. With the above-introduced parameters of the SMF's mode field diameter being MFD = 5 μm, a focal length of the focusing objective of $f_{10\times} = 15.5\,\text{mm}$ and the magnification of $M = 2.5$ induced by the concave mirror CM I ($f_{CMI} = 500\,\text{mm}$) and the collection lens ($f_{collect} = 200\,\text{mm}$), the field of view becomes FoV = MFA$/f_{10\times}/M$ = 130 μrad. The magnitude of this number can be put into context to an entangled photon-pair distribution over a 144 km turbulent air link with a mean AoA of 75 μrad [104], where naturally, much stronger wavefront distortions compared to the presented case in the lab are expected. It is important to mention, that higher intensity oscillations due to stronger turbulences require smaller FoV, however, especially in a real-life free-space experiment, smaller FoV is favored also with respect to background light. Hence, it has to be assured that although intensity fluctuations due to wavefront distortions can occur, the signal arriving at the receiving aperture (here the SMF's fiber tip) will not decrease to zero. The accompanying background light contribution to the signal in the lab can be held small relatively easily by darkening the lab room and using black cloth for covering photo-sensitive elements such as the APD's.

The above-mentioned turbulences in the atmosphere translate to a decrease in coupling efficiency regarding the SMF. Moreover, the use of concave mirrors prevents the introduction of a timing uncertainty due to the prevention of chromatic aberration (see Fig. 3.12). However, the propagation through the atmosphere induces a timing jitter of the absolute delay of photons which could lead to phase fluctuations between the pump and the SPDC photons, and hence undesired noise. Laser ranging measurements with pulsed laser beams were conducted in Ref. [135] over a large distance ($> 4\,\text{km}$) to measure the time of propagation, its absolute delay and jitter. The latter was in the order of several ps in the optical band. Comparing this to the pump photons coherence time $t^p_{coh} = 2\,\text{ns}$, it can be concluded that the effect of turbulences in the atmosphere, even for large distances, does not affect the phase relations of the pump and SPDC photons which propagate within the same temporal mode. Moreover, the insensitivity of the single photon's phase fluctuations enables successful transmission of highly phase-dependent OAM-modes over a turbulent free-space link [136]. Phase fluctuations occur within the Mach-Zehnder interferometer, which separates and combines again the SPDC and the pump photons. These fluctuations are induced by thermal and mechanical oscillations of the optical elements comprising the interferometer, where due to the interferometer arm lengths (in the order of $10^{-1}\,\text{m}$) even small deviations lead to an offset in phase between the pump and SPDC photons. The measured intensity oscillations due to phase fluctuations are in the order of several $10^{-1}\,\text{Hz}$. Continuous translatory movement of the stepper motor in the range of several Hz and long measurement times ($10^2\,\text{s}$) is necessary to neglect this effect.

Concluding, the propagation of pump and SPDC photons through turbulent air will result in random changes in coupling efficiencies and hence intensity oscillation in the detected photon counts. Adaptive optics systems with tip-tilt correction by means of a tiltable mirror aid to reduce wavefront distortions in order to greatly decrease the coupling loss into an SMF and hence to recover high visibility [137].

Influence of the intensity mismatch on the visibility

Assuming perfect indistinguishability of the photon pairs created in two nonlinear crystals, the measured intensities of the overlapping photons lead to oscillations described in Eq. 3.15 and Eq. 3.18. However, the derivation assumes equal transmission amplitudes of the respective photon pairs, which is not given in reality due to losses of either pump or signal or idler beam in the course of propagation through the system, as well as due to different focusing conditions at the crystals. Moreover, the above-discussed turbulences and their influences on the intensities

can lead to intensity mismatches, what effectively decreases the visibility. A derivation of the visibility influenced by different transmission losses for the photons shall be given. It follows the considerations made in [40].

The losses of the respective photons during propagation can be simulated by implementing beam splitters with transmission $T_s = \mathrm{t}_s^2$, $T_i = \mathrm{t}_i^2$ and $T_p = \mathrm{t}_p^2$ for the signal (s), idler (i) and pump (p) photons, with $t_j \in \mathbb{R}$. Hence, the two-photon SPDC state derived in Eq. 3.5 can be rewritten as:

$$\begin{aligned}|\psi\rangle = |vac\rangle|vac\rangle &+ A\left\{\mathrm{t}_s\mathrm{t}_i e^{i\phi_s}e^{i\phi_i} + \mathrm{t}_p e^{-i\phi_p}\right\}|1\rangle_s|1\rangle_i \\ &+ A\mathrm{t}_i\sqrt{1-\mathrm{t}_s^2}e^{i\phi_i}|0\rangle_s|1\rangle_i + A\mathrm{t}_s\sqrt{1-\mathrm{t}_i^2}e^{i\phi_s}|1\rangle_s|0\rangle_i \\ &+ A\sqrt{1-\mathrm{t}_s^2}\sqrt{1-\mathrm{t}_i^2}|0\rangle_s|0\rangle_i,\end{aligned} \tag{3.29}$$

where the terms in the second line account for the cases where either the signal or idler photon is lost and the last term considers that both photons are lost.

Now, the first-order correlation function can be calculated:

$$\begin{aligned}\mathcal{C}_{s/i} &= \left\langle \psi \left| a_{s/i}^\dagger a_{s/i} \psi \right| \right\rangle \\ &= |A|^2 \left\{ \left| \mathrm{t}_s\mathrm{t}_i e^{i(\phi_s+\phi_i)} + \mathrm{t}_p e^{-i\phi_p} \right|^2 + \left(1-\mathrm{t}_{i/s}^2\right)\mathrm{t}_{s/i}^2 \right\} \\ &= |A|^2 \left\{ \mathrm{t}_s\mathrm{t}_i^2 + \mathrm{t}_p^2 + \mathrm{t}_s\mathrm{t}_i\mathrm{t}_p(e^{i(\phi_s+\phi_i)}e^{-i\phi_p} + e^{-i(\phi_s+\phi_i)}e^{i\phi_p}) + \left(1-\mathrm{t}_{i/s}^2\right)\mathrm{t}_{s/i}^2 \right\} \\ &= |A|^2 \left\{ \mathrm{t}_s\mathrm{t}_i^2 + \mathrm{t}_p^2 + 2\mathrm{t}_s\mathrm{t}_i\mathrm{t}_p\cos\left(\phi_s+\phi_i-\phi_p\right) + \left(1-\mathrm{t}_{i/s}^2\right)\mathrm{t}_{s/i}^2 \right\} \\ &= |A|^2 \left\{ \mathrm{t}_{s/i}^2 + \mathrm{t}_p^2 + 2\mathrm{t}_s\mathrm{t}_i\mathrm{t}_p\cos\left(\phi_s+\phi_i-\phi_p\right) \right\},\end{aligned} \tag{3.30}$$

which leads to the following visibility (see definition 2.43) for signal and idler count rates:

$$\mathcal{V}_{s/i} = \frac{2\sqrt{T_s T_i T_p}}{T_{s/i} + T_p} \tag{3.31}$$

Similarly, the second-order function can be calculated:

$$\begin{aligned}\mathcal{C}_{\mathcal{C}} &= \left\langle \psi \left| a_i^\dagger a_s^\dagger a_s a_i \psi \right| \right\rangle \\ &= |A|^2 \left| \mathrm{t}_s\mathrm{t}_i e^{i(\phi_s+\phi_i)} + \mathrm{t}_p e^{i\phi_p} \right|^2 \\ &= |A|^2 \left\{ \mathrm{t}_s^2\mathrm{t}_i^2 + \mathrm{t}_p^2 + 2\mathrm{t}_s\mathrm{t}_i\mathrm{t}_p\cos\left(\phi_s+\phi_i-\phi_p\right) \right\},\end{aligned} \tag{3.32}$$

resulting in the following visibility for coincident count rates:

$$\mathcal{V}_{\mathcal{C}} = \frac{2\sqrt{T_s T_i T_p}}{T_s T_i + T_p}. \tag{3.33}$$

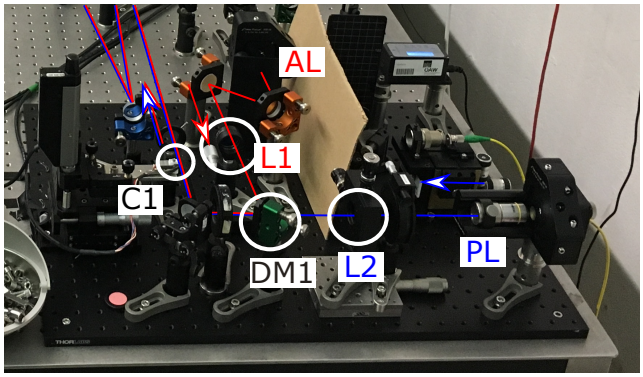

Figure 3.19: Overlapping a strong IR laser beam (Alignment laser - AL) with a CWL equal in wavelength to the SPDC emission (810 nm) with the pump laser beam (PL) mimicked the propagation behavior of the SPDC photons over the free-space link. The lenses L1 and L2 focused the beams into the nonlinear crystal (C1), which are overlapped by using a dichroic mirror (DM1). Following the dichroic mirror, both beams propagated collinearly through the experimental setup, where the detection system was aligned by measuring the intensity of the alignment laser AL.

Both Eq. 3.31 and Eq. 3.33 predict the interferometric visibilities to depend not on the absolute values but on the relative value of the transmission probabilities: for example, a transmission loss of 10 dB (0.1% transmission) for the pump beam and 20 dB (0.01% transmission) for both signal and idler beams leads to a visibility for coincident count rates $\mathcal{V}_C = 6.3\%$. High visibility $\mathcal{V}_C = 99.9\%$ can then be regained by introducing a loss solely on the pump beam of 39.6 dB (0.00011% transmission). Summarized, the matching of the respective intensities plays an essential role in the success of the experiment, as a high loss of one of the photon beams has to be compensated by intentionally introduced loss by the others. This can be done experimentally e.g. by misalignment of the system.

3.3.5 Experimental procedure

Before letting both the pump and the down-conversion beam propagate for longer distances, the feasibility of the experimental setup was tested by setting the two nonlinear crystals as close as possible to each other (limited by the geometrical arrangement of the setup on the optical table) and preparing the system to reach a high value of visibility $\mathcal{V}$.

The pump laser diode had to be mode filtered to ensure a high degree of spatial indistinguishability of the SPDC photons, which was done via coupling into a single-mode fiber (S405 HP) with the aid of two adjustable mirrors and an objective (Olympus RMS40× magnification plan achromat objective with $f_{40\times} = 4.5\,\text{mm}$) focusing into the core of the fiber. This coupling technique is called "beam walking" where the mirrors are rotated in both x and y direction such that the beam will be guided to a point of choice in space with a specific angle. Building an adjustable outcoupling stage for the pump laser (PL) exiting the SMF with an objective for collimation (Olympus RMS10× magnification, $f_{10\times} = 15\,\text{mm}$) ensured collimated propagation into the system as depicted in Fig. 3.19 and Fig. 3.20. Additionally, to mimic the SPDC propagation direction and behavior, an IR laser beam was coupled into the same spatial mode via a dichroic mirror (DM1 FF670, cut-on wavelength of 670 nm) at the sending station [see Fig. 3.19 and (1) in Fig. 3.20]. The N-BK7 plano-convex spherical lens L1 of the alignment laser (AL) was chosen to match the predicted SPDC beam waist at the crystal's central position ($\omega_{s/i} = 13.6\,\mu\text{m}$),

namely $f = 100\,\text{mm}$[16] [see (2) in Fig. 3.20]. Subsequently, a $4f$ optical system[17], hence lacking the multi-reflection mirror-system (3) introduced in section 3.3.2, was built, with f being the focal length of the focusing lenses between crystal I and crystal II. As introduced above, to avoid chromatic aberration, concave mirrors with $f = 500\,\text{mm}$ were implemented. Additionally, only ultra-broadband coated dielectric mirrors to guide the beams from the sending to the receiving station were used.

At the receiving station, a Mach-Zehnder interferometer (4) for phase difference introduction, which separated the pump from the SPDC photons, had to be implemented (see Fig. 3.20). Due to the rather long coherence length of the pump beam ($l^p_{coh} = 596\,\text{mm}$) and interferometer arm lengths (4a and 4b) of the same order of magnitude, a coarse estimation verified by a ruler sufficed for the build-up. A dichroic mirror (Semrock DM2 and DM3 FF705, cut-on wavelength of 705 nm) ensured high transmission for wavelengths in the IR range (above 705 nm) and high reflection probability for lower wavelengths including the pump beam's (405 nm). The trombone system TS consisting of two mirrors facing each other by 45° fixed on a translation stage, where two additional mirrors guide the signal into and from the translation stage, was implemented in the "SPDC path" (4b). Also here, several dielectric mirrors aided to guide both beams between the two dichroic mirrors. A strong laser [sent via SMF from the detection system (6)] with both a wavelength close to the cut-on wavelength of the DM and a coherence length longer than the interferometer arms was used to align the interferometer ensuring a high degree of interference. Following the pump laser being focused into the second nonlinear crystal (C2), the detection system (5 and 6) was implemented, where the pump beam was blocked by filtering elements, simultaneously ensuring high transmission for beams with wavelengths around 810 nm. The signal collected by the SMF (Thorlabs 780HP) within the detection system, where its intensity was monitored by a powermeter (Thorlabs PM100A), was used for further alignment steps. The fiber coupling systems for both fibers comprised an x-y-z stage (Elliot Gold MDE122 series XYZ flexure stage) with a high precision manual adjuster (Elliot Gold MDE216), where the coarse adjustment offered a 1 μm resolution and the fine adjustment a 20 nm resolution.

Alignment procedure

In the following, an alignment procedure is introduced for technically implementing two nonlinear sources and observing interference effects of photon pairs. Note that the temperature of both crystals for the degeneracy of signal and idler photons was assumed to be known via local measurements (see section 3.3.1).

1) Before ensuring that SPDC photons from either crystal were detected, the incoming pump laser [see (PL) in Fig. 3.20] intensity could be measured with the detection system (6). The assumption that both pump and SPDC beams created in the first crystal (C1) entered the detection system collinearly, was valid if and only if the Mach-Zehnder interferometer (4) was aligned properly. For now, the alignment of the interferometer was not of importance. Therefore, all filters that later ensured blocking the pump intensity had to be removed. With the "beam walking" technique, the pump laser's intensity at both detectors had to be maximized.

2) By setting the temperature of the crystals (C1 and C2) to 166.10° C, which ensured degen-

[16] The SMF's mode field diameter was $5.0 \pm 0.5\,\mu$m, which led to a collimated beam radius with an aspheric objective lens manufactured by Newport (5726-B-H) with a focal length of 15.3 mm. Ultimately, this resulted in a beam waist at the crystal (C1) of $16.3\,\mu$m with L1.

[17] A $4f$ optical system is a system architecture utilizing the Fourier transforming properties of 2 lenses. The structure is basically a telescope with one focal distance f to the left of the objective and one focal distance f to the right of the collector, respectively.

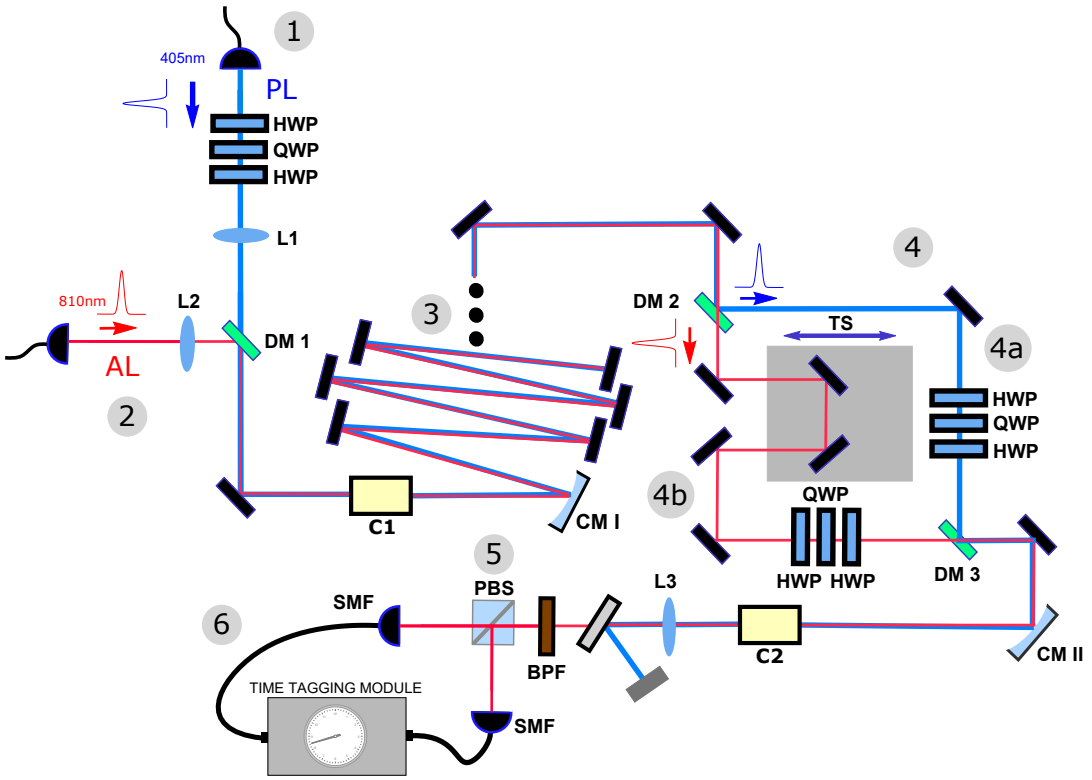

Figure 3.20: A sketch of the experimental and important points for the alignment is depicted. The pump beam is indicated by the blue straight line, the SPDC photons (and the alignment laser) are illustrated in red. The three black dots in the multi-reflection mirror system indicate that more mirrors than depicted were used in the final experiment over longer distances ($< 20\,\mathrm{m}$).

eracy and high conversion efficiency of the signal and idler photons, and implementing all filters to solely transmit wavelengths near 810 nm, an SPDC signal could be detected. This could be verified by a near-IR single photon spectrometer (Ocean Optics QE65000) while making sure that no other undesired light source entered the detection system. Now, with the implemented APD's and coincidence logic, via a *LabView* program, which could be used as an interface to monitor the count rates, the parameters such as coincident timing window ($t_c = 1.5$ ns) and the time delay introduced by the difference in path lengths from the PBS (5) to the detectors (1.56 ns) were set. Finally, the coincident count rates of the incoming SPDC signal had to be maximized by beam walking within the detection system. After maximizing the SPDC coincident count rates of the second nonlinear crystal (C2), the mirrors in the detection system remained untouched as the mirrors in the Mach-Zehnder interferometer (4a) were adjusted such that the coincident count rates were maximized, too.

3) Now, interference within the interferometer had to be ensured with help of e.g. an alignment laser close to the cut-on wavelength of the beam separating dichroic mirror DM (in the presented case, a wavelength-tunable laser diode with CWL around 700 nm, sent from an SMF in (6) was used). By prior ensuring that the interferometer arms were equal roughly within the coherence length of the pump laser (~ 600 cm) with help of a mechanical ruler, the mirrors in the "SPDC path" (4b) were rotated, such that interference fringes were visible at the output of the interferometer (4). By moving the TS and prior beam walking, the interference was maximized. Then, a strong IR laser beam (AL, ~ 10 mW) overlapping spatially with the pump beam (PL) at the sending module (via DM1) and ultimately maximizing the intensity in the detection system (via 4b) ensured high coupling efficiency of the SPDC signal from the first crystal (C1). That the incoming SPDC signal arose from the first nonlinear source (C1) could be ensured by removing the second crystal (C2) from the path of the pump laser[18] or blocking the pump beam within the interferometer (4a).

4) An iterative approach to maximize both SPDC intensities by performing steps 2) and 3) had to be done. Changing the linear polarization of the pump beam by implementing a system of half-, quarter-, half-wave (HQH) plates in the interferometer (4a) ensured the matching of the intensities. An optional, but sub-optimal, approach would be the misalignment of one of the photon pair beams (e.g., via 4b). The SMF in the detection system (6) ensured the spatial overlap of the photon pairs.

5) Unblocking both arms of the interferometer (4a and 4b) and turning on the stepper motor for phase difference introduction led to periodic oscillations within intensity as predicted in Eq. 3.15 and Eq. 3.18. The visibility now had to be maximized, by slight changes in the temperature of the crystals, matching the intensities of the SPDC signal arising from either one of the nonlinear crystals (via 4a and 4b) and changing the polarization accordingly. Both beams experienced unintentional unitary transformations in polarization while propagating through the experimental setup (e.g. reflections on mirrors). The photon pairs had to be indistinguishable in all their degrees of freedom. Here, the polarization modes for the pump and SPDC beam were made identical individually by the HQH-systems (4a and 4b), which made it possible to reach any point on the Poincaré sphere (see section 2.1.1). Moreover, the bandpass filters in the detection system ensured spectral indistinguishability of the photon pairs. In this experiment, two bandpass filters for CWL

[18] Note that this alignment technique was solely possible due to the small length (1 mm) of the nonlinear crystal, as ppKTP is a highly refractive material. For longer crystal lengths, the coupling efficiency at the SMF could be distorted.

of 810 nm with FWHM 3 &6 nm were used.

6) With maximum achieved visibility, the propagation distance between the sending and receiving station could be increased (see section 3.3.2), and steps 1)-5) were repeated.

Dark counts

The contribution of undesired photons to the signal effectively lowered the maximum achievable visibility below 1. Firstly, using bandpass filters and dichroic mirrors ensured that solely photons with their central wavelength (810 nm) and a small bandwidth arrived at the detectors. To investigate the absence of pump photons at 405 nm within the count rates, the intensity dropped significantly by removing the nonlinear crystals from the setup, as no down-conversion photons were produced any longer. Additionally, rotating the polarization of the pump photon the intensity of down-conversion changed respectively, which was realized technically by rotating an HWP through which the pump beam propagated before being focused into a nonlinear crystal. However, not only undesired pump photons contributed to the background of the signal: APD dark counts created within the detectors and photons arising from other sources such as fluorescence effects on optical elements in the setup or from ambient light in the lab also had to be taken into account. Filters and covering the APD's as well as the coupling stages with black cloth or other highly absorptive, flexible material proved to be very efficient in that sense and ensured a reasonable signal-to-noise ratio throughout the measurements.

3.4 Measurement Results

In the following section, the measurement results of the single and coincident count rates for interfering SPDC photon pairs created in the down-conversion crystals I & II, with three different distances in between, namely 2 , 20 and 70 m, are shown. The measurements were conducted with the experimental setup as introduced in section 3.3.

Eq. 3.15 and Eq. 3.18 predict an oscillating behavior of the count rates while scanning the phase difference between the SPDC photons created in the first crystal and the pump photons. However, the most crucial limitation was distinguishability between the interfering particles, which leads to the fact that the expected visibility was lower than 1. Any information that led to the exclusive knowledge about one of the interfering particle's state resulted in a decrease in visibility. Limitations regarding the uncertainty of the visibility were of technical and systematic nature such as shot noise[19] and turbulences in the air which introduced fluctuations to the signal.

3.4.1 Data analysis for propagation distance of 2m

Fig. 3.21 and Fig. 3.22 depict the coincident and single count rates of the down-conversion photon pairs while scanning $\Delta\mathcal{L}$ with the help of a trombone system comprising a stepper motor with velocity v_m, with 2 m distance between crystal I and crystal II. The trombone system was installed within a Mach-Zehnder interferometer separating the SPDC from the pump photons. The arm of the interferometer in which the down-converted photons traveled, is called the "SPDC arm". While moving the trombone system, $\Delta\mathcal{L}$ changed, and therefore the phase difference $\phi_p = \mathrm{k}_p\Delta\mathcal{L}$ between the pump and down-conversion photons was scanned. According to Eq. 3.15 and Eq. 3.18, this led to the observed oscillating behavior, while the oscillation period of both coincident and the singles counts were, as predicted, equal to half of the wavelength of the

[19] Shot noise can be equated to quantum noise and was caused by the intrinsic discreteness and randomness of the SPDC process.

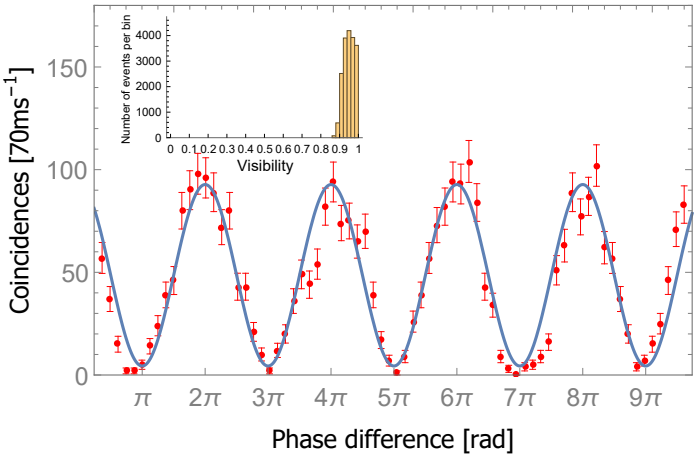

Figure 3.21: The coincident count rates of SPDC photon pairs created in two coherent nonlinear crystals while moving the trombone system and hence changing $\Delta\mathcal{L}$ after a propagation distance of 2 m are shown. The red dots represent the experimental results. The error bars assume Poissonian distribution. The inset shows the visibility distribution calculated by a Monte-Carlo simulation.

pump beam λ_p. The phase difference was introduced onto the SPDC photon pairs, where due to the correlated nature of the SPDC two-photon state any phase difference introduction applied on one of the photons acted in fact on the whole product state. Note that neither signal nor idler photons were equipped with a well-defined phase as neither of them were in a pure state. After propagation through the system, the idler (cf. Fig. 3.22 (a)) and signal (cf. Fig. 3.22 (b)) photons with perpendicular polarization were separated with a PBS and then focused onto a single-mode fiber which was coupled to a APD.

As expected, the absolute count rates of coincidences were lower than the ones from the single count rates, which was due to experimental imperfections such as misalignment and the fact, that the APD's used in this experiment had efficiencies $< 100\%$, which represented a probabilistic upper bound for simultaneous timing events. The discrepancy in amplitudes of the count rates can be explained by the fact that fluctuations due to Poissonian photon number statistics are the minimum oscillations expected in a count rate for photon experiments involving random parametric processes such as SPDC. Air fluctuations during the propagation of the photons could have led to unstable oscillations in the SPDC photon's intensities, which were higher than fluctuations one would expect arising from statistical nature. However, over the relatively small distance of 2 m, these effects were expected to be negligible.

The error bars in the plots of the count rates correspond to counting statistics assuming Poissonian distribution given by $\Delta n = \pm\sqrt{n}$ where n is the number of photons being used in the process of measurement. Note that the typical dark count rates for the APDs used in this experiment were not exceeding 2×10^2 counts per second (cps), which, compared to the single count rates yielded here, were negligible ($\mathcal{C}_{A,B} \sim 10^4$ cps). Moreover, accidental coincident counts $\mathcal{C}_{acc}$, which contributed to the coincidence signal in the form of uncorrelated photon pairs and therefore a non-zero background, could have ultimately led to a decrease in visibility in the coincident count rates. The accidental coincident count rates $\mathcal{C}_{acc} = \mathcal{C}_A\mathcal{C}_B t_c$ were around 0.5 cps and 0.036 counts per integration time $t_{int} = 70$ ms, which, compared to the measurement counts in the order of 50 counts per 70 ms, had negligible impact on the visibility (see discussion in section

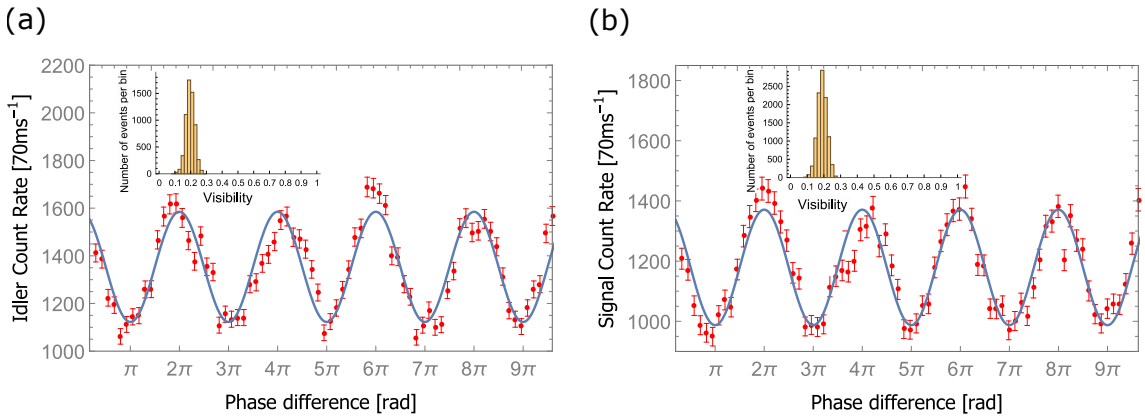

Figure 3.22: (a) The Idler and (b) signal count rates of SPDC photons while changing $\Delta\mathcal{L}$ after a propagation distance of 2 m are depicted. Equal to the results shown in Fig. 3.21, the red dots represent the experimental results.

2.2.4).

It is important to mention that during the alignment process the visibilities were optimized for the coincident count rates only. Hence, the single count rates suffered in terms of visibility. It is worth mentioning, that loss effects of any kind of one partner of the photon pair would lead to, even with 100% detection efficiency, a certain decrease in indistinguishability and hence in visibility. This is due to the fact, that the transmission loss could leak which-crystal information in principle about the photon's origin and hence the origin of its partner photon. Therefore, the visibility in the coincident count rates was higher, since detecting simultaneous events acted as a filter of the which-crystal information via post-selection.

Throughout the measurements with a propagation distance of 2 m, the velocity of the stepper motor had been chosen to be 180nm/s and the measurements were taken over a time window of 70 s. The measured visibilities for the single and coincident count rates are

$$\mathcal{V}^{2\mathrm{m}}_{idler} = 19.90\% \pm 2.61\%, \tag{3.34}$$

$$\mathcal{V}^{2\mathrm{m}}_{signal} = 18.79\% \pm 2.70\%, \tag{3.35}$$

$$\mathcal{V}^{2\mathrm{m}}_{coincidences} = 96.15\% \pm 2.86\%. \tag{3.36}$$

The distributions of visibilities (see insets in Fig. 3.21 and Fig. 3.22) and hence the mean values of $\mathcal{V}^{2m}$ with respective errors were evaluated by considering only the extrema of the coincident and single count rates. Then, a high number sampling ($\sim 10^5$) with their respective statistical distributions was performed, which were expected to follow a Poissonian distribution. This list of data points comprised a high number of maxima and minima, which were attributed to the harmonic oscillations of the signal. Hence, the mean values of the extrema gave the mean value of the visibility $\mathcal{V}$ by simply calculating $(Max\text{-}Min)/(Max{+}Min)$, where Max (Min) denotes the mean value of the maxima (minima) of the oscillating SPDC signal. The extrema for each data set were evaluated by the $FindPeaks$-function of the mathematical processing software *Wolfram Mathematica*[20], which returned a list of values of local extrema. As single-photon counts are

[20] *Wolfram Mathematica* Version 11.0.1.0

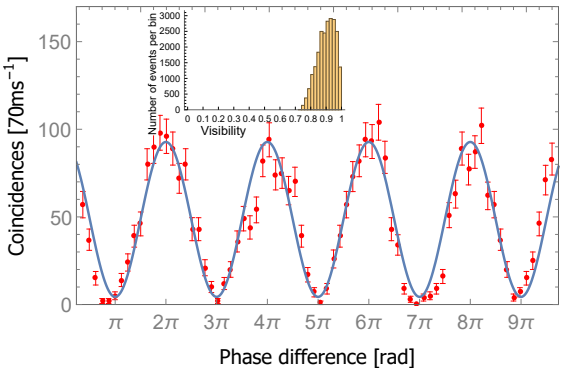

Figure 3.23: The coincident count rates of down-conversion photons while moving the trombone system and hence changing $\Delta\mathcal{L}$ after a propagation distance of 20 m are depicted.

discrete events, a typical count rate measurement comprises multiple local extrema within a single oscillation fringe. The expected oscillation period of the interference fringes within the count rates could easily be estimated from Eq. 3.15 and Eq. 3.18 and the motor velocity v_m of the trombone system, which helped to filter out the "physically correct" extrema. By performing a Monte Carlo simulation via combining the sampled distributions of the extrema of one data set, a high number of visibilities was calculated as displayed in Fig. 3.21 and Fig. 3.22. The standard deviations of the resulting distributions led to the errors for the $\mathcal{V}^{2m}$. As can be seen in the inset of Fig. 3.21, the visibility distribution of the coincident count rates is equipped with an asymmetric error bar, as the value 1 represents the maximum bound by definition (see Eq. 2.43). The distributions of the minimum, maximum count rates, and the visibilities are summarized in appendix A2.

The visibilities of the single count rates, however, as displayed in Fig. 3.22, did not show asymmetrical behavior within their statistical distribution due to the fact that the minimum count rates were substantially above zero. The errors in the visibilities for the single count rates are given within one standard deviation σ assuming Poissonian statistics. Note that due to the high number of evaluated statistics during measuring (70 s total measurement time per measurement session) and the accumulated high sampling number, the error of the mean value was negligibly small. The effects from systematic influences such as phase fluctuations and wavefront distortions due to propagation in free space could be neglected over the distance of 2 m. This could be extracted from the comparison of the measured and the ideally expected error bars of the visibilities. Assuming solely deviations arising from Poissonian distributed shot noise effects (standard deviation equal to $\Delta n = \pm\sqrt{\bar{n}}$, with $\bar{n}$ being the average number of photons) within the count rates would result in following visibility errors by performing Gaussian Error Propagation: $\Delta_{sn}\mathcal{V}^{2\mathrm{m}}_{idler} = \pm 1.88\%$, $\Delta_{sn}\mathcal{V}^{2\mathrm{m}}_{signal} = \pm 2.03\%$ and $\Delta_{sn}\mathcal{V}^{2\mathrm{m}}_{coincidences} = \pm 2.70\%$. As can be seen, these deviations in visibility compared to the measured values (Eq. 3.34-3.36) differed only slightly (by the factors 1.39, 1.33, and 1.06) and were expectedly smaller due to imperfections of the laser source and phase fluctuations introduced by the Mach-Zehnder interferometer, hence representing a lower bound of noise also for larger propagation distances, where turbulences in the air will have a significant impact. The phase fluctuations arose through mechanical oscillations within the optical elements comprising the interferometer. Note that due to the lower absolute count rates of the coincidences with respect to the single count rates, the relative error differed, as a low photon number n increased the relative error according to

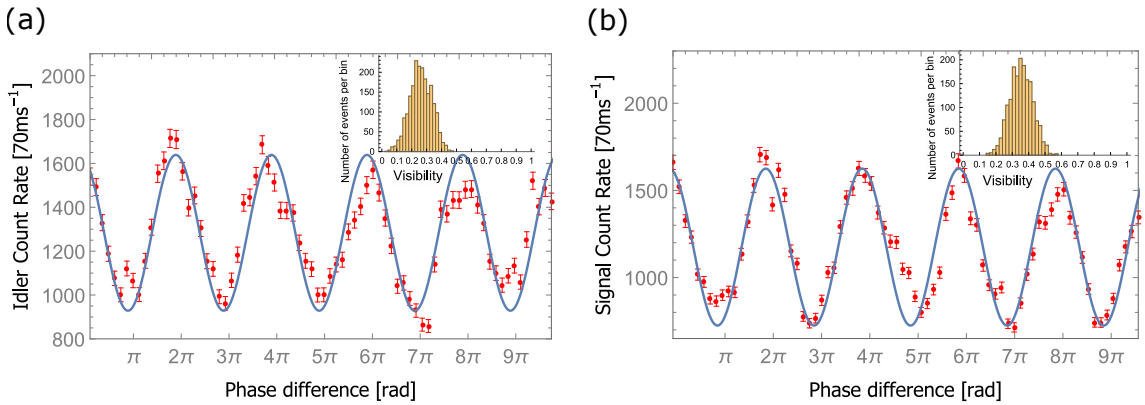

Figure 3.24: (a) The idler and (b) signal count rates of down-conversion photons while moving the trombone system and hence changing $\Delta\mathcal{L}$ after a propagation distance of 20 m are depicted.

$1/\sqrt{n}$. This translated also to the lower factor while comparing the induced "shot noise" with the measured error.

3.4.2 Data analysis for propagation distance of 20m

Fig. 3.23 and 3.24 depict the single and coincident count rates of the down-conversion photons pairs while scanning the phase difference by changing $\Delta\mathcal{L}$ between the pump and down-conversion photons, with 20m distance between crystal I and crystal II.

By further increasing the propagation distance of the beams between the two nonlinear crystals, additional challenges arose. As discussed in section 3.3.2, multiple 1" ultra-broadband BK7 mirrors were placed at both ends of the optical table to let the beams travel from the sending station to the receiving station.

For the measurements the velocity of the stepper motor v_m had been chosen to be, again, 180 nm/s and the integration time t_{int} of the detection system 70 ms. The measured visibilities for the single and coincident count rates were

$$\mathcal{V}^{20\mathrm{m}}_{idler} = 26.16\% \pm 7.32\%, \tag{3.37}$$

$$\mathcal{V}^{20\mathrm{m}}_{signal} = 35.62\% \pm 7.08\%, \tag{3.38}$$

$$\mathcal{V}^{20\mathrm{m}}_{coincidences} = 92.05\% \pm 5.65\%. \tag{3.39}$$

The post-processing approach for the shown results (also for 70 m) was equal to the approach presented for the measurements over 2 m. By comparing these results of $\mathcal{V}^{20\mathrm{m}}$ with the ones over 2 m ($\mathcal{V}^{2\mathrm{m}}$) one notices only a slight decrease in visibility regarding the coincident count rates, in combination with an increase in error bars in the single and coincident count rates. The single count rate visibilities, however, experienced an increase in magnitude, which was solely an unintentional byproduct, as the focus was laid on maximizing the visibilities in the coincident count rates. The absolute count rates were nearly equal, which came from the fact that over the distance of 20 m, the beams were reflected solely once per mirror, while the mirrors were implemented for propagation between sending and receiving station (see Fig. 3.13). Also here, the parameters and the statistical distributions are displayed in A2.

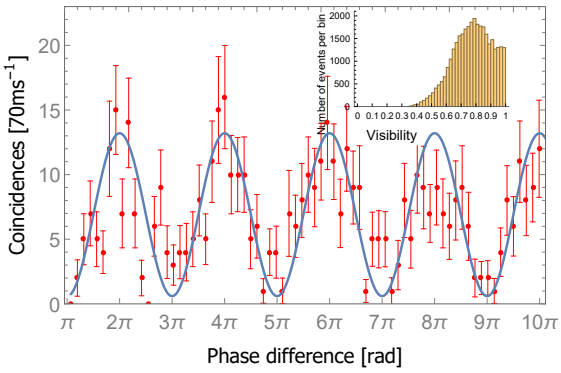

Figure 3.25: The coincident count rates of down-conversion photons while moving the trombone system and hence changing $\Delta\mathcal{L}$ after a propagation distance of 70 m are depicted.

The decrease in visibility, however, was attributed to the effects of beam wandering through the longer free-space propagation in turbulent air, and hence intensity matching (see Eq. 3.33) turned out to be experimentally more challenging. The visibility therefore would be expected to decrease as the signal detectors "see" more non-interfering background [98]. Apparently, this effects also explained the deviations from the mean value of the visibility distribution, which was emphasized by comparing them to the "shot-noise" induced deviations: $\Delta_{sn}\mathcal{V}^{20\mathrm{m}}_{idler} = \pm 1.97\%$, $\Delta_{sn}\mathcal{V}^{20\mathrm{m}}_{signal} = \pm 1.99\%$ and $\Delta_{sn}\mathcal{V}^{20\mathrm{m}}_{coincidences} = \pm 4.97\%$. Within the single count rates (Eq. 3.37 and Eq. 3.38), a significant increase of the visibility error (by factors of 3.72 and 3.56) could be observed, as expected for the large propagation distance in air. Due to the equal intensities of the single count rates for 2 and 20 m, the "shot-noise" errors were roughly the same. However, a significant increase of the deviation in visibility could not be observed within the coincident count rates (factor 1.17). Moreover, in contrast to the 2 m measurements, the errors within the coincident count rates were smaller than the ones for single count rates. This fact came from the intrinsic property of discrete event counting statistics such as photons created in an intrinsically random SPDC process. In quantum optics, counting photons enables detecting and identifying quantum states. As observed over 2 m, the low photon number of the coincident count rates ($\sim 10^2$ per integration time t_{int}) broadens the error bar significantly. Further quantitative statements regarding the impact of additional noise such as induced by turbulences in the atmosphere can solely be done by the number of photons n while comparing different measurements (such as 2 with 20 m) with detecting equal intensities.

3.4.3 Data analysis for propagation distance of 70m

Figures 3.25 and 3.26 show the results of the count rate measurements over a traveling distance of 70 m between the two down-conversion sources. The integration time t_{int} and the stepper motor velocity v_m were chosen to be the same as for the measurements for 2 m and 20 m. The results reflect, that the visibilities decreased and reached the following values for coincident and for single count rates:

$$\mathcal{V}^{70m}_{idler} = 8.42\% \pm 5.20\%, \tag{3.40}$$

$$\mathcal{V}^{70m}_{signal} = 10.86\% \pm 3.44\%, \tag{3.41}$$

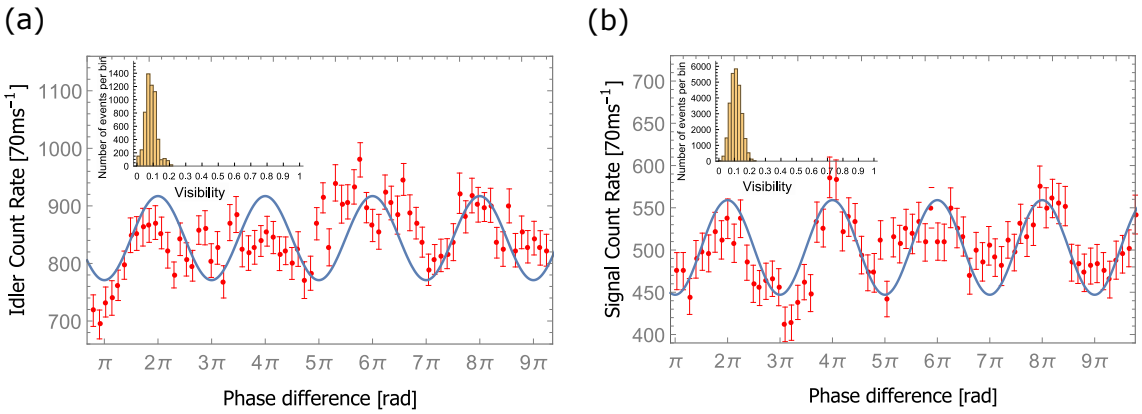

Figure 3.26: (a) The idler and (b) signal count rates of down-conversion photons while moving the trombone system and hence changing $\Delta\mathcal{L}$ after a propagation distance of 70 m are depicted.

$$\mathcal{V}^{70m}_{coincidences} = 83.90\% \pm 12.98\%. \tag{3.42}$$

The mean values of the visibilities $\mathcal{V}^{70\mathrm{m}}$ compared to 20 m further decreased but accompanied by decreasing errors for the signal and idler count rates. For the single count rates, the low visibility could be attributed to being close to an incoherent mixture of the nonlinear signal beams. The visibility distribution within the coincident count rates showed a distribution around the mean value of 83.9%, as during the alignment process the visibilities were optimized for the coincidences only. Apparently, in contrast to the single count rates, the errors of the visibility for the coincident count rates increased, significantly.

The expected errors arising solely from shot noise were once more estimated via Gaussian error propagation: $\Delta_{sn}\mathcal{V}^{70\mathrm{m}}_{idler} = \pm 2.41\%$, $\Delta_{sn}\mathcal{V}^{70\mathrm{m}}_{signal} = \pm 3.17\%$ and $\Delta_{sn}\mathcal{V}^{70\mathrm{m}}_{coincidences} = \pm 14.20\%$. Unexpectedly, with respect to the measured errors and comparing them to the results over 20 m, no further increase of the errors could be observed (factors for singles: 2.16 and 1.09, coincidences: 0.91)[21], as one would have expected due to the larger propagation distance. The reason could be found in the photon count rates n, as within discrete events following Poissonian distribution, the relative error decreased for high n. The mean photon number over the 70 m measurements for the coincident count rates (few counts per integration time t_{int}) as well as the single count rates ($< 10^3$ counts per t_{int}) were significantly lower than compared to 2 and 20 m (coincidences: $\sim 10^2$ counts per t_{int}, singles $\sim 1.5 \times 10^3$ counts per t_{int}). With decreasing n, the relative error can become dominant over sources of noise such as turbulences in the air. This is the case when the calculated errors arising from shot noise are close to equal to the measured error, where in general, no quantitative statements regarding the influence of systematic noise on the intensity fluctuations can be done. To do so, one could either increase the intensity of the incoming signal or increase the turbulences to a magnitude, where the ratio of the systematic noise greatly exceeds the "shot noise" error.

The observation of the error of shot noise dominating the observed error was apparent within both the single and the coincident count rates, as the photon number in the latter was close to zero. Due to the higher photon number in the single count rates, the error in their visibility was

[21] A value smaller than 1 signifies that the measured standard deviation is smaller than the expected standard deviation arising from the shot noise. This artificial fact could solely be attributed to the imperfect post-processing method and could be neglected as long the value differs only slightly from 1.

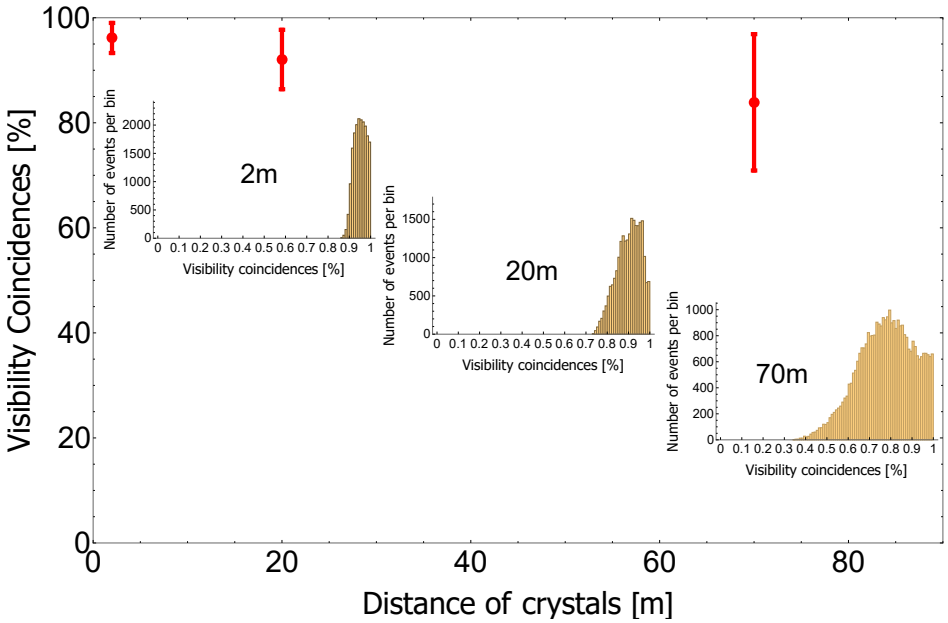

Figure 3.27: A summary of all coincident count rates over the distance between the two nonlinear crystals and a distribution of visibilities (see histograms) over the respective propagation distances is shown. The red dots correspond to the peak value of the respective distribution and the red error bars equal the standard deviation of the estimated distributions. Note that the error of the measured distances between the crystals is not included, which did not exceed ± 1 m for 20 and 70 m.

smaller than the visibility for coincident count rates. Compared to the errors in the measured visibility distributions over 20 m, the decrease in error could be explained by the dominant shot noise error due to the low photon number. Finally, these significant fluctuations in intensity due to the small photon number n resulted in an experimentally challenging matching of the SPDC intensities, which in the end represented the main cause for the low visibilities.

Summary

A summary of the visibilities of the coincident count rates in dependency of the distance between the crystals is displayed in 3.27. While the width of distribution for coincident counts was relatively narrow for 2m, for longer distances the error bars increased, and the position of the peak went to lower visibilities. Note that due to the high number of evaluated statistics, i.e. high number of photons n, during measuring (70 s total measurement time per measurement session) and the accumulated high sampling number in post-processing, the error of the mean value was negligibly small. The broadening of the error of the visibility distributions could be explained with the fact that, as for the three measurements the measurement times were equal, the count rates over 70 m were lower in magnitude (few counts per integration time $t_{int} = 70$ ms, see 3.25) compared to the ones for the other distances ($\sim 10^2$ counts per t_{int}, see 3.21 and 3.23). Obviously, higher statistical significance could have been achieved by focusing on the single count rates, which, however, proved to be more experimentally challenging, as the visibility of single count rates was highly dependent on the information about the partner photon. By definition, within the coincident count rates, no information was leaked to the environment and coherence was conserved.

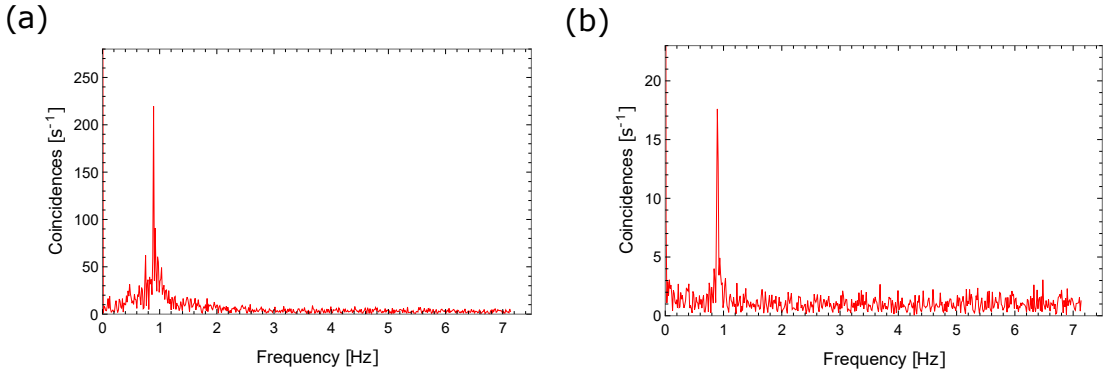

Figure 3.28: The Fourier transform performed on coincident count rate with a propagation distance of 2 m (a) and 70 m (b) shown in Fig. 3.21 and Fig. 3.25 are depicted, respectively. The characteristic peaks are at position ∼0.91 Hz (a) and ∼0.89 Hz (b), respectively.

As mentioned before, the error bars broadened due to low photon numbers accompanied by intensity fluctuations above shot noise. These were attributed to turbulences in the air, while the latter could have affected the visibility in either the spatial or temporal regime of the involved photon beams as the photons experienced more deviations over larger distances. Hence, to achieve proper statistical significance within the same experimental setup, higher count rates (and therefore low loss) and e.g. adaptive optics [132], are needed to lower intensity fluctuations further on. Moreover, mechanical oscillations of the optical elements in the Mach-Zehnder interferometer led to noise in the phase. Choosing the stepper motor velocity and the integration time of the measurement devices and finally locking the interferometer with the help of a closed-loop control of a reference mirror [124] could tackle these issues. Longer measurement times than performed in the shown experiment would not yield smaller errors with respect to the Poissonian distribution, since its the standard deviation is directly proportional to the photon number, namely via $\sqrt{n}$.

As the width of the (asymmetrical) distribution of the coincidence visibilities for 70m broadened significantly it can be summarized, that with the presented experimental setup no significant statement for the systematic behavior of the count rates over larger distances could be made. The results show that the mean value of the visibility would decrease, but solely due to the experimentally challenging alignment technique for matching the intensities of the nonlinear signals over time. Due to the above-mentioned techniques to prevent these intensity fluctuations, we see no reason to believe that there exists no reason whatsoever to claim that the interference effects are physically impossible over larger distances.

3.4.4 Fourier analysis for interference verification

Intensity fluctuations introduced by turbulent air exacerbate the alignment process in terms of intensity matching of the interfering nonlinear signals. The results presented above introduced an effective method to quantify interferometric visibilities. With increasing fluctuations over time, this technique loses its effectiveness (see Fig. 3.26).

The Fourier transform, as a simple tool often used in signal processing, shall remedy the above-mentioned problems to a certain limit. It is important to mention, that this method should serve only for interference verification, but not for a qualitative measure of the magnitude of visibility. Performing a Fourier transform on electronic signals decomposes them into harmonic functions

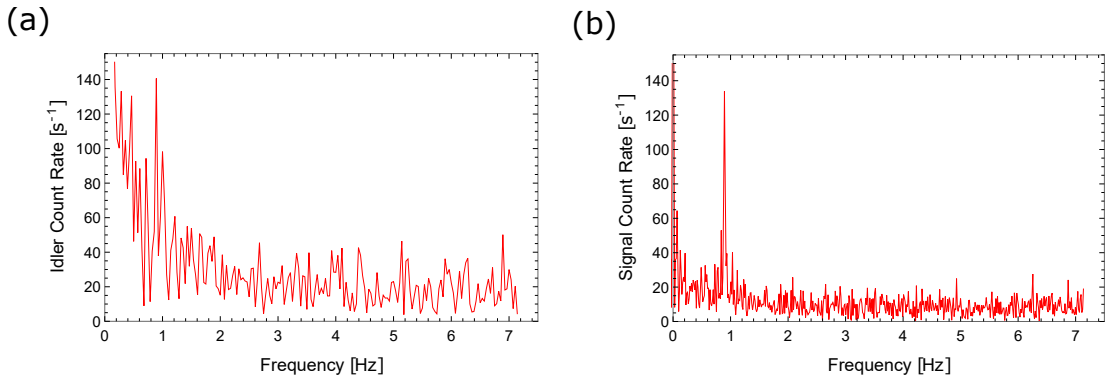

Figure 3.29: The Fourier transform performed on idler (a) and signal (b) count rates with a propagation distance of 70m shown in Fig. 3.26 is depicted. The characteristic peaks are in both spectra at position ∼0.88 Hz. The difference in the signal-to-noise ratio arises from the fact that the visibility from the idler single count rates is lower compared to the signal count rates.

with certain frequencies. In the presented case, the Fourier transform converts the photon count rate, which is given in counts per time increment, into a data set in the inverse space regime, namely the frequency regime, by the fact that the Fourier transform breaks the signal up into complex exponentials. Therefore, the Fourier space of a signal shows contributions of frequencies within the signal, which can be found at characteristic positions.

With the help of the Fourier transform on count rates involving the mixing of down-converted beams from different sources, one can definitely prove that interference occurred, as no other effect can be responsible for the respective peaks. Their position in the Fourier spectrum can be exactly derived by theory, as can be seen in Fig. 3.28 for the coincident count rates after a propagation distance of 2m and 70m, respectively. Even single-photon count rates which do not clearly follow the harmonic behavior on bare sight, such as in Fig. 3.26 over 70m, will reveal a characteristic peak by taking an insight in the Fourier spectrum, as shown in 3.29. The position of the characteristic peak and hence the expected frequency of the intensity oscillations can be calculated with the help of the motor velocity v_m and the wavelength of the pump photon λ_p: $v_m/(\lambda_p/2)$, which has the dimension of frequency $[\mathrm{s}^{-1}] = [\mathrm{Hz}]$. As the integration time t_{int} during the measurements was chosen to be 70 ms and the stepper motor velocity v_m was 180 nm/s, the oscillation frequency is 0.89 Hz. Furthermore, the high values at the origin of the coordinate system arise from the non-vanishing offset from the origin within the count rates.

By comparison of the Fourier spectra of both the coincident count rates after traveling 2 m and 70 m respectively, one can see a vast difference in signal-to-noise ratio, as expected because of the intensity fluctuations. Also, the magnitude of the amplitudes in the Fourier spectrum differs as the intensities in the count rates are not equal. Finally, higher visibilities will lead to a higher magnitude of the characteristic peak in the Fourier spectrum as well.

The maximum value of frequencies that can be properly sampled, as shown on the right end of the abscissa, is set by the sample rate $\tau_s = 1/t_{int} = 14.3\,\mathrm{Hz}$, which was already discussed above. The maximum frequency, that can be successfully sampled, can be given by the Nyquist-limit [123], which is equal to $\tau_s/2 = 7.15\,\mathrm{Hz}$, as the Fourier transform results show (Fig. 3.28). The positions of the characteristic peaks also do not match, although the same velocities of the same trombone system were chosen. The occurrence of the disagreement can be explained due to the fact that the integration time, which is vital for the qualitative statement of the Fourier

spectrum used for the measurements, does not coincide with the "actual" integration time. This fact finally results in a systematic error in the form of a shift within the absolute value of the integration time. The results shown with Fig. 3.28 do not replace standard techniques in order to prove interference effects on photon experiments such as finding a fit function for the count rate measurements as shown in Fig. 3.21-3.25, as the oscillation fringes can even be seen with the bare eye. However, the Fourier transform comes in strikingly handy when the visibilities are expected not to be high and show behavior close to an incoherent mixture, as the interference fringes cannot be easily decomposed from noise such as turbulences with the mentioned techniques. A clear distinction can hence be made by estimating the observed frequencies arising from turbulences or random phase fluctuations from the ones expected from the trombone system (or other techniques intentionally introducing a periodic phase difference between photons), to finally prove that interference effects occurred.

3.4.5 Classical interpretation of the interference effect

Nonlinear interference effects demand certain constraints in the measured visibilities to prove that no classical explanation for the results can be given. Within the framework of quantum mechanics, an explanation of the nonlinear effect is that two possible ways of creating the photon pairs interfere with each other, hence showing nonclassicality.

One classical explanation of the effect can be given by considering that the pump beam propagating between the nonlinear crystals acts as a parametric amplifier for the two inputs, namely the photon pair created in the first crystal [100]. Here, a prediction of the photon count rates also follows a harmonic behavior equipped with a certain value in visibility, depending on the pump power intensity. Following calculations already performed by Herzog and Yariv [40, 96], which involve integrating the coupled wave equations in the undepleted pump approximation with the assumption of perfect phase-matching [138] in the limit of small coupling ($|\kappa E_p L| \ll 1$), lead to the following estimation of the visibility:

$$\mathcal{V} \approx 2\kappa \left|E_p\right| L \tag{3.43}$$

with the coupling constant

$$\kappa = \frac{8\pi\omega_i\omega_s d_{eff}}{\sqrt{\mathrm{k}_i \mathrm{k}_s c^2}} \tag{3.44}$$

where ω_i, s and k_i, s denote the angular frequency and the wave vectors of the signal and idler fields, respectively, d_{eff} is the effective nonlinear coefficient, E_p denotes the pump field amplitude and L is the length of the crystal. Now, an estimation for the expected visibility within a parametric amplification process for the present case can be given. With an intensity of 7740.88 $\mathrm{W/cm^2}$, a crystal length $L = 0.1\,\mathrm{cm}$, an effective nonlinear coefficient for type-II $d_{eff} = d_{yyz}2/\pi = 3.6\,\mathrm{pm/V}$[22] and assuming degeneracy of the SPDC wavelengths $\lambda_s = \lambda_i = 810\,\mathrm{nm}$, one arrives at the following estimated visibility:

$$\mathcal{V} \approx 8\%, \tag{3.45}$$

[22]The additional factor $2/\pi$ for quasi-phase-matching arises from the periodical inversion of the material's nonlinear coefficient, see [41, 139] for a more detailed treatment.

which is much smaller than all visibilities observed in the presented experiment (above 79% for the coincident count rates). In fact, explaining the shown results classically, a 2 orders of magnitude higher pump intensity would be necessary. Additionally, the visibility is provably independent of the pump power and the crystal length with respect to the single count rates, In coincidence count rates, due to the finite timing resolution of the detectors, there is a nonlinear dependency of the visibility on the mean photon pair number μ (see discussion in section 2.2.4). Therefore, one is not able to admit a parametric amplifying description in that sense, that the results cannot be described with the classical theory.

Additionally, classical amplification of the down-converted fields can be ruled out by considering the coherence time of the signal and idler photons, which is in the range of $t_{coh}^{DC} = 100\,\text{fs}$. Thus, only within this period of time, an amplification process can occur, while the APD's used in this experiment are not able to distinguish between photons in this time range, as the timing resolution (or jitter) in the presented experiment is $\tau_{jitt} \approx 350\,\text{ps}$. If constructive interference arose from the classical amplification process, it should therefore not be possible to be observed [40].

3.5 Conclusion and outlook

The presented results show for the first time the suppression and enhancement of down-conversion photons over a large distance in free space between two nonlinear sources, while the pump photons travel collinearly with the signal and idler photons.

The results of this experiment shall aid the expansion of our knowledge for the scope of application of quantum physics, as quantum theory predicts a vast area of validity. As long as no empirical tests are performed, these areas of validity are solely hypothetical. Hence, the expertise gained from experiments involving superposition states of photons (such as long-distance coherent photon pair creation) can lead to highly sensitive measurement techniques, e.g. lowering the standard quantum limit in terms of phase measurements.

The distance between the two crystals was increased to a magnitude where effects related to long-distance free-space experiments such as distorting the photon's wavefront through turbulences in air occured. These distortions effected the pump and SPDC photon differently, ultimately introducing *which-crystal* information which resulted in a lower visibility. These turbulences translated into beam wandering, AoA fluctuations and phase fluctuations experienced during the photon's propagation through air. Most importantly, due to the high loss of photons, statistical significance in coincidence measurements decreased with larger distances between the two down-conversion sources (see Fig. 3.27).

Therefore, in order to lower the uncertainty for increasing distances, higher photon counts and/or longer measurement times are crucial, as shown by the results given in this thesis. This could be tackled by choosing the aperture size of the optical elements accordingly or by concentrating on the single count rates rather than on coincident count rates. Given the fact that the turbulences affecting the beams after traveling a long distance via atmosphere will be significantly higher than in the lab, those fluctuations have to be actively compensated, to ensure feasibility. This can be done, e.g., by implementing an adaptive optics system involving fast steering mirror (FSM), a position-sensing detector (PSD) and a feedback-loop control system, which has to operate in the order of kHz, as the expected turbulences are supposed to be in the range of 10^2Hz to finally ensure a high coupling efficiency into the single-mode fiber even under strong turbulence conditions. Additionally, a locking system with a closed-loop control of a reference mirror leads to phase stability arising from fluctuations of the optical elements within the interferometer.

These techniques could aid in ensuring the essential criterion for high visibility, namely the matching of intensities of the photon pairs arising from the two nonlinear sources, as this was the main challenge in this thesis. In accordance to the arguments given in this thesis, no evidence points to a fundamental reason that would prohibit expanding this scheme to even longer distances in open air.

Chapter 4

Wavelength-multiplexed entanglement-based quantum cryptography

The exchange of pure quantum states can be exploited for the transfer of information, being ultimately secure due to intrinsic laws of quantum mechanics. When transferred between two distant parties with, say, Alice preparing the state, and Bob performing local measurements on it, a third party, Eve, interacting on the quantum state would induce a perturbation of the wave function describing the quantum state. The no-cloning theorem [9] prevents Eve from extracting any information unrecognizable by the two information exchanging parties, Alice and Bob. Ultimately, the lack of possibility of cloning random quantum states also prevents faster-than-light communication. Due to quantum mechanic's counter intuitive and non-classical nature, protocols involving quantum systems can provide information-theoretic security for establishing a secret quantum key between at least two parties [140]. In general, a cryptographic key is a binary string, which enables a specific transformation of encrypted information. Shor's algorithm [141] endangers the security of widely-used classical encryption techniques, as solving factorization and discrete logarithm problems by quantum protocols are being developed, such as the development of using variational quantum algorithms [142].

Quantum key distribution (QKD) enjoys great popularity as protocols based on classical encryption are vulnerable to attacks by the advancing success of quantum computing technology [143]. Groundbreaking steps of quantum cryptography were developed by Bennett and Brassard in the form of the BB84 protocol [144, 145], where non-orthogonal states are used for encoding a random key distributed between two users. Any attempts initiated from an unauthorized party with the goal to gain information about the key perturbs the system, inevitably introducing a bit error according to the non-cloning theorem. This bit error is traceable in post-processing of the users and hence promises information-theoretical security [146].

For discrete variables QKD (DV-QKD) protocols, which rely on the distribution of entangled quantum states, the work of Ekert paved the way with the BB91 protocol [147]. Entangled photon pairs are an essential resource in the research field of quantum information. This is because they proved to be a powerful candidate for secure communication due to their intrinsic property of sharing a bipartite entangled quantum state leading to non-local correlations as well as their high-

brightness character in sources. Entanglement-based QKD allows for high bit rates, facilitates networks without trusted nodes [148, 149], and features multi-user network implementations [31, 150–152]. Furthermore, entanglement-based QKD forms the basis of measurement device-independent QKD [153, 154] and is directly linked to fundamental tests of physical reality [155, 156].

The main goal of modern QKD research lies in increasing the key rates and developing loss-resistant strategies for long-distant QKD while simultaneously minimizing the resource costs, thus enabling viable and scalable long-distant QKD. An essential limiting factor in the quantum key generation rate appears to be the timing resolution in detecting the information carriers, in the presented case, photons. Increasing the pair generation rate eventually and unavoidably leads to uncorrelated photon pair rates, which decreases the key rate, ultimately resulting in the detector's saturation in time. Moreover, this leads to a significant decrease in the visibility of the polarization correlation [56, 59], which in turn results in a reduced key rate. This obstacle cannot be overcome by merely distributing the signal onto different detectors, as this probabilistic separation of photons prevents assigning only correlated detection events accurately to each other.

A possible way to circumvent this problem is to exploit the intrinsic properties of the entangled photon pairs created in an SPDC process. Due to energy conservation in the SPDC process, the created photon pairs are perfectly correlated in their spectral properties. These correlations can be harnessed if it is possible to separate the wavelength at both communication sides, Alice and Bob. In this way, the signal and idler beams are deterministically separated in their wavelength components, which preserves the quantum correlations and allows for reaching higher key rates without saturating the detectors using the same source in time.

In this thesis, a scheme to overcome this fundamental limitation is presented and experimentally demonstrated. The intrinsic quantum correlations of entangled photons employing wavelength multiplexing to generate a quantum secure key are harnessed. The findings pave the way also for a high-loss, long-distance quantum communication, as the shown technique can be applied to both fiber-optic and free-space systems. Additionally, the scalability of this method is shown, which can be extended to the full photon-pair spectrum and bears the potential of increasing the attainable secret key rate by several orders of magnitude.

4.1 Preamble

The primary goal of cutting-edge QKD research is to achieve higher secure key rates allowing for long-distance quantum communication. QKD based on photons show scalable behavior in terms of the key rate when exploiting additional degrees of freedom for encoding information. Hence, one possibility of achieving the goal of higher key rates lies in exploiting higher-dimensional degrees of freedom of the entangled photon pairs, which include, but are not limited to, the orbital angular momentum [157], time-domain [158], and in frequency [159]. Moreover, for a given QKD link, the arguably easiest way of achieving higher key rates is to untwine the photon-pair production rate in the SPDC source by increasing the pump power or the overall heralding efficiency $h = \mathcal{C}_c/(\sqrt{\mathcal{C}_A\mathcal{C}_B})$ [59, 114] with $\mathcal{C}_i$ being count rates for coincidences (c) and singles (Alice A and Bob B), respectively.

The finite timing resolution in the detection system constitutes a fundamental limit for an increased SPDC photon-pair production with respect to the recorded count rate. Namely, due to the random nature of the SPDC process, in which the photon pairs are created within a nonlinear interaction of a pump laser with a nonlinear crystal, photon pairs are created with a specific rate

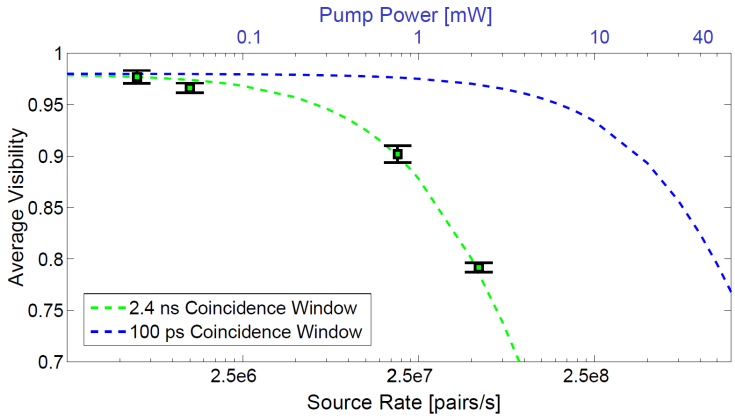

Figure 4.1: Polarization analysis results are shown for different pump intensities. Increasing the number of photon pairs created in a nonlinear photon source and detecting pairs in a certain coincident timing window t_c results in the creation of a background floor in the recorded coincident count rate and hence in a decrease of the polarization visibility $\mathcal{V}$. Decreasing t_c can restore the polarization visibility, due to the decrease in probability of falsely identifying uncorrelated photon pairs. Adapted from [59].

depending on the intensity of the pump field. For reasons of comprehension, a more detailed view of the timing resolution's contribution on the distributed secure key rate is given.

QKD protocols which rely on the encoding of information in entangled photons comprise timing measurements of incoming photons from the communicating partners Alice and Bob. Depending on the photon pair's degree of freedom, upon which the information is encoded, local measurements have to be performed to finally form a secret bit string. In section 4.4 such a QKD protocol is introduced in more detail, which concludes that the measured key rate R can be calculated via

$$R \geqslant q \left\{ \mathcal{P}_c \left[1 - f H_2 \left(Q \right) - H_2 \left(Q \right) \right] \right\} . \tag{4.1}$$

Here, $\mathcal{P}_c$ is the coincidence detection probability between Alice and Bob within a certain time window t_c, $H_2(x)$ being the binary Shannon entropy and Q being the quantum bit error rate (QBER). The parameters q and f are chosen to be constants. In order to extract a key from the recorded timing data, it is crucial to correctly identify corresponding measurement outcomes at both communication partners by associating each detection event with a local clock at both ends. However, such an association is only possible up to a specific time interval, usually called the coincident timing window t_c. The coincident timing window accounts for the uncertainty in the timing precision, which stems from technical limitations, such as the detector's timing resolution and its dead time or chromatic dispersion effects, as well as ultimately fundamental restrictions, such as the photon's coherence time. These local measurements can be, e.g., polarization analysis measurements, where the measured parameter, the interferometric polarization visibility $\mathcal{V}$, dictates the secret key rate, due to its relation to the QBER via $\mathcal{V} = 1 - 2Q$ (see Eq. 4.11 in Section 4.4). With increasing pump power (which translates into a higher flux of photon pairs, see Section 2.2.1) and since the coincident timing window (around 1 ns) exceeds the coherence time of SPDC photon pairs (around 10^2 fs) by far, the contribution of uncorrelated photon pairs leads to a background floor in the recorded count rate (see Section 2.2.4). This, in turn, lowers the visibility $\mathcal{V}$ in polarization analysis measurements (see Fig. 4.1), simultaneously increas-

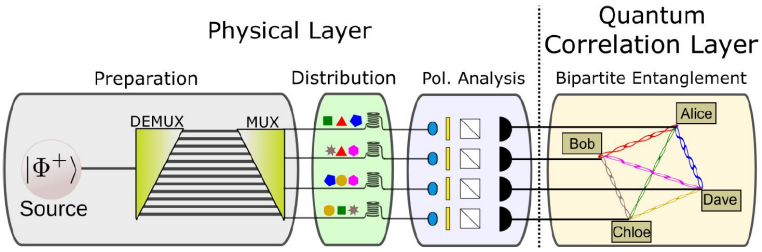

Figure 4.2: A fully connected quantum network of 4 users is depicted. A single polarization-entangled photon-pair source is distributed via multiplexing to 4 users ("Preparation" and "Distribution"), where each user shares a bipartite quantum state with one other user. Via polarization measurements ("Pol. Analysis") the entanglement can be verified and QKD protocols can be used to generate a secure key between the user pairs ("Quantum Correlation Layer"). Adapted from [151].

ing the QBER. The limits mentioned above in the photon-pair detection of a typical DV-QKD system require solutions by either further technological advancements in detector research and timing electronics or by exploiting intrinsic properties of a given system, e.g., the photon-pair state created in the process.

Spectral multiplexing or so-called Wavelength Division Multiplexing (WDM) has revolutionized classical optical communication [160] resulting in a leap in the classical communication capacity building the basis of modern telecommunication networks. Dense WDM represents the most powerful optical communication technology in terms of signal density with a mode spacing of around 25 up to 100GHz in the short-wavelength-infrared frequency band [161, 162]. Therefore, this technology can be exploited to achieve a similar advancement in QKD.

First advancements in integrating the WDM technology into QKD were made in the late 1990s, as simultaneous transmission of a quantum cryptographic key distribution and conventional data over an existing installed fiber using wavelength-division multiplexing was carried out [163]. The primary motivation at that time was to transmit secure quantum information as part of the classical data channel traffic. The design of the quantum channel "coexisting" with a classical channel has been described in detail in the mid-1990s [164, 165]. The co-propagation of classical and quantum information in existing fiber links has undergone a mature process in the last years [166–172], as the co-propagation with Tbit/s classical data-carrying channel with 100 WDM channels was recently demonstrated [173].

Recent findings in WDM-based quantum networks have paved the way for two-party QKD protocols to connect multiple users [151, 174–177]. These implementations efficiently distribute entangled photons between network end users, even only using a single photon-pair source. Moreover, security in entanglement-based networks is given through the fact that no trusted nodes are required. The experimental scheme of an entanglement-based quantum network using WDM to effectively distribute entangled photon pairs between 4 users is depicted in Fig. 4.2. Here, the polarization-entangled photon pairs created in a single SPDC source were separated by wavelength with a demultiplexing (DEMUX) and multiplexing (MUX) implementation, where shared entanglement between 4 end-users was verified by polarization measurements on the photons. Each user shared a bi-photon state with one other user, respectively. To deterministically distribute the photon pairs to the users, the photon pairs were separated by wavelength via multiplexing, where wavelength-correlated pairs (signal and idler) were identified according to the SPDC energy conservation ($\frac{1}{\lambda_p} = \frac{1}{\lambda_s} + \frac{1}{\lambda_i}$). Due to the intrinsic wavelength correlations

of the SPDC photon pairs, a high degree of polarization entanglement can be provided in all channels, simultaneously. In that way, the users are part of a fully connected quantum network where entanglement-based bipartite QKD protocols can be used for the generation of secure keys exchangeable between all user pairs. The intrinsic SPDC correlations can be exploited whenever it is possible to separate the wavelengths at both end-user locations (Alice and Bob), in a correlated manner. In this way, the signal and idler beams are deterministically separated in their wavelength components, which preserves the quantum correlations in other degrees of freedom, e.g., polarization or time. These intrinsic correlations of the photon pairs can be used to detect the two photons pairwise in correlated wavelength channels.

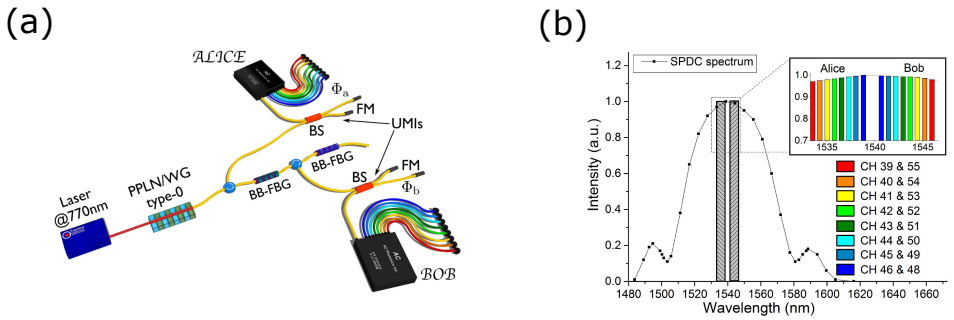

Figure 4.3: An experimental setup conducted by Aktas [178] of a multiplexed time-bin entangled photon-pair source and the wavelength selection via WDM is depicted. (a) A cw-laser produces energy-time entangled photon pairs which are separated into 2×8 DWDM channels simultaneously. (b) The DWDM systems on both Alice and Bobs modules pairwise selected wavelength fractions of the spectral distribution of the SPDC photon pairs, which were identified as wavelength correlated pairs in the detection system. Figure modified from Ref. [178].

As mentioned above, numerous fiber-based quantum communication implementations have been conducted in the past, mainly due to the deployment of classical fiber architecture. To tackle the optical birefringence effects inevitably occurring in fiber, technical compensation is required. In order to avoid the effortful implementation of this technical compensation, the information encoding has been done via time-bin entanglement [178, 179]. Specifically, an experiment has been conducted exploiting the wavelength correlations of time-bin entangled photon pairs, enabling two parties to share a quantum secure random bit sequence by multiplexing the signal into multiple WDM channels (see Fig. 4.3) [178]. A continuous-wave pump laser produced SPDC photon pairs in a periodically poled lithium niobate waveguide, where the time-energy entangled photon pairs were distributed via two broadband fiber Bragg grating filters (BB-FBG) between two users, Alice and Bob. The analysis modules on the receiving sites comprised an unbalanced Michelson interferometer (UMI) (consisting of a beam-splitter (BS) and two Faraday mirrors (FM)) to reveal the energy-time entanglement, and the WDM detection system [see Fig. 4.3 (a)]. The latter included a commercially available 8-channel DWDM (dense wavelength division multiplexing) system, which separates the incoming overall SPDC signal into 2×8 complementary channels, at the same time [see Fig. 4.3 (b)]. Standard DWDM bases on optical filtering by thin-film-coated optical glass, which forms stable solid-state single-frequency Fabry–Pérot interferometers [180]. By deterministically separating wavelength-correlated photon pairs and detect them in multiple channels simultaneously, the coincident count rate can be effectively increased by a factor n equal to the number of channels. The authors found that the SPDC photons' higher-order contributions can be mitigated by multiplexing, hence decreasing the number of

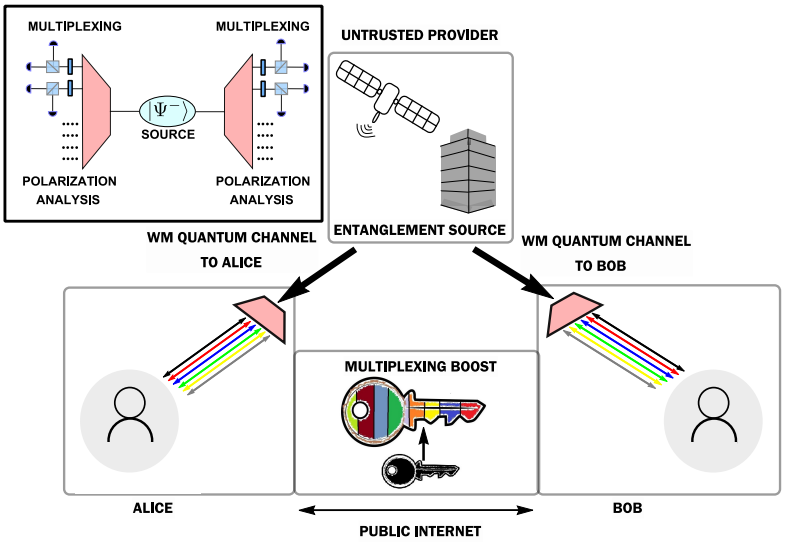

Figure 4.4: The proposed multiplexed communication scheme is illustrated. An entangled photon-pair source provided by an untrusted provider such as a satellite or ground station distributes photons to the parties generating a quantum key by measuring the polarization correlations of the multiplexed quantum signal. The number of channels can be increased depending on the wavelength selection bandwidth as well as the bandwidth of the SPDC source leading to a significant boost in secure key rate. The inset depicts a more technical scheme, including the polarization-analysis stages located at each user site.

uncorrelated photons in the analysis system. Merely increasing the number of photon pairs produced in the SPDC source would ultimately cause single-photon detector's saturation in time, effectively decreasing the signal-to-noise ratio while increasing the visibility $\mathcal{V}$.

Verifying time-bin entanglement requires users to implement stabilized matching interferometers, where the stabilization is realized by utilizing an additional stable laser, increasing the technical complexity compared to polarization-entangled states. Moreover, the exponential attenuation of the single photon's intensity with increasing transmission distance proves to be a significant drawback in fiber-based communication, requiring the implementation of quantum repeaters. These devices promise to amplify noiselessly any unknown quantum state; however, the induced errors on the quantum state lead to the fact that these technologies are not yet suitable for long-distance quantum communication [181–183]. Furthermore, it has been shown that both repeater-less in-fiber QKD and (classical) optical fiber communication are fundamentally upper-bounded regarding the transmission of information [184].

Satellite-based QKD is a promising alternative on a global scale, mainly due to the significantly reduced losses compared to terrestrial links [185]. The launch of the first quantum-based communication satellite in 2016 [186] enabled the distribution of a secret key over a range of $7,600\,\mathrm{km}$ [187]; as a comparison, the highest successful transmission in fiber was performed over $500\,\mathrm{km}$ [188]. As numerous satellite missions are currently under development [189], solutions to increase the efficiency of free-space QKD ideas and implementations are of high scientific value.

As observed by Aktas, any deterministic separation of the SPDC signals led to an increase in visibility $\mathcal{V}$ and therefore to a decrease in QBER. This finding lays the foundation for the experiment and scientific exploration shown in this thesis: the presented experiment aims at

increasing the secret key rate of QKD protocols for free-space implementations by utilizing an intrinsic property of two photons sharing a polarization-entangled state, namely the wavelength. To illustrate the general idea of this approach (see Fig. 4.4), a high-bandwidth photon source with bipartite polarization entanglement was used, which is multiplexed into multiple wavelength channels. Finally, a quantum state tomography confirming a high degree of entanglement was performed. Hence, an approach to overcome the timing limit in the photon-pair detection by exploiting their intrinsic wavelength correlations is shown. Apart from that, a scalable generation of high secure key rates encoded within polarization-entangled photon pairs is achieved. With this approach, the detector's saturation in time is overcome, which results in an effective decrease of the QBER. Two end-users, Alice and Bob, then analyze and detect the photon pairs in each correlated wavelength channel separately and generate a secure key from the measurement outcomes. In this way, the limitations imposed by conventional single-channel photon detection in QKD systems can be overcome beyond their saturation in time.

Subsequently, each wavelength fraction is analyzed in its polarization degree of freedom (see inset of Fig. 4.4). Hence, detector's saturation in time is avoided, and the system shows a significant improvement for extracting a secure key rate. The observed behavior clearly illustrates the advantage and potential of the proposed QKD scheme, which increases the secure key rate by almost two orders of magnitude using state-of-the-art WM bulk systems.

It is worth mentioning that wavelength-multiplexing techniques have been reported in the context of continuous variable QKD; see, e.g., [166, 169, 173]. However, these approaches involving weak coherent pulses are not able to exploit correlations, e.g., in frequency, as no bipartite correlated quantum states are used. Furthermore, each wavelength channel needs, in principle, a separate manipulation and encoding stage. Hence, these continuous variable schemes cannot exploit the scaling potential of entanglement-based QKD schemes where one single entanglement source provides the correlations and encoding intrinsically.

The experiment specifically features a novel architecture designed for free-space-based QKD systems, including optical bulk materials as well as space-suitable APD. The setup's heart consists of a WM system implemented at both receivers using Volume Holographic Gratings (VHG), which allows for sharp wavelength separation and subsequent individual polarization measurement of each wavelength component. In this case, the analyzed number of wavelength components was 4, hence implementing in total 2 WM channels as a proof-of-principle experiment. Based on the results found in the 2-channel system, the scalability of the secure key rate for a potentially high number of wavelength channels was studied. With this configuration, a higher secure key rate without perturbing existing photon sources but only introducing a novel concept at the receiver was achieved. In this sense, the presented approach can fully harness bright SPDC sources' potential without the problem of saturating the detection modules in time. Importantly, the VHG's acceptance angle of incidence is larger than the angle-of-arrival fluctuations in long-distance experiments due to atmospheric turbulence, expanding the shown techniques application area even to satellite-based implementations.

In summary, a technique to circumvent the timing resolution in order to decrease the QBER effectively was found. Hence, even if detectors technologies continue to decrease the timing resolution so that unprecedented high key rates are possible in a conventional way, the presented technique shows an improvement on top of that. The timing resolution of the detectors defines a lower limit of the coincident timing window t_c for identifying photon pairs. As stated above, increasing the photon pair rate of the source in the same order of magnitude of t_c leads to an increase of QBER. Hence, decreasing t_c could prevent uncorrelated photon pairs from identifying as correctly correlated pairs. However, the detector's timing resolution poses a technical limit of

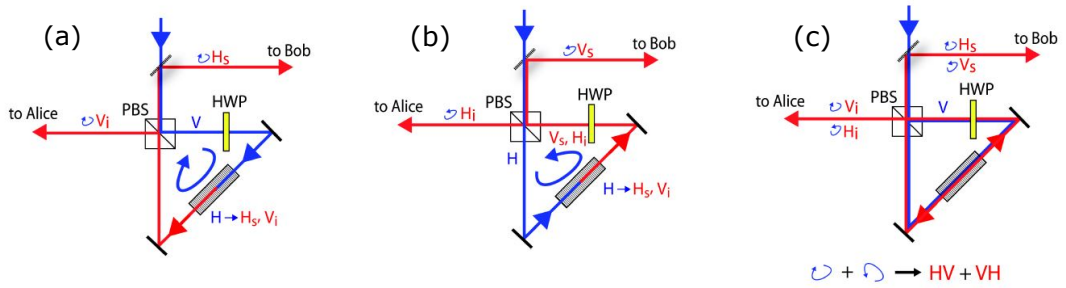

Figure 4.5: A step-wise graphical explanation of how an entangled type-II SPDC photon-pair state is created in a Sagnac interferometer is given. Adapted from [57]. (a) The V-polarized fraction of the pump beam gets reflected by a dPBS, is rotated to H-polarization, and creates via SPDC a H_s- and V_i-polarized photon pair, with s, i indicating the signal and idler, respectively. In this clockwise run-through (↻), the dPBS separates the signal from the idler beam into the modes ↻$\mathrm{H_s}$ and ↻$\mathrm{V_i}$. (b) In the counter-clockwise run-through (↺), the H-polarized fraction of the pump beam (transmitted by the dPBS) creates H_s- and V_i-polarized photon pairs, which are then rotated in polarization to H_i and V_s. Again, the SPDC photon pairs are separated into the modes ↺$\mathrm{V_s}$ and ↺$\mathrm{H_i}$. (c) If the crystal is pumped coherently from both directions (↻ + ↺), the final SPDC state is in the form of $HV + VH$.

decreasing t_c. Finally, an increase of higher key rates compared to conventional QKD systems is shown, even if the timing resolution becomes smaller through technological breakthroughs.

4.2 Sagnac-interferometric source of entangled photon pairs

The generation of entangled photon pairs with a high number of pairs per time increment enables novel quantum optical experiments. Moreover, desired properties on the quantum state for generation of high-quality entanglement are a high state fidelity F with respect to a maximally entangled state, high spectral purity, and high heralding efficiency h. It is crucial to mention, that in sources using bulk nonlinear crystals, one drawback is the intrinsic trade-off between brightness B, coupling efficiency, and spectral purity [113, 190].

In the following section, a specific class of entangled photon sources shall be introduced, which will provide photon pairs with desired characteristics for these purposes. As introduced prior in section 3.1, interferometers provide coherent output states enabling specific unitary transformations in the interferometer arms, also in the single-photon regime. In particular, nonlinear interferometers (see a list of interferometers in Fig. 3.1) exploit nonlinear interaction of the photons within a nonlinear medium to create, e.g., multiple photons in a specific superposition state.

The Sagnac interferometer [see Fig. 3.1 (d)] contains a beam separation element (e.g., 50:50 beam splitter or polarizing beam splitter) and two mirrors, where the incoming beam is guided following two different directions within the same interfering path, hence being intrinsically stable concerning phase, as perturbations experienced in the path affects both directions of the beam equally. Implementations creating polarization-entangled photon pairs which were created within the Sagnac configuration have been realized, e.g., with type-II [191] and type-0 [59] down-conversion. For a detailed description of the implementation and a profound understanding of a polarization Sagnac interferometer, the reader is referred to [41, 191]. Here, only a brief introduction of the working principle shall be given.

A graphical overview of a type-II down-conversion polarization Sagnac interferometer is given in Fig. 4.5. For reasons of comprehension, the working principle is subdivided in 3 steps, captured in Fig. 4.5 (a-c). A polarizing dual-beam splitter (dPBS, hence effective for pump and SPDC wavelengths) reflects the V-polarized fraction of the pump beam, which experiences a rotation of 90° in polarization by a dual-wavelength half-wave plate (dHWP) rotated by 45°. The H-polarized pump photons create via type-II SPDC (see a detailed introduction into SPDC in section 2.2) photon pairs being H- and V-polarized, pairwise. The SPDC photon pairs produced in the clockwise run-through (↻) exit the Sagnac interferometer depending on their polarization into the spatial modes denoted by "↻$\mathrm{H_s}$" and "↻$\mathrm{V_i}$", with s, i being the indices for signal and idler [Fig. 4.5 (a)]. Both are sent to Alice and Bob, respectively, while a dichroic mirror in the "↻$\mathrm{H_s}$" mode separates the SPDC beam from the back-propagating pump beam. In the counter-clockwise run-through (↺), the H-polarized fraction of the pump beam is transmitted by the dPBS and also creates pairwise $\mathrm{H_s}$ and $\mathrm{V_i}$ SPDC photon pairs [Fig. 4.5 (b)]. The photon pairs are then rotated in polarization by 90° by the dHWP to $\mathrm{H_i}$ and $\mathrm{V_s}$ and exit the interferometer again depending on their polarization. Now, the V-polarized signal photons ("↺$\mathrm{V_s}$") propagate in the "↻ $\mathrm{H_s}$" mode from the clockwise run-through (↻) and the H-polarized signal photons ("↺$\mathrm{H_i}$") propagate in the "↻$\mathrm{V_i}$" mode.

Depending on the state of the pump beam entering the interferometer, a coherent superposition of the two cases, being $|↺\rangle + e^{i\phi}\,|↻\rangle$, can be achieved, with the pump state being:

$$|\Psi_p\rangle = \frac{1}{\sqrt{2}}\left[|H\rangle + e^{i\phi_{pump}}\,|V\rangle\right]. \tag{4.2}$$

If the incoming pump photons are in the state in Eq. 4.2, the crystal is pumped coherently from both directions. The phase ϕ_{pump} can be manipulated prior to the setup with a combination of half-, quarter-, half-wave (HQH) plates. Hence one obtains the following SPDC photon-pair state in the spatial modes after the PBS:

$$|\Psi\rangle = \frac{1}{\sqrt{2}}\left[|H\rangle_i\,|V\rangle_s + e^{i\phi}\,|V\rangle_i\,|H\rangle_s\right], \tag{4.3}$$

which is a maximally entangled state in the polarization HV basis. Now, the phase ϕ describes the phase relation between the pump phase ϕ_{pump} and the phases of the SPDC photons, experienced while propagating through the interferometer. Manipulating the phase ϕ (mainly by the HQH-system) can be done in order to create e.g. the singlet polarization $|\Psi^-\rangle$-Bell state:

$$|\Psi^-\rangle = \frac{1}{\sqrt{2}}\left[|H\rangle_i\,|V\rangle_s - |V\rangle_i\,|H\rangle_s\right]. \tag{4.4}$$

Note that there exists no information that reveals any distinguishability regarding whether the photons were created in the clockwise or counter-clockwise run-through (a proof is given in in [57]).

In this thesis, a type-0 nonlinear crystal was used (see Fig. 4.6). In the type-0 phase-matching condition in a nonlinear crystal (see section 2.2.2), the polarization of the three fields involved in the SPDC process (signal, idler, and pump) are equal ('$e - ee$' or '$o - oo$'). Hence, the SPDC photon pairs remain in the same spatial mode, also when exiting the interferometer. Implementing an additional separation element in the SPDC path outside the interferometer such as a 50:50 beam splitter or a dichroic mirror separating a non-degenerate wavelength distribution

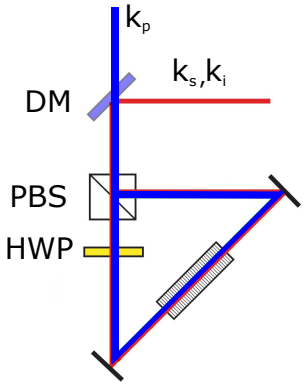

Figure 4.6: A Sagnac polarization-entangled photon-pair source with a type-0 nonlinear medium pumped with a laser beam (k_p, blue line) is depicted. The SPDC photon pairs (with the wave numbers k_s and k_i, red line) exit the interferometer within the same mode. Figure modified from Ref. [57].

of signal and idler can be done to separate the two modes. With the pump photons being in the quantum state described with Eq. 4.2, the SPDC photon-pair state can be given with:

$$|\Psi\rangle = \frac{1}{\sqrt{2}}\left[|H\rangle_i |H\rangle_s + e^{i\phi} |V\rangle_i |V\rangle_s\right]. \tag{4.5}$$

Again, the phase of the incoming pump beam can be changed such that, e.g., the $|\phi^-\rangle$-Bell state can be created:

$$|\phi^-\rangle = \frac{1}{\sqrt{2}}\left[|H\rangle_i |H\rangle_s - |V\rangle_i |V\rangle_s\right]. \tag{4.6}$$

4.3 Polarization-spectral hyperentangled states of SPDC photon pairs

The previous section showed the generation of polarization-entangled photon-pair states. The phenomenon of entanglement is accompanied by indistinguishability within the degrees of freedom of the entangled particles, which was subject with respect to interference in section 3. A high degree of indistinguishability e.g. in the temporal and spatial degree of freedom is crucial for the creation of strongly entangled particles. The polarization degree of freedom can be exploited to encode information (see section 2.1) and other degrees of freedom of photons can be utilized for information encoding, such as orbital angular momentum [192], time-energy [193] and path [194]. Subsequently, these high-dimensional entangled systems inhabit a higher information density than two-dimensional (qubit) entangled states.

Alternatively, additional degrees of freedom of photonic systems can be utilized for deterministic, rather than probabilistic separation, offering the possibility to effectively change the photon statistics in a quantum optical setup. As introduced in section 4.1, the spectral correlations of SPDC photon pairs can be exploited for deterministic separation of a quantum signal in a QKD setup, leading to a possible increase of the secure key. In the following section, the SPDC photon's correlations in wavelength will be presented. The spectral distribution of SPDC photon

pairs can be described by the two-photon mode function $\phi_{\zeta_s\zeta_i}(\omega_s, \omega_i)$, commonly referred to as joint spectral amplitude (JSA), which has been extensively discussed in section 2.2.3.

The JSA function can be expressed as

$$\phi_{\zeta_s\zeta_i}(\omega_s, \omega_i) \approx \mathrm{v}_p(\omega_s + \omega_i)\mathcal{P}(\omega_s, \omega_i) \tag{4.7}$$

with $\mathrm{v}_p(\omega_s + \omega_i)$ being the pump envelope amplitude and $\mathcal{P}(\omega_s, \omega_i)$ being the phase-matching amplitude. A visualization of the spectral distribution can be seen in Fig. 2.5, where the pump envelope intensity takes the form of a Gaussian distribution, $|\mathrm{v}_p(\omega_s + \omega_i)|^2 = \exp(-\frac{\omega_s+\omega_i-\omega_p}{\sigma_p}^2)$, with σ_p being the spectral bandwidth of the pump beam. A collinear phase-matching condition is assumed, hence the phase-matching intensity takes the form $|\mathcal{P}(\omega_s, \omega_i)|^2 = [\mathrm{sinc}(\frac{\Delta \mathrm{k} L}{2})]^2$, with Δk being the wave vector mismatch in the nonlinear medium with length L. Entanglement in the spectral regime is given, when the JSA cannot be factorized in the form: $\phi_{\zeta_s\zeta_i}(\omega_s, \omega_i) \neq \phi_{\zeta_s}(\omega_s)\phi_{\zeta_i}(\omega_i)$. In this thesis, solely the spectral correlation relations are exploited, hence verifying entanglement will not be of interest.

In accordance with the energy conservation, the spectral distribution shows an anti-correlation in the signal and idler frequencies: $\omega_s = \omega_p - \omega_i$. With introducing a variable transformation, namely $\omega_s = \frac{\omega_p}{2} - \omega$ and $\omega_i = \frac{\omega_p}{2} + \omega$[1], the two-photon SPDC state (Eq. 2.32) can be expressed as (see the integration transformation calculated in [195]):

$$|\Psi\rangle_{SPDC} = \int d\omega \mathcal{Y}(\omega) \left|\frac{\omega_p}{2} + \omega\right\rangle \left|\frac{\omega_p}{2} - \omega\right\rangle, \tag{4.8}$$

where the newly introduced function $\mathcal{Y}(\omega)$ takes the role of the two-photon mode function $\phi_{\zeta_s\zeta_i}$. The central frequency of the whole SPDC photon pair distribution is determined by the pump frequency ω_p. However, depending on the specific form of $\mathcal{Y}(\omega)$ and manipulating the parameters such as the poling period Λ, the central wavelengths of the signal (ω_s) and idler (ω_i) photons can be altered, respectively, according to $\omega_p = \omega_s + \omega_i$ (see Fig. 2.6).

The quantity most commonly used in quantum optical experiments, especially in the optical elements' manufacturer specifications, with respect to the spectral properties is the wavelength λ. Also in this thesis, the spectral properties will be described in dependency of photon's wavelength λ. Hence, it is advantageous to reformulate the two-photon SPDC state form Eq. 4.8 to the following form:

$$|\Psi\rangle_{SPDC} = \int d\lambda \, \mathcal{X}(\lambda) |2\lambda_p + \lambda, 2\lambda_p - \lambda\rangle, \tag{4.9}$$

where $2\lambda_p$ is the central wavelength of the SPDC spectrum and the newly introduced $\mathcal{X}(\lambda)$ is a continuous function of the wavelength λ which describes the spectrum of the SPDC source. Moreover, it is assumed that $\lambda \ll \lambda_0$. Here, the anti-correlation in wavelength is in accordance with the energy conservation $\frac{1}{\lambda_s} = \frac{1}{\lambda_p} - \frac{1}{\lambda_i}$.

A Sagnac-interferometric photon-pair source (as introduced in section 4.2) can be operated in the way that it provides photon pairs being in a maximally polarization-entangled Bell state,

[1] This transformation is valid, as adding the transformations leads to the energy conservation formula $\omega_s + \omega_i = \omega_p$.

e.g., $|\psi\rangle_{pol} = \frac{1}{\sqrt{2}}(|H,V\rangle + e^{i\phi}|V,H\rangle)$. When the wavelength distribution of the signal and idler photons is taken into account, the final state generated in the Sagnac interferometer is a hyperentangled state which reads as

$$|\Psi\rangle = \int d\lambda\, \mathcal{X}(\lambda)|2\lambda_p + \lambda, 2\lambda_p - \lambda\rangle \otimes |\psi\rangle_{\mathrm{pol}}. \tag{4.10}$$

In this way, the anti-correlated joint spectra of the SPDC emission can be exploited in order to implement the wavelength demultiplexing deterministically, while preserving the polarization entanglement between the photon pairs. In other words, elements that spatially separate the quantum signal by wavelength (e.g., bandpass filter or holographic grating), can be implemented to deterministically split the photons by means of the spectral degree of freedom. Being now in separate spatial modes, the signal can be further used for applying unitary transformations on each wavelength fraction or generating a secure bit string for QKD.

4.4 Theoretical error model for secure key rate estimation

The counter intuitive and non-classical nature of pure quantum states enables the ultimately secure transfer of information. By performing local projective measurements on quantum states distributed between two users, say, Alice and Bob, a binary bit string that can be used for a secure key can be generated. In an entanglement based QKD scheme, namely the BBM92 protocol [196], an ideally maximally entangled photon pair, e.g., $|\Psi^-\rangle = \frac{1}{\sqrt{2}}(|HV\rangle - |VH\rangle)$ is emitted to two end-users, Alice and Bob, with the desire to establish a secure key. Both Alice and Bob perform measurements on the photon's polarization state in two mutually unbiased bases, e.g. in the HV and DA basis. As discussed in section 2.1.2, measuring in these bases enables proving the result's randomness or security, due to their maximum amount of unbiasedness [29]. The measurement outcomes as well as the information of the randomly chosen measurement bases are recorded. Subsequently, both users declare the assignment of binary values to respective measurement outcomes, e.g., the value "1" to H and D and "0" to V and A, which ultimately generate the binary bit string. By evaluating the bit error in post-processing with help of classically exchanged information, any impact of malicious eavesdropper with the desire to gain information on the exchanged bit string can be tracked, due to the quantum state's inevitable perturbation. Hence, the secure key's security is guaranteed by the laws of quantum physics.

However, due to the non-ideal conditions and imperfect devices in the setup, in real-world QKD implementations, errors are inevitably given. The QBER is rooted in, e.g., the quality of the quantum state, higher-order photon emission arising from the source, background light, and non-ideal polarization-analyzing optical elements such as PBS and HWP. The QBER, independent from its origin, has to be assigned as perturbations arising from a malicious eavesdropper for the attempt of distributing a quantum key being unconditional secure. Knowledge of potentially arising errors in the system and their theoretical analysis regarding the impact on the QBER will aid in estimating a secure key rate of the QKD system shown in this thesis, which will be subject to in the following section.

A theoretical model describing the QKD system's performance with parameters available for the experimenter will be given. The QBER stands in the following relation to the system's visibility $\mathcal{V}$ (see Eq. 2.43) [197]:

$$Q = \frac{\text{erroneous counts}}{\text{total counts}} = \frac{1-\mathcal{V}}{2}. \tag{4.11}$$

In the model, the requirement is to describe and understand the behavior of the visibility $\mathcal{V}$ (and hence of the QBER) with respect to the systematic error arising from experimental imperfections $\mathcal{V}_{sys}$ and, due to the detector's finite timing resolution, from the intrinsically occurring of accidental coincident counts $\mathcal{V}_{acc}$ (see section 2.2.4) [197]. Experimentally, the systematic visibility $\mathcal{V}_{sys}$ can be measured in the low-power regime, where the influence of $\mathcal{V}_{acc}$ is negligible. Both parameters are taken into account in the final visibility by $\mathcal{V}_{final} = \mathcal{V}_{acc} \times \mathcal{V}_{sys}$. The theoretical model is fed by experimentally obtained data, and the derivation from known parameters such as the single count rate $\mathcal{C}_{A,B}$, the coincident count rate $\mathcal{C}_c$ and the dark count probability $D_{A,B} \times t_c$ is given in Appendix A1.

An estimation of the error's impacts on the QBER was given by Ma [198], in which an entanglement-based QKD scheme and the statistical and systematic error sources were considered. Hence, Ma derived an expression for the expected n-photon gain, composed by the conditional probability of a coincident detection, when the source emits an n-photon pair, and the source's photon number distribution. The author estimated a lower bound of the secure key rate per coincident timing window including the Koashi and Preskill's security proof [199]:

$$R \geqslant q \left\{ \mathcal{P}_c \left[1 - f H_2 \left(Q_b \right) - H_2 \left(Q_p \right) \right] \right\}, \tag{4.12}$$

with the binary Shannon entropy $H_2(x)$ being defined as

$$H_2(x) = -x \log_2(x) - (1-x) \log_2(1-x), \tag{4.13}$$

where Q_b is the bit error rate, and Q_p is the phase error rate, which both describe the quantum bit error in two mutually unbiased bases (Q_b in HV basis and Q_p in DA basis), respectively. The detected mean photon number per coincident timing window $\mathcal{P}_c$ was derived in Appendix A1 and is composed of experimental parameters. Moreover, f is the bi-direction error correction efficiency [200] and q is the basis reconciliation factor [198], while the latter accounts for the random basis choice. Note that the estimated key rate in Eq. 4.12 holds in the asymptotic limit of a key with infinite length [198]. Finally, to obtain a greater-than-zero secure key rate, the QBER has necessarily to be lower than 11% [201].

4.5 Technical realization

The realization of the proposed ideas in the introducing section above into technical implementation required essentially four tasks to be fulfilled: first, the production of highly polarization-entangled photon pairs with high spectral brightness B_λ, hence the probability density for the collection of a photon pair within a certain bandwidth (in terms of nm^{-1}), was mandatory for a high quality of security and high rate of the secure key. Second, a transmission link for the distribution of the quantum signal to two end-users was required. Three, small-bandwidth wavelength selection elements on both the end-users sites were needed. Finally, detection electronics were required to detect single photon pairs with the respective wavelength with high efficiency. A graphical representation of the experimental setup as built and tested is depicted in Fig. 4.7. All essential technical aspects regarding the implementation and the alignment process shall be outlined.

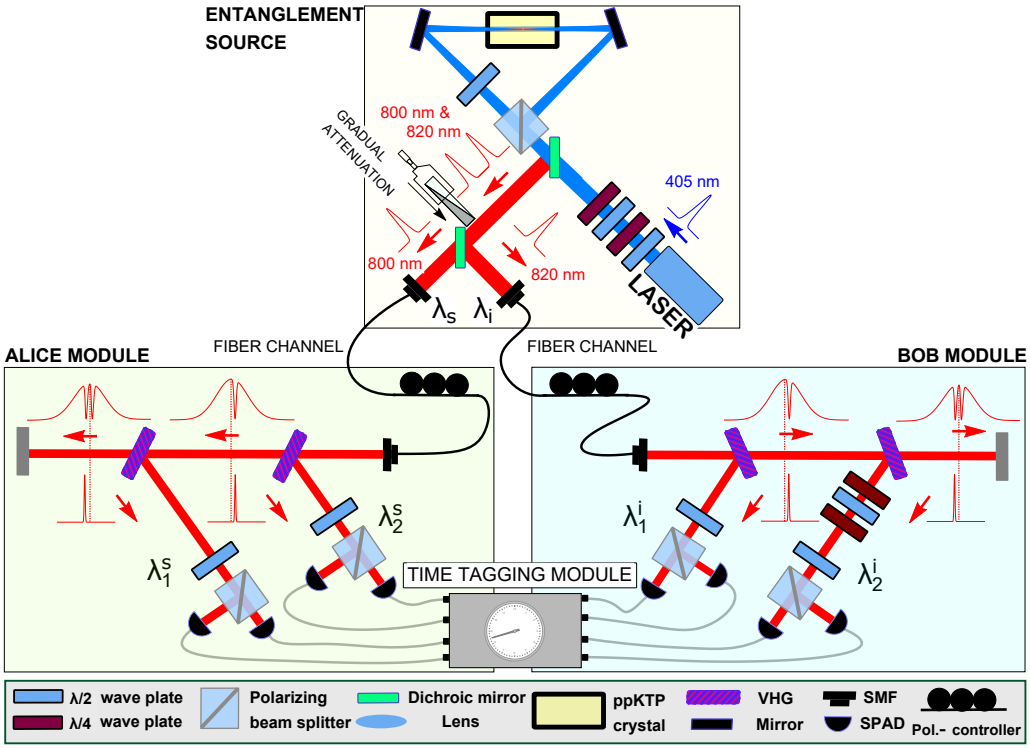

Figure 4.7: A technical scheme of the entangled photon-pair source and the receiving end-users Alice and Bob including the polarization-analysis stage and wavelength selection elements is depicted. The polarization-entangled SPDC photon pairs ($\lambda_{SPDC}^{CWL} = 810$nm) were produced in a Sagnac-interferometric configuration where a type-0 ppKTP nonlinear crystal was pumped bidirectionally by a cw-pump laser ($\lambda_p^{CWL} = 405$nm). Each of the photon pair's partner photon was distributed to Alice and Bob via fiber channel, respectively. The SPDC photons were a narrow-band wavelength selected (~ 0.12nm and ~ 0.24nm, for Alice and Bob respectively) by the VHGs located in the receiving sites and polarization measurements are performed. The count rates and timestamps measured by single-photon avalanche photodiodes were guided to a time tagging module, recording correlations within a certain timing window t_c (coincident timing window) of around 1ns. Note that the broadened SPDC spectra shown on Alice's and Bob's modules were solely inserted for the VHG working principle's comprehension and did not correspond to the spectra from the source.

4.5.1 Entangled photon-pair source

Pump laser source

To provide entangled photon pairs, a nonlinear bulk crystal was bidirectionally and symmetrically pumped in a Sagnac-like configuration by a cw-pump diode laser. The grating-stabilized laser diode (Toptica Photonics DL pro) was tuned to a CWL of $405.0020 \pm 0.0003\,\text{nm}$, measured with a high-accuracy wavelength meter with an absolute accuracy of $0.2 - 0.3\,\text{pm}$. The FWHM linewidth of $\Delta\nu = 150\,\text{kHz}$ [202] ensured a coherence length of $l^p_{coh} = 636\,\text{m}$ and a coherence time of $t^p_{coh} = 2\,\mu\text{s}$. The feedback-loop grating-based stabilization guaranteed the single-mode, mode-hopping free stable performance of the diode laser for hours of operations.

Achieving ultimately entangled SPDC photon pairs, a high degree of indistinguishability in both temporal and spatial regimes is required. Hence, the pump laser beam has to be spatially filtered, which has been done via coupling into a single-mode fiber (see Fig. 4.8). The mode field diameter of the SMF (Schäfter-Kirchhoff PMC-405Si) was $2.8\,\mu\text{m}$, in which the pump laser was coupled via a $f = 6.25\,\text{mm}$ plan achromat objective. In the experimental setup, a system was implemented which allowed the laser beam produced in the laser cavity, to prevent unwanted feedback coming from the source. The back-propagating signal could cause damage to the optical oscillator or result in a variety of instabilities such as frequency shifts and loss of mode lock. The isolation system comprised polarizing beam splitter[2] (PBS), a Faraday rotator (FR), and a polarizer (Pol). A Faraday rotator is a magneto-optical device that applies a rotation of the polarization state of the incoming electromagnetic field proportional to the applied longitudinal magnetic field. This causes circular birefringence, the optical rotator changes the polarization state of the light traversing the device along the field lines independent from which side it enters. In other words, an H-polarized laser beam, whose polarization state was ensured by traversing a PBS, was rotated by the factory-tuned FR (Thorlabs IO-5-405-LP) of the design wavelength by 45°, hence then being D-polarized [following the dark blue arrow in Fig. 4.8 (a)]. Backward propagating light entering from the source[3], had to propagate initially through a polarizer set at 45°, ensuring that solely D-polarized light was transmitted [following the light blue arrow in Fig. 4.8 (a)]. Now, the FR rotates the light by an additional 45°, hence then being V-polarized. Note that a wave plate introduces birefringence fundamentally differently: the angle between the axis perpendicular (ordinary) and the axis parallel (extraordinary) to the optical axis of the birefringent crystal defines the angle of rotation of the light's polarization irrespective of the incoming direction. Subsequently, the now V-polarized back-propagating light is reflected from the PBS, preventing the light from traveling into the laser diode. Rotating the half-wave plate ensured manipulating transmission/reflection-ratio of the light traversing the PBS, which aided in increasing the light coupled into the SMF by increasing the H output of the PBS.

The isolation arrangement served an additional purpose: the high intrinsic degree of phase and spatial stabilization within a Sagnac-interferometric configuration is owed to a stable implementation of the technical arrangement of the interferometer when aligned optimally. The two paths coincided due to the position of the two mirrors with respect to the PBS (see Fig. 4.5 and 4.6). Hence, a high degree of indistinguishability was ensured when the signal separated by the PBS equally, exits within the same spatial mode, given the dHWP in the interferometer was set to flip the polarization from H to V and vice versa. Subsequently, the signal was coupled back into

[2]The (transmission) extinction ratio, hence the ratio of transmitted H- and V-polarized light at the input states being H and V, respectively, was equal to $1:514$.

[3]Although lacking the knowledge about the exact phases experienced by the pump beam while propagating through the source, it can be shown that due to the unitary transformations the polarization state back-coupling into the SMF is equal to the exiting state, given that the two propagation directions inside the Sagnac interferometer are balanced [203].

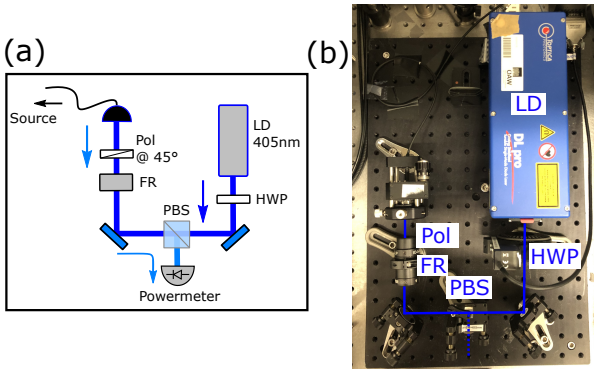

Figure 4.8: Depiction of the pump diode laser coupled into a single-mode fiber (SMF) equipped with an optical isolator system, in a schematic (a) and photographic form (b) is shown. (a) The darker blue arrow indicates the direction of the laser beam produced from the laser diode (LD) coupled into the single-mode fiber. The lighter blue arrows show the direction of the back-propagating light coming from the source. To prevent back-coupling into the laser cavity, the coupling stage comprised a polarizer (Pol), a Faraday rotator (FR), and a polarizing beam splitter (PBS), filtering light coupled back from the SMF into the other output of the PBS, while its intensity could be measured by a powermeter. Monitoring the intensity of the back-propagated light at the reflected output of the PBS aided in aligning the Sagnac interferometer, as explained in more detail in the text. Due to the predominantly linearly polarized laser light created in the laser cavity, rotating the half-wave plate (HWP) in combination with the PBS was used for maximizing the laser power coupled into the SMF.

the same SMF, in which it entered the source. The signal's back-propagating intensity could then be detected, due to the isolation system implemented in the pump-coupling stage (see Fig. 4.8). Monitoring the back-coupled intensity is a useful alignment technique, which was used in this experiment for the preparation of the photon-pair source (see alignment technique in section 4.5.4).

Focal parameters

The choice of the focal parameters requires some comments. As discussed in section 3.3.1, a trade-off between brightness B and heralding efficiency h is fundamentally given in bulk SPDC systems [113]. Moreover, quantitative analysis has been conducted on the spectral brightness B_λ with respect to the focusing condition [41]. The findings were, that the overall spectral bandwidth of the SPDC photon pair spectrum increases for strong focusing conditions, while a higher peak spectral brightness B_λ can be achieved via loosely focusing. Choosing small beam parameters supported the mandatory requirement of achieving high spectral brightness B_λ, as the non-degeneracy of the SPDC photon pair's spectrum was intended, resulting in narrower bandwidths for both signal and idler photons. Moreover, small pump beam waists ensured a high heralding efficiency, which, at this point of the experiment, was desirable, as a high heralding efficiency decreased the probability of detecting an uncorrelated photon pair due to accidental coincident counts, defined as $\mathcal{C}_{acc} = \mathcal{C}_\mathcal{A}\mathcal{C}_\mathcal{B}t_c$, with t_c being the coincident timing window. An extensive discussion on the influence of uncorrelated photons on the polarization analysis is given in section 2.2.4. Concluding, a small pump focal parameter, $\xi_p = 0.02$ was chosen.

The spatially filtered (via SMF) pump beam was focused into the center position of the ppKTP crystal, as can be seen in the technical implementation of the Sagnac-interferometric source in Fig. 4.9. The output coupler (PUMP) consisted of an aspheric lens with a focal length

$f = 2.7 \pm 0.2\,\text{mm}$, which resulted, with the numerical aperture of the SMF being $NA = 0.11$, in a collimated beam radius $\omega_p^{coll} = 297\,\mu\text{m}$. A bi-convex BK-7 lens (L1) focused the pump into the ppKTP crystal with a beam waist of $\omega_p^{focus} = 217\,\mu\text{m}$, which was verified by a beam profiler camera (Ophir Spiricon LBA-FW SCOR 20), where the measured beam waist was $\sim 220\,\mu\text{m}$ (both beam waists were in accordance with $\xi_p = 0.02$). The difference between the theoretical and measured quantity of the beam waist was reasoned by the imperfect alignment of the aspheric lens for collimating the beam. The Rayleigh length of the pump beam around the focal point ($z_R = 0.38\,\text{m}$) greatly exceeded the crystal length of 30 mm, which supported the approximation of the Gaussian-shaped pump beam being a plane wave through the entire crystal volume (see section 2.2 for the formalism of the SPDC process). The maximum pump power, measured at the position prior to the Sagnac interferometer, was $50.3\,\text{mW} \pm 0.05\,\text{mW}$, leading to an intensity of $326.49\,\text{W/cm}^2 \pm 0.33\ \text{W/cm}^2$ at the center of the crystal ($\omega_p^{focus} = 220\,\mu\text{m}$). Preceding the Sagnac interferometer, the pump beam experienced a polarization rotation depending on the angle set by an $HQHQ$-system (half-, quarter-, half-, quarter-wave plates) with respect to the H-polarized beam, ensured by transmission through a PBS (Semrock PBP01-405/10). The PBS played a role in the alignment process, discussed in a later section. The $HQHQ$-system performed a unitary transformation on the pump beam's state (see Eq. 4.2) by manipulating the pump's phase ϕ_{pump}, which entered the Sagnac loop via the dual-wavelength polarizing beam splitter (dPBS). An extensive discussion of the working principle of a Sagnac-interferometric entanglement source is given in section 4.2.

Periscope system

In order for the Sagnac-interferometric entangled photon-pair source to function properly, the flip in polarization by 90° in the interferometer was crucial (see discussion in section 4.2). Technically, this can be implemented in numerous ways, e.g., by the usage of either a Fresnel-rhomb, a Babinet–Soleil compensator, or a dual-wavelength half-wave plate (dHWP) oriented at 45°. The Fresnel rhomb, being a bulk optical prism, introduces a 90° phase difference between the orthogonal polarization components of an incoming electromagnetic field via total reflection on the inner sides of the prism. However, the N-BK7 made optical prism introduces a dispersion on the different wavelengths along the optical path within the glass. This makes it indispensable to implement two rhomboids in either path after the PBS for compensating temporal walk-offs which could reveal which-path-information with respect to the polarization [41]. Equally, a Babinet–Soleil compensator, as being a combination of birefringent crystalline quartz plates, a compensation for the temporal walk-off is required. The order of a wave plate defines the retardance of the optical path through the wave plate following a specified number of full wavelengths. Hence, dual-wavelength wave plates have to be of higher orders in order to function for a wider range of wavelengths, as a zero-order wave plate would solely introduce exactly one specified retardance. However, higher-order wave plates show sensitive behavior to wavelength and temperature changes, whereby wavelength-dependent variations of the retardance could lead to decreasing visibility; that is the case, when the SPDC photon pairs that are produced in the two directions of the Sagnac loop experience an unequal polarization flip. On the other hand, the lack of proper flipping of the polarization in the pump beam would have affected the efficiency of the SPDC process.

The implementation of a cross-faced periscope (P1) solved the problem of wavelength-dependent effects by flipping the coordinate system along the optical path for both the pump and the SPDC photons. It comprised an arrangement of two ultra broad-band mirrors, vertically stacked with respect to the optical table, and the mirror surfaces enclosed an angle of 90°. Hence, the optical path in the interferometer left the optical plane of the dPBS, which required the implementation

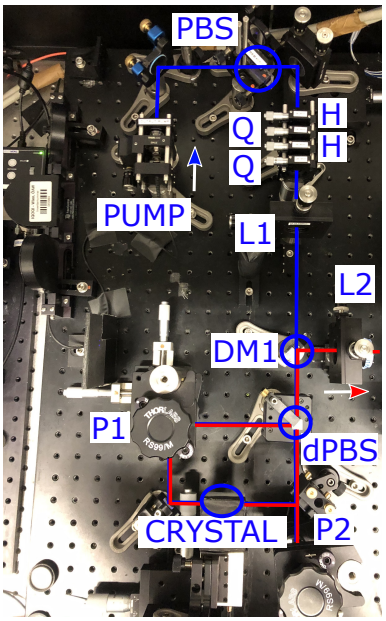

Figure 4.9: A photograph of the entangled photon-pair source in a Sagnac-interferometric implementation is shown. The spatially filtered pump laser propagated through an $HQHQ$-system (preceded by a PBS, which plays a role in the alignment process) for introducing a phase onto the entangled state created by bi-directionally pumping a nonlinear type-0 crystal, providing SPDC photon pairs within the same temporal and spatial modes. The bi-convex lens L1 ($f_{L1} = 500\,\text{mm}$) focused the pump into the central position of the crystal. The Sagnac interferometer comprised a dPBS, the nonlinear crystal, and two periscopes, with a cross-faced (P1, for the polarisation rotation) and a parallel-faced (P2) arrangement. A dichroic mirror (DM) separated the SPDC from the pump photons feeding the detection system. The SPDC photon were recollected by the bi-convex lens L2 ($f_{L2} = 400\,\text{mm}$).

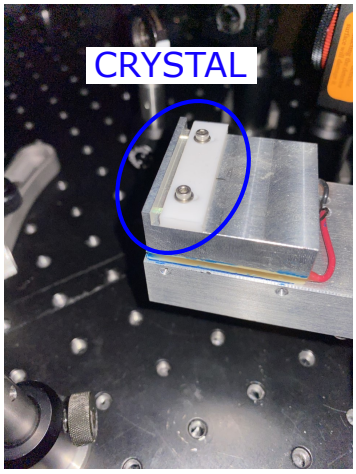

Figure 4.10: A photograph of the type-0 KTiOPO4 nonlinear bulk crystal (blue circle), embedded in a temperature-controlled oven, on a translation stage for positioning the crystal with respect to the optical path in the x, y and z direction is depicted. The Peltier element and the PT100 platinum resistance are located below the aluminum block, acting as a heat conductor.

of an additional, in this case a parallel-faced periscope (P2). On the contrary, no rotation in polarization by traversing was performed in a parallel-faced periscope, where the mirror surfaces face each other.

Nonlinear crystal

The SPDC photon pairs were created by bi-directional pumping a $1 \times 1 \times 30\,\mathrm{mm}^3$ periodically poled KTiOPO4 nonlinear bulk crystal manufactured by Raicol (see Fig. 4.10) with the poling period $\Lambda = 3.425\ \mu$m. Similar to the nonlinear crystals used in the other experiment presented in this thesis (see section 3), the temperature of the crystal was measured by a PT100 platinum resistance, controlled with a Peltier module, adjacent to an aluminum fixation. A temperature controller (Thorlabs TC200) monitored the temperature and stabilized the crystal oven within the range of 0.1° C. Effective and coherent generation of signal and idler fields was dictated by the phase-matching condition in the crystal (see discussion in section 2.2.2). The type-0 phase-matching condition ensured that the signal, idler, and pump beams partaking in the down-conversion process, had equal polarization ('$e - ee$'- or '$o - oo$'- polarization, see section 2.2.2). Due to the quasi-phase-matching condition, the SPDC photon pairs emitted the nonlinear crystal in a collinear way.

The theoretical simulations of the two-photon mode function $\phi_{\zeta_s\zeta_i}$ (see section 2.2.3) with the input parameters being the refractive index n, the poling period Λ, the crystal length L and the temperature T support the prediction of the expected spectral distribution of the SPDC photons. The Sellmeier equations describing the variation of extraordinary refractive index n_e for ppKTP by wavelength and their behavior when undergoing temperature changes were derived by Manjooran [204] based on empirically obtained data (verified by experimental values obtained by Zhao [205]):

$$n_e^2 = A + \frac{B}{1 - C/\lambda^2} + \frac{D}{1 - E/\lambda^2} - F\lambda^2, \tag{4.14}$$

Constants	
$A = 2.12725$	$D = 0.6603$
$B = 1.18431$	$E = 100.00507$
$C = 5.14852 \times 10^{-2}$	$F = 9.68956 \times 10^{-3}$
$a_0 = 9.9587 \times 10^{-6}$	$b_0 = -1.1882 \times 10^{-8}$
$a_1 = 9.9228 \times 10^{-6}$	$b_1 = 10.459 \times 10^{-8}$
$a_2 = -8.9603 \times 10^{-6}$	$b_2 = -9.8136 \times 10^{-8}$
$a_3 = 4.1010 \times 10^{-6}$	$b_3 = 3.1481 \times 10^{-8}$

Table 4.1: The coefficients for the Sellmeier equation and the deviation in temperature for the extraordinary index n_e for ppKTP [204] are depicted.

where the extraordinary refractive index n_e, being the quantity of interest with respect to the type-0 phase-matching case, deviates with the temperature T (in °C) such as described as

$$\Delta n_e = n_1 \left(T - 25^\circ\mathrm{C}\right) + n_2 \left(T - 25^\circ\mathrm{C}\right)^2 \tag{4.15}$$

with

$$\begin{aligned} n_1 &= a_0 + \tfrac{a_1}{\lambda} + \tfrac{a_2}{\lambda^2} + \tfrac{a_3}{\lambda^3} \\ n_2 &= b_0 + \tfrac{b_1}{\lambda} + \tfrac{b_2}{\lambda^2} + \tfrac{b_3}{\lambda^3}. \end{aligned} \tag{4.16}$$

The constants $A-F$, a_0-a_3 and b_0-b_3 are displayed in 4.1, which, by solving the phase-matching condition $\Delta k(n(\lambda, T), \Lambda) = 0$ (see Eq. 2.36), yield in the expected degenerate temperature.

Solving the phase-matching equation with the inputs provided by the manufacturer of $L = 30\,\mathrm{mm}$ and a poling period of $\Lambda = 3.425\,\mu\mathrm{m}$ yield a temperature regarding the degeneracy of the spectrum of 36°C. Experimentally, by detecting the photon pair's spectrum via single-photon spectrometer, the temperature was found to be 23.65°C [see Fig. 4.11 (a)]. Again, solving the phase-mismatch equation for the measured temperature leads to an effective poling period $\Lambda^{eff} = 3.435\ \mu\mathrm{m}$. As discussed in section 3.3.1, where the temperature of degeneracy also deviated from theory, the discrepancy can be attributed to firstly, the manufacturer's tolerances of the crystal dimensions and secondly, to a small deviation from the normal incidence of the pump beam on the crystal surface [119]. Again, thermal expansion's impact of the nonlinear crystal in x-direction [120], which results in an altering $\Lambda^{eff'}$, on the spectral distribution is negligible [119].

The spectral properties of the SPDC photons were varied by the phase-matching temperature of the SPDC crystal, controlled by the Peltier element and the temperature controller in the experiment. The signal's and idler's central wavelengths concerning their wavelength distributions were altered such that the ratio of the transmission to the reflection band of the dichroic mirror (Chroma Technology Corporation T810lpxr) was sufficiently large, with a cut-on wavelength edge of around 20 nm (from $\sim 6.7\%$ at 799 nm to $\sim 98.0\%$ at 821 nm reflection intensity with respect to the incident intensity, provided by the manufacturer Chroma Technology Corporation, see Fig. 4.12). The center of the dichroic mirror's cut-on wavelength edge was manufactured to be 810 nm.

Generally spoken, type-0 phase-matching crystals show high spectral brightness behavior B_λ [158,190,206] with brightness in the order of $10\,\mathrm{MHz\ nm^{-1}}$, which is predestined for our purposes

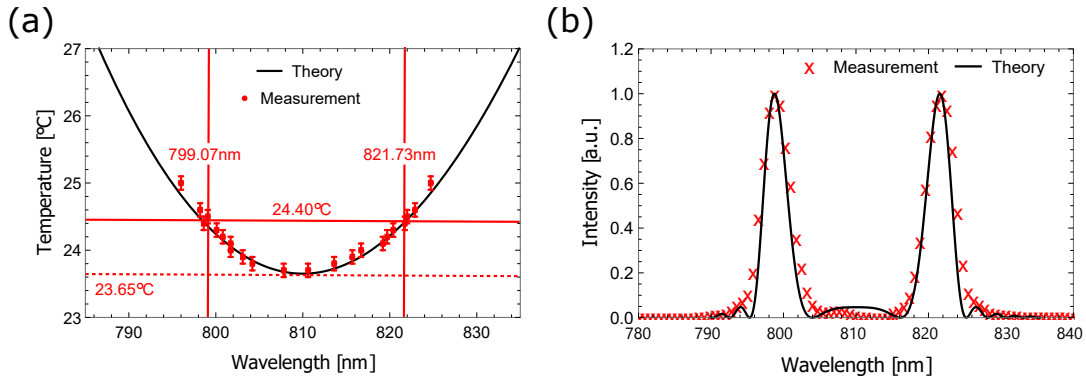

Figure 4.11: (a) The wavelength tuning of signal and idler with temperature is theoretically predicted (black line) by solving Eq. 2.36 with the inputs $\Lambda^{eff} = 3.435\,\mu$m and $L = 30$ mm. In comparison, the measured CWL's (red dots), with error bars given by the spectrometer's and temperature controller's resolution are shown. A degenerate wavelength distribution was experimentally recorded, meaning equal CWl's for both signal and idler, at 23.65° C (dotted line). The temperature was chosen according to the cut-on wavelength and the reflection efficiency of the dichroic mirror, which separated signal from idler spectrally. Reasonable efficiency was observed with CWL's of 799.07 nm and 821.73 nm at a temperature of 24.40°C (red solid line). (b) A comparison of measured data of the nondegenerate SPDC photon's wavelength distribution (red crosses) with the theoretical model (black solid line) is given. The crystal was set to a temperature of 24.4° C, read off and monitored by the temperature controller. The signal's and idler's emission spectra were normalized to the stronger signal for comprehensive comparison to the theoretical prediction.

of narrow spectral filtering (in the order of 10^{-1} nm) of the quantum signal. In the experiment, by coupling the SPDC photons into single-mode fibers (Thorlabs 780HP) and identifying coincident counts resulted in a spectral brightness of $B_\lambda = 12.167 \times 10^6$ photon pair events/s/mW/nm^{-1}. Due to energy conservation, the signal's and idler's full width at half maximum (FWHM) were roughly the same, namely $\sim$4.73 nm.

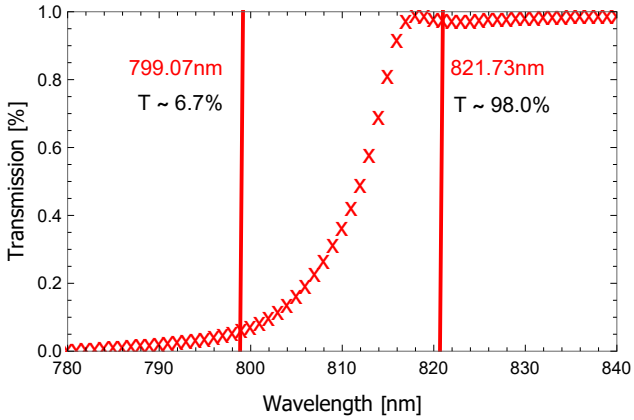

Figure 4.12: The transmission band of the dichroic mirror separating the signal from the idler photons by an angle of incidence of 45° provided by the manufacturer is shown. The CWL's of the SPDC emission (799.07 nm and 821.73 nm) were chosen such that the intensity separation ratio was sufficiently large.

Source's coupling system

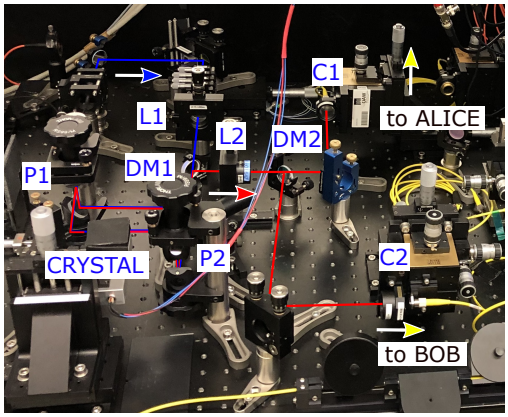

Figure 4.13: A photograph of the coupling system, which collects the entangled photon pairs produced in the Sagnac-interferometric source, is depicted. A bi-convex lens (L2) collimates the SPDC photons, which are separated spectrally by the dichroic mirror (DM2). Subsequently, the photons are coupled into single-mode fibers (C1 and C2), which are used to let the quantum signal propagate to the users, Alice and Bob.

Due to the non-degenerate spectral distribution of the SPDC emission [see Fig. 4.11 (b)], the signal and idler modes were separately fed into a single-mode fiber by a bulk dichroic mirror "DM2" (Chroma Technology Corporation T810lpxr) with a cut-on wavelength close to the central wavelength of the SPDC spectrum (810 nm). The coupling system, which essentially provided polarization-entangled photon pairs for two users, is depicted in Fig. 4.13. This deterministic separation of photons showed advantageous behavior compared to the probabilistic splitting via a 50/50 beam splitter with regard to the heralding efficiency h, as the random separation effectively decreased η by a factor of $\frac{1}{2}$ and hence the total brightness B_{total}.

The collinear propagating SPDC photons were collimated by a bi-convex lens $f = 400\,\text{mm}$ preceding a longpass filter to spectrally remove the remaining and undesired pump signal. The separated signal and idler modes were coupled into the single-mode fibers with a mode field diameter of $5.0 \pm 0.5\,\mu\text{m}$, where the SMF acted as spatial filters. As introduced in section 3.3.3, maximal coupling efficiency was experimentally found, expressed in a relationship between an arbitrary pump and SPDC focal parameters: $\xi_{s/i} \approx \sqrt{2.84\xi_p}$ [113]. This and the measured pump waist at the position of the crystal center $w_p^{focus} = 220\,\mu\text{m}$ led to to a SPDC beam waist of $\omega_{s/i}^{focus} = 93.4\,\mu\text{m}$. The collimated beam after traversing the $f = 400\,\text{mm}$ (L2) had a beam radius of $\omega_{s/i}^{coll} = 1.1\,\text{mm}$, which finally led to a beam waist at the single-mode fiber tip equipped with an achromat objective with $f_{achromat} = 11\,\text{mm}$ of $\omega_{s/i}^{SMF} = 2.57\,\mu\text{m}$. Note that due to the chosen non-degeneracy of the SPDC central wavelengths, the beam parameters of the signal and idler beams deviated slightly. With CWL's of 799 nm and 821 nm, the optimal focusing condition were given with beam waists of $\omega_{799\text{nm}} = 92.7\,\mu\text{m}$ and $\omega_{821\text{nm}} = 94.0\,\mu\text{m}$, which translated into a beam waist at the single-mode fiber tips to $2.55\,\mu\text{m}$ and $2.586\,\mu\text{m}$, respectively, hence ensuring highly efficient fiber coupling.

To reduce further noise contributed by remaining pump photons or background light, a band-pass filter with a CWL of 810 nm and an FWHM of 10 nm was implemented. The fibers had a length of 5 m, which was sufficient to reach both the Alice and Bob modules, located adjacent

to the source. According to the manufacturer, the attenuation was $\leqslant 3.5\,\mathrm{dB/km}$, hence having negligible influence in terms of loss in the presented case. The symmetrical channel attenuation simulating the link loss was introduced before the dichroic mirror. Different attenuation levels were implemented through a graduated neutral-density filter (Thorlabs NDL-25C-2) on a motorized translation stage (Newport Model 436) which consisted of a crossed-roller bearing for a motorized actuator (Newport Model LTA-HS 50 mm travel range) and a remotely controlled single-axis DC motor motion controller (Newport SMC100CC, see Fig. 4.14). This technique enabled the observation of the QKD's performance over various attenuation levels, namely from 0.4 to 20 dB (optical density OD from 0.04 to 2.0).

The polarization in the fibers were controlled by manual polarization controllers (Thorlabs FPC033) to compensate for rotations on the polarization state while propagating through the fiber. In the polarization controlling device, the single-mode fiber was wrapped around a set of three spools, which resulted in a transformation of the light's polarization state due to stress-induced birefringence. By wrapping the fiber two, four, two, and four times around the four spools, respectively, the polarization controller effectively acted as a $QHQH$-system, hence allowing a transmitting polarization state to be compensated arbitrarily by rotating the so-called polarization paddles. Additionally, independent unitary transformations on either signal and idler photons could change the overall entangled photon-pair state. In this way, Alice and Bob effectively shared an entangled Bell state $|\psi\rangle = 1/\sqrt{2}(|HV\rangle + e^{i\phi}|VH\rangle)$, where the phase ϕ was given by the polarization pump state (see Eqs. 4.2 and 4.5). A more detailed discussion on the polarization compensation concerning the final entangled quantum state is given in section 4.5.4.

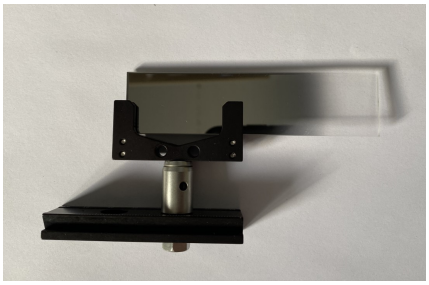

Figure 4.14: For simulating the attenuation experienced a loss over a transmission link, an optical filter with variable light transmission was implemented, where the optical density (OD) varied from 0.04 - 2.0. Fixed with a filter holder (Thorlabs FH2) on a motorized translation stage, a systematic and repeatable introduction of loss of the photon pairs could be realized.

4.5.2 Volume holographic grating

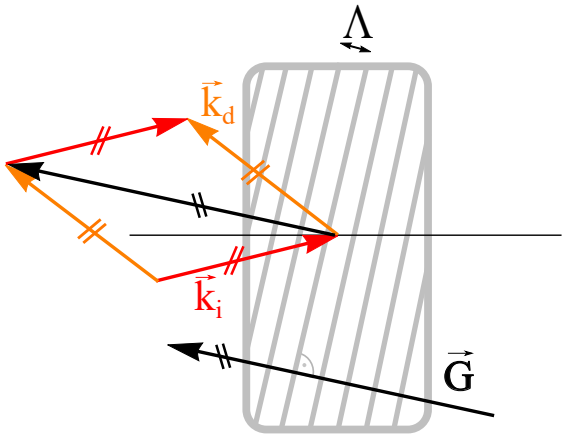

Figure 4.15: The working principle of the Volume Holographic Grating (VHG) is based on periodic perturbations of the diffractive optical media's refractive index. A narrow spectral bandwidth of incoming light is reflected, when the Bragg condition is met via $\vec{k}_i - \vec{k}_d = \vec{G}$, where G is the grating vector and k_i, k_d are the wave vectors of the incoming (i) and diffracted (d) light, respectively. Figure modified from Ref. [203].

In order to exploit the anti-correlation in wavelength of SPDC photon pairs due to energy conservation of the parametric process over a given spectrum, the photons have to be narrowly filtered at both sites in wavelength symmetrically to the central wavelength of the SPDC spectrum. Wavelength selective optical elements aim at the wavelength-dependent reflection or transmission of incoming light. Many physical principles are distinguished within optical filters including acousto-optic filters, Lyot Filters, while in quantum optics, mainly absorptive and interference filters are utilized, depending on the experimental demands. Interference filters consist of multiple dielectric layers and exploit wavelength-dependent phase shifts during propagation.

An ideal candidate for narrow-band wavelength selection is the family of volume holographic gratings (VHG), which are, for example, used for wavelength stabilization in laser cavity systems [207]. In comparison to surface gratings, only a small range of wavelengths will be reflected, when the Bragg condition, hence the correct angle for the respective wavelength, is met (see Fig. 4.15). In equivalence to optical gratings, the VHGs constitute diffractive optical media (e.g., photo-refractive crystals such as LiNbO3 or BGO) permeated by periodic perturbations of their refractive index, that is, through the entire volume of the VHG. The periodic refractive index can be described as $n(\vec{r}) = n_0 + n_1 \sin\left(\vec{G} \cdot \vec{r}\right)$, with n_0 being the average refractive index, n_1 is the grating strength of the refractive index modulation and $\vec{r}$ is the spatial direction in the volume of the element. The grating vector $\vec{G}$, with $|\vec{G}| = 2\pi/\Lambda$ (with Λ being the grating's period) determines the diffraction condition (or Bragg condition). The Bragg condition can be written as

$$\vec{k}_i - \vec{k}_d = \vec{G}, \tag{4.17}$$

with

$$\left|\vec{k}_i\right| = \left|\vec{k}_d\right| = \frac{2\pi}{\lambda}, \tag{4.18}$$

where k_i, k_d are the wave vectors of the incoming (i) and diffracted (d) light, respectively. The diffraction properties of such gratings have been studied by Kogelnik [208], where the sensitivity in wavelength can be described as

$$\frac{\eta_\lambda}{\eta_B} = \mathrm{sinc}^2\left(\frac{\lambda_B - \lambda}{\Delta\lambda}\right), \tag{4.19}$$

with

$$\Delta\lambda = \frac{\lambda^2}{2n\cos\theta_n D}, \tag{4.20}$$

where η_B is the diffraction efficiency, λ_B the wavelength for which the Bragg condition is satisfied, θ_n is the incident angle within the medium of refractive index n and D is the thickness of the VHG. Hence, the wavelength sensitivity depends on the modulation of the refractive index $n(\vec{r})$ and the thickness D. Finally, the wavelength for which the Bragg condition ($\lambda_B = 2\Lambda\sin\theta$) is satisfied is given by the grating period Λ and the angle of incidence θ. Hence, with a fixed grating period Λ, a deviation of the angle of incidence changes the CWL, for which the light's narrow wavelength distribution is reflected.

The above-mentioned fact, namely the sensitivity of the diffracted light's CWL to the angle of incidence with respect to the incoming light, can be exploited for an alignment procedure, where only a rough knowledge of the actual angle of incidence in the setup is given and the target angle is provided by the manufacturer. A bright laser beam with non-zero spectral bandwidth with a known CWL which matches the manufacturer's reflection angle for the respective wavelength is reflected, when the Bragg condition is met, which is verified by measuring the reflected intensity output or simply by using a photosensitive detection card.

In the experiment, at the two receiver sites, to which the entangled photon pairs were sent, VHGs (Ondax ASE-810@19.1-95-6-5-2 and ASE-810@19.1-70-5-5-3) were employed to separate the SPDC photons into their wavelength components with an FWHM of 0.12 nm ($\sim$ 40 GHz) and 0.24 nm ($\sim$ 80 GHz) according to the manufacturer on Alice and Bob's site, respectively. Availability and applying the same wavelength selection characteristics per channel (one wavelength channel comprised a pair of VHGs with either FWHM with 0.12 nm and 0.24 nm, respectively) predefined the choice of elements and its place of implementation. The alignment technique including the VHG holder mount is depicted in Fig. 4.16. A multi-axis stage with the option to tilt the mount in the horizontal plane was used to rotate the VHG (with dimensions 6.0 mm $\times$ 5.0 mm $\times$ 2.0 mm and 5.0 mm $\times$ 5.0 mm $\times$ 3.0 mm) with respect to the light [see Fig. 4.16 (a)]. To align the detection system for the wavelength selected SPDC signal, a tunable laser diode (Thorlabs TCLDM9 Temperature Controlled Laser Diode with a laser diode L808P030) tuned to the CWL of signal and idler was coupled out of an SMF (Thorlabs 780HP) and the reflected signal was focused via an objective lens into another SMF [see Fig. 4.16 (b)]. The TCLDM enabled the regulation of the current applied on the laser diode (via the Thorlabs LDC500 laser diode controller) regulation and controls the temperature of the diode's environment (via the Thorlabs TEC2000 temperature controller). By changing the laser diode's applied current and the temperature, the laser beam's CWL could be tuned. The CWL of the laser diode beam was confirmed

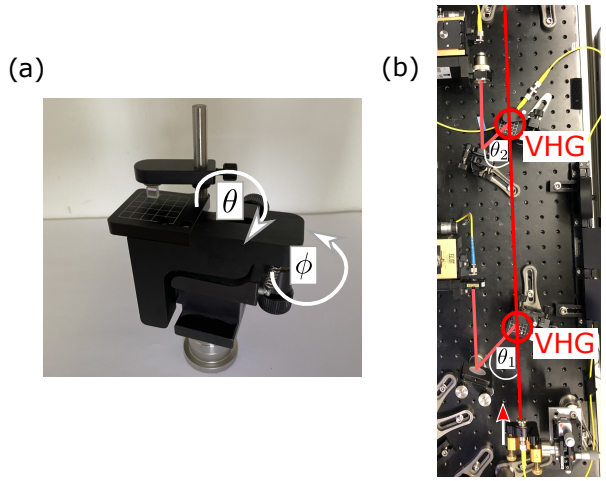

Figure 4.16: A graphical overview of the coupling technique with the VHG mount is given. (a) A multi-axis stage rotation angles in horizontal (ϕ) and vertical (θ) axis with a resolution of 0.75° (13 mrad) was used as mount for the VHG. (b) The incoming light beam is reflected when the photon's CWL satifies the Bragg condition of the VHG, which is given by the grating period Λ and angle of incidence θ_1 and θ_2.

with a spectrometer, while the initial angle of incidence was set to the Bragg angle given by the manufacturer. Two identical VHGs implemented at Alice site, where the SPDC photons with CWL of around 799 nm were sent to, with an angle sensitivity of $\Delta\theta = 0.047°$ (820 μrad) and a given starting angle of $\theta_B = 25.95°$ for $\lambda_B = 795$ nm (grating period $\Lambda = 277.819$ nm, thickness $d = 3.0$ mm and refractive index $n = 1.494$). On Bob's site, which received the SPDC photon partners with CWL around 821 nm, the grating's angle sensitivity was also $\Delta\theta = 0.047°$, while the given Bragg angle was $\theta_B = 14.70°$ for $\lambda_B = 820$ nm (grating period $\Lambda = 283.707$ nm, thickness $d = 2.0$ mm and refractive index $n = 1.494$). When a beam of incident light satisfied the Bragg phase-matching condition, it was reflected by the VHG. Hence, setting the respective angle of the VHG with respect to the broad bandwidth of the SPDC beam led to the reflection of different wavelengths. With having the expected reflection angle for the given CWL of the incoming alignment laser beam in mind, the VHG was rotated with respect to the optical propagation direction, until a clear signal on the reflection output was observed. Further maximizing the intensity of that signal ensured the rotation angle being in the optimal position with respect to the CWL of the laser beam (θ_1). The grating reflected a narrow bandwidth of the wavelength distribution being FWHM of 0.12 nm ($\sim$ 40 GHz) and 0.24 nm ($\sim$ 80 GHz), for Alice's and Bob's VHGs, respectively. The transmitted signal contained the remaining spectrum, which could be used for further wavelength selection. Now, the angle of incidence (θ_2) differed from the prior, as the transmitted spectrum experienced intensity depletion from the first VHG ($\theta_2 \neq \theta_1$). This alignment technique enables the identification of wavelength-correlated photon pairs, which will be discussed in more detail later. It is crucial to mention, that only the relative wavelengths with respect to each other and the central wavelength of the SPDC spectrum (which is defined by the central wavelength of the pump laser) were the leading parameters for alignment procedures.

Detector name	Timing resolution [ps]	Dead time [ns]	QE [%]
PicoQuant τ-APD Fast	$150 - 400$	70	45-50
Excelitas SPCM-AQRH	350	22-35	40-55
Laser components COUNT	1000	42-45	40-50

Table 4.2: The implemented single-photon avalanche photodiodes differed in their detection characteristics. The quantum efficiencies (QE) were roughly equal, whereas the timing resolution and the dead time varied partly drastically.

Due to birefringence, the VHGs introduced a polarization-dependent probability for the incoming photon's reflection. Given by the manufacturer, the reflection efficiency difference for $s-$ and $p-$polarized photons amounted to a polarization-dependent loss in intensity of $\sim 8.7\%$. However, this fact has no influence on the entanglement quality of the $|\Psi^-\rangle$ photon-pair state, as the difference in efficiency solely introduced a loss in photon pair number. Note that the above-made statement holds true under the reasonable assumption, that the polarization-dependent loss was equal in both transmission arms and that a $|\Psi^-\rangle$-state was produced as a result.

4.5.3 Measurement modules

In the experiment, two pairs of correlated wavelength channels (channels 1 and 2) were selected to show the working principle and demonstrate the advantage of wavelength-multiplexed quantum communication. At this point, the experimenter reserved the right to choose the scheme of the two-party setup, the options being an asymmetric (source and one user share one site) or a symmetric scheme (source is in between the users). The spatial modes of the signal and idler photons produced in the Sagnac source were separated spectrally and distributed via fiber or free-space channels to Alice and Bob (cf. Fig. 4.7).

Single-photon avalanche photodiode

The photons were detected by silicon single-photon avalanche photodiodes, which are listed in Table 4.2. Due to the number of multiplexed wavelength channels and the polarization analysis, in total 8 detectors (3 different models) were implemented to record the single photons. Availability restricted the choice of detectors, which resulted in differing characteristics of the detection performance. While the detection efficiencies at $\sim 810\,\text{nm}$ differed only slightly ($\sim 45\%$), the dead time, which describes the timing window in which the electron avalanche of the detector is activated, hence the detector being effectively blind for any further incoming photons, range from 22 to 70 ns. More drastically, the timing resolution varied from 150 to 1000 ps. These different properties led to the fact, that the channels would not behave equally in terms of detection rate performance.

At Alice's site, the detection system comprised 4 detectors where the signal was guided via FC/PC connection from optical fibers into the modules. The pre-mounted fiber connectors induced losses around 10% according to the manufacturers. For optimized coupling efficiency, the numerical aperture (NA) with the fiber in combination with the module was recommended to be $\leqslant 0.29$. Alternatively, single-photon detectors can be implemented as a free-beam module, hence lacking the fiber connector. The active area diameters were $500\,\mu$m and $100\,\mu$m, which required focusing the incoming signal propagating in free space via optical lenses onto the active area.

Time-tagging module TTM8000

The detection events were time-tagged using a time-tagging module (AIT TTM 8000) and the photon pairs were identified by coincident events within a simultaneous timing window of 1 ns. The TTM recorded the timing of electronic pulses by measuring the input's level transition (low-to-high or high-to-low) at in total 8 external inputs [209]. The number of inputs together with the transition's direction were compared with the current value of the high-resolution clock within the TTM (see Fig. 4.17). The timing resolution, in other words, the resolution of the rising and falling edges' steepness, was determined by a clock running at a constant rate of 12.15 GHz, hence being 82.3045 ps (1/12.15 GHz). The recorded data could then be sent via standard Gbit-Ethernet (UDP/IP) to a connected PC (Windows/Linux/Mac), where the event table was processed by a self-programmed software. Here, upon the arrival of photons, the single-photon detectors generated a TTL-pulse, which was sent via SMB-cables to the external inputs of the TTM and the timing was recorded. In post-processing, the timestamps of several detectors connected with the TTM could be compared, whereby the coincident timing window was chosen to be 1 ns. Photons measured within this time frame were identified as coincident photon pairs. In this way, up to 4 detector pairs could be compared upon the photon's timely arrival on one and only one TTM, without the requirement of synchronizing two TTM's located on the receiver sites.

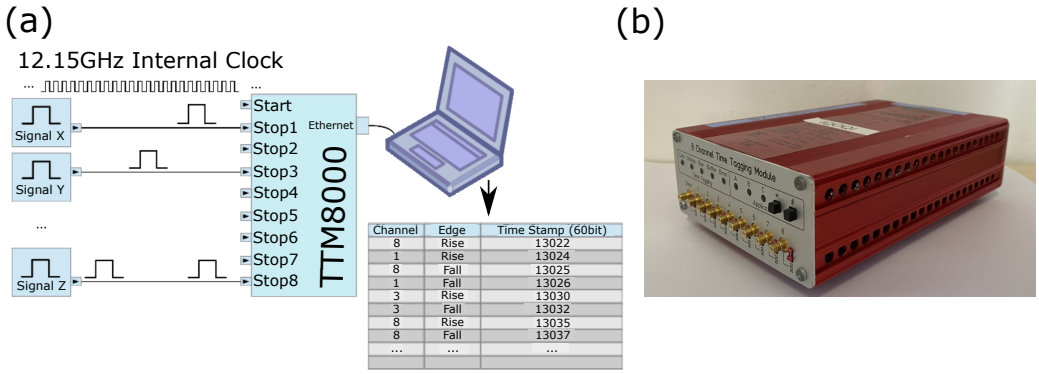

Figure 4.17: The working principle and a photograph of the TTM8000 are depicted. (a) The transition levels of incoming electronic pulses are recorded and compared with an internal clock with a resolution of $\sim$ 82 ps. The event table is sent via Ethernet to a PC for post-processing. Figure modified from Ref. [209]. (b) The compact-built TTM8000 can monitor up to 8 external inputs via connecting the single-photon detectors with BNC-cables (with SMB connectors as intermediate pieces) to the TTM's front panel.

Wavelength-mode resolved polarization analysis

The quantum signal was guided to both Alice and Bob via single-mode fibers, passing through manual polarization paddles as those waveguides tend to change the polarization unintentionally for the experimenter. On each site, after being outcoupled from the fibers via a fixed focused collimator with FC/PC connectors for single-mode fibers, the collimated photons propagated in free space, where the narrow-band wavelength selection via VHG was performed. Both Alice's and Bob's detection modules comprised an equal amount of optical elements with solely few deviations, which are discussed below. The technical implementation of Bob's module is shown in Fig. 4.18, which forms the foundation for the outline of the setup, as discussed in the following. The photon pairs traversed a polarization-analysis module for each channel, which comprises an

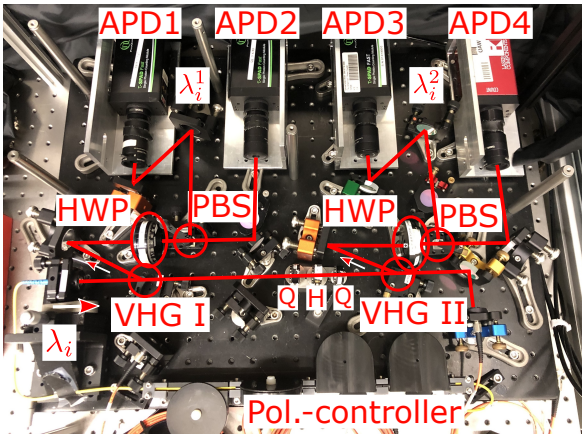

Figure 4.18: The Bob detection module comprised the wavelength-selection grating (VHG1 & VHG2) to multiplex the incoming quantum signal (λ_i) into 2 wavelength bands (λ_i^1 & λ_i^2). Subsequently, the polarization correlations were measured by traversing HWP, followed by a PBS, and ultimately, the photons were detected by single-photon avalanche photodiodes (APD1-4). Unintentional polarization rotations experienced by the narrow-band wavelength fractions were compensated by polarization controllers (Pol.-controller). Wavelength-dependent rotations introducing different rotations for each wavelength band were compensated for one channel by implementing a QHQ system.

HWP for basis choice and a polarizing beam splitter. The half-wave plates were used to apply unitary transformations on the polarization state of one partner of the entangled photon pair, on each Alice's and Bob's site, respectively. Depending on the rotation angle of the HWP, and hence the introduced rotation of the polarization state, as well as the produced entangled photon-pair state, the photon's polarization state could be analyzed by measuring the photons exiting the PBS's outputs. An extensive discussion on the expectations values of the polarization-entangled state and the polarization measurement follows below. Subsequently, the photons were detected by single-photon detectors.

The single-mode fibers, which collected the two spatial modes of the SPDC photon pairs (with CWL $\lambda_i = 791\,\text{nm}$, and $\lambda_s = 821\,\text{nm}$), were identical in construction, with a mode field diameter of $5.0 \pm 0.5\,\mu\text{m}$ and a numerical aperture of 0.13. In Alice's module, the free-space collimator (Schäfter-Kirchhoff 60FC-F-0-M12NIR-10) had a focal length of $f_{out} = 12\,\text{mm}$ which led to a beam radius for 799 nm to 1.22 mm, resulting in a Rayleigh length of 5.85 m, which exceeded the propagation distances to the (in total 4) collecting multi-mode fibers (M31l05 and MMJ-3S3S-IRVIS). The coupling into the MMF's (with mode field diameters of $62.5\,\mu\text{m}$) was done by $10\times$-magnification plan achromat objectives (Olympus RMS10X) with $f_{10\times} = 18\,\text{mm}$ and $10\times$-magnification aspheric objective lenses (Newport 5726-B-H) with $f'_{10\times} = 15.3\,\text{mm}$. Both objective lenses were implemented twice, hence the detection system comprised 4 detector channels. The beam waists in the focus of the objectives were therefore $3.75\,\mu\text{m}$ and $3.19\,\mu\text{m}$, ensuring high coupling efficiency into the MMF's. To guide the SPDC photons through the polarization analysis system and finally into the MMF, 25.4 mm dielectric mirrors (Thorlabs BB1-E03 and Semrock MM2-311S-25.4) were implemented with reflection efficiencies over $> 99.7\%$ for IR light. The coupling stage comprised an x-y-z flexure stage (MDE122 Elliot Gold Series) enabling fine control of 20 nm resolution of the high precision manual adjuster (MDE216). To reduce background noise, for each multi-mode fiber, which was connected to the APD's, optical filtering elements were implemented, namely bandpass filters with a bandwidth of 20 nm around 810 nm (Semrock FF01-

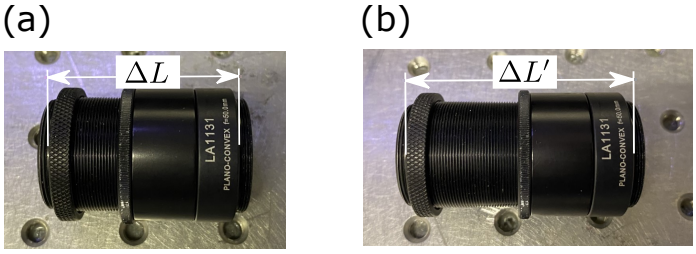

Figure 4.19: To shield the highly sensitive single-photon detectors from ambient light, a tube system containing a thread and a counter piece with the possibility to fixate 25.4 mm SM-threaded mounts was implemented. The combination of the counter piece and the outer thread could be used for changing the distance (indicated by ΔL and $\Delta L'$) from the detector to, e.g., optical lenses on SM-threaded mounts. The tube system also comprised a pinhole with a diameter of 100 μm, and optical filtering elements to further decrease the dark count rate.

810/20-25) and red-colored glass filter (Thorlabs FGL780). The SPDC photons transmitted by the VHGs, hence being redundant for further signal-processing, were collected by a fiber collimator (Schäfter-Kirchhoff 60-FC-F-0-A6.2.S-02) with $f = 6.61$ mm coupling the light into a single-mode fiber (780HP) with a mode field diameter of 5.0 ± 0.5 μm. By monitoring the spectrum with the signal collected by the grating transmission collecting fiber, the stable operation of the entangled source could be ensured.

The Bob module's setup (see Fig. 4.18) was in principle built for the same purpose, however, due to availability, the optical elements and hence the beam parameters differed from the ones in Alice's detection module. A fiber collimator with $f = 8$ mm (Thorlabs F240FC-780) collimated the quantum signal in free space with a CWL of $\lambda_s = 821$ nm to a beam radius of 836.26 μm, leading to a Rayleigh length of 5.7 m. Subsequently, the photons were focused in the detector's active area with a diameter of 250 μm and 50 μm by plano-convex optical lenses with $f = 50$ mm. The resulting beam waist at the position of the active area was 15.63 μm. Also here, IR-coated 25.4 mm dielectric mirrors with reflection efficiencies $> 99.7\%$ (Thorlabs BB1-E03 and Semrock MM2-311S-25.4) were implemented to guide the photons through the module. The light transmitted by the grating was collected by a fiber collimator with $f = 8$ mm into an MMF of a mode field diameter of 105 μm (M43L01). Due to the relatively large active areas of the free-space detectors, shielding the incoming signal from undesired background light was crucial for the photon-sensitive measurements. Hence, a 25.4 mm tube system, where threads and counter pieces enabled the variation of distance between the focusing lens and the detector's active area and the implementation of various optical filters, was implemented. To further prevent ambient light from being registered by the detectors, single-band bandpass filters (Semrock FF02-809/81-25) with a CWL of 809 nm and an FWHM selection bandwidth of 81 nm, and red-colored glass filters for the 4 detectors (Thorlabs FGL780 longpass filter) were used. Moreover, a combination of a spatial filter with an aperture of 1.60 mm (Thorlabs S1TM09) at the entrance of the tube system and a pinhole (diameter of 100 μm) close to the detector active area (hence close to the focus of the incoming light) were implemented. Note that due to availability, in contrary to the Alice module, a QHQ-system for further polarization compensation (see discussion below) was solely implemented in the Bob module for one wavelength channel.

Quantum state characterisation

Both the detection module's were built to perform wavelength-resolved polarization analysis. The wavelength selection by the volume holographic gratings and their implementation are discussed

in section 4.5.2. In each wavelength channel, Alice and Bob were able to analyze the photonic quantum state in the polarization degree of freedom. A tomographic reconstruction of the state with respect to a certain degree of freedom (e.g., polarization) can be performed based on local projective measurements. In a bi-photon quantum state, correlations between photon pairs can be measured to ultimately verify entanglement via an entanglement witness (see section 2.1.2). As discussed in section 2.1.2, entanglement of a bipartite quantum state can be verified by measuring the visibility in at least two mutually unbiased bases, e.g., the HV and the DA basis. Depending on the basis, onto which the local projective measurements are performed, the visibility can be written as [57]

$$\mathcal{V} = \left| \frac{\mathcal{C}_c(\alpha,\beta) + \mathcal{C}_c\left(\alpha^\perp,\beta^\perp\right) - \mathcal{C}_c\left(\alpha^\perp,\beta\right) - \mathcal{C}_c\left(\alpha,\beta^\perp\right)}{\mathcal{C}_c(\alpha,\beta) + \mathcal{C}_c\left(\alpha^\perp,\beta^\perp\right) + \mathcal{C}_c\left(\alpha^\perp,\beta\right) + \mathcal{C}_c\left(\alpha,\beta^\perp\right)} \right|, \tag{4.21}$$

where $\mathcal{C}_\rfloor$ indicate the coincident counts within a certain measurement window at the settings α and β, which have to be chosen with respect to the corresponding measurement basis. The security and hence the length of secure bit strings for distributing a secure key in QKD implementations, the $\mathcal{V}$, which directly results in the QBER, dictates the ability to produce highly entangled photon pairs, and hence yields a secure key rate estimation. In this proof-of-principle experiment, the visibility $\mathcal{V}$ (and hence the QBER of the system) of the quantum state was quantified to prove the increasing impact of multiplexing on the generation of a secure key.

To measure the polarization state in a specific basis (see the introduction in section 2.1.1), a set of a half-wave plate preceding a polarizing beam splitter was implemented. The PBS unambiguously fulfilled the criterion for spatially separating the incoming signal in the parts of the H (transmitted mode) and V-polarization (reflected mode), which is formulated by the PBS's SU(2) complex Jones operator $\hat{J}_{PBS} = \left(\begin{smallmatrix} 1 & 0 \\ 0 & i \end{smallmatrix}\right)$. The HWP acted as a phase retarder between the fast and slow axis, hence enabling, e.g., the rotation of a H-(V-) polarized photon into a D-(A-) polarized photon, hence effectively changing the measurement basis. This unitary transformation (and hence norm-conserving) can be formulated in the respective SU(2) complex Jones operator:

$$\hat{J}_{HWP}(\theta) = e^{-\frac{i\pi}{2}} \begin{pmatrix} \cos^2\theta - \sin^2\theta & 2\cos\theta\sin\theta \\ 2\cos\theta\sin\theta & \sin^2\theta - \cos^2\theta \end{pmatrix}, \tag{4.22}$$

where the angle θ is equal to the fast axis with respect to the horizontal axis. Therefore the angle $\theta = 22.5^\circ = \pi/8$ effectively rotated $H(V)$ polarization into $D(A)$ polarization[4]. The joint probability of a photon pair in a certain state can be calculated with the free parameter θ as the fast axis angle of the HWP. The Sagnac source effectively locally produced a $|\phi^-\rangle = \frac{1}{\sqrt{2}}(|HH\rangle - |VV\rangle)$ state (see Eq. 4.6). However, before directing the photon pairs to the detecting modules, the polarization of the quantum state was changed, such that Alice receives its photons faithfully, while Bob rotated his photons by 90°. This unitary transformation changed the state to $|\Psi^-\rangle = \frac{1}{\sqrt{2}}(|HV\rangle - |VH\rangle)$. Note that the maximally entangled $|\Psi^-\rangle$-state is invariant under basis transformation, hence yielding

$$|\Psi^-\rangle = \frac{1}{\sqrt{2}}(|HV\rangle - |VH\rangle) = \frac{1}{\sqrt{2}}(|DA\rangle - |AD\rangle). \tag{4.23}$$

[4] A comprehensive calculation can be performed with the identity $\cos(\pi/8) = \frac{\sqrt{2+\sqrt{2}}}{2}$ and $\sin(\pi/8) = \frac{\sqrt{2-\sqrt{2}}}{2}$.

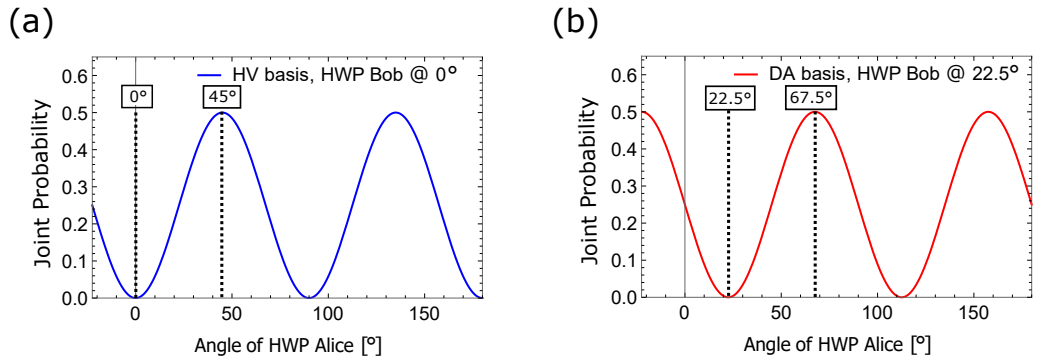

Figure 4.20: The joint detection probabilities calculated for a $|\Psi^-\rangle$-state, undergoing local projective measurements performed by Alice and Bob, are depicted. Both modules comprised an HWP and a PBS with detectors on both outputs of the PBS, respectively. For basis choice, one HWP (e.g., Alice's) was fixed at a certain value, while the conjugate HWP (Bob's) was scanned. (a) Correlations in the HV basis were performed by setting the Bob's HWP at $\theta_B = 0°$. A maximum (minimum) value in correlations was found at the angle setting $\theta_A = 45°$ ($\theta_A = 0°$). (b) The correlations in the DA basis are depicted, with Bob's HWP was set to $\theta_B = 22.5°$. Compared to the correlations in HV basis, the sin^2-function is shifted by 22.5°. Hence, the maximum (minimum) value in correlations were found at the angle setting $\theta_A = 22.5°$ ($\theta_A = 67.5°$).

The joint probabilities for detecting photon pairs of an incoming $|\Psi^-\rangle$-state traversing half-wave plates with the angles θ_A and θ_B at the H_A, H_B and V_A, V_B outputs of PBS of Alice (A) and Bob (B), respectively, can be calculated via $|\langle V_A, V_B|\hat{J}_{PBS}\hat{J}_{HWP}|\Psi^-\rangle|^2$ and $|\langle H_A, H_B|\hat{J}_{PBS}\hat{J}_{HWP}|\Psi^-\rangle|^2$

$$P_{\mathcal{C}}^{H_A,H_B}(\theta_A,\theta_B) = P_{\mathcal{C}}^{V_A,V_B}(\theta_A,\theta_B) = \frac{1}{2}\sin^2(2(\theta_A - \theta_B)), \tag{4.24}$$

where the factor $\frac{1}{2}$ ensures the conservation of photon number in the system. The joint probabilities yielded the expectations values for coincident counts at certain HWP settings for the incoming $|\Psi^-\rangle$-state. As stated before, the visibility $\mathcal{V}$ and hence the QBER of a QKD-ready system can be extracted from coincident polarization measurements. Therefore, for a proof-of-principle experiment it is sufficient to take polarization measurements a the HWP's angle settings which yield the minimum (maximum) probabilities for a coincident count (see Fig. 4.20). For a $|\Psi^-\rangle$-state, minimum (maximum) count rates are expected for the Alice's HWP angle setting of $\theta_A = 0°$ ($\theta_A = 45°$) in HV basis (Bob's HWP $\theta_B = 0°$) and $\theta_A = 22.5°$ ($\theta_A = 67.5°$) in DA basis (Bob's HWP $\theta_B = 22.5°$). Hence, due to the (ideal) quantum state's invariance under basis transformation (see Eq. 4.23), perfect anti-correlation in the polarization measurements were expected.

Importantly, due to limitations of availability of optical elements and single-photon detectors, the simultaneous measurement in both HV and DA basis was unfeasible. As an alternative, implementing a 50/50 beam splitter for random basis choice would enhance the security of the QKD setup, however, this technique would require a duplication in technical elements in terms of the polarization analysis system.

4.5.4 Experimental procedures

The implementation of a multiplexed QKD system with volume holographic grating required foremost a polarization-entangled photon-pair source with high spectral brightness B_λ and correlations in the spectral degree of freedom. In the following, the alignment procedure of the production of wavelength correlated photon pairs and the implementation of separated wavelength channels for ultimately extracting a secure key is outlined.

Alignment of the Sagnac-interferometric source

The alignment techniques of a Sagnac-interferometric source are documented in variety, whereas extensive technical instructions are given by my co-workers Neumann [203] and Wengerowsky [57]. Hence, solely an overview of the alignment approach is outlined in the following, where locations of the setup's interest are referred to via Fig. 4.21.

The optical isolation system implemented in the pump coupling stage was exploited for alignment purposes (see section 4.5.1). Any light back-propagating into the outcoupling stage [(1) in Fig. 4.21] of the pump beam, which fed the pump laser into the Sagnac source, was monitored by measuring the intensity in the reflection output of the PBS (2) in the optical isolation system (see Fig. 4.8). Hence, this gave an initial indication of whether the Sagnac loop was aligned in terms of the pump beam's overlap in both propagating directions such that the pump beam propagated back exactly into the same mode (TEM_{00} due to the SMF). For coarse alignment of the Sagnac interferometer, this technique bore the advantage of the lack of requirement of either implementing the focusing lens as well as the implementation of the nonlinear crystal. By choosing the polarization state of the pump laser entering the Sagnac loop with the $HQHQ$-system (3) to be a coherent superposition of H- and V-polarization (e.g., by rotating the pump state to $|D\rangle = 1/\sqrt{2}(|H\rangle + |V\rangle)$, hence the pump phase being $\phi_{pump} = 0$) and maximizing the intensity on the pump coupling stage (1), it was ensured that both propagation directions overlap spatially, which was crucial for the removal of the $which-path$ information.

The back-coupling alignment technique was used for coarse alignment, while the final minimizing of the $which-path$ information was done by directly observing interference effects in the Sagnac-interferometer. The observation of interference proved to be a great indicator ensuring maximum bi-directional coherent pumping of the nonlinear crystal and hence, the production of highly entangled photon pairs. For the production of entangled photon pairs, the cross-faced periscope's role (P1) was to rotate the polarization state of the pump and SPDC photons by 90°. Only then, the photons exited the Sagnac interferometer into the SPDC coupling system. For alignment purposes, a dual-wavelength multi-order half-wave plate (faintly colored dHWP) rotated by 315° was implemented, to compensate the 90◦ polarization flip of the cross-faced periscope. Hence, the beam exited the other output of the Sagnac interferometer's PBS (4). Interference in form of concentric rings were observed by implementing a polarizer rotated by 45° after the PBS (3), when the state exiting the Sagnac loop was indeed a superposition of both paths. Any mixed state (hence revealing $which-path$ information) lowered the contrast of the interference rings, where the contrast was optimized by rotating the mirrors adjacent to the crystal until a contrast 1:100 was observed [57].

Afterwards, the focusing lens (L1), which focused the pump beam finally into the nonlinear crystal, was implemented. This was done by coarsely measuring the distance from the central position of the Sagnac interferometer to the position of the lens by a mechanical ruler. By changing the position with respect to the optical propagation axis (in the plane of the Sagnac loop) via a manual translation stage, the beam waist was minimized using a beam profiler camera (Ophir Spiricon LBA-FW SCOR 20). Thereafter, the nonlinear crystal was inserted,

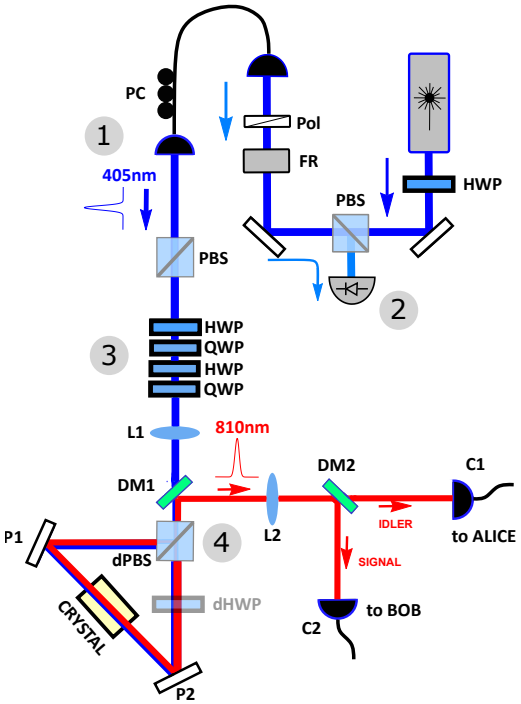

Figure 4.21: A schematic overview of the experimental setup comprising the pump coupling stage, the Sagnac-interferometric source and the SPDC coupling system, is shown, which provided polarization-entangled photon pairs in two spatial modes.

which resulted in a slight spatial misalignment of the Sagnac loop, requiring repetition of the above-mentioned alignment technique.

Alignment of the SPDC collection system

Ensuring that the SPDC coupling system collected a high number of SPDC photon pairs, a spatial overlap of both the SPDC collection mode and pump's mode was required. Before separating the SPDC signal spectrally by the dichroic mirror (DM2, Chroma Technology Corporation T810lpxr), the collinear propagation of signal and idler photons were exploited by sending an alignment laser beam with CWL of 810 nm (Thorlabs TCLDM9 Temperature Controlled Laser Diode with a laser diode L808P0) from the SPDC coupler (C1, comprising an aspheric lens to collimate the laser beam exiting the single-mode fiber) into the Sagnac loop. Note that the SPDC coupler of interest here was the one that later collected the transmission of the signal and idler separating dichroic mirror (C1 in Fig. 4.13). By monitoring both the pump's and the alignment laser's beam waists on multiple positions in the Sagnac loop, the overlap was maximized by changing the outcoupling condition in the various degrees of freedom of the SMF's x-y-z stage (Elliot Gold MDE122 series XYZ flexure stage) with a high precision manual adjuster (Elliot Gold MDE216), without touching the mirrors in the well-aligned Sagnac-loop. At this point, the inserted dHWP was removed. Alternatively, by removing the spectral filters which separated the pump from the SPDC beam, a non-vanishing intensity of the pump beam was detected at the SPDC coupler (C1), which also indicates spatial overlap of the collection and the pump mode.

Successful collection of the SPDC photons was observed initially by sending the coupled SPDC

photons via the single-mode fiber to a single-photon spectrometer (Ocean Optics QE65000). In that way, the SPDC signal was further maximized by rotating the mirrors preceding the SMF. Additionally, the CWL's of both signal and idler by changing the crystal's temperature were tuned via the temperature controller (Thorlabs TC200). By coarsely tuning the signal's and idler's CWL to 799 nm and 821 nm (finally to 24.4°) with respect to the dichroic mirror's (DM2) cut-on wavelength edge of around 20 nm (from ∼ 6.7% at 799 nm to ∼ 98.0% at 821 nm reflection intensity with respect to the incident intensity, provided by the manufacturer Chroma Technology Corporation, see Fig. 4.12), an effective SPDC signal separation was achieved.

By placing the dichroic mirror (DM2) in the SPDC beam, the reflection mode was collected by using the same IR alignment laser with CWL of 810 nm, which was sent from the other SPDC coupler. To meet the spectral separation condition as provided by the manufacturer, the dichroic mirror's angle of incidence with respect to the SPDC mode had to be set to 45°. Due to the choice of the alignment laser's CWL matching the cut-on wavelength of the dichroic mirror, the separation ratio was expected to be low. However, a spatial overlap of the two SPDC collection modes was achieved by first using a fiber beam splitter (Thorlabs TN808R5F2) and monitoring the beam's overlap on several positions in the Sagnac loop, while changing the position of the SMF's x-y-z stage. Afterwards, by still only changing the second SPDC coupling stage (C2, hence the dichroic mirror's reflection arm), the alignment laser's intensity was coupled into the first SPDC SMF (C1), and the signal was maximized. Again, the successful coupling of SPDC into the collection fiber was confirmed by sending the signal to a single-photon spectrometer, although the CWL's of the newly tuned signal and idler modes deviated from the alignment laser's CWL. Finally, by using the single-photon detectors, the coincident count rate of the SPDC was optimized by carefully moving the same degree of freedom for both SPDC couplers in a systematic way. Another degree of freedom was the temperature of the crystal, as tuning the CWL increased the dichroic mirror's separation ratio.

The crystal was fixated on a rotation mount, enabling the rotation in the horizontal and vertical plane, with respect to the pump laser's propagation direction. During the alignment process, the SPDC coincident count rate was increased by rotating the crystal, which can be understood that the phase-matching condition slightly changes for different pump laser's angle of incidence with respect to the crystal surface. Interestingly, while performing measurements with already implemented narrow-band VHGs, e.g., increasing the pump laser power led to a decrease in single-photon count rates. To regain the expected count rate, the temperature controller's PID controller was adjusted to the set temperature, as apparently the increased lasing power led to an increase of the crystal's temperature.

Alignment of the wavelength-multiplexed photon pairs

The alignment technique for the narrow-bandwidth wavelength selection of volume holographic gratings was discussed in section 4.5.2. The produced SPDC photon pairs with signal and idler CWL's being 799 nm and 821 nm were guided via SMF to the detection modules. Again by using a wavelength-tunable alignment laser mimicking the propagation behavior of the SPDC photons, the VHGs narrow-band reflection modes were sent to the detector's coupling stages of both Alice and Bob. Due to the wavelength-sensitive response of the VHGs on the incoming signal, the alignment laser's CWL had to be tuned according to the actual SPDC CWL's, which was confirmed by the single-photon spectrometer. Due to the roughly known Bragg-angle for the reflection condition for the known CWL's, the reflected intensity was observed by turning the angle of incidence of the VHG with respect to the incoming alignment beam. Maximizing the intensity via a powermeter ensured the angle of incidence matching the CWL's characteristic Bragg angle. This was confirmed additionally by implementing a mirror into the VHGs reflection

mode and furthermore via observing the narrow-band beam's spectrum coupled into a multi-mode fiber.

While the coupling into the MMF's on Alice's module was done by "beam walking" (hence changing the mirror's angles systematically with respect to the MMF's fiber tip) and subsequently maximizing the intensity measured on a powermeter, the coupling on Bob's module was performed slightly differently due to the use of free-space detectors instead of fiber-coupled detectors. Instead of measuring the intensity at the MMF's end, an IR viewer (FIND-R-SCOPE 84499C) was used to comprehend the position of the beam on a certain point via fluorescence, caused by the interaction of the beam with the optical elements in the setup. To guide the beam onto the active area of the free-space detectors, two fluorescing alignment disks for IR light (Thorlabs VRC2RMS) were implemented onto the one end of the tube system's thread, which was fixated on the detector (see Fig. 4.19), and directly onto adjacent to the active area. By monitoring the beam position on the centers of both disks while removing and inserting the tube system, a systematic "beam walking" ensured that the beam propagates centrally of the tube system. Afterwards, the lens focusing the signal onto the active area was implemented in the tube system, where with the help of a ruler the coarse distance from the lens to the active area was adjusted. Finally, while observing the SPDC photons via the counts detected by the free-space single-photon detectors, by rotating the lens and the counter pieces in the thread and hence changing the distance between the focusing lens and the detector's active area, the counts were maximized.

Given, that the SPDC counts were coupled into the single-photon detectors (via fiber like Alice or via free space like Bob) on each detection module such that the counts were at least distinguished from dark counts, the goal was to identify photon pairs within the narrow wavelength selection via coincidence measurements. The TTL signals, generated by the Si avalanche photodiodes upon photon impingement, were sent via BNC cables and SMB connectors to the TTM. The timestamps of the inputs were recorded and processed by a self-programmed software for Linux OS, where simultaneous clicks were identified within a timing window of $12 \times 1/12.16\,\mathrm{GHz} = 82.24\,\mathrm{ps} = 9.87 \times 10^{-10}\,\mathrm{s}$. The software enabled monitoring the registered photon pairs arriving on the detectors, respectively. The pairwise wavelength selection (on Alice's and Bob's site, respectively) enabled the effective separation of the quantum signal into wavelength channels, given, that the VHG-reflected signals on both sites matched according to the SPDC photon's energy conservation $1/\lambda_s = 1/\lambda_p - 1/\lambda_i$. The crucial degree of freedom to change the reflection mode's CWL was the angle of incidence. In accordance with a specific wavelength reflection efficiency with respect to the angle of incidence (see Eq. 4.19 and Eq. 4.20), rotating the multi-axis stage onto which the VHG was embedded, the reflected signal's CWL effectively changed. The direction of rotating the knob, which changed to the angle of incidence, was ascertained while monitoring the spectrum via the single-photon spectrometer. Knowledge of the response of the reflected spectrum on the rotation direction of the mirror's knob gave a feeling for the experimenter, whether the CWL increased or decreased, even without monitoring the spectrum. This technique allowed to scan the CWL of one partner of the SPDC photon pair while observing the coincident counts of the SPDC signal reflected from two conjugate VHGs, respectively. The other VHG remained untouched, as solely the relative position of the wavelength selection on both sides led to coincident counts.

After one pair of conjugate VHG-reflected SPDC signals were maximized, the alignment approach was on the other pair. Due to the high reflection efficiencies ($\sim 70\%$ and $\sim 90\%$ for Alice and Bob, respectively), the alignment laser's CWL had to be detuned away from the previous used CWL; with at least one selection bandwidth difference ($\sim 0.12\,\mathrm{nm}$ and $\sim 0.24\,\mathrm{nm}$ for Alice

and Bob, respectively). Finally, the coincident count rates for both wavelength channels were maximized by either changing the crystal's temperature and the VHGs angle of incidence.

Multiplexed quantum state alignment

The degree of entanglement gives an estimation of the secure key generation, and scalability arguments can be investigated. High contrast in the visibility observed at the usually unused output port of the Sagnac interferometer (see alignment technique above) ensured the coherent bi-directional propagation of the pump beam through the loop, which was defined by the $QHQH$-system. However, although the polarization state was typically stable for a time scale of hours, the single-mode fibers transmitting the quantum signal to the detection modules experience a constant rotation of the polarization state mainly due to the fiber's geometrical torsion[5]. Though being unitary transformations, the polarization state rotations had to be compensated to align the reference frames of the sent photons to the detection system. Hence, the compensation was performed via a manual polarization controller. Monitoring, whether the sent polarization state exited the fiber on the detection modules in the same polarization state, was done by implementing a polarizer in the coupling system in front of the SMF and measuring the SPDC photon's polarization by detecting the signal on either the H and the V output port of the detection module's PBS. For compensation in the HV basis, the manual polarization controller recovered the signal's polarization state sent from the source with respect to the HV basis of the receiver's polarization analysis module. By setting the polarizer in the sources coupling system to 0° (90°), hence transmitting H- (V-) polarized light, the manual polarization controller was rotated by minimizing the orthogonal PBS's output, in this case, the V (H) output. In other words, the measurements were expected to be perfectly orthogonal. However, there remained an unknown phase ϕ in the polarization state, being $|H\rangle + e^{i\phi}|V\rangle$. By defining effective D/A axes in the polarization analysis module, hence turning the HWP prior to the PBS to 22.5°, the intensity at the output ports was minimized by changing the phase ϕ between H and V via rotating the paddle acting as a QWP. By rotating the polarizers at the source to 45° (135°) ensured that photon's polarization state when entering the fiber was equal to $|D\rangle$ ($|A\rangle$). In a systematic and iterative way, an optimization of the quantum state's polarization compensation was achieved by switching between the two bases. To improve the quality of quantum state, this technique was performed by monitoring the coincident count rates on the detectors positioned behind the output ports, where the minimal signal was expected.

The above-discussed polarization compensation technique had to be performed for not only both Alice and Bob, but also for each wavelength channel, and hence for each conjugate pair of VHG reflected spatial modes. This was due to wavelength-dependent polarization rotations introducing different rotations for each wavelength band. For that, a polarization compensation for one specific wavelength channel with the manual polarization controller were performed, which coarsely compensated the other channel, too. However, small deviations in the compensation, especially in the DA basis, required the implementation of an additional QHQ-system on Bob's module in the wavelength channel, which was not optimized.

4.6 Measurement results

Initially, the entangled photon-pair source's performance had to be checked at low pump power, and hence low photon pair number, where the contribution of accidental coincident counts was minimal. By measuring the polarization correlations with low brightness B, the systematic error's

[5]Other influences of rotations of the polarization state in optical fibers were temperature fluctuations and mechanical stress.

influence on the visibility, $\mathcal{V}_{sys}$, was investigated. Subsequently, the final pump power was chosen in such a way that the multiplexing technique's improvement, in comparison to a QKD system lacking one, was observed via wavelength-multiplexing the quantum signal into 2 wavelength channels. A post-processing approach in order to reverse the multiplexing is introduced later in this thesis and the secure key rates for both cases are investigated. By estimating the secure key rate based on the measurement results, scalability arguments can be done.

With a pump power of 0.94 mW, in one wavelength channel (0.12 nm at Alice, 0.24 nm at Bob) the visibility of measuring a $|\psi^-\rangle$-state reached 98.62% ($Q_b = 1\%$) in HV basis and 96.47% ($Q_p = 2\%$) in DA basis. This mismatch in visibilities with respect to the bases could be explained either by misalignment within the Sagnac loop or the lack of proper choice of the pump laser's polarization state prior to entering the Sagnac interferometer (see Eq. 4.2). Note that due to the rather high degeneracy of the signal and idler photons ($\Delta\lambda = |\lambda_s - \lambda_i| \sim 22\,\text{nm}$), the optical elements implemented in the detection modules acted differently. For instance, the used half-wave plates introduced a retardance of 0.506λ for a wavelength around 799 nm and 0.490λ for a wavelength around 821 nm, respectively, introducing an error rate with respect to the polarizing beam splitter. This indeed would lead to a non-vanishing cross-talk, meaning clicks in wrong polarization outputs. However, this effect was tackled by proper polarization compensation. The visibility was measured at 0.94 mW ($\mu = 0.00155$), hence being attributed to low accidental coincident counts ($\mathcal{C}_{acc} = \mathcal{C}_A\mathcal{C}_B t_c \approx [9 \times 10^3]^2 \times 10^{-9} = 0.081\,\text{s}^{-1}$, including the dark count rate $\Delta_{A,B} \approx 500\,\text{s}^{-1}$)[6] as compared to the coincident count rate ($\mathcal{C}_c \approx 200\,\text{s}^{-1}$). Therefore, the measured visibility at low pump power could be used as an estimate for $\mathcal{V}_{sys}$.

4.6.1 Multiplexed quantum state characterisation

The wavelength-multiplexing technique presented in this thesis exploits the intrinsic wavelength correlations of SPDC photon pairs. In section 4.3, the polarization-spectral hyperentangled states, created in a SPDC process are discussed. In fact, observing the desired improvement of a QKD system via wavelength-multiplexing does not require the verification of spectral entanglement. Hence, when the overall quantum state is multiplexed into a total number of N channels in the signal and idler modes, the multiplexed total state can be more accurately described as

$$|\psi^-\rangle_{\text{tot}} = \prod_{j=1}^{n} \otimes |\psi_j^-\rangle, \tag{4.25}$$

where the index j indicates a wavelength channel comprising a polarization-entangled Bell-state ($|\psi_j^-\rangle$) in two conjugate wavelength bands. By narrowly filtering the signal and idler photons into 2×2 pairwise corresponding wavelength bands by implementing 2 VHGs on both Alice's and Bob's detection module, the overall multiplexed state takes the following form:

$$|\psi^-\rangle_{MUX} = \prod_{k=1}^{2} \otimes \frac{1}{\sqrt{2}} \left(|H_{\lambda_\text{s}^k} V_{\lambda_\text{i}^k}\rangle - |V_{\lambda_\text{s}^k} H_{\lambda_\text{i}^k}\rangle \right), \tag{4.26}$$

where the labels describe the specific wavelength of the signal (λ_s^k) and idler photons (λ_i^k) in the k-th channel. Each wavelength channel constitutes a polarization-entangled $|\psi^-\rangle$-state, and polarization correlations can be performed via coincidence measurement, which results in a secure key rate estimation for each channel, separately.

[6] Due to the use of different detector models, the system's total dark count rates varied between $100 - 1000\,\text{s}^{-1}$.

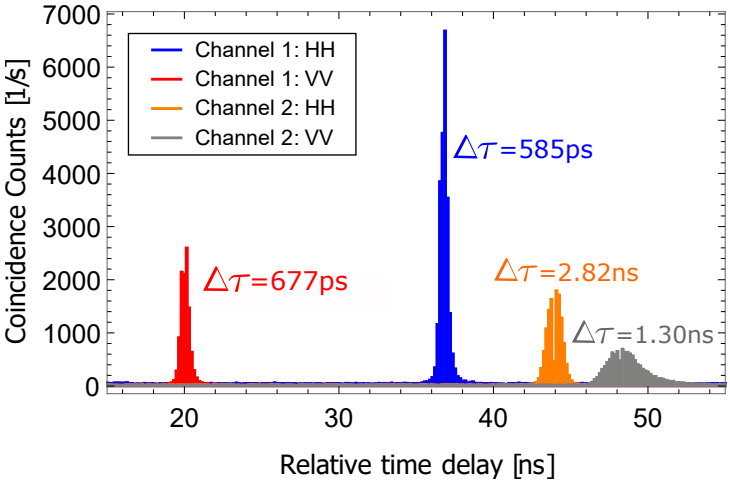

Figure 4.22: The temporal cross-correlations of in total 4 detector pairs are depicted. The measurements in both wavelength channels (channel 1 and channel 2) were recorded by measuring polarization correlations in the HV basis. Each detector pair showed a characteristic peak with respect to the relative time delay to each other. The different time delays were rooted in the difference in absolute signal travel distances from the point of separation over the impingement on the detector to, finally, the time tagging module. The peak widths were mainly determined by the detector's timing resolution, which differed due to the use of various detectors.

4.6.2 Temporal cross-correlations

To identify correlated photon pairs and hence define simultaneous detector pair clicks, the temporal correlations between the SPDC photon pairs have to be observed. The cross-correlation functions between the time recordings of the detector pairs are depicted in Fig. 4.22.

Here, the detector clicks in the polarization modes of equal PBS outputs (HH and VV) of the 2 wavelength channels were compared within a coincident timing window of 1 ns. Succeeding the separation of the signal and idler photons, which were then sent to Alice and Bob, respectively, the photons propagate different distances up until the impingement on the detector's active areas. Moreover, the TTL signal created in the single-photon detectors was sent via differently long BNC cables to the TTM's input channel. Due to the absolute time durations from the photon pair separation to the TTL signal's arrival at the TTM for each detector, it was necessary to introduce a relative time delay between the detector pairs for identifying simultaneous clicks. Hence, each detector pair's correlation function occupied a characteristic peak position (see Fig. 4.22). Moreover, due to the differing properties of the single-photon detectors in terms of, e.g., the timing resolution and quantum efficiency (see section 4.5.3, Fig. 4.2), each correlation function inhabited a characteristic FWHM and peak magnitude. The FWHM ranged from 585 ps to 2.82 ns, whereby the FWHM was mainly governed by the timing resolution of the detectors.

4.6.3 Wavelength-multiplexed channels

As discussed in section 4.5.1, the SPDC photon's wavelength distribution was tuned such that a high spectral brightness B_λ was ensured and that the signal's and idler's central wavelengths were such that the ratio of the transmission to reflection band of the dichroic mirror was, in terms

of total loss, sufficiently high. The SPDC photon's wavelength distribution is depicted in Fig. 4.23. The data points, indicating the measurement points, were recorded with a near-IR single-photon spectrometer with a spectral resolution of 0.19 nm. The measurements were performed by coupling the non-degenerate SPDC spectrum into the single-mode fibers and sending the signal to the spectrometer. The SPDC photons were spectrally separated by the dichroic mirror, whose non-ideal transmission/reflection efficiency can be observed by the non-vanishing contribution of the signal (red crosses) spectrum in the idler (blue crosses) spectrum (see Fig. 4.23). Note that the undesired contribution of the signal was filtered out by the VHGs, hence no increase of accidental coincident count probability occured.

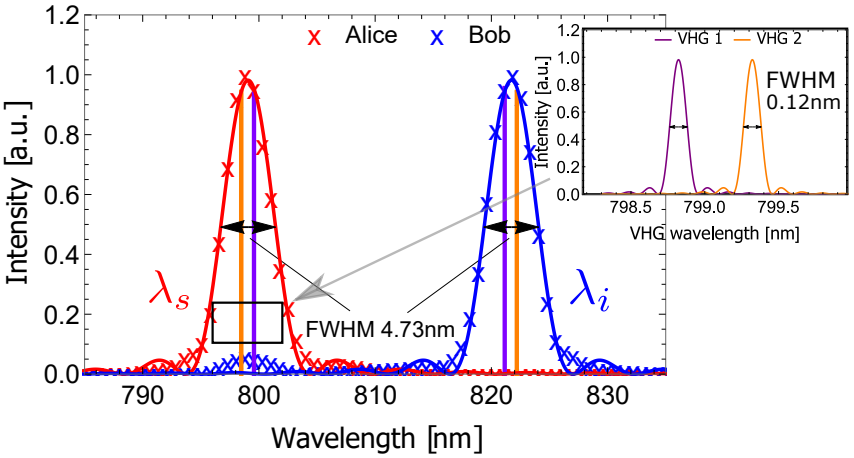

Figure 4.23: The measured non-degenerate wavelength distribution of the SPDC photons is shown. The crystal's temperature was tuned such that the photon pair's CWL's, separated spectrally by a dichroic mirror, were $\lambda_s = 799\,\text{nm}$ (signal) and $\lambda_i = 821\,\text{nm}$ (idler), with both having the same bandwidth with an FWHM of ~ 4.73nm. The spectra of signal and idler photons were normalized to each other, while the crosses indicate the measured data points (measured with a single-photon spectrometer) and the straight line equals the fit function proportional to the $sinc^2$-function (in accordance with the SPDC two-mode function $\phi_{\zeta_s\zeta_i}$, see Eq. 2.33). Furthermore, the wavelength bands, which selected a narrow bandwidth via the VHGs, are depicted. Due to availability and to equal the spectral selection for both wavelength channels, the FWHM bandwidths were $\sim 0.12\,\text{nm}$, and $\sim 0.24\,\text{nm}$ for Alice and Bob, respectively. The inset shows the theoretical prediction of the VHG reflected spectra, provided by the manufacturer.

The maximal amount of reflected light by the VHGs in the detection modules was achieved by setting the grating's angle of incidence with respect to the incoming signal. When photon pairs of conjugate VHGs located on Alice's and Bob's modules were successfully identified and measured, the coincident count rate was further increased by varying the crystal's temperature. The spectral and bandwidth of the VHG reflected spectra are depicted in Fig. 4.23, while the signal photon's FWHM is ~ 0.12nm (Alice) and the idler's FWHM is $\sim 0.24\,\text{nm}$ (Bob). The list of the wavelength channel's respective CWL and the mode spacings are given in Tab. 4.3. Prior to the polarization analysis, the signal and idler modes were multiplexed into in total two pairs of wavelength channels, namely λ_s^1 & λ_i^1(Channel 1) and λ_s^2 & λ_i^2 (Channel 2). In this way, they effectively shared two maximally entangled Bell states $|\psi_1^-\rangle$ and $|\psi_2^-\rangle$ in each channel, respectively, and secure key rates could be independently established.

#Color Channel	Wavelength[nm]	Mode spacing[GHz]
λ_s^1	798.80 ± 0.19	235 ± 42.4
λ_s^2	799.32 ± 0.19	-
λ_i^1	821.31 ± 0.19	239 ± 44.5
λ_i^2	820.77 ± 0.19	-

Table 4.3: A list of channel wavelengths and respective mode spacings is shown. The center wavelength of the signal (Alice) and idler (Bob) mode spectra were chosen depending on the properties of the dichroic mirror and concluding the high spectral brightness B_λ. The wavelengths were recorded with a near-IR single-photon spectrometer, with the resolution for this spectrometer being approximately 0.19 nm. The mode spacings indicated the spacings between two color channels per user, hence between λ_s^1 and λ_s^2 and between λ_i^1 and λ_i^2.

4.6.4 Results

Choice of pump power

In order to increase the degree of improvement of the wavelength-multiplexing QKD scheme with respect to common QKD implementations, the desired regime of operation had to be close to the optimal value of the system's mean photon pair number $\mu = Bt_c$. In this photon number regime, the finite timing resolution with respect to the photon-pair source's brightness increases the probability of identifying uncorrelated photon pairs. In other words, a close-to-optimal μ_{opt} determines the optimal secure key rate for a given system. In the regime of small mean photon pair number ($\mu << 1$), on one hand, the probability of identifying uncorrelated photon pair clicks as coincidences are small. However, the mere number of transmitted photons pairs and hence to secure key rate is low, too. On the other hand, for a high mean photon pair number ($\mu >> 1$), the accidental coincidences' contribution on the measurement effectively increases the system's QBER to a point (11% and higher [201]), where no secure key rate can be established. Hence, for a real-scenario QKD system, a trade-off has to be made between the two-photon pair number regimes.

In Fig. 4.24 (a), the estimated key rate over the mean photon pair number μ is shown. The data points (red crosses) were calculated with the recorded polarization measurements in one wavelength channel for different pump powers and finally inserted in the key rate formula in Eq. 4.12. The polarization measurements consisted of coincidence measurements in HV and DA basis, hence measuring the visibilities in the respective basis, resulting in Q_b and Q_p. Fig. 4.24 (b) depicts the visibility measured in two mutually unbiased bases (HV and DA) while scanning the mean photon pair number μ. Also here, the coincident timing window t_c was kept constant and the laser pump power was changed. The systematic visibility $\mathcal{V}_{sys}^{CH1}$ indicated the contribution to the visibility by, e.g., non-ideal optical elements, which was measured with low pump power (0.94 mW), where the impact of the SPDC's higher-order emission on the system was negligible. Similar to the loss calculation in section 3.3.2, the loss settings (in all following presented measurement results) were estimated by coincident measurements via $\eta_\mathrm{A} = \frac{\mathcal{C}_c}{\mathcal{C}_B}$ and $\eta_\mathrm{B} = \frac{\mathcal{C}_c}{\mathcal{C}_A}$ (using Eqs. A1 and A4), where the dark counts $\Delta_{A,B}$ were measured in a separate measurement and under the assumption of low accidental coincident counts $\mathcal{C}_{acc}$. Subsequently, the mean photon-pair number μ emitted by the source per coincident timing window t_C for each pump power was estimated via $\mu = Bt_c = \frac{\mathcal{C}_c}{\eta_A \eta_B} t_c$. Importantly, the loss settings, as well as the brightness values, were calculated on both HV and DA basis, separately, followed by using the mean value for the final values.

As introduced in section 4.4, a theoretical model (red straight line) was derived to understand the

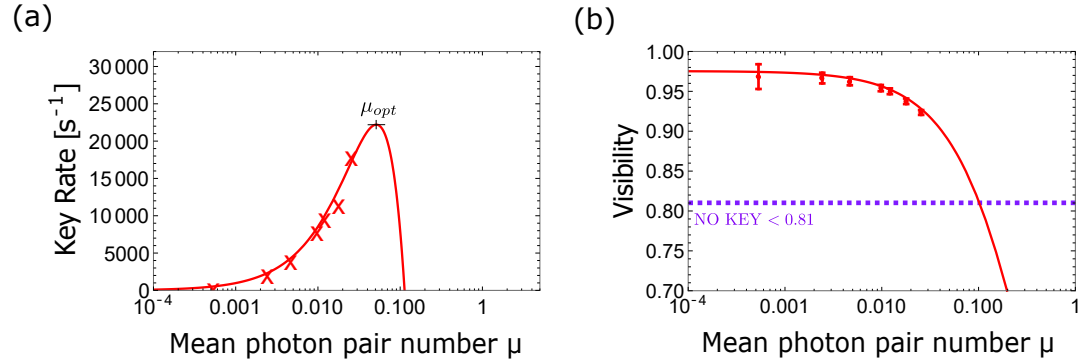

Figure 4.24: (a) The secure key rate over the mean photon pair rate μ for one wavelength channel of the presented QKD system is shown. The recorded measurement results (red crosses) were obtained via polarization measurements with varying laser pump powers in two mutually unbiased bases, namely HV and DA basis. The theoretical model (red straight line) deviates due to the assumption of a fixed symmetrical link loss. The optimal mean photon pair number was calculated to be $\mu_{opt} = 0.0511$. (b) The visibility obtained by polarization measurements decreased with increasing mean photon pair number $\mu = Bt_c$ due to higher-order SPDC emission. The systematic visibility $\mathcal{V}_{sys}^{CH1}$ was measured with low pump power, while a contribution of uncorrelated photon pairs was assumed to be insignificant. For the visibility's errors, a Poissonian distribution of the coincident count rates was assumed, and Gaussian error propagation was used.

system's behavior for different μ and to predict the optimal photon pair number μ_{opt} in terms of the secure key rate. As predicted from the model, increasing μ (here, increasing the laser diode's output pump power) increases the system's key rate to the point, where the probability of falsely identifying uncorrelated photon pairs as coincident counts becomes significant. This effect is indicated by a steep drop in the secure key rate. According to the theoretical model, the optimal photon pair number was calculated to be $\mu_{opt} = 0.0513$ at this specific link loss setting. Importantly, μ_{opt} deviates with different link loss settings, while theory predicts a decrease of $\mu_{opt} = \mu_{opt}(\eta_A\eta_B)$ with increasing link loss, with $\eta_{A,B}$ being the photon's total transmission loss from the source up until the photon was recorded. In a real-life QKD scenario, a link budget is estimated prior to the measurements, and the mean photon pair number μ is optimized for a given link loss setting. The secure key rate over the total link loss, which will be shown below, will differ for deviating μ_{opt}, as discussed in Ref. [198]. In the presented case, due to the given maximum available laser pump power, μ_{opt} was never reached for any link loss setting.

The measurements were performed by both end-users, Alice and Bob, performing polarization measurements with different pump powers, starting with 0.94 mW ($\mu = 0.000525$) up to the maximum available pump power 50.30 mW ($\mu = 0.0257$). The choice of the pump power for the final measurements was based on these results, hence, the maximum available power was used. For ultimately comparing the wavelength-multiplexed scenario with a non-wavelength-resolved system, a photon pair number closer to the optimal value would be advantageous. This is due to the fact, that the difference in secure key rates becomes apparent with mean photon pair number greater than μ_{opt}, which experiences a steep decrease in key rate [see Fig. 4.24 (a)].

As discussed in section 4.4, in the theoretical model certain assumptions were made and restrictions were inherent. This results in deviations of the theoretically derived model to the measured key as can be seen in Fig. 4.24. Assumptions were made such as symmetrical photon loss, as well as an overall estimated dark count probability per user. Due to the use of two different detectors

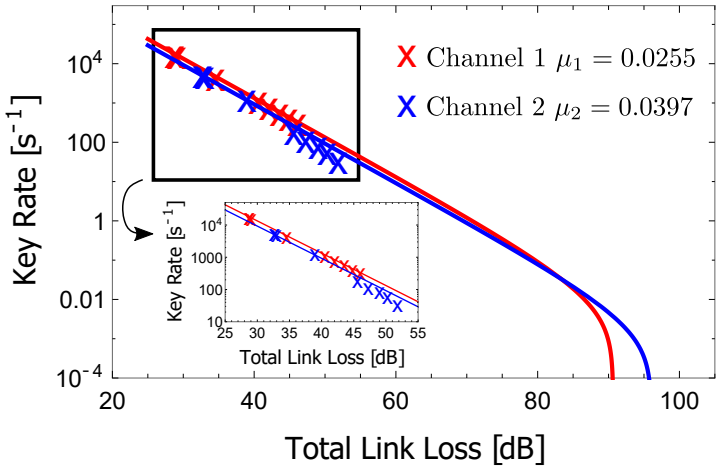

Figure 4.25: The measured and theoretically predicted estimation of secure key rates for wavelength channels 1&2 are shown. Due to low photon number statistics, the measurements (crosses) were conducted from a total link loss of $\sim 29-52$ dB. The theoretical prediction is indicated by the straight lines, where the theoretical model presented in section 4.4 was used. The inset gives a better insight into the channel's secure key rate performance in the recorded low-loss regime.

per user, a mean value was used[7]. Note that the brightness and link losses were calculated via the experimentally measured coincident count rates and the single count rates, while the dark counts were subtracted to minimize the false coincidence probability (see Appendix A1). This resulted in slightly different values of the link losses for different pump powers. A more sophisticated model requires the consideration of different link loss values for varying pump powers.

Key rate over loss

As discussed above, the maximum pump power of 50.3 mW was used in order to obtain the measurement results, which are presented in the following section. The case in which Alice and Bob treat each wavelength channel separately, is analyzed. In this way, they effectively share two Bell states $|\psi_1^-\rangle$ and $|\psi_2^-\rangle$ representing both channels, respectively. From the obtained coincidence data (shown in Table 4.4), the communication partners can then extract two keys that can be added to obtain the overall key in this configuration. The extracted key rates of the individual channels for different attenuation levels are presented in Fig. 4.25. The total link loss, which describes the loss experienced by the photon pairs along their propagation path to Alice and Bob ($\eta_{tot} = \eta_A \eta_B$), was introduced with a graduated neutral-density filter (see Fig. 4.14), which was moved between the measurement sessions via a motorized translation (for more information see section 4.5.1).

From the results can be deduced, that channel 1 exhibits a higher secret key performance than channel 2 in the low-loss regime from $29 - 52$ dB (see inset of Fig. 4.25). However, the latter proved to be more resilient against high losses, hence, contrary to channel 1, from channel 2 a greater-than-zero key was extracted at a total link loss > 90 dB. Note that the maximum

[7] In the theoretical model, a symmetrical loss of 28.76 dB was assumed, estimated from measurement results obtained with a pump power of 50.3 mW. The dark counts per second were measured while blocking the pump laser, which were $\Delta_A^{CH1} = 2100.51\, s^{-1}$ for a mean value for Alice and $\Delta_B^{CH1} = 107.21\, s^{-1}$ for Bob. Finally, the remaining parameters were chosen such that $q = 1$ [198], $f = 1.1$ [200] and $\mathcal{V}_{sys}^{CH1} = (98.62\% + 96.47\%)/2 = 97.55\% \pm 2.60\%$.

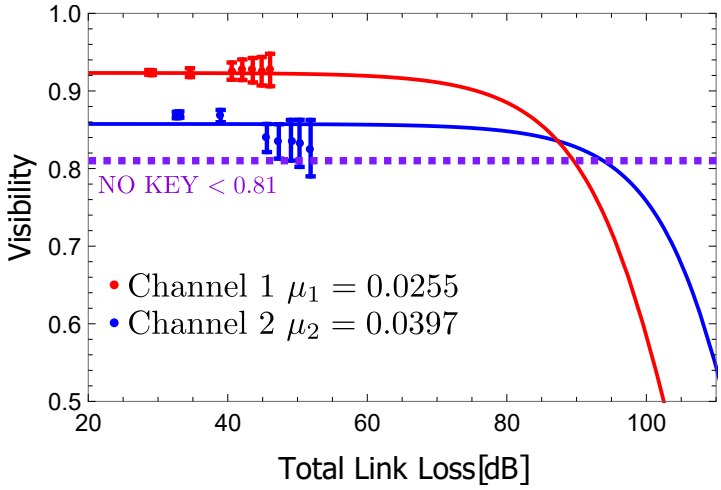

Figure 4.26: The overall measured and theoretically predicted visibility $\mathcal{V}_{final} = \mathcal{V}_{acc} \times \mathcal{V}_{sys}$ while scanning the total attenuation in both photon paths is shown. Wavelength channel 2 (blue dots) underperforms channel 1 (red dots) with respect to the visibility measured in HV and DA basis due to imperfect polarization compensation (see text). The error bars correspond to the Poissonian distribution of the coincident counts, and Gaussian error propagation to ultimately calculate the visibility's error was performed.

measured total link loss was $\sim 52\,\mathrm{dB}$ due to the low photon number statistics in that regime (see crosses in Fig. 4.25). The theoretical prediction is indicated by the straight lines, using a theoretical model introduced in section 4.4. The governing parameter for a high-loss resilience in a QKD system is the mean photon pair number μ with respect to the dark count probability (signal-to-noise ratio). The reason for this is that a finite number of dark counts induce a non-vanishing number of accidental coincidenct counts, effectively decreasing the key rate [210].

Due to the higher dark count rates in channel 1 ($\Delta_A^{CH1} = 2100.51\,s^{-1}$ & $\Delta_B^{CH1} = 107.21\,s^{-1}$) with respect to channel 2 ($\Delta_A^{CH2} = 482.82\,s^{-1}$ & $\Delta_B^{CH2} = 106.29\,s^{-1}$) with roughly equal photon number at the detectors, the secure key performance channel 2 was higher in the high-loss regime. In fact, the higher mean photon pair number in channel 2 ($\mu_2 = 0.0397$) compared to channel 1 ($\mu_1 = 0.0255$) would normally result in a higher key rate also for lower total link loss. However, the difference in key rates was owed to the respective systematic visibilities ($\mathcal{V}_{sys}^{CH1} = 97.55\% \pm 1.55\%$ & $\mathcal{V}_{sys}^{CH2} = 92.60\% \pm 2.59\%$), or in other words, the degree of entanglement in the respective channel. Note that the systematic visibilities were calculated by the mean value of the measured visibilities in HV and DA basis, and contributed to the overall system's visibility via $\mathcal{V}_{final} = \mathcal{V}_{acc} \times \mathcal{V}_{sys}$. Hence, this value gives a lower bound of the measured quantum state's fidelity $F(\rho, |\Psi^-\rangle)$ (section 2.1.2 for details). The overall visibility $\mathcal{V}_{final}$ for both wavelength channels over the total link loss is shown in Fig. 4.26. Here, the impact of the systematic visibility $\mathcal{V}_{sys}$ can be observed, as it dictates the maximum obtainable visibility, even at low losses ($< 25\,\mathrm{dB}$). Again, due to the different dark count probabilities in the wavelength channels, the visibility in channel 2 deteriorated at higher loss settings compared to channel 1, similar to the key rate. The steep decrease in visibility around 85 dB (channel 1) and 100 dB (channel 2), which could also be observed in the key rate, was attributed to the accidental coincidences' contribution on the visibility due to higher-order SPDC emission (see discussion in section 2.2.4). Moreover, the difference in the degree of entanglement, and hence the difference in the wavelength

channel's visibilities was clearly visible.

The visibility in channel 1, for which the quantum state $|\psi_1^-\rangle$ was optimized via the in-fiber polarization controllers and by manipulating the pump polarization state with the $QHQH$-system prior to the Sagnac loop (see section 4.5.4), was measured to be higher compared to channel 2. This is due to the fact, that the alignment of the fiber birefringence for different wavelengths could not be done arbitrarily for all channels simultaneously, as observed also by Wengerowsky [57]. The zero-order half-wave plate's performance, which defined the polarization analysis setting in the detection module, highly depended on the wavelength, which had to be addressed while compensating, for each wavelength independently. This resulted in a drop in visibility in DA basis in channel 2 over the scanned total link loss, namely from $\sim 84.96\% \pm 0.50\%$ to $\sim 81.78\% \pm 4.43\%$. However, in HV basis the decrease in visibility was measured to be from $\sim 89.0\% \pm 0.45\%$ to $\sim 83.5\% \pm 4.21\%$. This drop resulted in the non-perfect agreement with the theoretical prediction (see straight lines in Fig. 4.25 and 4.26), as the theoretical model required the systematic visibility $\mathcal{V}_{sys}$ to be a single input parameter. Comparing to channel 1, the visibility was rather constant for all attenuation losses, namely $\sim 92.6\%$ ($\pm 0.28\%$ for the lowest loss and $\pm 2.14\%$ for the highest loss) in HV basis and $\sim 92.5\%$ ($\pm 0.30\%$ for the lowest loss and $\pm 2.04\%$ for the highest loss) in DA basis. A way of polarization compensation for each wavelength channel was chosen by implementing an additional QHQ-system on Bob's detection module (see discussion in section 4.5.4). Although the visibility in DA basis was increased significantly ($< 70\%$ prior to the alignment), it still underperformed with respect to channel 1. Moreover, with increasing link loss accompanied by low photon number statistics, the alignment of channel 2 was aggravated, as for every measurement setting, that visibility in channel 1 was optimized once more, resulting in turn in a decrease in visibility in channel 2. The decrease in both bases can be explained by the not proper polarization alignment between the measurement session, as both the pump's polarization state was altered by the $QHQH$-system, as well as the polarization paddles were rotated, while optimizing the state in channel 1. This significantly altered the state measured in channel 2 (especially between the measurements at the total link losses 33 and 39 dB), and the initial polarization compensation techniques (see section 4.5.4) had to be repeated.

Also observed by Wengerowsky [57], another possible explanation for deteriorating visibility in different wavelength channels, was given by the possible fact, that the quantum state produced in the source, was unequal for differing wavelengths. Due to the sufficiently high visibility ($> 81\%$), as still a greater-than-zero secure key could be extracted, a more detailed observation was not conducted. An additional implementation of an achromatic QHQ-system on Alice's channel 2 polarization module and achromatic half-wave plates for the basis settings could minimize the difference in visibility.

The coincidence measurements to obtain Q_b in HV basis and Q_p in DA basis (see Table 4.4) to finally estimate the system's secure key rate were conducted as discussed in section 4.5.4, where the HWP's angles in the polarization analysis modules for Alice and Bob, respectively, were chosen to be $\theta_A = 0^\circ$ & $\theta_B = 0^\circ$ and $\theta_A = 45^\circ$ & $\theta_B = 0^\circ$ in HV basis and $\theta_A = 22.5^\circ$ & $\theta_B = 22.5^\circ$ and $\theta_A = 67.5^\circ$ & $\theta_B = 22.5^\circ$ in DA basis. The integration time was chosen to be 0.5 s and one measurement session lasted for 50 s. The data acquisition was conducted by processing the timestamps via a C++ software recorded by the TTM, which was fed by the detectors TTL-signal upon photon impinging. The resulting singles and coincident count rates were guided via an Ethernet cable to a PC, which showed the count rates in real-time in the interface panel. Finally, the experimental data were analyzed and quantified in the *Wolfram Mathematica* software. To sum up, with the implemented multiplexed QKD system, it was possible to suc-

Loss setting	#Channel	Basis setting	Coincidences	Singles Alice	Singles Bob
28.78dB	1	HH&DD HV&DA	646&681 17072&16520	374345	583116
32.71dB	2	HH&DD HV&DA	590&823 9974&10127	408589	496652
28.80dB	1	HH&DD HV&DA	643&679 17084&16432	374477	582502
32.73dB	2	HH&DD HV&DA	585&819 9977&10032	407271	494626
29.12dB	1	HH&DD HV&DA	597&633 15777&15209	361230	554157
33.05dB	2	HH&DD HV&DA	539&753 9185&9307	393398	470400
34.58dB	1	HH&DD HV&DA	170&177 4457&4304	191978	295215
38.98dB	2	HH&DD HV&DA	148&205 2481&2503	208306	249270
40.56dB	1	HH&DD HV&DA	44&42 1136&1101	98039	152598
45.61dB	2	HH&DD HV&DA	50&53 599&597	105055	128091
42.08dB	1	HH&DD HV&DA	29&28 786&761	80701	127285
47.32dB	2	HH&DD HV&DA	36&37 409&409	86759	106718
43.59dB	1	HH&DD HV&DA	21&20 558&543	68733	108063
49.06dB	2	HH&DD HV&DA	24&26 285&283	73066	90744
44.86dB	1	HH&DD HV&DA	16&15 418&408	59751	94318
50.29dB	2	HH&DD HV&DA	18&20 217&214	63705	79009
46.07dB	1	HH&DD HV&DA	12&10 313&305	51900	81358
51.88dB	2	HH&DD HV&DA	14&15 156&153	54502	68097

Table 4.4: The raw coincident and single count rates recorded in the polarization analysis modules for both wavelength channels (channel 1 and channel 2) with different total link losses are depicted. The measurement time was 50 s and the integration was 0.5 s, with the coincident timing window being $t_c = 987.09$ ps. The single count rates were roughly equal in both bases and basis settings as well, hence solely the mean number is shown.

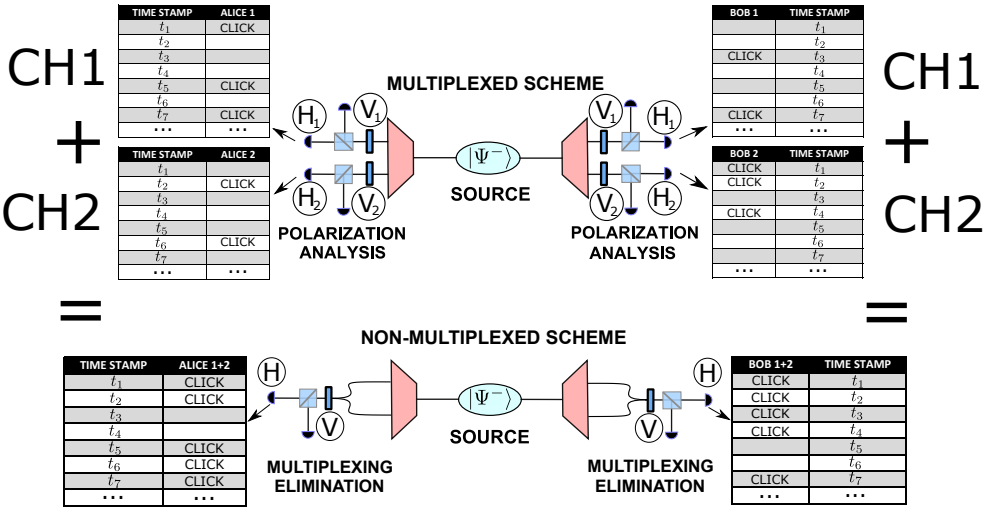

Figure 4.27: In order to compare the multiplexed scenario with the non-multiplexed scenario, where the wavelengths are jointly measured, the photon count lists recorded by the detection system were merged. The lists of count rates recorded in the polarization analysis modules in the respective wavelength channels (multiplexed scheme) were combined such that two lists resulted in a single list containing the elements of the previous lists, including the respective timestamps. This was done by bringing together equal PBS output detectors (H_1&H_2 and V_1&V_2) of the different wavelength channels effectively to a singles count list.

cessfully give an estimation of secret key rates for two wavelength channels, with the fidelities being $F_{CH1}(\rho, |\Psi^-\rangle) = 92.39\% \pm 0.29\%$ & $F_{CH2}(\rho, |\Psi^-\rangle) = 86.89\% \pm 0.39\%$ for the lowest link loss and $F_{CH1}(\rho, |\Psi^-\rangle) = 92.70\% \pm 2.09\%$ & $F_{CH2}(\rho, |\Psi^-\rangle) = 82.63\% \pm 3.63\%$ for the highest link loss.

Comparison to the non-multiplexed scenario

The advantage of the spectral multiplexing of the quantum signal in terms of the system's secure key rate performance compared to non-multiplexing QKD systems shall be outlined in the following. The multiplexed case will be compared with the scenario, in which both wavelengths were jointly measured with only one polarization analyzer at Alice and Bob's sides. The joint-measurement case was implemented in a post-processing fashion, which provided the best comparability between the two cases as systematic differences due to changes in the experimental setup were avoided. The count rates of the respective channels were effectively merged to half of the number of detectors, mimicking the scenario, where the multiplexed separation of the quantum signal was eliminated (see Fig. 4.27). In other words, by merging the recorded data of the corresponding detectors, the wavelength information was erased and the desired case, where no multiplexing was used, was obtained. This effectively eliminated the (anti-)correlations in frequency and changed the state from Eq. 4.26 to:

$$|\psi^-\rangle_{\text{NO WM}} = \frac{1}{\sqrt{2}}(\left|H_{\lambda_s^+}V_{\lambda_i^-}\right\rangle - \left|V_{\lambda_s^+}H_{\lambda_i^-}\right\rangle). \tag{4.27}$$

The multiplexing procedure, which resolved the quantum signal in the spectral degree of freedom by filtering the photon pair's spectrum, was eliminated by effectively "merging" the detector's

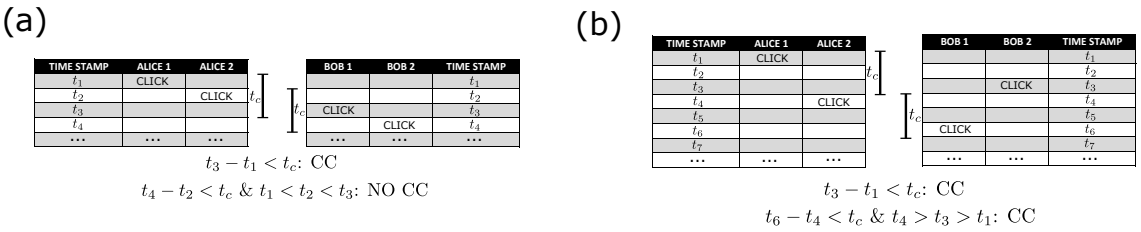

Figure 4.28: Two effects, which occur during the identification of coincident counts of two merged detector lists, are outlined. (a) Although two coincident counts were identified in the multiplexed case, in the non-multiplexed scenario, there exists a finite probability that the pairs, which overlap with respect to their coincident timing windows t_c, are only identified as one photon pair (instead of two in the wavelength-resolved case). The conditions for this specific effect to occur, the relationships of the timestamps and coincident timing window t_c as stated in the picture have to be fulfilled. (b) Due to the high number of photons in the single count rates, falsely identifying uncorrelated photon pairs can occur and lead to an increase of accidental coincident counts, given the conditions as depicted.

count rates. The "merging" technique performed in post-processing is outlined in Fig. 4.27, where the detector's lists of photon counts, which were recorded by the TTM fed by the APD's TTL signals upon photon-impinging, were brought together in a way that the counts, together with the respective timestamps, are shown. In this case, the detector's lists of the two wavelength channels of the same PBS's output ports were merged, such that as a result, one single list was formed. In Fig. 4.27, the resulting detector lists in the non-multiplexed scheme were shown by merging the wavelength channel's $H-$ outputs of the polarization analysis modules. Afterwards, identifying coincident counts were conducted equally compared to the multiplexed case, namely by assigning pairs of counts within the coincident timing window t_c to each other and by writing these coincident events in a separate list. Hence, the wavelength-resolved identification of coincident counts was eliminated, as assigning photon counts as pairs to each other occurred independently of the respective wavelength correlations. As a result, the probability of identifying uncorrelated photon pairs as coincidences increased, which would negatively affect the secure key rate, as will be discussed below.

The resulting detector's lists are shown in Table 4.5. As compared to Table 4.4, which depicts the wavelength-resolved count rates, the single count rates are the sum of the channel's single count rates[8]. However, the coincident count rates decreased. This can be explained by the fact, that close coincident counts in the time regime, which were resolved in the multiplexed-case, are neglected [see Fig. 4.28 (a)]. This effect occurs, when the initially identified coincident counts overlap in their respective coincident timing window, as outlined in Fig. 4.28 (a). As mentioned above, due to the higher counts rates in the resulting lists, the probability of falsely identifying photon pairs as coincidences increased [see Fig. 4.28 (b)]. Note that the loss settings were calculated equally to the multiplexed case, hence not being the mean value of the two channel's loss settings.

[8]The probability of two merged count rate lists containing two elements in one and the same timestamp was negligible, as could be comprehended by the comparison of the maximum single count rate ($\sim 6 \times 10^5$ Hz) to the TTM's clock cycle $\sim$ 12 GHz. Therefore, the assumption of taking the sum of the single count rates, even by avoiding simultaneous clicks (within $\sim 1/12$ GHz$\approx$ 82 ps), was justified.

Loss setting	Basis setting	Coincidences	Singles Alice	Singles Bob
31.81dB	HH&DD HV&DA	1854&2327 22746&23714	782934	1079767
31.84dB	HH&DD HV&DA	1857&2298 22731&23563	781748	1077128
32.10dB	HH&DD HV&DA	1701&2134 21061&21914	754628	1024557
37.39dB	HH&DD HV&DA	487&606 6114&6293	400284	544486
43.07dB	HH&DD HV&DA	126&159 1629&1650	203094	280689
44.62dB	HH&DD HV&DA	88&109 1136&1139	167462	234003
46.10dB	HH&DD HV&DA	63&79 812&808	141800	198808
47.20dB	HH&DD HV&DA	47&61 625&617	123457	173327
48.55dB	HH&DD HV&DA	35&44 460&455	106402	149456

Table 4.5: The raw data of the non-multiplexed scenario comprising the coincident and single count rates of the system is shown. While the single count rates are equal to the sum compared to the multiplexed case (see Table 4.4), the coincident count rates are lower. Note that the measurement time was chosen to be 50 s, the integration time was 0.5 s, and the coincident timing window was $t_c = 987.09$ ps, too.

In the following, the secure key rates of the multiplexed compared to the non-multiplexed case are analyzed. In Fig. 4.29, the obtained secure key rates of wavelengths channels 1 & 2, the "merged" channels and also the theoretical predictions are depicted. Also here, the secure key rates were calculated based on the measured coincident counts of the corresponding detectors at Alice and Bob's sides (see section 4.4). In particular, the overall key rate achieved from the two multiplexed channel pairs will be compared with the case in which the multiplexing system was removed.

In fact, the jointly measured case yielded worse key rates compared to the ones of one single multiplexed channel, namely for channel 1, for all attenuation levels even though the coincident count rates were higher. With respect to channel 2 however, the secret key performance was better, which was mainly caused by the low systematic visibility $\mathcal{V}_{sys}^{CH2} = 92.60\% \pm 2.59\%$ of channel 2 compared to the non-multiplexed case $\mathcal{V}_{sys}^{\text{NO WM}} = 95.87\% \pm 0.92\%$, which was also measured at a low pump power, namely 0.94 mW. For high losses however, the non-multiplexed case deteriorated the strongest, due to the respectively chosen dark count rates[9] and the resulting inferior signal-to-noise ratio (SNR) compared to the wavelength channels.

The dictating cause for the decrease in key rate was the deteriorating visibility (see Fig. 4.30) or increasing QBER. The reduction of the visibility was due to multi-pair emission and saturation of the detectors which led to accidental coincidences. In this case of the non-multiplexed case, the polarization visibility of $83.49\% \pm 0.25\%$ in the lowest loss setting was obtained, while the

[9] For the dark counts for the non-multiplexed scenario, a mean value of the multiplexed dark count rates were chosen: $\Delta_A^{\text{NO WM}} = (\Delta_A^{CH1} + \Delta_A^{CH2})/2 = 1291.67\, s^{-1}$ and $\Delta_B^{\text{NO WM}} = (\Delta_B^{CH1} + \Delta_B^{CH1})/2 = 106.75\, s^{-1}$.

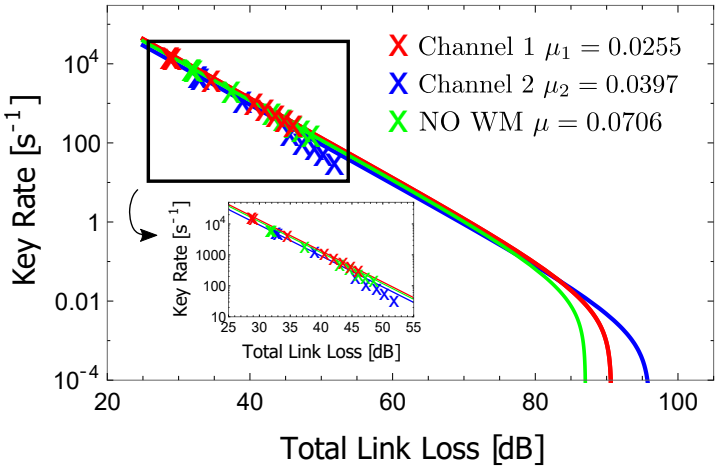

Figure 4.29: The measured (crosses) and theoretically predicted (straight lines) secure key rates over the total link loss of wavelength channels 1 & 2 and the non-multiplexed scenario are shown. While channel 1 outperformed the non-multiplexed system in the low-loss regime (28 dB-52 dB), channel 2 deteriorated due to the low systematic visibility (see text). Due to the dark count probabilities compared to the count rate probabilities, the high-loss regime (> 83 dB) was dominated by the multiplexed system.

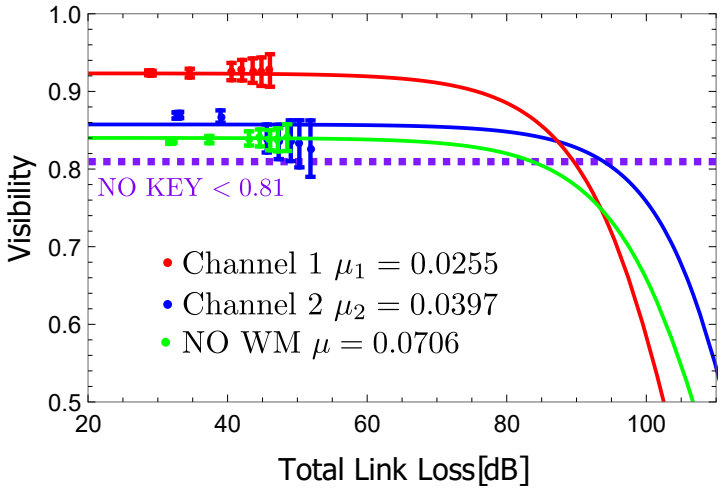

Figure 4.30: The visibility's behavior of the multiplexed and non-multiplexed scenarios over the total link loss is shown. Although the non-multiplexed visibilities became greater than the ones of channel 2, channel 1 exhibited the highest visibility with respect to the measured data points. The error bars correspond to the coincident count rate's Poissonian error, where for the resulting visibility the Gaussian error propagation was conducted.

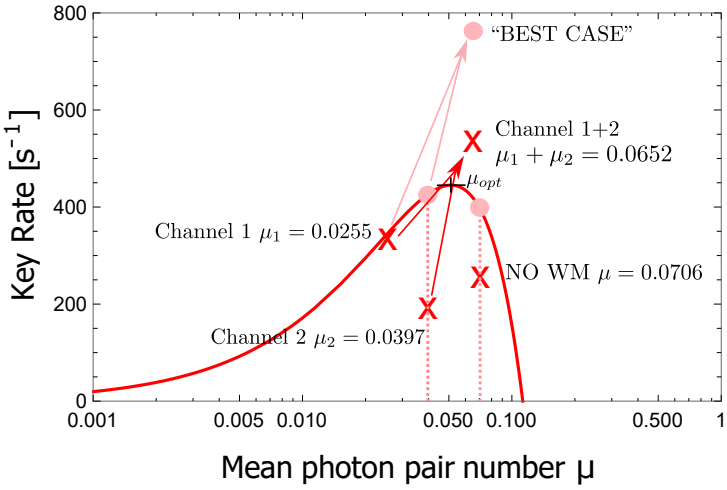

Figure 4.31: The secure key rates over the mean photon pair rate μ for two wavelength channels and the non-multiplexed system of the presented QKD system are shown. The recorded measurement results (red crosses) were obtained via polarization measurements in two mutually unbiased bases, namely HV and DA basis at a fixed loss setting around 46 dB. The improvement of multiplexing the quantum signal in a QKD system yielded a higher key rate $[R(\mu_{1+2}) = 542.60\,s^{-1}]$ compared to the system, which lacked the multiplexing technique $[R(\mu = 0.0706) = 262.89\,s^{-1}]$. The theoretical model (red straight line) deviates due to the assumption of a fixed symmetrical link loss, dark count probabilities, and systematic visibility, which all were chosen with respect to channel 1. The faintly colored dots indicate the obtainable key rates, where the respective systems (channel 2 and non-multiplexed system) performed equal to channel 1 in terms of the above-mentioned experimental parameters. The optimal mean photon pair number was calculated to be $\mu_{opt} = 0.0511$.

visibility remained roughly constant ($84.05\% \pm 1.72\%$ in the highest loss setting) compared to channel 2 ($82.63\% \pm 3.63\%$ in the highest loss setting). Interestingly, at the loss setting of 93 dB, the higher dark counts in channel 1 resulted in a stronger deterioration in visibility with respect to the non-multiplexed case. The dotted line in Fig. 4.30 indicates the minimum amount of visibility to still extract a secure key ($>81\%$).

The secure key rate was affected due to uncorrelated photon pairs contributing to the background of the quantum signal in terms of visibility. Therefore, the discrepancy in visibility between the exploitation and elimination of the frequency correlation lied within the difference in the number of uncorrelated photon pairs compared to the quantum signal recorded in a detector. In other words, the use of bandpass (or interference) filters or narrow-band gratings reduces the number of SPDC photons in a certain frequency band and therefore effectively the μ, as less photons are present within the coincident timing window. Consequently, this decreases the effect of multi-pairs on the visibility in a given system. A way of increasing the mean photon pair number $\mu = Bt_c$ with a fixed wavelength filtering element, either the brightness B (via stronger pump laser power) and/or the coincident timing window t_c can be increased.

The improving effect of multiplexing with respect to the secure key rate is shown schematically in Fig. 4.31. The measured data points are indicated by the red crosses, while the red straight line shows the theoretical prediction. Importantly, the theoretical prediction of the secure key rate over the mean photon pair number μ required a fixed systematic visibility $\mathcal{V}_{sys}$, dark count

probabilities, and loss setting as input parameters[10]. Here, the parameters of the best performing system, namely channel 1, were chosen, which is reflected in a good agreement with the respective data point ($\mu_1 = 0.0255$), which yielded a secure key rate of $R^{CH1}(\mu_1) = 345.64\,s^{-1}$. Due to the specific choice of parameters, the secure key rate of channel 2 [$R(\mu_2 = 0.0397) = 200.11\,s^{-1}$] and the non-multiplexed system [$R(\mu = 0.0706) = 262.89\,s^{-1}$] did not agree with the theoretical prediction. Most importantly, however, the sum of secure key rates of wavelength channel 1 and 2 [$R(\mu_{1+2}) = R(\mu_1) + R(\mu_2) = 542.60\,s^{-1}$] greatly exceeded the scenario where the channels were jointly measured, resulting in an enhancement factor of 2.06. A similar improvement was given, when channel 2 performed equal to channel 1, in terms of dark count probabilities, systematic visibility $\mathcal{V}_{sys}$, and loss setting. This is indicated by the faintly colored dot on the secure key rate function above the measured data point. While the non-multiplexed system would perform better as well [$R^{CH1}(\mu = 0.0706) = 395.61\,s^{-1}$], the two wavelength channels combined ("BEST CASE") would yield $R^{CH1}(\mu_{1+2}) = 771.97\,s^{-1}$, resulting in an enhancement factor of 1.95. The optimum available secure key rate could be obtained by operating the system at $\mu_{opt} = 0.0511$. Two wavelength channels with the above-mentioned parameters of the system would yield $2 \times R^{CH1}(\mu_{opt}) = 890.18\,s^{-1}$, while the non-multiplexed system would yield $R^{CH1}(2\mu_{opt}) = 131.656\,s^{-1}$, resulting in an enhancement factor of 6.76. Therefore, the multiplexing technique inhabits huge potential with respect to the scaling characteristics, which will be in the center of attention in the following section.

In Fig. 4.31, the non-linear behavior of the secure key rate function $R(\mu)$ is clearly visible. It follows, that in the regime of $\mu \sim \mu_{opt}$ the relation $R(\mu_i + \mu_j) \neq R(\mu_i) + R(\mu_j)$ holds, which can be exploited with the multiplexing technique in terms of increasing the key rate effectively. By choosing 2 or more multiplexed channels with the mean photon pair number μ_i per channel such that $\sum_i \mu_i \geqslant \mu_{opt}$, the non-multiplexed case shows worse behavior in terms of the secure key rate. This is due to the fact, that multiplexing the quantum signal mitigates the mean photon number $\sum_i \mu_i$ into i wavelength channels, effectively. In the non-multiplexed scenario however, the QKD system picks up the whole signal with mean photon number $\sum_i \mu_i$, which results in the undesired detection of uncorrelated photon pairs and increase in QBER. On the other hand, choosing the mean photon number such that $\sum_i \mu_i < \mu_{final}$, where the resulting μ_{final} is located on the steep positive-gradient slope of the left-hand side (with respect to μ_{opt}) of the function, the non-multiplexing technique shows advantageous behavior. Hence, the choice of mean photon pair number μ in any QKD system is crucial for the secure key rate performance. Crucially, however, the fact has to be taken into account, that the optimal mean photon pair number deviates for different link losses, as discussed before.

Importantly, the Si avalanche photodiodes themselves are equipped with a certain dead time t_d, which defines the period of time, where they remain in a recovery state, being therefore effectively blind to arriving photons. While merging several detectors to one single detector in post-processing, one has to consider that some events would not be recorded in reality, due to overlapping dead times, respectively. This results in the fact, on one hand, that the effective photon number will decrease, however, on the other hand, the probability of false identification of uncorrelated photon pairs will decrease as well [see merging effect shown in Fig. 4.28 (b)]. Similar to the above-introduced non-multiplexed case, the dead time was considered and the secure key rate was estimated. In Fig. 4.31, the secure key rate performances of the non-multiplexed scenarios, including one considering the dead time, and the sum of channel 1 and 2 are shown. In agreement to prediction in Fig. 4.31, the effective decrease of the mean photon pair number from $\mu = 0.0706$ to $\mu = 0.0615$ led to an increase of the key rate, also with respect to the

[10]The loss setting for the theoretical model was chosen to be 46.07 dB, while the other parameters are shown in the text above.

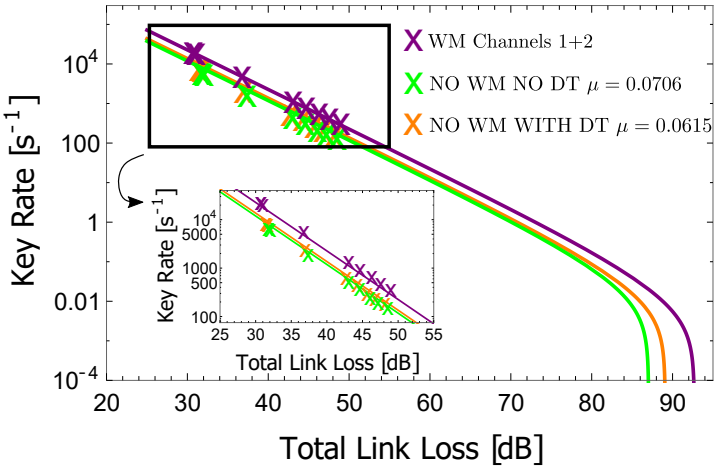

Figure 4.32: The secure key rates over the total link loss for two non-multiplexed scenarios including the consideration of the detector's dead time in the merging process and the combination of channels 1 and 2 are shown. A significant improvement of the multiplexing technique by exploiting the SPDC photon pair's wavelength correlations (WM Channel 1+2) with respect to the non-multiplexing cases can be observed. Considering the single-photon detector's dead times in the count rate list's merging process, the mean photon pair number μ is effectively decreased, which results, in agreement to Fig. 4.31, in an increase of the secure key rate over all link loss settings.

theoretical prediction, given equal parameters in terms of dark counts[11] and systematic visibility $\mathcal{V}_{sys}^{\text{NO WM}} = \mathcal{V}_{sys}^{DT} = 95.87\% \pm 0.92\%$. This can be explained by the effective increase of the visibility being $\mathcal{V}^{DT} = 84.83\% \pm 0.24\%$ and $\mathcal{V}^{DT} = 85.11\% \pm 1.69\%$ for the lowest and highest loss, respectively, compared to $\mathcal{V}^{\text{NO WM}} = 83.49\% \pm 0.25\%$ and $\mathcal{V}^{\text{NO WM}} = 84.05\% \pm 1.72\%$, also for the lowest and highest loss, resulting in a higher key rate despite the lower absolute coincidence count rates.

4.7 Scalability

With the shown proof-of-principle experiment, a demonstration was successfully conducted to show the advantage of WM-featured QKD by considering two wavelength channels on both receiver sides with respect to non-multiplexed QKD. In the following, the scaling potential of the multiplexing technique will be discussed to show that using several channels can unfold the full potential of the presented approach, which results in a significant increase of the attainable secrete key rate from a single SPDC source. In fact, the so-far discarded part of the spectrum can be exploited, allowing for scaling the advantage in the secure key rate [see Fig. 4.33 (a)]. Depending on the bandwidth of the SPDC spectrum as well as the filtering selection width, more than two correlation channels and therefore a number of users respectively can share an entangled photon pair, which was subject to theoretical considerations about 25 years ago [211] and was experimentally implemented in a QKD network numerous times [150–152, 212] as well as other DV-QKD systems [167, 213]. These architectures comprised wave-guides in the form of fibers, which led the quantum signal to the partaking users. Due to great advancements in satellite-

[11] The dark counts were chosen equal to the non-multiplexed case as mentioned in the text: $\Delta_A^{\text{NO WM}} = \Delta_A^{DT} = 1291.67\,s^{-1}$ and $\Delta_B^{\text{NO WM}} = \Delta_B^{DT} = 106.75\,s^{-1}$, where the index DT indicates the non-multiplexing scenario considering a finite dead time during the merging process of the detector's count rate lists.

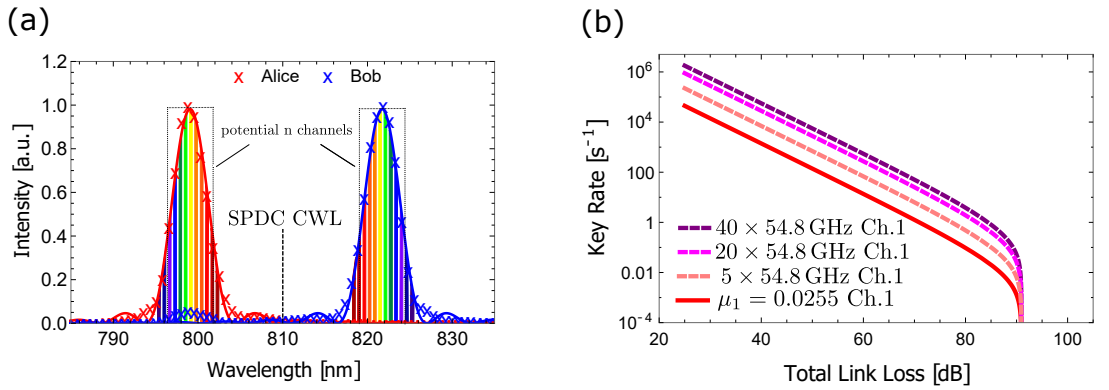

Figure 4.33: The scalability potential of the presented wavelength-multiplexing technique in QKD systems by using more than two channels is illustrated. (a) The colors within the measured signal and idler spectra (crosses) correspond to the pairwise spectral correlations with respect to the central wavelength of the overall SPDC spectrum (CWL∼ 810nm). The spectrum intensities were normalized for simplicity, while the single-photon spectrometer's resolution was approximately 0.19nm. The bar widths were chosen to be ∼ 0.24 nm with a mode spacing of ∼ 0.61 nm, resulting in 12 shown wavelength channels. The solid lines correspond to the theoretically predicted spectrum (see Section 4.5.1). (b) The theoretically estimated secure key rates of channel 1 and additional N channels with $N = 5, 20$ and 40 over the total link loss. As discovered in section 4.6, the system's total obtainable secure key rate equals the sum over all wavelength channel's key rates, hence achieving an improvement of key rate by a factor of 40. The assumed equal setup behavior in each channel results in equal deterioration of key rate at the same link loss setting (∼ 91 dB).

based free-space QKD systems [186,187], which are affected naturally by the same limits as fiber-based systems, novel designs tackling these problems, such as the implementation of the bulk volume holographic gratings, are necessary. In this way too, it is possible to perform wavelength multiplexing into a total number of N channels, which results in an overall transmitted state $|\psi^-\rangle_{\text{tot}} = \prod_i^N \otimes |\psi_i^-\rangle$, where each $|\psi_i^-\rangle$ represents the entangled state in two corresponding wavelength bands (see Eq. 4.25).

The VHG-selected wavelength bands (0.12 nm and 0.24 nm) of the produced SPDC photon pair spectrum (see Fig. 4.23) are significantly smaller than the SPDC spectrum (4.73 nm), and only a small fraction of the SPDC spectrum for the presented QKD experiment was used. The unused (transmitted by the VHG) part of the spectrum can, however, also be utilized for the key generation. Given the respective number of equally narrow VHGs and detection modules as well as the photon pair spectrum used in the experiment, it is possible to select up to $4.73/0.12 \approx 40$ correlated spectral bands from the used SPDC spectrum. The implementation of several wavelength channels to exploit the SPDC spectral correlations is outlined in Fig. 4.33 (a). Here, the wavelength channels are indicted by pair-wise bars, where correlated wavelengths inhabit equal colors. For displaying simplicity, the finite bar widths were chosen equal to ∼ 0.24 nm with a mode spacing of ∼ 0.61 nm, which resulted in 12 wavelength channels.

With the 0.12 nm (54.8 GHz at CWL=810 nm) wavelength-band selection of the VHG as used in the presented experiment, where the implementation of N wavelength channels can be achieved via a stacked arrangement of $2N$ VHGs including subsequent polarization analysis and detection modules of each band, an estimation of obtainable secret key rates of the used system can be conducted. This scaling potential for $N = 5, 20$ and 40 wavelength channels is depicted in Fig. 4.33 (b). For simplicity, it is assumed, that each additionally implemented channel equals in

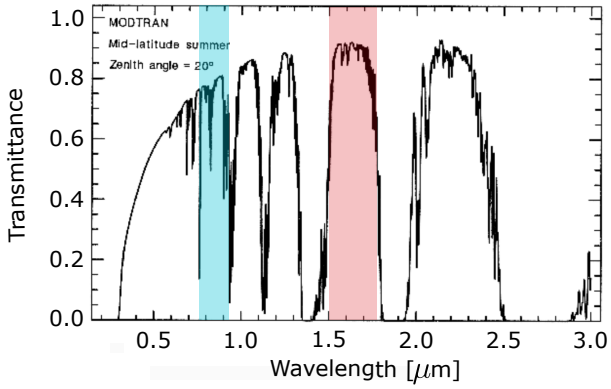

Figure 4.34: The optical transmittance through the atmosphere, measured for vertical propagation from ground to space is shown. The faintly colored areas indicate the wavelength regimes around 800 nm (blue) and 1550 nm (red), which will be discussed in the text. The data is provided by the U.S. Geological Survey (*https : //www.ugpti.org/smartse/research/citations/downloads/Clark − Manual_Spectroscopy_Rocks_Minerals_Book − 1999.pdf*).

performance of the measured wavelength channel 1, with respect to dark count probabilities, systematic visibility, and brightness. Moreover, the spectral shape was assumed to be uniformly rectangular as indicated by the dotted rectangles in Fig. 4.33 (a). As discussed in section 4.6, the overall key rate of N equally performing wavelength channels (yielding each a secure key rate R) increases by a factor of N, hence

$$R_{total}^{WM} = \sum_{k}^{N} R_k = NR, \tag{4.28}$$

which agrees with the findings of Aktas' observation to sum over the coincidence of wavelength-multiplexed SPDC signal [178]. This allows an increase of secure key rate from $R(\mu_1, 25\,\mathrm{dB}) = 44472.4\,s^{-1}$ for one channel to $40 \times R(\mu_1, 25\,\mathrm{dB}) = 1.78 \times 10^6\,s^{-1}$ for 40 channels, while the laser pump power remained constant at 50.3 mW. Importantly, without the multiplexed detection one would saturate the detectors and it would be virtually impossible to generate a key in this scenario. Due to the assumption of equal performance, the theoretical model predicts that all potential channel key rates collapse at the same link loss setting. As mentioned above, the limiting factor in the entanglement-based QKD are the detectors and not the SPDC sources. Conversely, the shown experiment demonstrates that WM allows to fully exploit the whole potential of photon-pair sources both in-fiber and in free space.

Scaling behavior for free-space and in-fiber QKD systems

As stated above, the scaling potential is mainly governed by the bandwidth of the SPDC spectrum and the mode spacing of the implemented WM elements. However, alongside these two driving parameters, the ability to successfully transmit the photon's wavelength distribution unitarily, the future laser and crystal design in terms of sustaining and withstanding high lasing power, and finally the detector's quantum efficiency play an essential role with respect to generating a secure key rate with a high number of wavelength channels, too. Importantly, due to the difference of used technologies, the scaling behavior of both free-space and in-fiber QKD systems will be discussed, separately.

Scalability arguments for free-space long-distance QKD systems can be given by taking the electromagnetic transmission through the atmosphere into consideration (see Fig. 4.34). As discussed in sections 3.3.3 and 3.3.4, atmospheric factors have an impact on the light's transmission from sender to receiver. The atmospheric influence comprises, essentially, scattering, absorption phenomena and refractive index fluctuations (optical turbulence) [214]. While the impact of diffraction-induced beam spreading in the light's transmission was discussed in section 3.3.4, scattering and transmission caused by aerosol and atmospheric molecules will be reviewed in the following. In general, this results in a transmission spectrum, leading to a wavelength dependency of the optical transmittance through the atmosphere. The spectral-dependent transmittance of electromagnetic waves in the (near) IR-regime, measured for vertical propagation from ground to space, is depicted in Fig. 4.34. As driving sources of radiation absorption in the atmosphere are water vapor, CO2, NO2, CO, and ozone [214]. To be precise, the absorption band between the oxygen A-band at 761 nm [215] and the water vapor absorption band at 970 nm [216] greatly influence the radiation transmittance around 800 nm[12] (see faintly blue-colored area in Fig. Fig. 4.34) [219] and have to be taken into account for possible future applications. However, the wavelength bands from $1500 - 1800$ nm (see the faintly red-colored area in Fig. Fig. 4.34) show advantageous transmission behavior, too. In classical optics, as well as quantum optics, the wavelength regime around 1500 nm is a well-known area of expertise, mainly due to the top-notch existing fiber-technology in this wavelength band [174, 220–222]. While the international safety specifications with respect to the allowed output power [223] favor longer wavelengths in free space [220], considering a combination of the effects of the collection and detection efficiency and the effects such as beam divergence and pointing error prefer wavelengths around 800 nm [224][13]. On a side note, the specific weather conditions play a major role in the QKD performance, while 785 nm, 850 nm, and 1550 nm experience equal attenuation while propagating through fog [225]. Recent detector technologies achieved quantum efficiencies for single photons with a wavelength around 1550 nm in the order of 85%. These rather high efficiencies, however, are achieved with superconducting nanowire single-photon detectors (SNSPD) [226]. These bulky devices are disadvantageous for satellite-based implementations due to the necessary fiber-coupling and the fact that a whole SNSPD comprises a closed-cycle cryostat and a helium compressor. Importantly, however, the wavelength selection presented in this thesis via volume holographic grating perform equally well at wavelengths around 1550 nm in terms of narrow-band filtering (~ 0.1 nm) and have a diffraction efficiency ($> 90\%$) [227], hence presenting a possible solution for free-space implementations.

[12] This wavelength regime was the operating quantum signal's wavelength of choice for past long-distance free-space [104] satellite-based [217, 218] QKD implementations.

[13] In Ref. [224], a comparison of the overall link loss was estimated for 1550 nm and 760 nm, respectively, whereby the signal was emitted from the satellite (low earth orbit, with an altitude of 600 km) to the ground station (downlink). While the emitter aperture located on the satellite was assumed to be 0.1 m, the pointing error was assumably 10 μrad. The detection efficiencies were set to be 20% (for the detectors at 1550 nm), and 70% (for the 760 nm wavelength), respectively. Finally, the collection efficiency of the optical system at the receiver was assumed to be 50%.

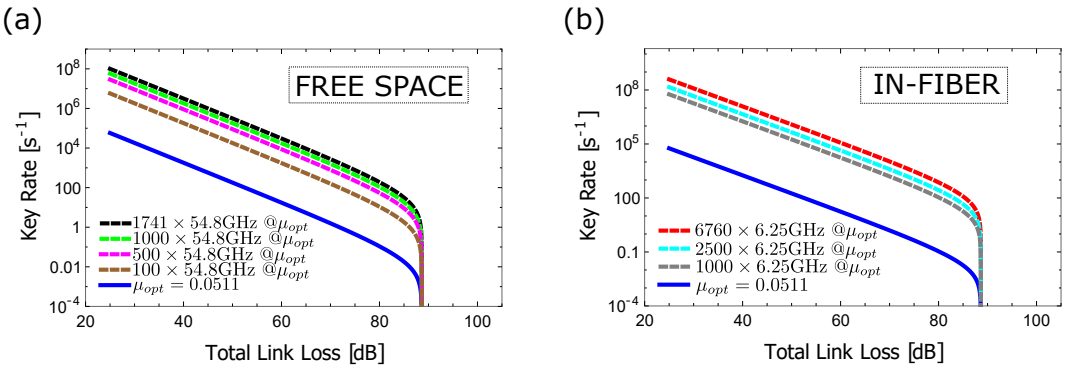

Figure 4.35: The recorded data and the extrapolation to more wavelength channels clearly illustrate the advantage and potential of the proposed QKD scheme, which gives rise to the possibility of boosting the secure key rate by two orders of magnitude using state-of-the-art WM systems. In the lower area of the figure, the brightness was increased, simulating the behavior of recording a signal of wider FWHMs (0.36 and 0.40 nm) and using only one channel, respectively. The lines in both plots correspond to a theoretical model to compare the results to, which is further described in the text. It clearly shows the advantageous behavior of the presented approach of exploiting wavelength correlations for both (a) free-space and (b) fiber implementations to conventional QKD systems also for high losses.

The following estimated secure key rates shall cover a free-space and an in-fiber scalable approach for wavelength-multiplexing in a QKD system. Importantly, the scalability arguments are done within an ideal framework, hence, dispersion, temperature, and atmospheric fluctuations are not considered. Here, the most essential parameters are the photon source's wavelength distribution and the transmission band. Top-notch broad-band entangled photon sources feature broad spectra with widths of 100nm and beyond both around a CWL of 800 nm [228, 229] and 1550 nm [151, 222, 230]. Given an SPDC photon pair wavelength distribution around 380 nm (166 THz) with a central wavelength of 802 nm [228] and the implementation of the same VHGs (bandwidth: 0.12 nm), the absorption band between the oxygen A-band at 761 nm [215] and the water vapor absorption band at 970 nm [216] allows for N=1741 wavelength channels at this wavelength regime [see Fig. 4.35 (a)]. Similar to the estimated key rate shown in Fig. 4.33 (b), the starting point for a single wavelength channel was a performance close to channel 1 in terms of dark count probability and systematic visibility. Now, the mean photon pair number was changed to the optimal value $\mu_{opt} = 0.511$, as shown in Fig. 4.31. This results in an estimated key rate at a low loss setting of $R(\mu_{opt}, 25\,\mathrm{dB}) = 57356.5\,s^{-1}$ for one channel and a maximum of $1741 \times R(\mu_{opt}, 25\,\mathrm{dB}) = 9.99 \times 10^7\,s^{-1}$ for $N = 1741$ channels. Importantly, to achieve the optimal mean photon pair number $\mu_{opt} = Bt_c$, either the brightness B (e.g. by increasing the laser pump power) or the coincident timing window t_c has to be increased. By choosing $t_c \approx 1$ ns, the spectral brightness B_λ of the broad-band SPDC source from Ref. [228] (93023.3 Hz/mW/nm)[14], a laser pump power of ~ 14.9 W would be necessary, which, by equal focal parameters as chosen in this thesis (see section 4.5.1), would result in an intensity of 97 W/cm^2. Note that according to the crystal manufacturer's specifications, laser operation with powers in the order of 10 W and beyond is possible [231].

Today's classical optical communication technology uses ultra-dense-wavelength-division-multiplexing (UDWDM) technology with mode spacings of 6.25 GHz [232]. One of the reportedly

[14]This brightness was calculated from ratio of single to coincident count rates and the laser power as reported. The reported heralding efficiency was 5%, hence due to the coupling difficulties the value of laser pump power represents not a higher bound.

highest generation of 1550 nm photon pairs with respect to the wavelength bandwidth in combination with the spectral brightness can be found in Ref. [230]. The authors report a bandwidth ranging from $1.2 - 2$ μm, with a spectral brightness of $B_\lambda = 38\,\mathrm{MHz/mW/nm}$. By taking a widely deployed telecommunication fiber into consideration, which enables the transmission of 1285 nm (with an attenuation of 0.35 dB/km) up to 1625 nm (with an attenuation of 0.23 dB/km) and the above-mentioned parameters, an implementation of up to $N = 6760$ channels is possible. The estimated secure key rate for $N = 6760$ wavelength channels, with equal assumptions as in Fig. 4.35 (a), is shown in Fig. 4.35 (b). This results in an estimated key rate at a low loss setting of a maximum of $6760 \times R(\mu_{opt}, 25\,\mathrm{dB}) = 3.88 \times 10^8\, s^{-1}$ for $N = 6760$ channels. Due to the higher reported spectral brightness compared to the source with CWL of 802 nm, 36.58 mW is necessary to achieve μ_{opt}. As reported in Ref. [64], a rough and optimistic estimation yields a possible $N = 15000$ wavelength channels, which takes the possibility of the 6.25 GHz mode spacing (UDWDM) and a photon pair source covering the absorption band in air as discussed above in a free-space implementation into account.

Multiplexed scaling behavior compared to probabilistic separation

The increasing photon pair number leads to an increase of uncorrelated photon pairs, where the impact on the visibility and therefore on the secure key rate manifests itself within the accidental coincident counts $\mathcal{C}_{acc}$ to true coincident counts $\mathcal{C}_{pairs}$, which will be shown in the following. As introduced in section 2.2.4 (see Eq. 2.44 and Eq. A3), the accidental coincident counts can be written as $\mathcal{C}_{acc} = t_c \mathcal{C}_A \mathcal{C}_B$, with the coincident timing window t_c and the single count rate $\mathcal{C}_{A,B}$, while the coincidence counts arising from the source take the form $\mathcal{C}_{pairs} = \eta_A \eta_B B$, with brightness B and the link losses $\eta_{A,B}$ (see Eq. A1). Hence, the accidental-to-coincidences ratio can be written as

$$\frac{\mathcal{C}_{acc}}{\mathcal{C}_{pairs}} = \frac{t_c \mathcal{C}_A \mathcal{C}_B}{\eta_A \eta_B B}, \tag{4.29}$$

which, by assuming that no dark counts are present, yields

$$\frac{\mathcal{C}_{acc}}{\mathcal{C}_{pairs}} = B t_c = \mu. \tag{4.30}$$

This result has been subject in the discussions before with respect to the mean photon pair number μ, which clearly gives an indication of the systems performance with respect to the visibility and secure key rate (see Figs. 4.24, 4.26, 4.30 and 4.31).

The deterministic mitigation of the accidental coincident counts is inherent in the improvement of the multiplexing technique. Here, the entangled photon pairs are multiplexed in N wavelength channels, which is not accompanied by a decrease in efficiency due to the intrinsic spectral correlations [229]. As shown above, the system's overall coincident count rate can be summed over all N wavelength channels; equally the accidental coincident counts:

$$\begin{aligned} \mathcal{C}_{pairs}^{WM} &= \sum_i^N \eta_A^i \eta_B^i B^i \\ \mathcal{C}_{acc}^{WM} &= t_c \sum_i^N \mathcal{C}_A^i \mathcal{C}_B^i. \end{aligned} \tag{4.31}$$

Under the ideal-case assumption, that the wavelength channels all perform the same in terms of losses, $\eta^i_{A,B} = \eta_{A,B}$, and that the single count rates are distributed equally, $\mathcal{C}^i_{A,B} = \mathcal{C}_{A,B}/N$, the multiplexed accidental-to-pair ratio yields:

$$\frac{\mathcal{C}^{WM}_{acc}}{\mathcal{C}^{WM}_{pairs}} = \frac{t_c \sum_i^N \mathcal{C}^i_A \mathcal{C}^i_B}{\eta_A \eta_B \sum_i^n B^i} = \frac{t_c \mathcal{C}_A \mathcal{C}_B}{\eta_A \eta_B B N} = \mu/N, \tag{4.32}$$

which clearly demonstrates the advantage of multiplexing in an entanglement-based QKD system, as with increasing channel umber N the accidental-to-pair ratio decreases.

Importantly, other particle's degrees of freedom offer possibilities for multiplexing the quantum signal and show improved QKD performance. Regarding photons, spatial correlation [38] or orbital angular momentum [233] can be exploited for that matter.

Exploiting the whole margin of typical entangled photon-pair sources can be conducted by probabilistically splitting the signal in an array of multiple detectors at the respective detection systems [234, 235]. The probabilistic separation system can be implemented with help of a simple intensity-multiplexing device (i.e. multi-mode splitter such as a beam-splitter or N-port devices [236]). This method tackles the saturation problem of the detector system, however, the multi-pair emission along the probabilistic nature of the separation of the signal will influence the system's visibility differently compared to the multiplexed (systematic) approach. While the detectors single count rates are equally split with respect to the total count rate, similar to the multiplexed case via $\mathcal{C}^i_{A,B} = \mathcal{C}_{A,B}/N$, the probabilistic splitting results in an effective loss in each channel, hence $\eta^i_{A,B} = \eta_{A,B}/N$. This results in the following accidental-to-coincidences ratio for the probabilistic splitting of the quantum signal:

$$\frac{\mathcal{C}^{prob}_{acc}}{\mathcal{C}^{prob}_{pairs}} = \frac{t_c \sum_i^N \mathcal{C}^i_A \mathcal{C}^i_B}{\eta_A/N \eta_B/N \sum_i^N B^i} = \frac{N t_c \mathcal{C}_A \mathcal{C}_B}{\eta_A \eta_B B} = \mu N. \tag{4.33}$$

Specifically, in a regime where the pump power of the SPDC starts to saturate the detectors in time (hence, the timing resolution overlap), the multiplexing scheme helps to reduce the counts per channel and reduces the accidental coincidences, and thus reduces the QBER. The probabilistic separation (Eq. 4.33) exhibits inferior scaling behavior with respect to the deterministic splitting (Eq. 4.32) of the signal, mainly because it is not possible to assign the correlated detection events with each other. Therefore, probabilistic multiplexing does not solve the problem of saturation in time. The scaling behavior of intensity-splitting systems experiences a threshold depending on the pair rate, whereas the one for multiplexing is ultimately limited only by experimental and technical factors such as wavelength-channel width and source spectra.

4.8 Conclusion and outlook

In conclusion, a wavelength multiplexing (WM) strategy for enhancing the secret key rate as well as the loss resistance between two communication partners performing QKD was implemented. Furthermore, it was shown that this approach entails strong scaling potential for both in-fiber and free-space applications. The presented approach leverages the deterministic separation of wavelength bands from the SPDC spectra, with which it is possible to select the correlated wavelength components of the signal and idler beams. In this way, it was shown that it is possible to overcome the detection limit in QKD and thus to fully make use of SPDC sources. Importantly, the proposed architecture of the QKD system requires only adjustments at the

photon-detection stages while no modifications at the entangled photon-pair source are needed. Here, the source provider ensures to send photon pairs equipped with a broad spectrum, as the parties sharing a secret key only have to implement respective gratings and detection systems on their respective sites.

In this thesis, a proof-of-principle realization of a bulk WM system for QKD setups to increase the secure key rate depending on the channels was presented. It was shown, that by performing QKD measurements with conventional methods, namely by the probabilistic nature of the signal separation via intensity-splitting, the multi-pair emission decreases the visibility depending on the photon pair rate and the loss/distance between the users compared to the presented technique. The shown results clearly show the advantages of this novel technique in terms of the scaling characteristics by exploiting additional wavelength channels. The driving factors besides the mitigation of uncorrelated photon pairs in the detection system are the possibility of implementing N additional channels as the bandwidth of the source as well as the wavelength selection method dictates how many wavelength channels can be used. Hence, the advancement in detectors technology both in broad-band quantum efficiencies and N-port array implementations for a high number of wavelength channels shall push the key rate limit to higher rates.

Furthermore, the setup is capable to cope with the detrimental influences of atmospheric turbulence. In particular, the acceptance angle of incidence of the holographic grating is larger than the angle-of-arrival fluctuations in long-distance experiments due to atmospheric turbulence. While the used VHGs have acceptance angles in the order of 900 μrad, a typical 10km horizontal link, which undergoes similar conditions compared to a vertical satellite-based low orbit (500km) down-link, has typical AoA fluctuations around a maximum of 10 μrad [237], allowing a realistic magnification of $M \sim 90$. Essentially, the optical magnification sets the ratio between the true size of an image (here, the incoming beam) and its "apparent" size, which propagates through the experimental setup and hence the grating. Note that in order to send and receive broad-band spectra, as presented in section 4.7, the implementation of concave mirrors (see section 3.3.2) is crucial, effectively counter-tackling chromatic aberration. An additional advantage of the proposed technique is that the narrowly filtered detection bands provide a drastically increased ratio between signal and environmental background radiation. For possible implementations over long-distance free-space links including space-suitable silicon single-photon avalanche photodiodes, the requirements for bulk material are met by the presented approach.

Appendix

A1 Derivation of the theoretical error model for secure key rate

The theoretical model for estimating the secure key rate of a given QKD system, will be derivated in the following. The requirements are the comprehension and understanding of the quantum bit error rate's (QBER) behavior with respect to systematic errors and falsely registered coincident counts due to the source's higher-order emissions. This is achieved by describing the coincident detection probability $\mathcal{P}_c$ in simple terms of experimentally available singles and coincident counts rate $\mathcal{C}$ and the influence of the photon-pair source's emission rate μ.

Coincident detection probability

A polarization-entangled photon-pair source emitting with an average rate per second of B, is used for distributing its photons to Alice and Bob, respectively. Alice's and Bob's measurement modules comprise a polarization analysis system, and the photon's transmission losses from source to the occurance of registration event in the detector are indicated by η_A and η_B.

Coincident measurements of correlated photon pairs are obtained by identifying detected photons by Alice and Bob and compare the time of arrival within the coincident window t_c. The source's photon-pair probability $\mathcal{C}_{pairs}t_c$, which solely comprises the "correctly" correlated photon pairs undergoing the total transmission loss $\eta_A\eta_B$, can hence be described as

$$\mathcal{C}_{pairs}t_c = B\eta_A\eta_B t_c. \tag{A1}$$

An additional contribution to the coincident detection probability arises from accidental coincidences $\mathcal{C}_{acc}$ (see section 2.2.4), which occur due to the detector's finite timing resolution resulting in a non-vanishing probability at a certain brightness level of identifying two uncorrelated photon pairs. Therefore, the detection probability not only arises from "correctly correlated" photon pairs, but also accidental coincidences:

$$\mathcal{C}_{max} = \mathcal{C}_{pairs} + \mathcal{C}_{acc}, \tag{A2}$$

where $\mathcal{C}_{max}$ are the coincident counts recorded by the two detectors at maximum polarization settings.

As derived in section 2.2.4, $\mathcal{C}_{acc}$ can be expressed with the single count rates detected by Alice ($\mathcal{C}_A$) and Bob ($\mathcal{C}_B$) as [58]:

$$\mathcal{C}_{acc} = \mathcal{C}_A\mathcal{C}_B t_c. \tag{A3}$$

Here, the single count rates are assumed to be contributed from photon pairs produced in the source and dark counts $\Delta_{A,B}$, while the latter comprise ambient light and counts that occur intrinsically in a detector without any incident light:

$$\mathcal{C}_{A,B} = B\eta_{A,B} + \Delta_{A,B}. \tag{A4}$$

Inserting Eq. A2 into A1 leads to:

$$\mathcal{P}_c = \mathcal{C}_{max} t_c = (B\eta_A\eta_B + \mathcal{C}_{acc}) t_c. \tag{A5}$$

By inserting Eq. A3 into the expression of $\mathcal{C}_{acc}$ and considering A4 into A5 while introducing the dark count probability $\Delta_{A,B} t_c$ results in:

$$\mathcal{P}_c = B\eta_A\eta_B t_c + (B\eta_A + \Delta_A)(B\eta_B + \Delta_B) t_c^2. \tag{A6}$$

This, in turn, leads to the following expression in terms of the mean photon number per coincident timing window emitted in the source $\mu = Bt_c$:

$$\begin{aligned} \mathcal{P}_c =& \mu[\mu\eta_A\eta_B + \eta_A\eta_B + t_c\eta_A\Delta_B + t_c\eta_B\Delta_A] + t_c^2\Delta_A\Delta_B = \\ & \mu[\mu\eta_A\eta_B + \eta_A\eta_B + \eta_A D_B + \eta_B D_A] + D_A D_B, \end{aligned} \tag{A7}$$

with D_A and D_B being the dark count probability per coincident timing window for Alice and Bob, respectively.

QBER

The contributions on the behavior of the QBER, which stand in relation with the measured visibility $\mathcal{V}_{final}$ via (see also Eq. 4.11)

$$Q = \frac{1 - \mathcal{V}_{final}}{2} = \frac{1 - \mathcal{V}_{acc}\mathcal{V}_{sys}}{2}, \tag{A8}$$

with $\mathcal{V}_{acc}$ being the visibility solely arising from accidental coincidences and $\mathcal{V}_{sys}$ considers systematic errors of the technical implementation, are twofold: As stated above, first, the imperfect devices in the experimental setup introduce a non-vanishing probability of uncorrelated photon pair detection, and second, the higher-order photon emission can result in identifying two actually uncorrelated photon pairs as coincidences.

In the following, the visibility $\mathcal{V}_{acc}$, which can be attributed to accidental coincident counts and can be described by measured parameters, will be derived. The visibility (see Eq. 2.43) considers a polarization measurement setup as described above with the maximum coincident count probability as in Eq. A7 as well as the accidental count probability via

$$\mathcal{V}_{acc} = \frac{\mathcal{P}_c - \mathcal{C}_{acc} t_c}{\mathcal{P}_c + \mathcal{C}_{acc} t_c}. \tag{A9}$$

A factor of $\frac{1}{2}$ with respect for $\mathcal{P}_c$ would be required when polarizers prior to the detectors are used for the polarization analysis, however, it can be neglected in this case due to the usage of half-wave plates instead of polarizators. The assumption now includes the fact that the erroneous counts arise from the accidental coincidence probability as defined in Eq. A3, which takes into account the dark count probability $D_{A,B}$ as well as the mean photon number per coincident timing window μ.

Therefore, by inserting Eq. A7, Eq. A3 and Eq. A4 into Eq. A9 leads to the final expression of $\mathcal{V}_{acc}$:

$$\begin{aligned}\mathcal{V}_{acc} =& \frac{P_c - \mathcal{C}_{acc}t_c}{P_c + \mathcal{C}_{acc}t_c} = \frac{(B\eta_A\eta_B + \mathcal{C}_{acc})t_c - \mathcal{C}_{acc}t_c}{(B\eta_A\eta_B + \mathcal{C}_{acc})t_c + \mathcal{C}_{acc}t_c} = \\ & \frac{B\eta_A\eta_B t_c}{B\eta_A\eta_B t_c + 2\mathcal{C}_{acc}t_c} = \frac{\mu\eta_A\eta_B}{\mu\eta_A\eta_B + 2(\mu\eta_A + D_A)(\mu\eta_B + D_B)}.\end{aligned} \tag{A10}$$

To finally estimate the overall QBER in a certain basis, the final visibility $\mathcal{V}_{final}$ comprises the theoretically derived visibility $\mathcal{V}_{acc}$ and $\mathcal{V}_{sys}$ via $\mathcal{V}_{final} = \mathcal{V}_{acc} \times \mathcal{V}_{sys}$, while the latter takes systematic errors, e.g., non-ideal extinction ratios from the polarizing beam splitter into account. The value $\mathcal{V}_{sys}$ can be obtained via evaluating each element's contribution to the overall systematic error in the technical implementation, which requires a thorough understanding of the element's optical and technical properties. Due to this rather challenging task, another approach, being ultimately sufficiently precise, is the direct measurement of the contribution of $\mathcal{V}_{sys}$ to $\mathcal{V}_{final}$ by assuring the value of $\mathcal{V}_{acc}$ being close to unity. The latter can be achieved by choosing the system's mean photon pair number $\mu << 0.1$, to minimize the accidental coincidences contribution to the measured visibility (see section 4.6.4). Finally, by choosing the parameters f (bi-direction error correction efficiency) and q (basis-reconciliation factor), a lower bound for the QKD system's secure key rate can be estimated via inserting the QBER into Eq. 4.12.

A2 Interference measurements supplementary data

The measurement results for 2m are given in Fig. A2.1,A2.2 and A2.3.

The measurement results for 20m are given in Fig. A2.4,A2.5 and A2.6.

The measurement results for 70m are given in Fig. A2.7,A2.8 and A2.9.

The figures contain the sum of maximum and minimum data points of the oscillating single and coincident count rates collected over a measurement time of 70 s.

2m

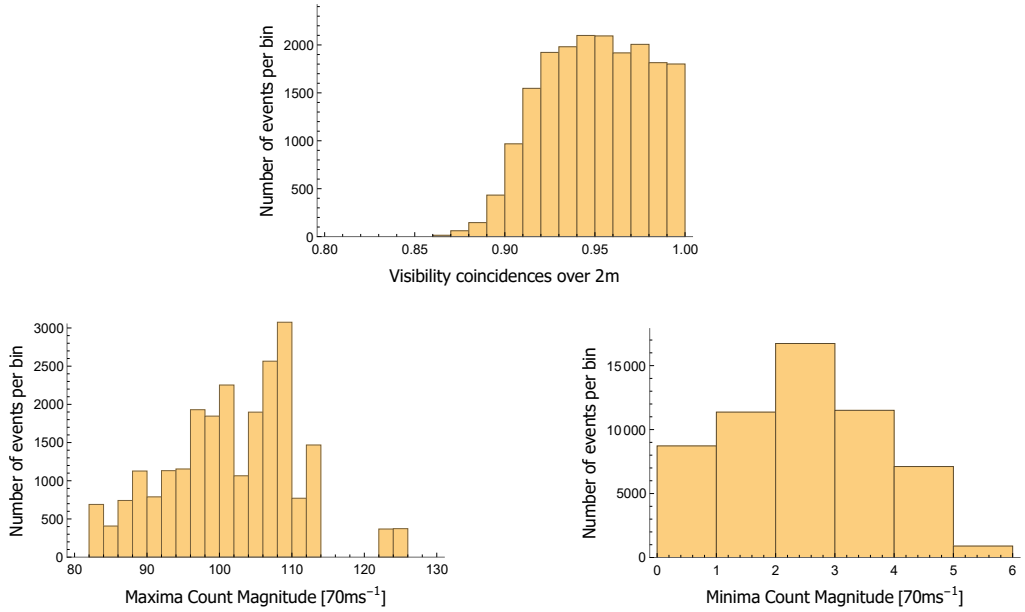

Figure A2.1: Histograms of statistical distribution of maxima (bottom left) and minima (bottom right), respectively, of coincident count rates over 2m (see 3.21) with sampling number of 10^5 are shown. A distribution of visibilities as calculated by the definition in 2.43 is displayed at the top.

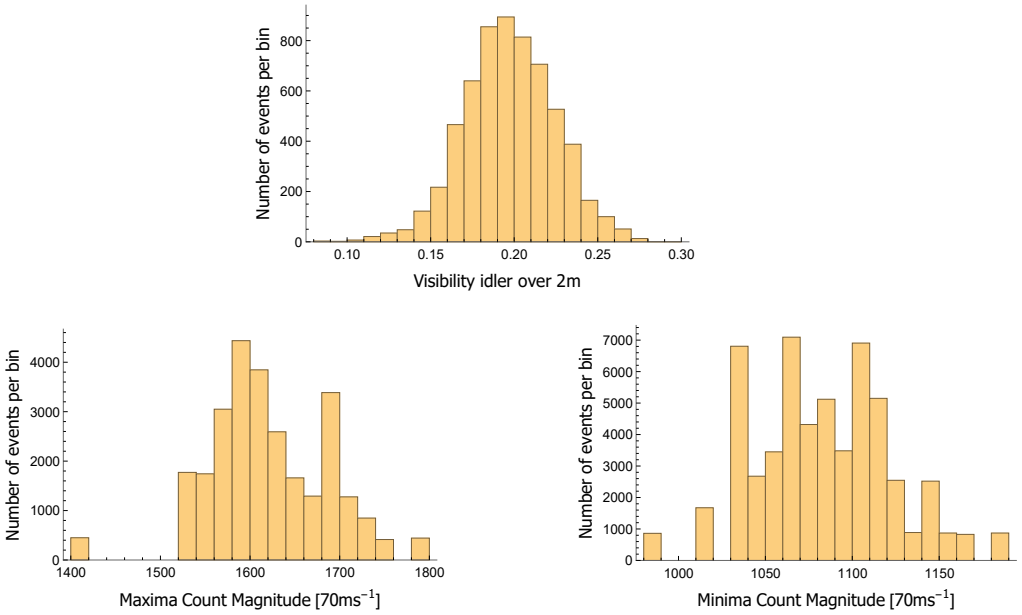

Figure A2.2: Histograms of statistical distribution of maxima (bottom left) and minima (bottom right) of idler count rates over 2m (see also 3.22) with sampling number of 5×10^5 are shown. A distribution of visibilities is displayed at the top.

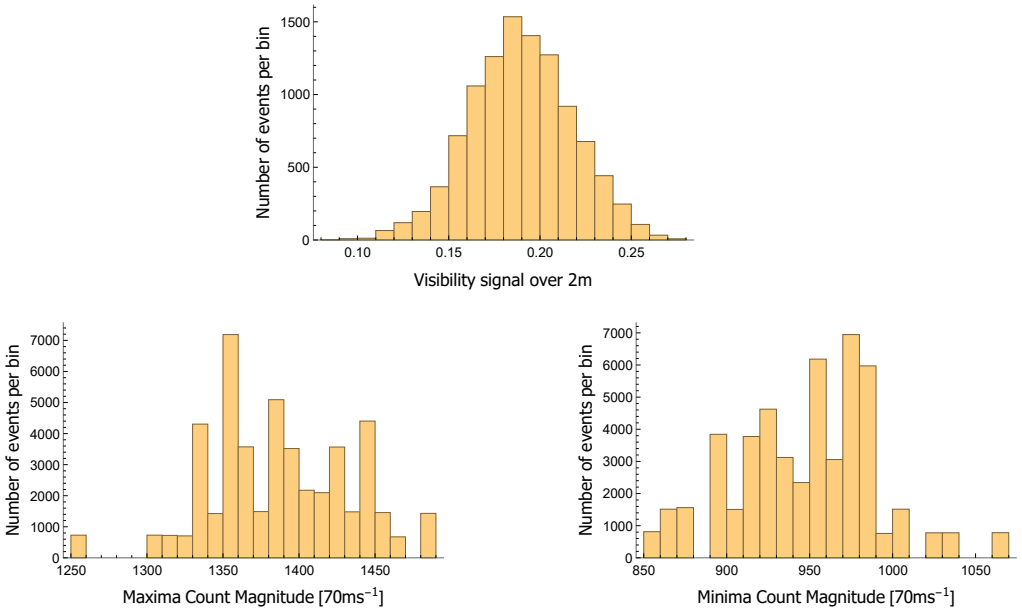

Figure A2.3: Histograms of statistical distribution of maxima (bottom left) and minima (bottom right) of signal count rates over 2m (see 3.22) with sampling number of 5×10^5 are shown. A distribution of visibilities is displayed at the top.

20m

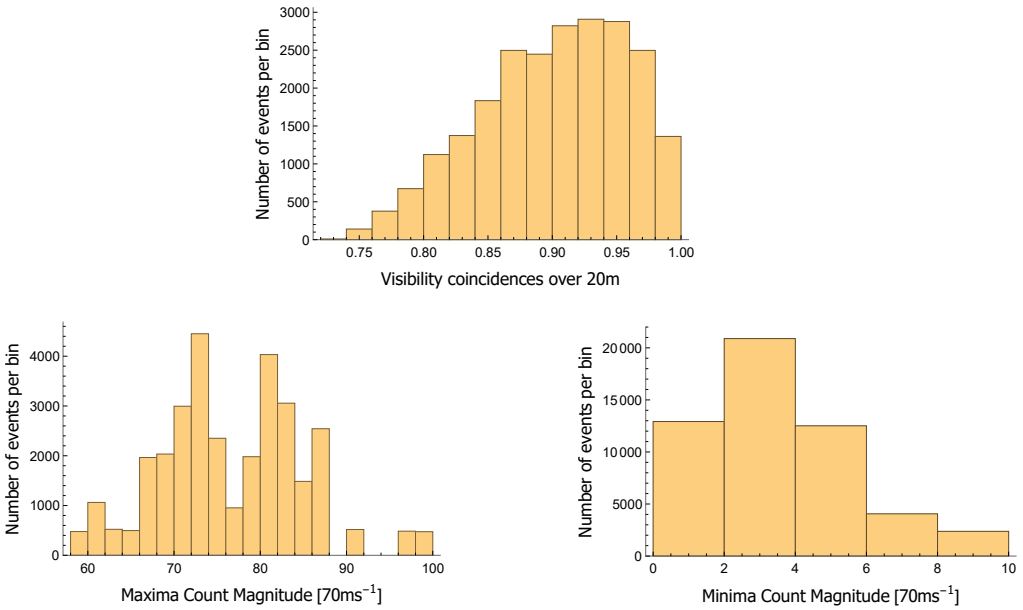

Figure A2.4: Histograms of statistical distribution of maxima (bottom left) and minima (bottom right), respectively, of coincident count rates over 20m (see 3.23) with sampling number of 10^5 are shown. A distribution of visibilities as calculated by the definition in 2.43 is displayed at the top.

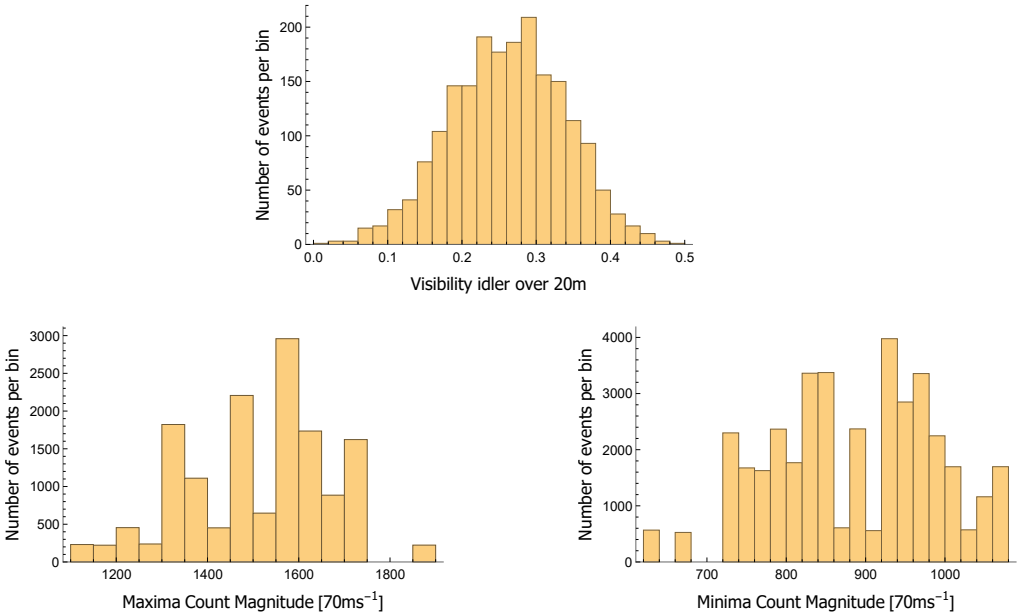

Figure A2.5: Histograms of statistical distribution of maxima (bottom left) and minima (bottom right) of idler count rates over 20m (see 3.24) with sampling number of 5×10^5 are shown. A distribution of visibilities is displayed at the top.

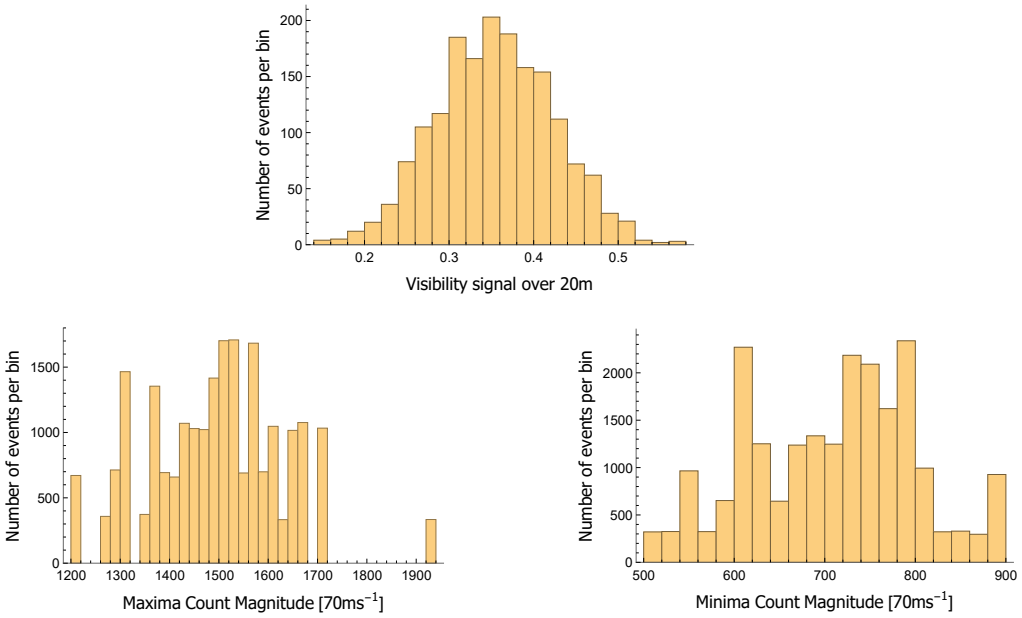

Figure A2.6: Histograms of statistical distribution of maxima (bottom left) and minima (bottom right) of signal count rates over 20m (see 3.24) with sampling number of 5×10^5 are shown. A distribution of visibilities is displayed at the top.

70m

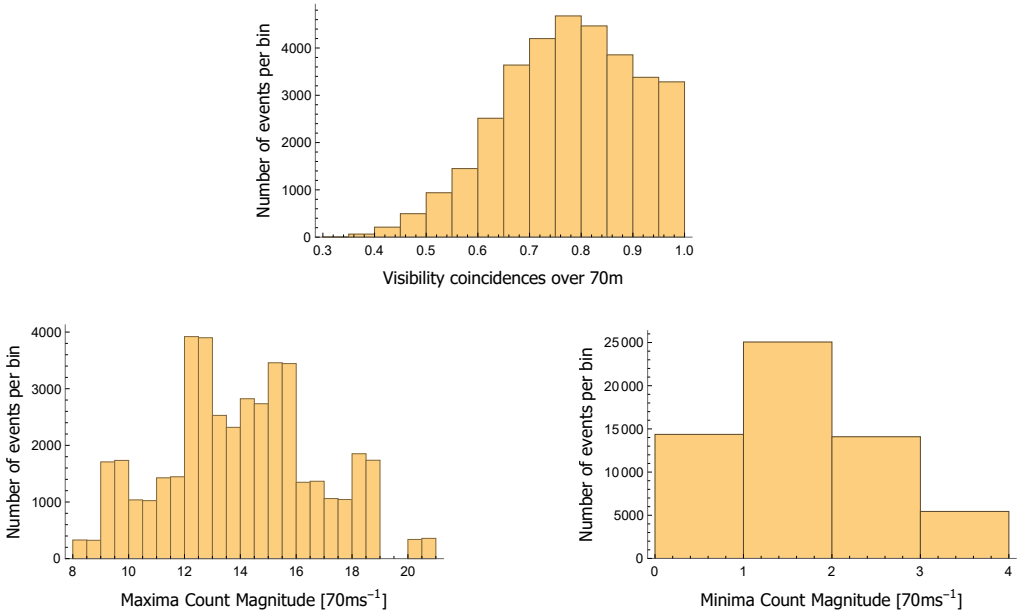

Figure A2.7: Histograms of statistical distribution of maxima (bottom left) and minima (bottom right), respectively, of coincident count rates over 70m (see 3.25) with sampling number of 10^5 are shown. A distribution of visibilities as calculated by the definition in 2.43 is displayed at the top.

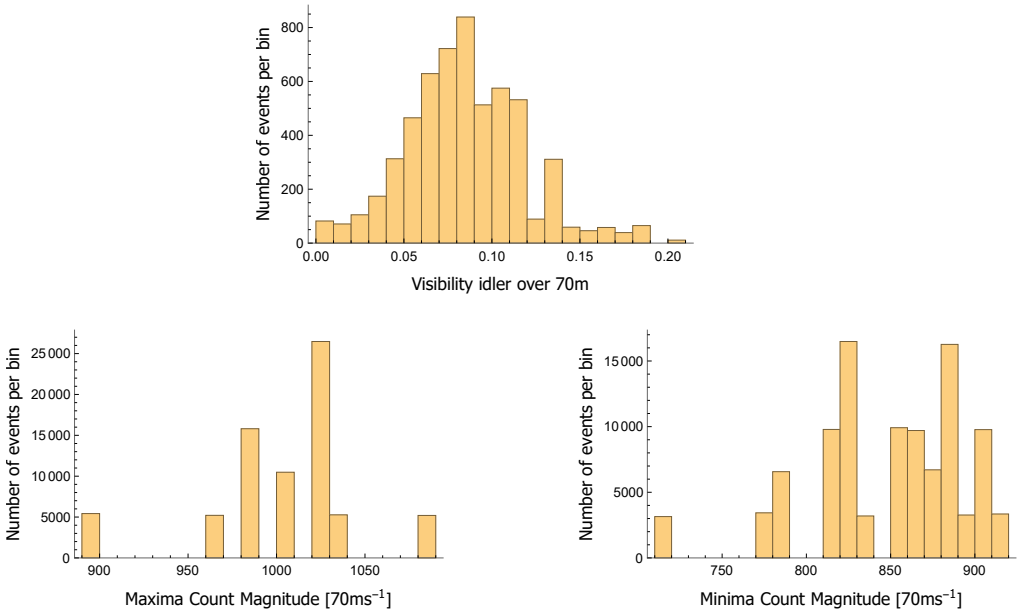

Figure A2.8: Histograms of statistical distribution of maxima (bottom left) and minima (bottom right) of idler count rates over 70m (see 3.26) with sampling number of 5×10^5 are shown. A distribution of visibilities is displayed at the top.

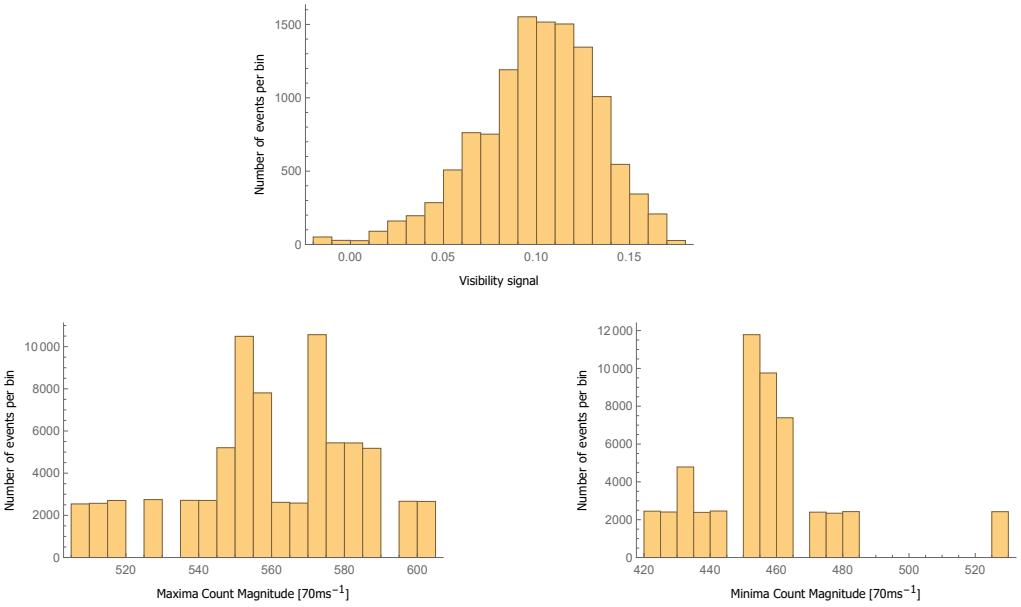

Figure A2.9: Histograms of statistical distribution of maxima (bottom left) and minima (bottom right) of signal count rates over 70m (see 3.26) with sampling number of 10^5 are shown. A distribution of visibilities is displayed at the top.

Bibliography

[1] C. Cohen-Tannoudji, B. Diu, and F. Laloë, "Quantum mechanics, volume 1: Basic concepts, tools, and applications," *Oxford University Press*, 3rd Edition, 2000.

[2] B. E. A. Saleh and M. C. Teich, "Fundamentals of photonics," *John Wiley and Sons Ltd*, vol. 1, 1991.

[3] C. Gerry and P. Knight, "Introductory quantum optics," *Cambridge University Press*, 2004.

[4] M. A. Nielsen and I. L. Chuang, "Quantum computation and quantum information," *Cambridge University Press*, 10th Anniversary edition, 2010.

[5] R. Loudon, "The quantum theory of light," *John Wiley and Sons Ltd*, vol. 1, 12, 2019.

[6] G. E. Moore, "Cramming more components onto integrated circuits, reprinted from electronics, volume 38, number 8, april 19, 1965, pp.114 ff.," *IEEE Solid-State Circuits Society Newsletter*, vol. 11, no. 3, pp. 33–35, 2006.

[7] G. M. D'Ariano, C. Macchiavello, and P. Perinotti, "Superbroadcasting of mixed states," *Phys. Rev. Lett.*, vol. 95, p. 060503, 2005.

[8] A. Pati and S. Braunstein, "Impossibility of deleting an unknown quantum state," *Nature*, vol. 404, pp. 164–5, 2000.

[9] W. K. Wootters and W. H. Zurek, "A single quantum cannot be cloned," *Nature*, vol. 299, no. 5886, pp. 802–803, 1982.

[10] J. A. Barandes and D. Kagan, "Measurement and quantum dynamics in the minimal modal interpretation of quantum theory," *Foundations of Physics*, vol. 50, no. 10, pp. 1189–1218, 2020.

[11] H. Terashima, "Local trade-off between information and disturbance in quantum measurements." *arXiv:2009.10944*, 2020.

[12] M. Born, "Zur Quantenmechanik der Stoßvorgänge," *Zeitschrift für Physik*, vol. 37, no. 12, pp. 863–867, 1926.

[13] B. R. L. Cour and M. C. Williamson, "Emergence of the born rule in quantum optics." *arXiv:2004.08749*, 2020.

[14] E. Schrödinger, "Die gegenwärtige Situation in der Quantenmechanik," *Naturwissenschaften*, vol. 23, no. 49, p. 823–828, 1935.

[15] A. Einstein, B. Podolsky, and N. Rosen, "Can quantum-mechanical description of physical reality be considered complete?," *Phys. Rev.*, vol. 47, no. 10, pp. 777–780, 1935.

[16] J. S. Bell, "On the einstein podolsky rosen paradox," *Physics Physique Fizika*, vol. 1, pp. 195–200, 1964.

[17] A. Baas and B. L. Bihan, "What does the world look like according to superdeterminism?." *arXiv:2009.13908*, 2020.

[18] S. Hossenfelder, "Superdeterminism: A guide for the perplexed." *arXiv:2010.01324*, 2020.

[19] J. F. Clauser, M. A. Horne, A. Shimony, and R. A. Holt, "Proposed experiment to test local hidden-variable theories," *Phys. Rev. Lett.*, vol. 23, pp. 880–884, 1969.

[20] A. Aspect, J. Dalibard, and G. Roger, "Experimental test of bell's inequalities using time-varying analyzers," *Phys. Rev. Lett.*, vol. 49, pp. 1804–1807, 1982.

[21] G. Weihs, T. Jennewein, C. Simon, H. Weinfurter, and A. Zeilinger, "Violation of bell's inequality under strict einstein locality conditions," *Phys. Rev. Lett.*, vol. 81, pp. 5039–5043, 1998.

[22] W. Tittel, J. Brendel, H. Zbinden, and N. Gisin, "Violation of bell inequalities by photons more than 10 km apart," *Phys. Rev. Lett.*, vol. 81, pp. 3563–3566, 1998.

[23] T. Scheidl, R. Ursin, J. Kofler, S. Ramelow, X.-S. Ma, T. Herbst, L. Ratschbacher, A. Fedrizzi, N. K. Langford, T. Jennewein, and A. Zeilinger, "Violation of local realism with freedom of choice," *Proceedings of the National Academy of Sciences*, vol. 107, no. 46, p. 19708, 2010.

[24] M. Giustina, A. Mech, S. Ramelow, B. Wittmann, J. Kofler, J. Beyer, A. Lita, B. Calkins, T. Gerrits, S. W. Nam, R. Ursin, and A. Zeilinger, "Bell violation using entangled photons without the fair-sampling assumption," *Nature*, vol. 497, no. 7448, pp. 227–230, 2013.

[25] B. G. Christensen, K. T. McCusker, J. B. Altepeter, B. Calkins, T. Gerrits, A. E. Lita, A. Miller, L. K. Shalm, Y. Zhang, S. W. Nam, N. Brunner, C. C. W. Lim, N. Gisin, and P. G. Kwiat, "Detection-loophole-free test of quantum nonlocality, and applications," *Phys. Rev. Lett.*, vol. 111, p. 130406, 2013.

[26] O. Guehne and G. Toth, "Entanglement detection," *Phys. Rev. Lett.*, vol. 474, pp. 1–75, 2009.

[27] C. A. Sackett, D. Kielpinski, B. E. King, C. Langer, V. Meyer, C. J. Myatt, M. Rowe, Q. A. Turchette, W. M. Itano, D. J. Wineland, and C. Monroe, "Experimental entanglement of four particles," *Nature*, vol. 404, no. 6775, pp. 256–259, 2000.

[28] T. Jennewein, R. Ursin, M. Aspelmeyer, and A. Zeilinger, "Performing high-quality multi-photon experiments with parametric down-conversion," *Journal of Physics B: Atomic, Molecular and Optical Physics*, vol. 42, p. 114008, 2009.

[29] M. Doda, M. Pivoluska, and M. Plesch, "Choice of mutually unbiased bases and outcome labelling affects measurementoutcome secrecy." *arXiv:2006.08226v2*, 2021.

[30] B. B. Blinov, D. L. Moehring, L.-. M. Duan, and C. Monroe, "Observation of entanglement between a single trapped atom and a single photon," *Nature*, vol. 428, no. 6979, pp. 153–157, 2004.

[31] X.-Y. Chang, D.-L. Deng, X.-X. Yuan, P.-Y. Hou, Y.-Y. Huang, and L.-M. Duan, "Experimental realization of an entanglement access network and secure multi-party computation," *Scientific Reports*, vol. 6, no. 1, p. 29453, 2016.

[32] A. Christ, B. Brecht, W. Mauerer, and C. Silberhorn, "Theory of quantum frequency conversion and type-II parametric down-conversion in the high-gain regime," *New Journal of Physics*, vol. 15, 2012.

[33] D. Burnham and D. Weinberg, "Observation of simultaneity in parametric production of optical photon pairs," *Phys. Rev. Lett*, vol. 25, 1970.

[34] C. Couteau, "Spontaneous parametric down-conversion," *Contemporary Physics*, vol. 59, no. 3, pp. 291–304, 2018.

[35] M. Rambach, "Narrowband single photons for light-matter interfaces," *Springer Nature Switzerland AG*, Cham, 2018.

[36] K. Spasibko, "Spectral and statistical properties of high-gain parametric down-conversion." *arXiv:2007.12999*, 2020.

[37] J. D. A. Aspect and G. Roger, "Experimental test of bell's inequalities using time-varying analyzers.," *Phys. Rev. Lett*, vol. 49, 1982.

[38] S. Walborn, C. Monken, S. Pádua, and P. Souto Ribeiro, "Spatial correlations in parametric down-conversion," *Physics Reports*, vol. 495, pp. 87–139, 2010.

[39] C. Hong and L. Mandel, "Theory of parametric frequency down-conversion of light," *Physical review. A*, vol. 31, pp. 2409–2418, 1985.

[40] T. J. Herzog, "An optical test of complementarity," (Dissertation, University of Innsbruck, 1995).

[41] F. Steinlechner, "Sources of photonic entanglement for applications in space," (Dissertation, ICFO-Institut De Ciències Fotòniques y UPC-Universitat Politècnica De Catalunya, 2015).

[42] W. B. Berestezki, L. P. Pitajewski, and E. M. Lifshitz, "Quantum electrodynamics, volume 4," *Butterworth-Heinemann*, 2nd edition, 1982.

[43] R. J. Glauber, "Coherent and incoherent states of the radiation field," *Phys. Rev.*, vol. 131, pp. 2766–2788, 1963.

[44] K. Zielnicki, K. Garay-Palmett, D. Cruz-Delgado, H. Cruz-Ramirez, M. F. O'Boyle, B. Fang, V. O. Lorenz, A. B. U'Ren, and P. G. Kwiat, "Joint spectral characterization of photon-pair sources," *Journal of Modern Optics*, vol. 65, no. 10, pp. 1141–1160, 2018.

[45] M. Yamada, N. Nada, M. Saitoh, and K. Watanabe, "First-order quasi-phase matched linbo3 waveguide periodically poled by applying an external field for efficient blue second-harmonic generation," *Applied Physics Letters*, vol. 62, no. 5, pp. 435–436, 1993.

[46] N. A. Salmon and S. R. Hoon, "A millimeter-wave bell test using a ferrite parametric amplifier and a homodyne interferometer," *Journal of Magnetism and Magnetic Materials*, vol. 501, p. 166435, 2020.

[47] M. M. Fejer, G. A. Magel, D. H. Jundt, and R. L. Byer, "Quasi-phase-matched second harmonic generation: tuning and tolerances," *IEEE Journal of Quantum Electronics*, vol. 28, no. 11, pp. 2631–2654, 1992.

[48] R.-B. Jin, R. Shimizu, K. Wakui, H. Benichi, and M. Sasaki, "Widely tunable single photon source with high purity at telecom wavelength," *Opt. Express*, vol. 21, no. 9, pp. 10659–10666, 2013.

[49] S. Karan, S. Aarav, H. Bharadhwaj, L. Taneja, A. De, G. Kulkarni, N. Meher, and A. K. Jha, "Phase matching in β-barium borate crystals for spontaneous parametric down-conversion," *Journal of Optics*, vol. 22, no. 8, p. 083501, 2020.

[50] X. P. Hu, P. Xu, and S. N. Zhu, "Engineered quasi-phase-matching for laser techniques," *Photon. Res.*, vol. 1, no. 4, pp. 171–185, 2013.

[51] M. V. Pack, D. J. Armstrong, and A. V. Smith, "Measurement of the $\chi(2)$ tensors of ktiopo4, ktioaso4, rbtiopo4, and rbtioaso4 crystals," *Appl. Opt.*, vol. 43, no. 16, pp. 3319–3323, 2004.

[52] H. Kogelnik and T. Li, "Laser beams and resonators," *Appl. Opt.*, vol. 5, no. 10, pp. 1550–1567, 1966.

[53] K. Edamatsu, R. Shimizu, W. Ueno, R. Jin, F. Kaneda, M. Yabuno, H. Suzuki, S. Nagano, A. Syouji, and K. Suizu, "Photon pair sources with controlled frequency correlation," *Progress in Informatics*, p. 19, 2011.

[54] S. M. Lee, H. Kim, M. Cha, and H. S. Moon, "Polarization-entangled photon-pair source obtained via type-ii non-collinear spdc process with ppktp crystal," *Opt. Express*, vol. 24, no. 3, pp. 2941–2953, 2016.

[55] Ocean Optics, *QE65000 Data Sheet*, 2007. `https://www.usna.edu/Users/physics/vanhoy/_files/SP425/LabDocs/Ocean%20Optics%202000/SpectraSuite/070131_1347%20R/documentation/Spectrometers%20and%20Software/QE65000.pdf`, Accessed: 2020-09-25.

[56] H. Takesue and K. Shimizu, "Effects of multiple pairs on visibility measurements of entangled photons generated by spontaneous parametric processes," *Optics Communications*, vol. 283, no. 2, p. 276–287, 2010.

[57] S. Wengerowsky, "Two-photon polarization entanglement for experiments and applications in quantum communications," (Dissertation, University of Vienna, 2020).

[58] M. Agüero, A. Hnilo, and M. Kovalsky, "Measuring entanglement of photons produced by a pulsed source," *Journal of the Optical Society of America B*, vol. 31, 2013.

[59] F. Steinlechner, P. Trojek, M. Jofre, H. Weier, D. Perez, T. Jennewein, R. Ursin, J. Rarity, M. Mitchell, J. Torres, H. Weinfurter, and V. Pruneri, "A high-brightness source of polarization-entangled photons optimized for applications in free space," *Optics express*, vol. 20, pp. 9640–9, 2012.

[60] T. Jennewein, R. Ursin, M. Aspelmeyer, and A. Zeilinger, "Performing high-quality multi-photon experiments with parametric down-," *Journal of Physics B: Atomic, Molecular and Optical Physics*, vol. 42, p. 114008, 2009.

[61] A. L. Migdall, D. Branning, and S. Castelletto, "Tailoring single-photon and multiphoton probabilities of a single-photon on-demand source," *Phys. Rev. A*, vol. 66, p. 053805, 2002.

[62] J. H. Shapiro and F. N. Wong, "On-demand single-photon generation using a modular array of parametric downconverters with electro-optic polarization controls," *Opt. Lett.*, vol. 32, no. 18, pp. 2698–2700, 2007.

[63] F. Bodog, P. Adam, M. Mechler, I. Santa, and M. Koniorczyk, "Optimization of periodic single-photon sources based on combined multiplexing," *Phys. Rev. A*, vol. 94, p. 033853, 2016.

[64] J. Pseiner, L. Achatz, L. Bulla, M. Bohmann, and R. Ursin, "Experimental wavelength-multiplexed entanglement-based quantum cryptography," *Quantum Science and Technology*, vol. 6, no. 3, p. 035013, 2021.

[65] R. P. Feynman, R. Leighton, and M. Sands, "The Feynman lectures on physics," *Addison-Wesley, Reading, Massachussetts*, 1963.

[66] C. Lupo and S. Pirandola, "Ultimate precision bound of quantum and subwavelength imaging," *Phys. Rev. Lett.*, vol. 117, p. 190802, 2016.

[67] P. Wang, C. Chen, and R. Liu, "Classical-noise-free sensing based on quantum correlation measurement." *arXiv:2009.10429*, 2020.

[68] C. L. Degen, F. Reinhard, and P. Cappellaro, "Quantum sensing," *Rev. Mod. Phys.*, vol. 89, p. 035002, 2017.

[69] L. Pezzè, A. Smerzi, M. K. Oberthaler, R. Schmied, and P. Treutlein, "Quantum metrology with nonclassical states of atomic ensembles," *Rev. Mod. Phys.*, vol. 90, p. 035005, 2018.

[70] D. Boschi, S. Branca, F. De Martini, L. Hardy, and S. Popescu, "Experimental realization of teleporting an unknown pure quantum state via dual classical and einstein-podolsky-rosen channels," *Phys. Rev. Lett.*, vol. 80, pp. 1121–1125, 1998.

[71] A. Fedrizzi, R. Ursin, T. Herbst, M. Nespoli, R. Prevedel, T. Scheidl, F. Tiefenbacher, T. Jennewein, and A. Zeilinger, "High-fidelity transmission of entanglement over a high-loss free-space channel," *Nature Physics*, vol. 5, no. 6, pp. 389–392, 2009.

[72] J. Yin, J.-G. Ren, H. Lu, Y. Cao, H.-L. Yong, Y.-P. Wu, C. Liu, S.-K. Liao, F. Zhou, Y. Jiang, X.-D. Cai, P. Xu, G.-S. Pan, J.-J. Jia, Y.-M. Huang, H. Yin, J.-Y. Wang, Y.-A. Chen, C.-Z. Peng, and J.-W. Pan, "Quantum teleportation and entanglement distribution over 100-kilometre free-space channels," *Nature*, vol. 488, no. 7410, pp. 185–188, 2012.

[73] J. Yin, Y. Cao, Y.-H. Li, S.-K. Liao, L. Zhang, J.-G. Ren, W.-Q. Cai, W.-Y. Liu, B. Li, H. Dai, G.-B. Li, Q.-M. Lu, Y.-H. Gong, Y. Xu, S.-L. Li, F.-Z. Li, Y.-Y. Yin, Z.-Q. Jiang, M. Li, J.-J. Jia, G. Ren, D. He, Y.-L. Zhou, X.-X. Zhang, N. Wang, X. Chang, Z.-C. Zhu, N.-L. Liu, Y.-A. Chen, C.-Y. Lu, R. Shu, C.-Z. Peng, J.-Y. Wang, and J.-W. Pan, "Satellite-based entanglement distribution over 1200 kilometers," *Science*, vol. 356, no. 6343, pp. 1140–1144, 2017.

[74] R. K. Chang, J. Ducuing, and N. Bloembergen, "Relative phase measurement between fundamental and second-harmonic light," *Phys. Rev. Lett.*, vol. 15, pp. 6–8, 1965.

[75] V. B. Braginsky, F. Y. Khalili, and K. S. Thorne, "Quantum measurement," *Oxford University Press*, 1992.

[76] C. Helstrom, "Minimum mean-squared error of estimates in quantum statistics," *Physics Letters A*, vol. 25, no. 2, pp. 101–102, 1967.

[77] M. Tse, H. Yu, N. Kijbunchoo, A. Fernandez-Galiana, P. Dupej, L. Barsotti, C. D. Blair, D. D. Brown, S. E. Dwyer, A. Effler, M. Evans, P. Fritschel, V. V. Frolov, A. C. Green, G. L. Mansell, F. Matichard, N. Mavalvala, D. E. McClelland, L. McCuller, T. McRae, J. Miller, A. Mullavey, E. Oelker, I. Y. Phinney, D. Sigg, B. J. J. Slagmolen, T. Vo,

R. L. Ward, C. Whittle, R. Abbott, C. Adams, R. X. Adhikari, A. Ananyeva, S. Appert, K. Arai, J. S. Areeda, Y. Asali, S. M. Aston, C. Austin, A. M. Baer, M. Ball, S. W. Ballmer, S. Banagiri, D. Barker, J. Bartlett, B. K. Berger, J. Betzwieser, D. Bhattacharjee, G. Billingsley, S. Biscans, R. M. Blair, N. Bode, P. Booker, R. Bork, A. Bramley, A. F. Brooks, A. Buikema, C. Cahillane, K. C. Cannon, X. Chen, A. A. Ciobanu, F. Clara, S. J. Cooper, K. R. Corley, S. T. Countryman, P. B. Covas, D. C. Coyne, L. E. H. Datrier, D. Davis, C. Di Fronzo, J. C. Driggers, T. Etzel, T. M. Evans, J. Feicht, P. Fulda, M. Fyffe, J. A. Giaime, K. D. Giardina, P. Godwin, E. Goetz, S. Gras, C. Gray, R. Gray, A. Gupta, E. K. Gustafson, R. Gustafson, J. Hanks, J. Hanson, T. Hardwick, R. K. Hasskew, M. C. Heintze, A. F. Helmling-Cornell, N. A. Holland, J. D. Jones, S. Kandhasamy, S. Karki, M. Kasprzack, K. Kawabe, P. J. King, J. S. Kissel, R. Kumar, M. Landry, B. B. Lane, B. Lantz, M. Laxen, Y. K. Lecoeuche, J. Leviton, J. Liu, M. Lormand, A. P. Lundgren, R. Macas, M. MacInnis, D. M. Macleod, S. Márka, Z. Márka, D. V. Martynov, K. Mason, T. J. Massinger, R. McCarthy, S. McCormick, J. McIver, G. Mendell, K. Merfeld, E. L. Merilh, F. Meylahn, T. Mistry, R. Mittleman, G. Moreno, C. M. Mow-Lowry, S. Mozzon, T. J. N. Nelson, P. Nguyen, L. K. Nuttall, J. Oberling, R. J. Oram, B. O'Reilly, C. Osthelder, D. J. Ottaway, H. Overmier, J. R. Palamos, W. Parker, E. Payne, A. Pele, C. J. Perez, M. Pirello, H. Radkins, K. E. Ramirez, J. W. Richardson, K. Riles, N. A. Robertson, J. G. Rollins, C. L. Romel, J. H. Romie, M. P. Ross, K. Ryan, T. Sadecki, E. J. Sanchez, L. E. Sanchez, T. R. Saravanan, R. L. Savage, D. Schaetzl, R. Schnabel, R. M. S. Schofield, E. Schwartz, D. Sellers, T. J. Shaffer, J. R. Smith, S. Soni, B. Sorazu, A. P. Spencer, K. A. Strain, L. Sun, M. J. Szczepańczyk, M. Thomas, P. Thomas, K. A. Thorne, K. Toland, C. I. Torrie, G. Traylor, A. L. Urban, G. Vajente, G. Valdes, D. C. Vander-Hyde, P. J. Veitch, K. Venkateswara, G. Venugopalan, A. D. Viets, C. Vorvick, M. Wade, J. Warner, B. Weaver, R. Weiss, B. Willke, C. C. Wipf, L. Xiao, H. Yamamoto, M. J. Yap, H. Yu, L. Zhang, M. E. Zucker, and J. Zweizig, "Quantum-enhanced advanced ligo detectors in the era of gravitational-wave astronomy," *Phys. Rev. Lett.*, vol. 123, p. 231107, 2019.

[78] G.-F. Jiao, K. Zhang, L. Q. Chen, W. Zhang, and C.-H. Yuan, "Nonlinear phase estimation enhanced by an actively correlated mach-zehnder interferometer," *Phys. Rev. A*, vol. 102, p. 033520, 2020.

[79] F. Hudelist, J. Kong, C. Liu, J. Jing, Z. Y. Ou, and W. Zhang, "Quantum metrology with parametric amplifier-based photon correlation interferometers," *Nature Communications*, vol. 5, no. 1, p. 3049, 2014.

[80] A. Ferreri, M. Santandrea, M. Stefszky, K. H. Luo, H. Herrmann, C. Silberhorn, and P. R. Sharapova, "Spectrally multimode integrated su(1,1) interferometer." *arXiv:2012.03751*, 2020.

[81] J.-D. Zhang, C. You, C. Li, and S. Wang, "Phase sensitivity approaching quantum cramer-rao bound in a modified su(1,1) interferometer." *arXiv:2012.04236*, 2020.

[82] M. V. Chekhova and Z. Y. Ou, "Nonlinear interferometers in quantum optics," *Adv. Opt. Photon.*, vol. 8, no. 1, pp. 104–155, 2016.

[83] B. Yurke, S. L. McCall, and J. R. Klauder, "SU(2) and SU(1,1) interferometers," *Phys. Rev. A*, vol. 33, pp. 4033–4054, 1986.

[84] A. V. Paterova and L. A. Krivitsky, "Nonlinear interference in crystal superlattices," *Light: Science & Applications*, vol. 9, no. 1, p. 82, 2020.

[85] E. D. Lopaeva, I. Ruo Berchera, I. P. Degiovanni, S. Olivares, G. Brida, and M. Genovese, "Experimental realization of quantum illumination," *Phys. Rev. Lett.*, vol. 110, p. 153603, 2013.

[86] D. A. Kalashnikov, A. V. Paterova, S. P. Kulik, and L. A. Krivitsky, "Infrared spectroscopy with visible light," *Nature Photonics*, vol. 10, no. 2, pp. 98–101, 2016.

[87] J. W. Rayleigh, "XXXI. Investigations in optics, with special reference to the spectroscope," 1879.

[88] M. Born and E. Wolf, "Principles of optics: Electromagnetic theory of propagation, interference and diffraction of light," *Cambridge University Press*, 1999.

[89] G. B. Lemos, V. Borish, G. D. Cole, S. Ramelow, R. Lapkiewicz, and A. Zeilinger, "Quantum imaging with undetected photons," *Nature*, vol. 512, no. 7515, pp. 409–412, 2014.

[90] R. A. Campos, B. E. A. Saleh, and M. C. Teich, "Quantum-mechanical lossless beam splitter: Su(2) symmetry and photon statistics," *Phys. Rev. A*, vol. 40, pp. 1371–1384, 1989.

[91] K. H. Drexhage, "IV Interaction of light with monomolecular dye layers," *Elsevier*, vol 12, pp. 163-232, 1974.

[92] C. K. Hong, Z. Y. Ou, and L. Mandel, "Measurement of subpicosecond time intervals between two photons by interference," *Phys. Rev. Lett.*, vol. 59, pp. 2044–2046, 1987.

[93] Z. Y. Ou, L. J. Wang, and L. Mandel, "Vacuum effects on interference in two-photon down conversion," *Phys. Rev. A*, vol. 40, pp. 1428–1435, 1989.

[94] L. J. Wang, X. Y. Zou, and L. Mandel, "Induced coherence without induced emission," *Phys. Rev. A*, vol. 44, pp. 4614–4622, 1991.

[95] T. P. Grayson and G. A. Barbosa, "Spatial properties of spontaneous parametric down-conversion and their effect on induced coherence without induced emission," *Phys. Rev. A*, vol. 49, pp. 2948–2961, 1994.

[96] T. Herzog, J. Rarity, H. Weinfurter, and A. Zeilinger, "Classical interpretation of frustrated two-photon creation via interference - reply," *Phys. Rev. Lett*, vol. 73, no. 22, pp. 3041–3041, 1994.

[97] M. Krenn, A. Hochrainer, M. Lahiri, and A. Zeilinger, "Entanglement by path identity," *Phys. Rev. Lett*, vol. 118, 2016.

[98] T. J. Herzog, J. G. Rarity, H. Weinfurter, and A. Zeilinger, "Frustrated two-photon creation via interference," *Phys. Rev. Lett.*, vol. 72, pp. 629–632, 1994.

[99] L.-A. Wu and H. J. Kimble, "Interference effects in second-harmonic generation within an optical cavity," *J. Opt. Soc. Am. B*, vol. 2, no. 5, pp. 697–703, 1985.

[100] I. R. Senitzky, "Classical interpretation of "frustrated two-photon creation via interference"," *Phys. Rev. Lett.*, vol. 73, pp. 3040–3040, 1994.

[101] M. Arndt, O. Nairz, J. Voss-Andreae, C. Keller, G. Zouw, and A. Zeilinger, "Wave-particle duality of c60 molecules," *Nature*, vol. 401, pp. 680–682, 1999.

[102] A. Belenchia, R. M. Wald, F. Giacomini, E. Castro-Ruiz, i. c. v. Brukner, and M. Aspelmeyer, "Quantum superposition of massive objects and the quantization of gravity," *Phys. Rev. D*, vol. 98, p. 126009, 2018.

[103] R. Fickler, R. Lapkiewicz, W. Plick, M. Krenn, C. Schaeff, S. Ramelow, and A. Zeilinger, "Quantum entanglement of high angular momenta," *Science (New York, N.Y.)*, vol. 338, pp. 640–3, 2012.

[104] R. Ursin, F. Tiefenbacher, T. Schmitt-Manderbach, H. Weier, T. Scheidl, M. Lindenthal, B. Blauensteiner, T. Jennewein, J. Perdigues, P. Trojek, B. Ömer, M. Fürst, M. Meyenburg, J. Rarity, Z. Sodnik, C. Barbieri, H. Weinfurter, and A. Zeilinger, "Entanglement-based quantum communication over 144 km," *Nature Physics*, vol. 3, no. 7, pp. 481–486, 2007.

[105] M. Krenn, M. Huber, R. Fickler, R. Lapkiewicz, S. Ramelow, and A. Zeilinger, "Generation and confirmation of a (100 x 100)-dimensional entangled quantum system," *Proceedings of the National Academy of Sciences of the United States of America*, vol. 111, 2014.

[106] N. Sangouard and H. Zbinden, "What are single photons good for?," *Journal of Modern Optics - J MOD OPTIC*, vol. 59, 2012.

[107] T. Nitsche, S. De, S. Barkhofen, E. Meyer-Scott, J. Tiedau, J. Sperling, A. Gábris, I. Jex, and C. Silberhorn, "Local versus global two-photon interference in quantum networks," *Phys. Rev. Lett.*, vol. 125, p. 213604, 2020.

[108] H. Weinfurter, "Experimental bell-state analysis," *Europhysics Letters (EPL)*, vol. 25, no. 8, pp. 559–564, 1994.

[109] R. J. Glauber, "The quantum theory of optical coherence," *Phys. Rev.*, vol. 130, pp. 2529–2539, 1963.

[110] A. Jha, M. O'Sullivan, K. W. Chan, and R. Boyd, "Temporal coherence and indistinguishability in two-photon interference effects," *Phys. Rev. A*, vol. 77, 2008.

[111] J. Brendel, W. Dultz, and W. Martienssen, "Geometric phases in two-photon interference experiments," *Phys. Rev. A*, vol. 52, pp. 2551–2556, 1995.

[112] Ondax, Inc, *Datasheet: Ondax LM Series Compact Single Frequency Laser Modules*, 2014. [Online]. Available: `https://www.laserdiodesource.com/files/pdfs/laserdiodesource_com/product-2418/SureLock_LM_Series_830_150_Sept_2014-1432163830.pdf` Accessed: 2020-07-23.

[113] R. S. Bennink, "Optimal collinear gaussian beams for spontaneous parametric down-conversion," *Phys. Rev. A*, vol. 81, p. 053805, 2010.

[114] M. V. Jabir and G. K. Samanta, "Robust, high brightness, degenerate entangled photon source at room temperature," *Scientific Reports*, vol. 7, p. 12613, 2017.

[115] O. Suzer and T. Goodson, "Does pump beam intensity affect the efficiency of spontaneous parametric down conversion?," *Optics express*, vol. 16, pp. 20166–75, 2009.

[116] H. Vanherzeele, J. D. Bierlein, and F. C. Zumsteg, "Index of refraction measurements and parametric generation in hydrothermally grown ktiopo4," *Appl. Opt.*, vol. 27, no. 16, pp. 3314–3316, 1988.

[117] J. D. Bierlein and H. Vanherzeele, "Potassium titanyl phosphate: properties and new applications," *J. Opt. Soc. Am. B*, vol. 6, no. 4, pp. 622–633, 1989.

[118] W. Wiechmann, S. Kubota, T. Fukui, and H. Masuda, "Refractive-index temperature derivatives of potassium titanyl phosphate," *Opt. Lett.*, vol. 18, no. 15, pp. 1208–1210, 1993.

[119] M. Fink, "Applications of a rigid source of entangled photons," (Dissertation, University of Vienna, 2019).

[120] S. Emanueli and A. Arie, "Temperature-dependent dispersion equations for ktiopo4 and ktioaso4," *Appl. Opt.*, vol. 42, no. 33, pp. 6661–6665, 2003.

[121] A. V. Sergienko, Y. H. Shih, and M. H. Rubin, "Experimental evaluation of a two-photon wave packet in type-ii parametric downconversion," *J. Opt. Soc. Am. B*, vol. 12, no. 5, pp. 859–862, 1995.

[122] P. E. Ciddor, "Refractive index of air: new equations for the visible and near infrared," *Appl. Opt.*, vol. 35, no. 9, pp. 1566–1573, 1996.

[123] E. T. Whittaker, "Xviii.—on the functions which are represented by the expansions of the interpolation-theory," *Proceedings of the Royal Society of Edinburgh*, vol. 35, p. 181–194, 1915.

[124] A. J. Fleming and B. S. Routley, "A closed-loop phase-locked interferometer for wide bandwidth position sensing," *Review of Scientific Instruments*, vol. 86, no. 11, p. 115001, 2015.

[125] T. Moroder, M. Curty, and N. Lütkenhaus, "Detector decoy quantum key distribution," *New Journal of Physics*, vol. 11, no. 4, p. 045008, 2009.

[126] T. Schmitt-Manderbach, "Long distance free-space quantum key distribution," (Dissertation, Ludwig-Maximilians-Universität München, 2007).

[127] A. N. Kolmogorov, "Local structure of turbulence in an incompressible viscous fluid at very high Reynolds numbers," *Soviet Physics Uspekhi*, vol. 10, no. 6, pp. 734–746, 1968.

[128] L. C. Andrews, "Field guide to atmospheric optics," *Spie Press Book*, FG02, 2004.

[129] J. H. Churnside and R. J. Lataitis, "Wander of an optical beam in the turbulent atmosphere," *Appl. Opt.*, vol. 29, no. 7, pp. 926–930, 1990.

[130] R. N. Lanning, M. A. Harris, D. W. Oesch, M. D. Oliker, and M. T. Gruneisen, "Quantum communication over atmospheric channels – a framework for optimizing wavelength and filtering." *arXiv:2104.10276*, 2021.

[131] A. Carrasco-Casado, N. Denisenko, and V. Fernandez, "Chromatic effects in beam wander correction for free-space quantum communications," *Microwave and Optical Technology Letters*, vol. 58, no. 6, pp. 1362–1365, 2016.

[132] D. J. Schroeder, "Astronomical optics: chapter 16 - Adaptive optics: An introduction," *Academic Press*, 2nd Edition, 2000.

[133] D. L. Fried, "Optical resolution through a randomly inhomogeneous medium for very long and very short exposures," *J. Opt. Soc. Am.*, vol. 56, no. 10, pp. 1372–1379, 1966.

[134] D. L. Fried, "Statistics of a geometric representation of wavefront distortion," *J. Opt. Soc. Am.*, vol. 55, no. 11, pp. 1427–1435, 1965.

[135] J. Blazej, I. Prochazka, and L. Kral, "Picosecond laser pulse distortion by propagation through a turbulent atmosphere," *Coherence and Ultrashort Pulse Laser Emission*, p. 435, 2010.

[136] M. Krenn, R. Fickler, M. Fink, J. Handsteiner, M. Malik, T. Scheidl, R. Ursin, and A. Zeilinger, "Communication with spatially modulated light through turbulent air across vienna," *New Journal of Physics*, vol. 16, no. 11, p. 113028, 2014.

[137] C. J. Pugh, J.-F. Lavigne, J.-P. Bourgoin, B. L. Higgins, and T. Jennewein, "Adaptive optics benefit for quantum key distribution uplink from ground to a satellite," *Advanced Optical Technologies*, vol. 9, no. 5, pp. 263 – 273, 01 Oct. 2020.

[138] R. W. Boyd, "Nonlinear optics," *Academic Press*, 3rd Edition, 2008.

[139] D. S. Hum and M. M. Fejer, "Quasi-phasematching," *Comptes Rendus Physique*, vol. 8, no. 2, pp. 180–198, 2007.

[140] S. Wiesner, "Conjugate coding," *SIGACT News*, vol. 15, no. 1, p. 78–88, 1983.

[141] P. W. Shor, "Polynomial-time algorithms for prime factorization and discrete logarithms on a quantum computer," *SIAM Review*, vol. 41, no. 2, pp. 303–332, 1999.

[142] E. Anschuetz, J. Olson, A. Aspuru-Guzik, and Y. Cao, "Variational quantum factoring," in *Quantum Technology and Optimization Problems* (S. Feld and C. Linnhoff-Popien, eds.), (Cham), pp. 74–85, Springer International Publishing, 2019.

[143] C. Cesare, "Encryption faces quantum foe: researchers urge readiness against attacks from future-generation computers," *Nature*, vol. 525, pp. 167+, 2015.

[144] C. Bennett and G. Brassard, "Quantum cryptography: Public key distribution and coin tossing," *Theoretical Computer Science - TCS*, vol. 560, pp. 175–179, 1984.

[145] C. H. Bennett, "Quantum cryptography using any two nonorthogonal states," *Phys. Rev. Lett.*, vol. 68, pp. 3121–3124, 1992.

[146] C. Portmann and R. Renner, "Security in quantum cryptography." *arXiv:2102.00021*, 2021.

[147] A. K. Ekert, "Quantum cryptography based on bell's theorem," *Phys. Rev. Lett.*, vol. 67, pp. 661–663, 1991.

[148] J. Armengol, B. Furch, C. de Matos, O. Minster, L. Cacciapuoti, M. Pfennigbauer, M. Aspelmeyer, T. Jennewein, R. Ursin, T. Schmitt-Manderbach, G. Baister, J. Rarity, W. Leeb, C. Barbieri, and H. Weinfurter, "Quantum communications at ESA: Towards a space experiment on the ISS," *Acta Astronautica*, vol. 63 (1-4), pp. 165 – 178, 2008.

[149] J. Pan, "Quantum science satellite," *Chinese Journal of Space Science*, vol. 34(5), pp. 547–549, 2014.

[150] H. C. Lim, A. Yoshizawa, H. Tsuchida, and K. Kikuchi, "Wavelength-multiplexed distribution of highly entangled photon-pairs over optical fiber," *Optics express*, vol. 16, pp. 22099–104, 2009.

[151] S. Wengerowsky, S. K. Joshi, F. Steinlechner, H. Hübel, and R. Ursin, "An entanglement-based wavelength-multiplexed quantum communication network," *Nature*, vol. 564, no. 7735, pp. 225–228, 2018.

[152] I. Herbauts, B. Blauensteiner, A. Poppe, T. Jennewein, and H. Hübel, "Demonstration of active routing of entanglement in a multi-user network," *Optics express*, vol. 21, pp. 29013–24, 2013.

[153] V. Zapatero and M. Curty, "Long-distance device-independent quantum key distribution," *Scientific Reports*, vol. 9, no. 1, p. 17749, 2019.

[154] C. Panayi, M. Razavi, X. Ma, and N. Lütkenhaus, "Memory-assisted measurement-device-independent quantum key distribution," *IOP Publishing*, vol. 16, no. 4, p. 043005, 2014.

[155] D. Rauch, J. Handsteiner, A. Hochrainer, J. Gallicchio, A. S. Friedman, C. Leung, B. Liu, L. Bulla, S. Ecker, F. Steinlechner, R. Ursin, B. Hu, D. Leon, C. Benn, A. Ghedina, M. Cecconi, A. H. Guth, D. I. Kaiser, T. Scheidl, and A. Zeilinger, "Cosmic bell test using random measurement settings from high-redshift quasars," *Phys. Rev. Lett.*, vol. 121, p. 080403, 2018.

[156] D. Bouwmeester, J.-W. Pan, K. Mattle, M. Eibl, H. Weinfurter, and A. Zeilinger, "Experimental quantum teleportation," *Nature*, vol. 390, no. 6660, pp. 575–579, 1997.

[157] D.-S. Ding, W. Zhang, Z. Zhou, S. Shuai, G. Xiang, X. Wang, Y.-K. Jiang, B.-S. Shi, and G.-C. Guo, "Quantum storage of orbital angular momentum entanglement in an atomic ensemble," *Phys. Rev. Lett*, vol. 114, 2014.

[158] F. Steinlechner, S. Ecker, M. Fink, B. Liu, J. Bavaresco, M. Huber, T. Scheidl, and R. Ursin, "Distribution of high-dimensional entanglement via an intra-city free-space link," *Nature Communications*, vol. 8, no. 1, p. 15971, 2017.

[159] P. Townsend, "Simultaneous quantum cryptographic key distribution and conventional data transmission over installed fibre using wavelength-division multiplexing," *Electronics Letters*, vol. 33, no. 3, pp. 188–190, 1997.

[160] O. DeLange, "Wide-band optical communication systems: Part ii-frequency-division multiplexing," *Proceedings of the IEEE*, vol. 58, pp. 1683 – 1690, 1970.

[161] V. R. Balaji, M. Murugan, and S. Robinson, "Optimization of dense wavelength division multiplexing demultiplexer with 25ghz uniform channel spacing." *arXiv:1608.00235*, 2016.

[162] D. Tan, A. Grieco, and Y. Fainman, "Towards 100 channel dense wavelength division multiplexing with 100ghz spacing on silicon," *Optics Express*, vol. 22, 2014.

[163] P. Townsend, "Simultaneous quantum cryptographic key distribution and conventional data transmission over installed fibre using wavelength-division multiplexing," *Electronics Letters*, vol. 33, pp. 188–190(2), 1997.

[164] P. Townsend, "Secure key distribution system based on quantum cryptography," *Electronics Letters*, vol. 30, pp. 809–811(2), 1994.

[165] C. Marand and P. D. Townsend, "Quantum key distribution over distances as long as 30 km," *Opt. Lett.*, vol. 20, no. 16, pp. 1695–1697, 1995.

[166] T. Eriksson, M. Sasaki, R. Luis, B. Puttnam, G. Rademacher, M. Fujiwara, Y. Awaji, H. Furukawa, N. Wada, and M. Takeoka, "Wavelength division multiplexing of 194 continuous variable quantum key distribution channels," *Journal of Lightwave Technology*, vol. PP, pp. 1–1, 2020.

[167] J. Mora, W. Amaya, A. Ruiz-Alba, A. Martinez, D. Calvo, V. Garcia-Muñoz, and J. Capmany, "Simultaneous transmission of 20x2 wdm/scm-qkd and 4 bidirectional classical channels over a pon," *Opt. Express*, vol. 20, pp. 16358–16365, 2012.

[168] K. A. Patel, J. F. Dynes, I. Choi, A. W. Sharpe, A. R. Dixon, Z. L. Yuan, R. V. Penty, and A. J. Shields, "Coexistence of high-bit-rate quantum key distribution and data on optical fiber," *Phys. Rev. X*, vol. 2, p. 041010, 2012.

[169] R. Kumar, H. Qin, and R. Alléaume, "Coexistence of continuous variable qkd with intense dwdm classical channels," *New Journal of Physics*, vol. 17, 2014.

[170] L.-J. Wang, K.-H. Zou, W. Sun, Y. Mao, Y.-X. Zhu, H.-L. Yin, Q. Chen, Y. Zhao, F. Zhang, T.-Y. Chen, and J.-W. Pan, "Long-distance copropagation of quantum key distribution and terabit classical optical data channels," *Phys. Rev. A*, vol. 95, p. 012301, 2017.

[171] B.-X. Wang, Y. Mao, L. Shen, L. Zhang, X.-B. Lan, D. Ge, Y. Gao, J. Li, Y.-L. Tang, S.-B. Tang, J. Zhang, T.-Y. Chen, and J.-W. Pan, "Long-distance transmission of quantum key distribution coexisting with classical optical communication over a weakly-coupled few-mode fiber," *Opt. Express*, vol. 28, no. 9, pp. 12558–12565, 2020.

[172] R. Alléaume, R. Aymeric, C. Ware, and Y. Jaouën, "Technology trends for mixed qkd/wdm transmission up to 80 km," in *Optical Fiber Communication Conference (OFC) 2020*, p. M4A.1, Optical Society of America, 2020.

[173] T. A. Eriksson, T. Hirano, B. J. Puttnam, G. Rademacher, R. S. Luís, M. Fujiwara, R. Namiki, Y. Awaji, M. Takeoka, N. Wada, and M. Sasaki, "Wavelength division multiplexing of continuous variable quantum key distribution and 18.3 tbit/s data channels," *Communications Physics*, vol. 2, no. 1, p. 9, 2019.

[174] S. K. Joshi, D. Aktas, S. Wengerowsky, M. Lončarić, S. P. Neumann, B. Liu, T. Scheidl, G. C. Lorenzo, Ž. Samec, L. Kling, A. Qiu, M. Razavi, M. Stipčević, J. G. Rarity, and R. Ursin, "A trusted node–free eight-user metropolitan quantum communication network," *Science Advances*, vol. 6, no. 36, 2020.

[175] X. Liu, X. Yao, R. Xue, H. Wang, H. Li, Z. Wang, L. You, X. Feng, F. Liu, K. Cui, Y. Huang, and W. Zhang, "An entanglement-based quantum network based on symmetric dispersive optics quantum key distribution," *APL Photonics*, vol. 5, no. 7, p. 076104, 2020.

[176] Y. Shi, S. Moe Thar, H. S. Poh, J. A. Grieve, C. Kurtsiefer, and A. Ling, "Stable polarization entanglement based quantum key distribution over a deployed metropolitan fiber," *Applied Physics Letters*, vol. 117, no. 12, p. 124002, 2020.

[177] N. B. Lingaraju, H.-H. Lu, S. Seshadri, D. E. Leaird, A. M. Weiner, and J. M. Lukens, "Adaptive bandwidth management for entanglement distribution in quantum networks." *arXiv:2010.10369*, 2020.

[178] D. Aktas, B. Fedrici, F. Kaiser, T. Lunghi, L. Labonté, and S. Tanzilli, "Entanglement distribution over 150 km in wavelength division multiplexed channels for quantum cryptography," *Laser & Photonics Reviews*, vol. 10, no. 3, pp. 451–457, 2016.

[179] T. Inagaki, N. Matsuda, O. Tadanaga, M. Asobe, and H. Takesue, "Entanglement distribution over 300 km of fiber," *Opt. Express*, vol. 21, no. 20, pp. 23241–23249, 2013.

[180] Z. Zhong and H. Li, "Analysis and simulation of morphology algorithm for fiber optic hydrophone array in marine seismic exploration," *Journal of Coastal Research*, pp. 145–148, 2019.

[181] H.-J. Briegel, W. Dür, J. I. Cirac, and P. Zoller, "Quantum repeaters: The role of imperfect local operations in quantum communication," *Phys. Rev. Lett.*, vol. 81, pp. 5932–5935, 1998.

[182] C.-W. Chou, J. Laurat, H. Deng, K. S. Choi, H. de Riedmatten, D. Felinto, and H. J. Kimble, "Functional quantum nodes for entanglement distribution over scalable quantum networks," *Science*, vol. 316, no. 5829, pp. 1316–1320, 2007.

[183] H. Bernien, B. Hensen, W. Pfaff, G. Koolstra, M. S. Blok, L. Robledo, T. H. Taminiau, M. Markham, D. J. Twitchen, L. Childress, and R. Hanson, "Heralded entanglement between solid-state qubits separated by three metres," *Nature*, vol. 497, no. 7447, pp. 86–90, 2013.

[184] S. Pirandola, R. Laurenza, C. Ottaviani, and L. Banchi, "Fundamental limits of repeaterless quantum communications," *Nature Communications*, vol. 8, no. 1, p. 15043, 2017.

[185] J. G. Rarity, P. R. Tapster, P. M. Gorman, and P. Knight, "Ground to satellite secure key exchange using quantum cryptography," *New Journal of Physics*, vol. 4, pp. 82–82, 2002.

[186] L. Shengkai, W.-Q. Cai, W. Liu, L. Zhang, Y. Li, J. Wang, J. Yin, Q. Shen, Y. Cao, Z.-P. Li, F.-Z. Li, X. Chen, L.-H. Sun, J.-J. Jia, J.-C. Wu, X.-J. Jiang, J.-F. Wang, Y.-M. Huang, Q. Wang, and J.-W. Pan, "Satellite-to-ground quantum key distribution," *Nature*, vol. 549, 2017.

[187] L. Shengkai, W.-Q. Cai, J. Handsteiner, B. Liu, J. Yin, L. Zhang, D. Rauch, M. Fink, J.-G. Ren, W. Liu, Y. Li, Q. Shen, Y. Cao, F.-Z. Li, J.-F. Wang, Y.-M. Huang, L. Deng, T. Xi, L. Ma, and J.-W. Pan, "Satellite-relayed intercontinental quantum network," *Phys. Rev. Lett*, vol. 120, 2018.

[188] J.-P. Chen, C. Zhang, Y. Liu, C. Jiang, W. Zhang, X.-L. Hu, J.-Y. Guan, Z.-W. Yu, H. Xu, J. Lin, M.-J. Li, H. Chen, H. Li, L. You, Z. Wang, X.-B. Wang, Q. Zhang, and J.-W. Pan, "Sending-or-not-sending with independent lasers: Secure twin-field quantum key distribution over 509 km," *Phys. Rev. Lett.*, vol. 124, p. 070501, 2020.

[189] R. Bedington, J. M. Arrazola, and A. Ling, "Progress in satellite quantum key distribution," *npj Quantum Information*, vol. 3, no. 1, p. 30, 2017.

[190] E. Meyer-Scott, N. Prasannan, C. Eigner, V. Quiring, J. M. Donohue, S. Barkhofen, and C. Silberhorn, "High-performance source of spectrally pure, polarization entangled photon pairs based on hybrid integrated-bulk optics," *Opt. Express*, vol. 26, no. 25, pp. 32475–32490, 2018.

[191] A. Fedrizzi, T. Herbst, A. Poppe, T. Jennewein, and A. Zeilinger, "A wavelength-tunable fiber-coupled source of narrowband entangled photons," *Opt. Express*, vol. 15, no. 23, pp. 15377–15386, 2007.

[192] G. Molina-Terriza, J. P. Torres, and L. Torner, "Twisted photons," *Nature Physics*, vol. 3, no. 5, pp. 305–310, 2007.

[193] T. Zhong, H. Zhou, R. D. Horansky, C. Lee, V. B. Verma, A. E. Lita, A. Restelli, J. C. Bienfang, R. P. Mirin, T. Gerrits, S. W. Nam, F. Marsili, M. D. Shaw, Z. Zhang, L. Wang,

D. Englund, G. W. Wornell, J. H. Shapiro, and F. N. C. Wong, "Photon-efficient quantum key distribution using time–energy entanglement with high-dimensional encoding," *New Journal of Physics*, vol. 17, no. 2, p. 022002, 2015.

[194] R. Fickler, R. Lapkiewicz, M. Huber, M. P. Lavery, M. J. Padgett, and A. Zeilinger, "Interface between path and orbital angular momentum entanglement for high-dimensional photonic quantum information," *Nature Communications*, vol. 5, no. 1, p. 4502, 2014.

[195] G. He, C. Zhu, Y. Jiang, J. Ren, Y. Guo, and J. Jing, "Generation of path-polarization hyperentanglement using quasi-phase-matching in quasi-periodic nonlinear photonic crystal," *Scientific reports*, vol. 7, no. 1, pp. 4954–4954, 2017.

[196] A. K. Ekert, "Quantum cryptography based on bell's theorem," *Phys. Rev. Lett.*, vol. 67, pp. 661–663, 1991.

[197] T. Scheidl, R. Ursin, A. Fedrizzi, S. Ramelow, X.-s. Ma, T. Herbst, R. Prevedel, L. Ratschbacher, J. Kofler, T. Jennewein, and A. Zeilinger, "Feasibility of 300 km quantum key distribution with entangled states," *New J. Phys.*, vol. 11, 2010.

[198] X. Ma, C.-H. Fung, and H.-K. Lo, "Quantum key distribution with entangled photon sources," *Phys. Rev. A*, vol. 76, 2007.

[199] M. Koashi and J. Preskill, "Secure quantum key distribution with an uncharacterized source," *Phys. Rev. Lett.*, vol. 90, p. 057902, 2003.

[200] D. Elkouss, A. Leverrier, R. Alléaume, and J. Boutros, "Efficient reconciliation protocol for discrete-variable quantum key distribution," *Computing Research Repository - CORR*, pp. 1879 – 1883, 2009.

[201] N. Gisin, G. Ribordy, W. Tittel, and H. Zbinden, "Quantum cryptography," *Rev. Mod. Phys.*, vol. 74, pp. 145–195, 2002.

[202] Toptica, Photonics, *Datasheet Tunable Diode Lasers*, 2018. `https://www.toptica.com/fileadmin/Editors_English/11_brochures_datasheets/01_brochures/toptica_BR_Scientific_Lasers.pdf`, Accessed: 2021-02-04.

[203] S. P. Neumann, "Towards narrow-band photon pair sources for continuous-wave entanglement swapping," (Master thesis, University of Vienna, 2015).

[204] S. Manjooran, H. Zhao, I. T. Lima, and A. Major, "Phase-matching properties of PPKTP, MgO:PPSLT and MgO:PPcLN for ultrafast optical parametric oscillation in the visible and near-infrared ranges with green pump," *Laser Physics*, vol. 22, no. 8, pp. 1325–1330, 2012.

[205] H. Zhao, I. T. L. Jr., and A. Major, "Peculiarities of temperature-dependent Sellmeier equations for periodically poled KTiOPO4 crystal in the near-infrared and visible ranges," in *Photonics North 2010* (H. P. Schriemer and R. N. Kleiman, eds.), vol. 7750, pp. 389 – 396, International Society for Optics and Photonics, SPIE, 2010.

[206] M. V. Jabir and G. K. Samanta, "Robust, high brightness, degenerate entangled photon source at room temperature," *Scientific Reports*, vol. 7, p. 12613, 2017.

[207] D. Richter, C. Voigtländer, R. Becker, J. Thomas, A. Tünnermann, and S. Nolte, "Efficient volume bragg gratings in various transparent materials induced by femtosecond laser pulses," in *2011 Conference on Lasers and Electro-Optics Europe and 12th European Quantum Electronics Conference (CLEO EUROPE/EQEC)*, pp. 1–1, 2011.

[208] H. Kogelnik, "Coupled wave theory for thick hologram gratings," *The Bell System Technical Journal*, vol. 48, no. 9, pp. 2909–2947, 1969.

[209] Roithner Lasertechnik, *TTM8000 Time Tagging Module with 8-Channels*, 2015. `http://www.roithner-laser.com/datasheets/accessories/ttm8000_manual.pdf`, Accessed: 2021-02-22.

[210] S. P. Neumann, T. Scheidl, M. Selimovic, M. Pivoluska, B. Liu, M. Bohmann, and R. Ursin, "A model for optimizing quantum key distribution with continuous-wave pumped entangled-photon sources," 2021.

[211] P. Townsend, S. Phoenix, K. Blow, and S. Barnett, "Quantum cryptography for multi-user passive optical networks," *Electronics Letters*, vol. 30, pp. 1875 – 1877, 1994.

[212] A. Ciurana, J. Martínez Mateo, M. Peev, A. Poppe, N. Walenta, H. Zbinden, and V. Martin, "Quantum metropolitan optical network based on wavelength division multiplexing," *Optics Express*, vol. 22, p. 1576–1593, 2014.

[213] K.-i. Yoshino, M. Fujiwara, A. Tanaka, S. Takahashi, Y. Nambu, A. Tomita, S. Miki, T. Yamashita, Z. Wang, M. Sasaki, and A. Tajima, "High-speed wavelength-division multiplexing quantum key distribution system," *Optics letters*, vol. 37, pp. 223–5, 2012.

[214] T. Scheidl, "A fundamental test and an application of quantum entanglement," (Dissertation, University of Vienna, 2009).

[215] N. Kiang, J. Siefert, G. Govindjee, and R. Blankenship, "Spectral signatures of photosynthesis. i. review of earth organisms," *Astrobiology*, vol. 7, pp. 222–51, 2007.

[216] S. Jacquemoud and S. Ustin, "Application of radiative transfer models to moisture content estimation and burned land mapping," *International Workshop on Remote Sensing and GIS Applications to Forest Fire Management (E. Chuvieco, P. Martin and C. Justice, eds), Ghent (Belgium)*, pp. 3-12, 2003.

[217] L. Shengkai, W.-Q. Cai, W. Liu, L. Zhang, Y. Li, J. Wang, J. Yin, Q. Shen, Y. Cao, Z.-P. Li, F.-Z. Li, X. Chen, L.-H. Sun, J.-J. Jia, J.-C. Wu, X.-J. Jiang, J.-F. Wang, Y.-M. Huang, Q. Wang, and J.-W. Pan, "Satellite-to-ground quantum key distribution," *Nature*, vol. 549, 2017.

[218] L. Shengkai, W.-Q. Cai, J. Handsteiner, B. Liu, J. Yin, L. Zhang, D. Rauch, M. Fink, J.-G. Ren, W. Liu, Y. Li, Q. Shen, Y. Cao, F.-Z. Li, J.-F. Wang, Y.-M. Huang, L. Deng, T. Xi, L. Ma, and J.-W. Pan, "Satellite-relayed intercontinental quantum network," *Phys. Rev. Lett*, vol. 120, 2018.

[219] J. A. Curcio, L. F. Drummeter, and G. L. Knestrick, "An atlas of the absorption spectrum of the lower atmosphere from 5400å to 8520å," *Appl. Opt.*, vol. 3, no. 12, pp. 1401–1409, 1964.

[220] E. Leitgeb, T. Plank, M. S. Awan, P. Brandl, W. Popoola, Z. Ghassemlooy, F. Ozek, and M. Wittig, "Analysis and evaluation of optimum wavelengths for free-space optical transceivers," *2010 12th International Conference on Transparent Optical Networks*, pp 1-7, 2010.

[221] S. Wengerowsky, S. K. Joshi, F. Steinlechner, H. Hübel, and R. Ursin, "An entanglement-based wavelength-multiplexed quantum communication network," *Nature*, vol. 564, no. 7735, pp. 225–228, 2018.

[222] H. Kim, O. Kwon, and H. S. Moon, "Pulsed sagnac source of polarization-entangled photon pairs in telecommunication band," *Scientific Reports*, vol. 9, no. 1, p. 5031, 2019.

[223] "Safety and laser products - part 1: Equipment classification and requirements," *International Electrotechnical Commission, (IEC-60825-1), Ed. 3*, 2007.

[224] ID Quantique, *Single photon detectors used in free space communication*, 2016. https://dvd.ilphotonics.com/Id%20Quantique%20-%20fiber-coupled%20detectors%20-%20electronics%20-%20fiber-coupled%20lasers/Detectors/Infrared%20Single-Photon%20Detectors/ID220_ApplicationNotes/Free%20Space%20Communication_Application%20Note.pdf, Accessed: 2021-03-29.

[225] I. I. Kim, B. McArthur, and E. J. Korevaar, "Comparison of laser beam propagation at 785 nm and 1550 nm in fog and haze for optical wireless communications," *Proc. SPIE 4214, Optical Wireless Communications III*, pp 26-37, 2001.

[226] Single Quantum, *Single Quantum Eos - SNSPD Closed-Cycle System*, 2019. https://singlequantum.com/wp-content/uploads/2019/05/Single-Quantum-Eos.pdf, Accessed: 2021-03-29.

[227] Ondax, Inc, *Datasheet ASE Suppression Filters*, 2013. https://edge.coherent.com/assets/pdf/04_NoiseBlock_ASE_Supression_Filters.pdf, Accessed: 2020-07-23.

[228] M. Okano, H. H. Lim, R. Okamoto, N. Nishizawa, S. Kurimura, and S. Takeuchi, "0.54 μm resolution two-photon interference with dispersion cancellation for quantum optical coherence tomography," *Scientific Reports*, vol. 5, no. 1, p. 18042, 2015.

[229] A. Lohrmann, C. Perumangatt, A. Villar, and A. Ling, "Broadband pumped polarization entangled photon-pair source in a linear beam displacement interferometer," *Applied Physics Letters*, vol. 116, no. 2, p. 021101, 2020.

[230] U. A. Javid, J. Ling, J. Staffa, M. Li, Y. He, and Q. Lin, "Ultra-broadband entangled photons on a nanophotonic chip." *arXiv:2101.04877*, 2021.

[231] Raicol crystals Ltd., *Datasheet: Nonlinear Crystal Pioneers*, 2018. [Online]. Available: http://raicol.com/wp-content/uploads/2018/11/raicolpages.pdf Accessed: 2020-07-23.

[232] T. Ohara, H. Takara, T. Yamamoto, H. Masuda, T. Morioka, M. Abe, and H. Takahashi, "Over-1000-channel ultradense wdm transmission with supercontinuum multicarrier source," *J. Lightwave Technol.*, vol. 24, no. 6, p. 2311, 2006.

[233] M. Krenn, M. Malik, M. Erhard, and A. Zeilinger, "Orbital angular momentum of photons and the entanglement of laguerre–gaussian modes," *Philosophical Transactions of the Royal Society A: Mathematical, Physical and Engineering Sciences*, vol. 375, no. 2087, p. 20150442, 2017.

[234] Y. Yun, A. Vetter, R. Stegmueller, S. Ferrari, W. H. P. Pernice, C. Rockstuhl, and C. Lee, "Superconducting-nanowire single-photon spectrometer exploiting cascaded photonic crystal cavities," *Phys. Rev. Applied*, vol. 13, p. 014061, 2020.

[235] R. Cheng, C.-L. Zou, X. Guo, S. Wang, X. Han, and H. X. Tang, "Broadband on-chip single-photon spectrometer," *Nature Communications*, vol. 10, no. 1, p. 4104, 2019.

[236] J. C. Matthews, X.-Q. Zhou, H. Cable, P. J. Shadbolt, D. J. Saunders, G. A. Durkin, G. J. Pryde, and J. L. O'Brien, "Towards practical quantum metrology with photon counting," *npj Quantum Information*, vol. 2, no. 1, p. 16023, 2016.

[237] D. Kolev and M. Toyoshima, "Satellite-to-ground optical communications using small optical transponder (sota) – received-power fluctuations," *Optics Express*, vol. 25, p. 28319, 2017.

Acknowledgements

In the course of my Ph.D., the amount of support was invaluable; not only in terms of working scientifically on a high level but also on a personal scope. Countless discussions and long hours of exchanging ideas enabled me to leap forward to successfully finish this very thesis.

This journey was made possible by my former supervisor Anton Zeilinger, who welcomed me to work in his research group at IQOQI Vienna in 2017 and gave me the chance to be part of an amazing team. This team was comprised of, amongst others, Mario Krenn and Manuel Erhard, who both spend many hours patiently answering my questions and introducing me to the world of quantum optics, both on a theoretical and experimental level. Together with numerous hours of discussions with Jaroslav Kysela, I conducted my first quantum-optical experiment, namely the nonlinear interference of two remote photon sources. This taught me that patience and persistence pay off eventually.

After two years, in 2019, Rupert Ursin took me into his research group, where, with more matured scientific knowledge, I could unfold myself in a fantastic experiment. The wavelength-multiplexing experiment was a simple but highly elegant idea of improving QKD systems. In his team, I was amazed by the unselfish commitment and helpfulness of all members. This included Lukas Bulla, Sebastian Neumann, and Sebastian Ecker, who introduced me to Sagnac-sources and inspired me with their enthusiasm and highly skilled knowledge. Later on, Martin Bohmann joined Rupert Ursin's group, who helped with great effort to formulate and articulate our ideas into a coherent form for the publication. The last member of the working group, but certainly not the least, I would like to thank is Lukas Achatz, who was a loyal and highly motivated co-worker and helped me through many hours of measurement.

Great thanks have to be expressed also to Marcus Huber, who swiftly took over the position as my supervisor, without hesitation, when the time of my PhD was coming to an end.

My mother, Sylvia, who patiently and extensively read and corrected my thesis, I have to thank a thousand times, as she put many a sentences and wordings into a contiguous form.

My dearest Hannah, the love of my life, stood at my side even at extremely challenging times, when I believed to have reached a dead end. She gave me the confidence and patience to overcome my fears and insecurities, which enabled me to carry on despite being in a desperate state.

Finally, I would like to thank Roland Blach, Krishna Dovzhik, Evelyn Ortega, Johannes Handsteiner, Armin Hochrainer, and Xuemei Gu for the many hours of discussions and helpful advice.